ISSN 1349-6832

JEOL NEWS

September 2014
Vol.49
No.1

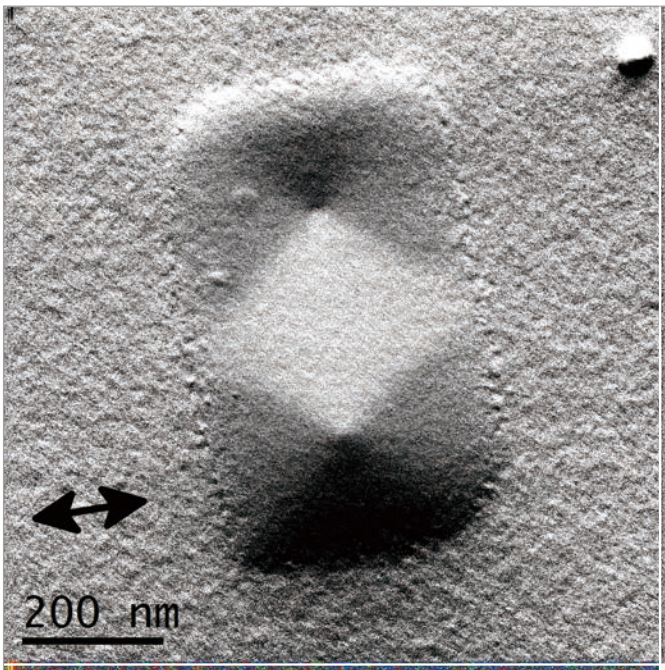

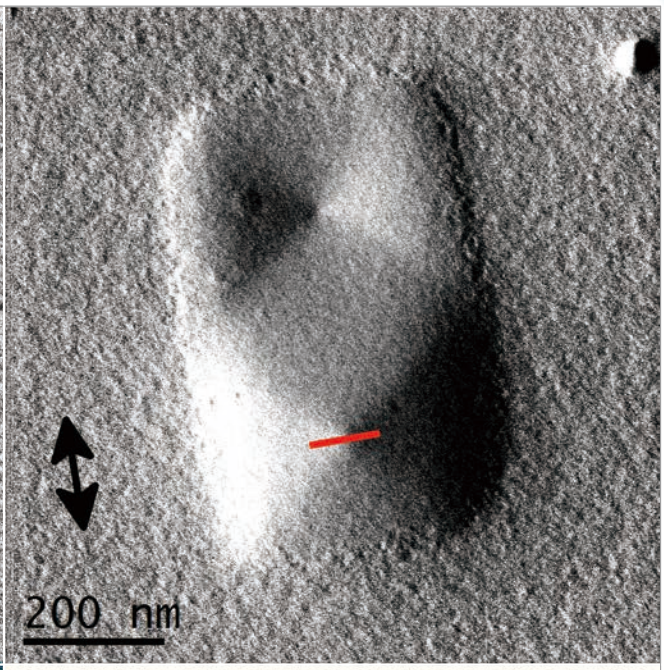

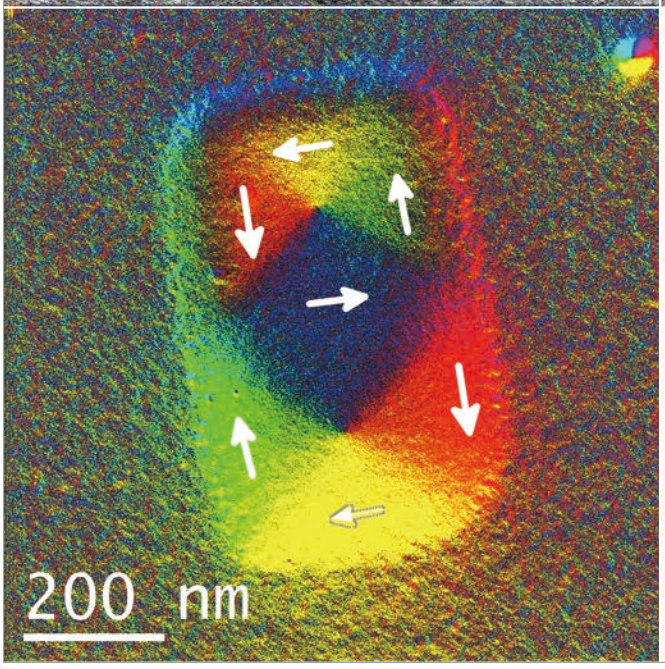

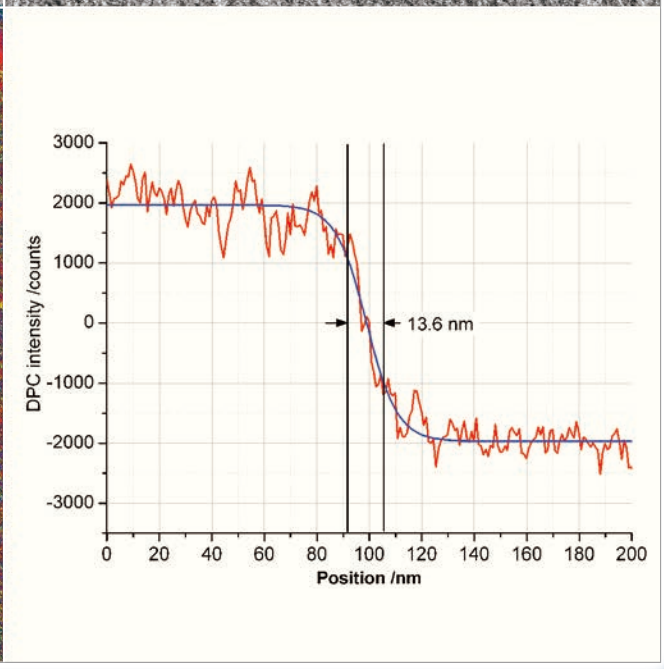

JEOL

Contents

JEOL News

September 2014 Vol.49 No.1

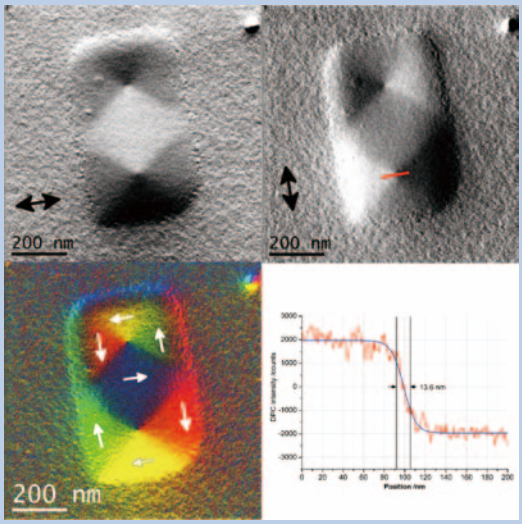

Cover micrograph

Aberration Corrected DPC STEM mapping of the two vortex magnetic domain structure in a 40 nm thick rectangular Fe element (topmost and bottom left images) and measurement of the vortex core magnetic induction profile (bottom right). (See page 7)

Development of Aberration Corrected Differential Phase Contrast (DPC) STEM

Damien McGrouther, Maria-Jose Benitez, Sam McFadzean, and Stephen McVitie

SUPA School of Physics & Astronomy, University of Glasgow

In this article we demonstrate that aberration correction for STEM probes has been achieved for field-free Lorentz STEM imaging of magnetic samples, and that, an order of magnitude improvement of spatial resolution has been obtained. We believe, that our achieved <1 nm spatial resolution is currently the best in the world for direct imaging of magnetic structure by electron microscopy.

Introduction

Correctors for spherical aberration (Cs) of electron lenses have resulted in a step-change in performance for both TEM and STEM instruments, making atomic scale imaging and analysis of materials routinely possible. Working in collaboration with JEOL and partners we show that aberration correction and other technologies have enabled an order of magnitude improvement in the capability to image magnetic behaviour in thin nano-scale structures important for current and future information technologies.

The imaging of magnetic structure in the electron microscope has a long history that extends back to the 1950's. The group of imaging techniques used to generate magnetic contrast are collectively known as "Lorentz microscopy" [1] as they can be understood in terms of the classical Lorentz force ($\underline{F} = -e(\underline{v} \times \underline{B})$) experienced by the beam electrons traversing the specimen. Thin magnetic samples also exhibit a quantum interaction with the beam, via the Aharonov-Bohm effect, whereby the phase of the passing electron waves are altered. Thus, for imaging magnetic samples the Lorentz techniques are a branch of phase contrast microscopy. In TEM mode, Fresnel and Foucault techniques have been extensively used. Both are effective in generating images showing strong magnetic contrast but are limited in spatial resolution or linearity. TEM Holographic techniques have been quite successful and shown to be capable of higher resolution imaging of magnetic induction [2], however, their basis is off-line image reconstruction and they cannot be applied to all sample geometries.

At the University of Glasgow, we have developed the STEM based Lorentz imaging mode of Differential Phase Contrast (DPC) over the last 30 years. In this article we demonstrate that in collaboration with JEOL, CEOS GmbH, Gatan Inc., Deben Ltd and University of Warwick, that aberration corrected DPC STEM has been achieved enabling the study of magnetic structure with world-leading spatial resolution better than 1 nanometre. Furthermore, in contrast to holographic techniques, these images are available in real time at near video frame-rates.

University of Glasgow, G12 8QQ, United Kingdom

E-mail: damien.mcgrouther@glasgow.ac.uk

Experimental

On a JEOL JEM-ARM200FCS TEM/STEM equipped with cold field emission gun (C-FEG), a CEOS Cs STEM probe corrector and HR pole-piece, several major developments have been made to successfully realise DPC mode imaging. After describing the general concept of the DPC mode we will deal with each of the required developments in turn.

Figure 1 depicts the setup required for DPC mode imaging, where the focused electron probe is raster-scanned across the specimen with the scattered transmitted cone of electrons being detected in the far-field by a segmented STEM detector. If the specimen is magnetic and contains regions with components of the magnetic induction $\underline{B}$ oriented in the specimen plane, then it can be shown that the beam is deflected through an angle:

$$\underline{\beta} = \frac{e\lambda}{h}\int \underline{B} \times \underline{n}\, dz$$

where e is the charge on the electron, λ it's wavelength, $\underline{B}$ the magnetic induction in the specimen and $\underline{n}$ the unit vector along the electron trajectory. The classical Lorentz deflection induced by a typical magnetic sample is relatively weak. The deflection angle, β, is in the range 1-100 micro-radians and is very much smaller than typical diffraction scattering angles which are generally >3 milli-radians. The segmented detector is used to detect such Lorentz deflection

of the beam by measuring difference signals from opposite quadrants. An alternative interpretation of the interaction of a thin magnetic sample on the beam is that the electron beam's wavefunction after passing through the region containing magnetic induction becomes phase-shifted due to the quantum mechanical Aharonov-Bohm effect [3]. Thinking in these terms, by the action of taking difference signals, the gradient of the phase-change due to the sample is measured and hence the technique produces images showing differential phase contrast.

The process of combining the signals from the detector segments to produce live DPC STEM images is described in more detail later.

STEM probe formation for magnetic imaging.

In standard STEM mode, the normally excited objective lens (OL), which produces focused STEM probes with semi-convergence angles, α = 3-30 mrad and has enabled imaging of Si-dumb-bells with information at 0.67 Å. However, the normally excited OL also subjects the sample to a magnetic field of strength ~2 Tesla. A field of such strength would completely saturate the vast majority of magnetic samples, obliterating any magnetic domain structure of interest. Thus, DPC STEM mode imaging must be performed with the OL completely de-excited and the sample residing in field-free or near to field-free conditions. This is easily achieved by switching the microscope into "LOW MAG" mode whereby, the OL goes off and STEM probe formation is controlled by a combination of the variable condenser (CL3) and condenser mini (CM) lenses. In this scenario, and in the absence of an aberration corrector, the diameter of the STEM probe would be dictated by the spherical aberration coefficient of the CM. In collaboration with us, JEOL and CEOS have developed a special optical configuration for the aberration corrector that compensates for the Cs of the CM and have enabled a magnification range that extends up to 2.0 million times. **Figure 2** shows an image for the resulting Ronchigram in this mode that exhibits a flat, aberration corrected, region that extends out to 3.2 milli-radian semi-convergence angle. Using a 70 µm condenser aperture, corresponding to the full diameter of the flat region, STEM imaging of a test sample, Au nano-particles, shown in **Fig. 3**(a), demonstrated that particles with sizes of the order of 1 nm and smaller could be resolved. In fact, Fig. 3(b) demonstrates

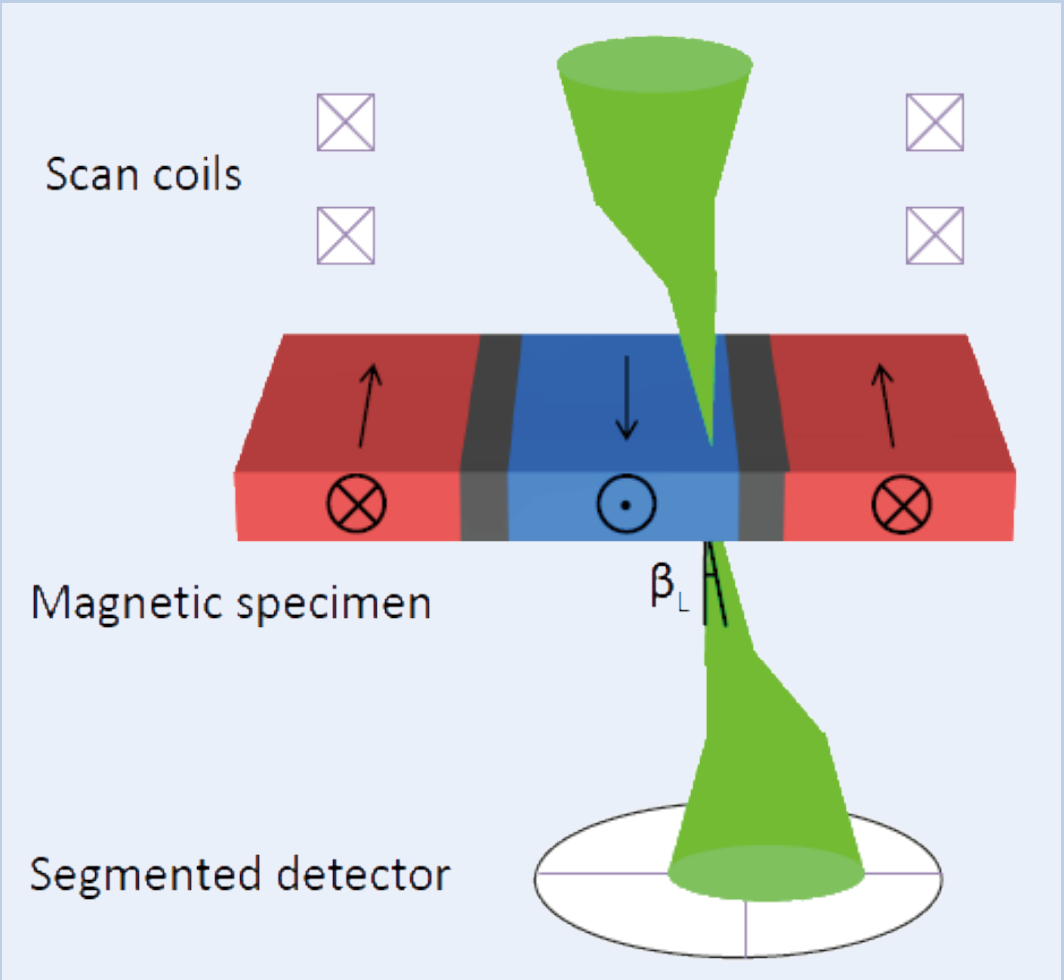

Fig. 1 Diagram illustrating the concept of DPC STEM imaging. Lorentz deflection of the focused electron probe, through an angle $ß_L$, by domains in a thin magnetic sample is detected using a segmented detector.

that the smallest particle that could be resolved had a width of the order of 0.7 nm. Taking the Fast Fourier Transform of Fig. 3(a) (inset of Fig. 3(c)) and forming a radially averaged line profile showed that Fig. 3(a) contains information content up to a maximum spatial frequency of 1.8 nm^{-1}. All of these observations are in agreement with calculations made by CEOS GmbH who expected that the C_S coefficient of the CM lens should be reduced to the order of several microns and should result in a FWHM probe diameter of 0.8-1.0 nm with spatial resolution defined as being half this value, 0.4.-0.5 nm.

While it would be desirable to always operate with the highest spatial resolution, inevitably a trade-off has to be made. Recalling that the Lorentz deflection angle, ß, can be as small as a few micro-radians, around 1000× smaller than the optimum probe semi-convergence angle α. Higher sensitivity to small Lorentz deflections can be obtained by reducing α at the expense of spatial resolution. This can easily be done by changing to the smallest 10 µm condenser aperture which reduces α to 450 micro-radians but means that the spatial resolution becomes limited by diffraction. Lorentz sensitivity can be increased by

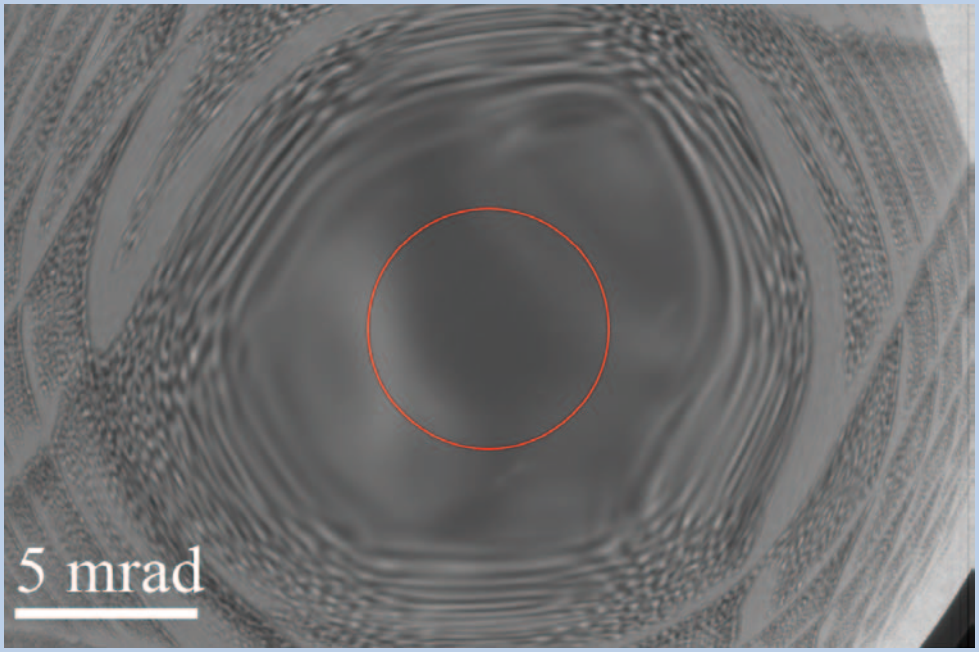

Fig. 2 Ronchigram obtained for (LOW MAG) field free operation on an Au cross-grating replica. The circled region corresponds to the diameter of the 70 mm condenser aperture, corresponding to a 3.2 mrad probe semi-convergence angle.

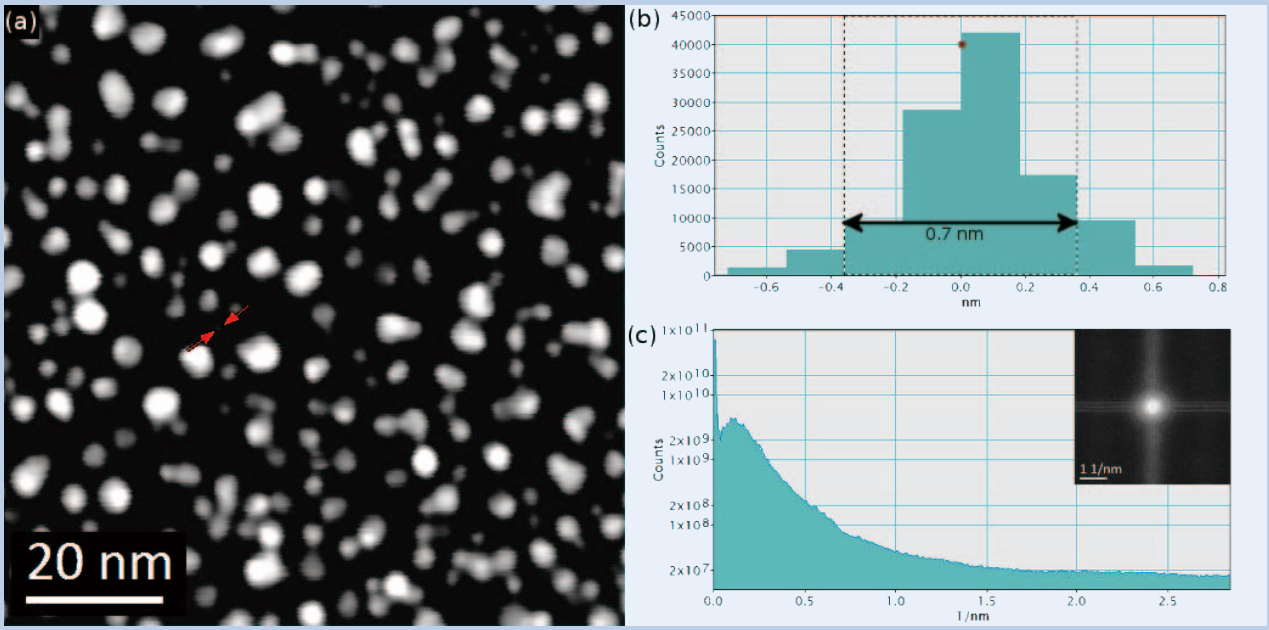

Fig. 3 Demonstration of ultimate (LOW MAG) field free spatial resolution. (a) HAADF image of Au nano-particle test sample, (b) intensity profile across smallest observed particle (indicated between red arrows in (a)), (c) Radially averaged intensity profile of FFT (inset) of (a) .

a further two times, α further reduced to 215 micro-radians, by the combined adjustment of the CL3 lens and the CEOS corrector's adapter lens element (ADL). Under these conditions spatial resolution has been measured to be in the range 3-5 nm.

Nulling and application of in-situ magnetic fields to the specimen

In "LOW MAG" mode, although the OL is completely de-excited, the sample still resides in a modest magnetic field, ~150 Oe directed perpendicular to its plane. This is the result of remanence from the ferromagnetic pole-pieces. For many thin film in-plane magnetised samples the out-of-plane oriented remanent field has little influence on the static magnetic structure. Its strength is generally very much weaker than the strength of the in-plane magnetic anisotropy. In-situ studies of magnetic reversal behaviour can be accomplished by using either the remanent field, or a stronger field applied by partially exciting the OL. Tilting the sample (generally up to +/- 30 degrees is possible) can then be used to nucleate and grow magnetic domains eventually leading to reversal and saturation of the film. For ultra-soft magnetic samples, where the coercivity is very much less than the remanent field strength, it is desirable to be able to reduce to near zero the strength of the remnant field. Utilising a system developed at University of Warwick we can measure the strength of the remanent field at the sample plane using a Hall-probe TEM rod and apply a reverse current through the OL to null it. In this way, very low field strengths, < 1 Oe can be achieved in the sample region.

Segmented DPC detector and video chain

Development of the segmented detector and DPC image acquisition system has required an extensive collaboration involving ourselves, JEOL, Gatan Inc., Deben Ltd and Andrew Armit Designs.

The geometry of the segmented detector employed is depicted in **Fig. 4**(a). It consists of eight segments arranged into an inner solid quadrant (INT0 to INT3) and an outer annular quadrant (EXT0 to EXT3). DPC STEM imaging, detecting the displacement of the transmitted electron disc, is most simply realised by using a camera length that projects the transmitted electron disc onto only the inner quadrants. However, in previous work [4], we have shown that for polycrystalline magnetic thin films, strong and unwanted electrostatic phase fluctuations arise due to diffraction from the nano-scale crystallites with varying orientations. By utilizing a cameral length that projects the transmitted electron disc across the outer annular (as well as the inner) quadrants, the higher spatial frequency electrostatic fluctuations can be "filtered" from the lower spatial frequency magnetic domain and domain wall features.

Conversion of charge signals from the detector segments into video-level voltage signals has been achieved through the development of the SuperFast 8-channel, 2 MHz bandwidth amplifier by Deben

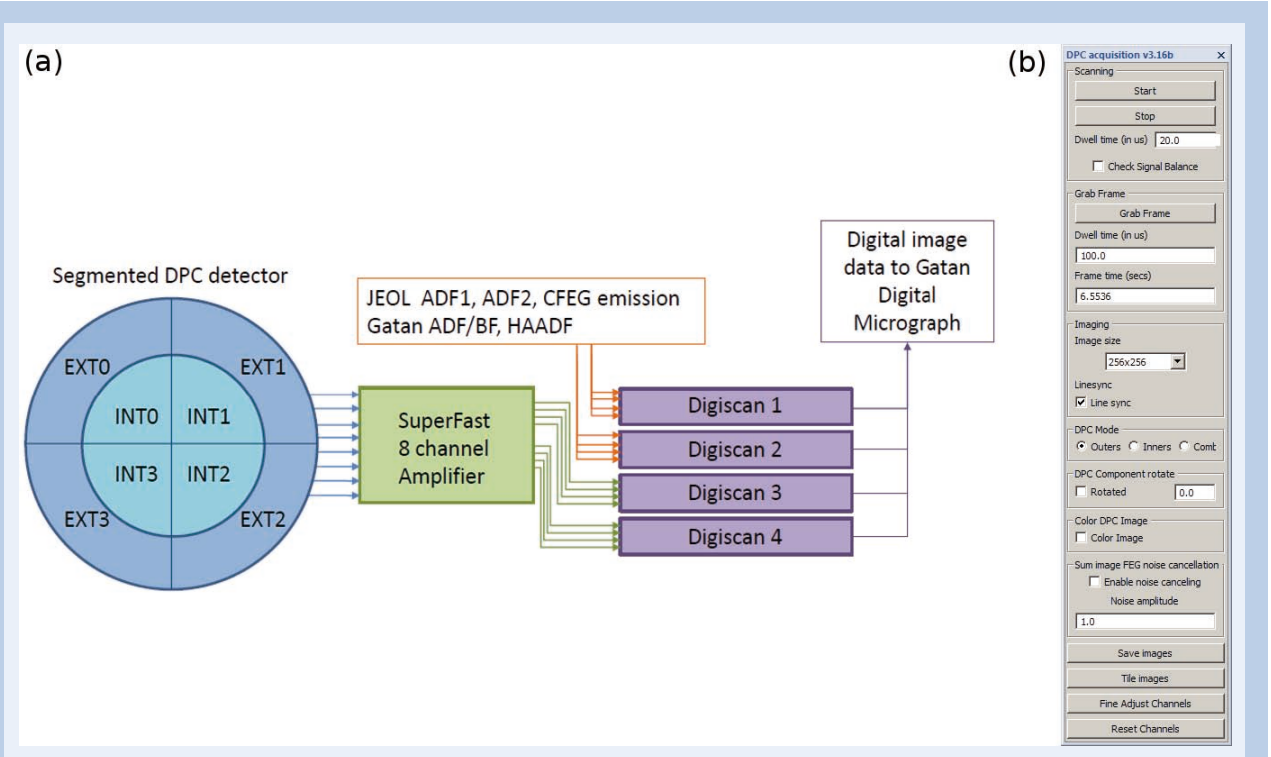

Fig. 4 (a) Schematic of the DPC STEM detector and video signal digitisation, (b) screenshot of the DPC control palette in Digital Micrograph.

& Andrew Armit designs. The SuperFast amplifier is controlled by software and has a wide range of settings enabling selection, for each channel, of input resistance/capacitance for noise reduction/bandwidth selection and gain. "On the fly" arithmetic mixing of channels, is possible and can be used to view live difference signals between segments. However, we prefer to perform such image arithmetic on acquired digital images and utilize the SuperFast amplifier to pass the segment signals unaltered.

Commonly on an advanced STEM instrument such as the JEM-ARM200F, combined image acquisition and point-wise analysis (via Electron Energy Loss Spectroscopy (EELS) or X-ray Energy Dispersive Spectrometry (EDS)) are controlled by Gatan's Model 788 Digiscan II system through Digital Micrograph software. On our JEM-ARM200FCS, the DPC detector adds 8 segment signals to the already lengthy list of signals to be acquired from the common STEM detectors (JEOL ADF1, ADF2, BF, Gatan Model 806 HAADF, Model 807 BF/ADF) and current measurement from the CFEG. Thus, in all, a total of 13 signals were required for acquisition, although not all would be used at any one time. Gatan developed a solution for this by implementing hardware and software that allowed 4 Digiscan II boxes to be operated in parallel. This was achieved in such a way that for recent releases of Digital Micrograph software (from GMS version 2.3.X), this capability is now part of the standard software-base.

Live DPC imaging, enabling magnetic contrast to be visualised, has been achieved through a control palette, Fig. 4(b), created in the Digital Micrograph scripting language by the author. By clicking “Start/Stop” or “Grab Frame” buttons, calls are issued to the Digiscan II boxes that start/stop the imaging process. The individual segment images are visible but magnetic contrast can only be seen by displaying live difference images between opposite segments. Two orthogonal direction components are necessary to reconstruct magnetic orientations and these are achieved by viewing the image pairs “INT0 – INT2”, “INT1 – INT3” if using the inner quadrant (“EXT0 – EXT2” & “EXT1 – EXT3” if using the outer quadrant). Based on these image pairs live colour images showing magnetic orientations are also presented. Quantitative determination of Lorentz deflection, and hence, BS×t, the product of the magnetic induction times the thickness of the specimen, is possible by relatively straightforward post-processing of the recorded DPC images. It is the intention to include a real-time capability so that DPC images can be calibrated in terms of quantitative Lorentz deflection.

Investigation of magnetic samples

In this section we present results obtained from applying the DPC system to investigate the properties and behaviour of magnetic specimens in some of our current research.

Iron nanostructures

The fabrication of nano-scale magnetic structures is a lengthy procedure, most commonly achieved by multi-step lithographic techniques in which the shapes to be created are written into a sensitive resist followed by chemical development, metallisation and "lift-off" steps. Alternatively, rapid direct-writing of magnetic nano-structures can be achieved in focused ion beam and scanning electron microscope (SEM) systems where a needle based system is used to inject an organometallic precursor gas into the region of the beam-scanning [5,6]. Using SEM, such electron beam induced deposition (EBID) has been employed to create rectangular iron elements, **Fig. 5**, and pillars with diameter around 50 nanometres, **Fig. 6**.

Fig. 5(a) and (b) show greyscale DPC images (obtained using Spot L1 and a 10 micron condenser aperture) that highlight the ground state arrangement of magnetisation in the approximately 600 nm × 400 nm × 40 nm thick rectangular elements which were fabricated on Si_3N_4 support membranes. As described earlier, Fig. 5 (a) & (b), are produced by subtracting the video signals from opposing segments on the DPC detector and produce a pair of images with orthogonal directions of sensitivity. Inside the elements strong black and white contrast can be seen that corresponds to the magnetic domain structure, while outside of the elements "noisy" phase contrast from the thin carbon coating used for charge dissipation is observed. The arrangement of the magnetic domain orientations in the element is most easily understood by forming the colour map in Fig. 5(c). From this Fig. it can be seen that the element has formed a flux-closing multi-domain Landau type pattern in which the magnetisation tends to be oriented parallel to the element edges and circulates around two vortices within the elements interior. The spatial extent of each of the vortices is dictated by the magnetic properties of the material, specifically the exchange stiffness and the saturation magnetisation. From polycrystalline alloys involving Co, Ni and Fe, vortex widths have been measured to range from 7-15 nanometres wide [7]. In Fig. 5(d), we have utilised the high spatial resolution afforded by aberration correction of the CM lens to measure a DPC intensity profile from the position of the red line in Fig. 5b. Fig. 5d, shows that for the EBID Fe element (with approximate chemical composition 60% iron, 40% carbon) that the measured width of the vortex core is 13.6 nm.

Narrow pillar-like magnetic structures can be formed by allowing the electron beam in the SEM to dwell on a single location. Such pillars have proved highly effective as magnetically switchable trapping sites when directly written on top of out-of-plane magnetised nanostrips (see reference [8] for a fuller explanation). For these pillars, due to their small diameter, ~ 50 nm, DPC imaging has been used to measure the magnetic field strength needed to switch the pillars magnetisation direction. Fig.s 6(a) and (b) shows colour DPC maps that depict the nanopillars grown on the edge of a grid support. The colour contrast inside the pillars is not simply interpretable in terms of magnetic structure as it is dominated by electrostatic phase gradients from the changing thickness associated with their circular cross-section. In the free-space region immediately surrounding the tip of the pillar, located inside the dashed ellipse, colour contrast relating to the pillar's de-magnetising

fields can be observed. Starting in Fig. 6(a), moving in a clockwise direction around the tip of the pillar, the colour contrast changes from blue to red to yellow. Referring to the colour-wheel inset, this indicates the magnetic fields emanating from the tip are divergent and thus it can be inferred that the pillar is magnetised in an upwards direction. A field of strength 1000 Oe was then applied to the pillar in-situ by partially exciting the OL lens and tilting the specimen to near 30 degrees. After de-exciting the OL and returning the specimen to its untilted state, the colour map in Fig. 6(b) was obtained. Again, the direction of the magnetisation in the pillar was inferred by examining the colour contrast associated with de-magnetisation field from the pillar tip. In Fig. 6(b) it can be seen that the colour contrast has altered and changes from yellow to green to blue when moving in a clockwise sense around the tip. This indicates that the de-magnetisation fields are now convergent at the tip and infers that the magnetisation direction has been switched to a downwards orientation by the applied field.

Multilayered ferromagnetic sample

The high spatial resolution afforded by aberration correction for the field-free mode makes it possible to investigate the behaviour of multi-layered magnetic films in a cross-section type geometry. For a repeated NiFe ferromagnet / FeMn antiferromagnet multilayer sample we have performed DPC imaging in order to understand aspects of its magnetic reversal behaviour. **Fig. 7** shows greyscale DPC images obtained from a

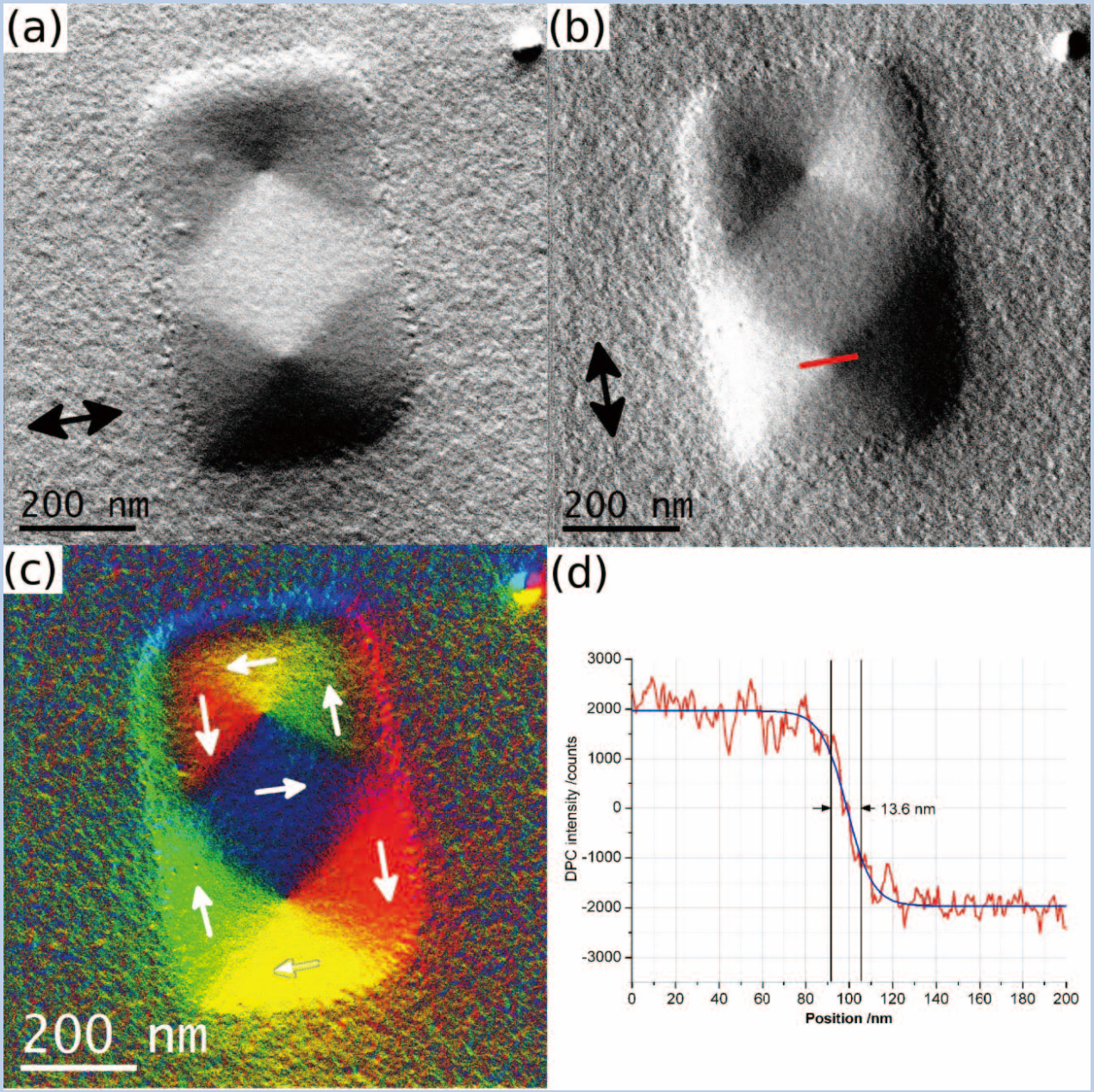

Fig. 5 DPC imaging of EBID Fe nano-element. (a) & (b) horizontal and vertical DPC component images, (c) colour map showing magnetic induction directions, (d) Line-trace measurement of vortex core diameter for line indicated in (b).

FIB cross-section of the multilayer (~ 50 nm thick) with the structure NiFe/(FeMn/NiFe)×10 grown on an oxidised Si substrate with a capping layer of 5 nm of Ta. The NiFe layers had a thickness of 16.5 nm and the FeMn layers 12.8 nm.

Initially the sample was immersed in a large field (around 1000 Oe) to have all the layers in parallel alignment. The DPC image component showing the magnetic induction parallel to the interfaces is shown in Fig. 7 (a) where the NiFe layers appear as bright stripes in the image and the FeMn layers are gray indicating no net induction component in these regions. The variation in contrast within the stripes is a consequence of the granular structure of the film and this gives rise to a diffraction contribution to the phase contrast image. A linetrace from the area indicated by the rectangle in Fig. 7 (a) is shown, this averages the signal over a 74 nm width to reduce the effects of the diffraction contrast from the grain structure. The profile shows the magnetised layer variation very clearly where each magnetic layer is around 16-17 nm wide (i.e. deposited thickness of the film) and the AF layer is 13 nm wide. By tilting the sample in the objective lens field the magnetic state could be altered with individual layers switching and an example of the state part way through the reversal process is shown in Fig. 7 (b) where seven of the eleven magnetic layers have switched their direction of magnetisation, one partially. This can also be seen by comparing the averaged linetraces for Fig.s 7 (a) & (b) for the two different states. The linetraces show the induction in the ferromagnetic layer very clearly and indeed the interface between the ferromagnetic and antiferromagnetic layers shows the transition which is on the order of 1-2 nm.

Reduction of magnetization in nano-scale regions by ion irradiation

Obtaining quantitative measurements regarding the strength of magnetic induction from DPC images is usually straightforward. We have been investigating the use of FIB based ion-irradiation to control the strength of magnetisation in Cr(3 nm)/$Ni_{80}Fe_{20}$(10 nm)/Cr(5 nm) films deposited on Si_3N_4 electron transparent membranes. The key aim for us was to create and characterise narrow irradiated line defects that could act as trapping sites for domain walls in magnetic nanowires [9,10]. **Fig. 8** shows quantitative DPC imaging of a line irradiated at a dose of 8×10^{15} ions cm^{-2}. The components of magnetic induction were mapped parallel, Fig. 8(a), and orthogonal, Fig. 8(b), to the irradiated line. In Fig. 8(a) the irradiated line is observed as a lower intensity feature while it is invisible in Fig. 8(b), the latter is consistent with the component of magnetic induction being continuous across an interface as proved from Maxwell's equations, even though the magnetization is discontinuous. The intensity profile from the region indicated in Fig. 8(a) is plotted in Fig. 8(c) where the vertical axis displays quantitative measurement of the Lorentz deflection of the beam. Quantitative determination of the deflection is achieved by dividing the difference images by the "SUM" image (i.e. summing the images from all segments). Since the diameter of the transmitted electron disc incident on the segmented detector relates to the beam convergence semi-angle, α, which is known, then the Lorentz deflection, ß, can be easily be recovered. In Fig. 8(c), the quantitative profile shows a measured Lorentz deflection angle of ~ 4.3 µrad for the unirradiated region. This is as expected. For a 10 nm thick $Ni_{80}Fe_{20}$ film with B_S = 1 Tesla, then the total beam deflection should be ß=6.5 µrad. With the DPC

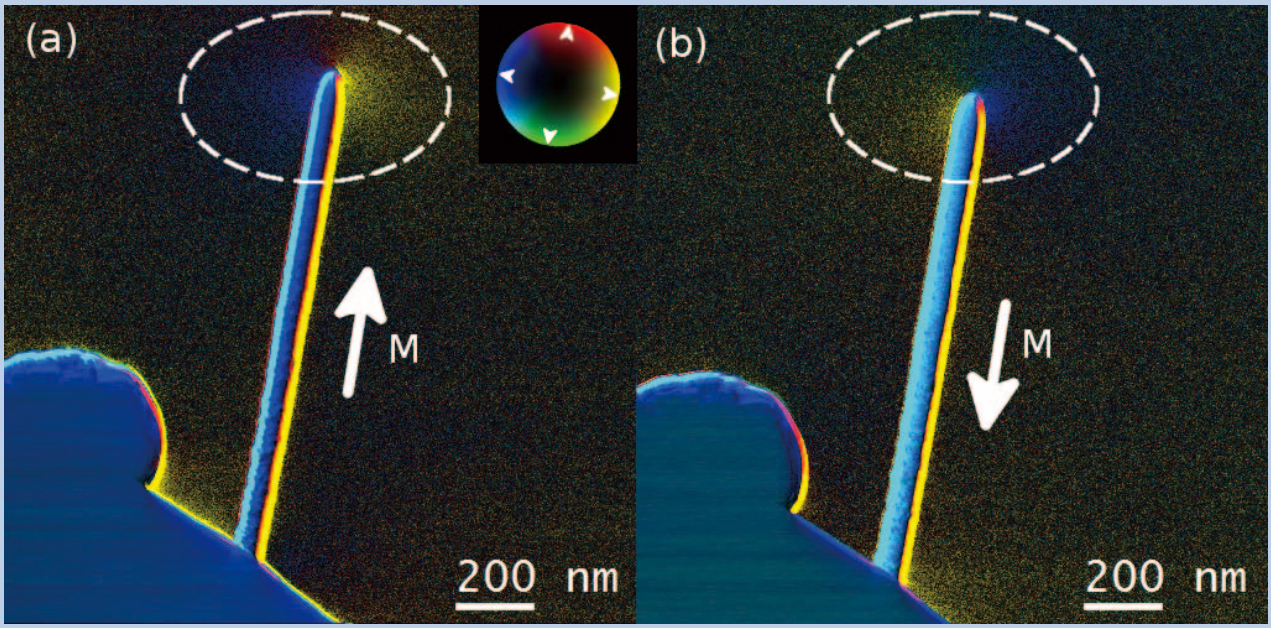

Fig. 6 (a) & (b) DPC colour maps showing magnetic fields emanating from the tip region (indicated by dashed ellipses) of 50 nm diameter EBID Fe-nanopillars.

sensitivity components being oriented at 45 degrees to the direction of the mean magnetisation in the film, then the measured ß is reduced by sin(45) = 0.7, yielding ß = 4.4 µrad. The irradiation dose of 8×10^{15} ions cm^{-2} has resulted in a line of width 50 nm, with a measured deflection of 1.3 µrad, corresponding to a reduction of 70% reduction in M_S.

Summary

In summary, our collaborative development of an aberration corrected STEM Differential Phase Contrast system has demonstrated quantitative imaging of magnetic structure with spatial resolution in the 1-6 nanometre range. As far as we are aware, apart from ultra-high vacumm based scanning tunnelling microscopy (UHV-STM) of atomic surfaces, we know of no other techniques that currently enables magnetic imaging at this length scale. Excitingly, we envisage that further improvements can be made. All results presented here were obtained with a beam energy of 200 keV. Recently we have begun performing DPC at 80 keV which should lead to around a 4× improvement in magnetic sensitivity and which will be essential for investigating new phenomena in ultrathin, 1-5 atom thick, magnetic layers. Furthermore, DPC imaging is not just limited to magnetic samples. Materials and films containing intrinsic electric fields and polarisation exert similar influence on the electron beam. However, the exciting prospect here is that the OL need not be de-excited for such work. Operating in the more usual aberration corrected OL ON mode, atomic resolution DPC investigations are enabled. We envisage that such powerful imaging may benefit the understanding of charge distributions in bonding, across interfaces and at surfaces and lead to the discovery of new aspects of materials physics.

Acknowledgments

The developments reported and procurement of the microscope were enabled by joint funding from the University of Glasgow and the Scottish Funding Council (through the Scottish Universities Physics Alliance (SUPA)).

The authors would like to take the opportunity to express their gratitude to all staff members of JEOL, Gatan Inc., CEOS GmbH, Deben Ltd., University of Warwick and to Andrew Armit for their invaluable efforts in this collaboration. We are grateful to the following collaborators for samples: EBID Fe nano-structures from the group of H. J. M. Swagten at TU Eindhoven, Netherlands; multilayer ferromagnetic samples from the group of R. M. Bowman at Queens

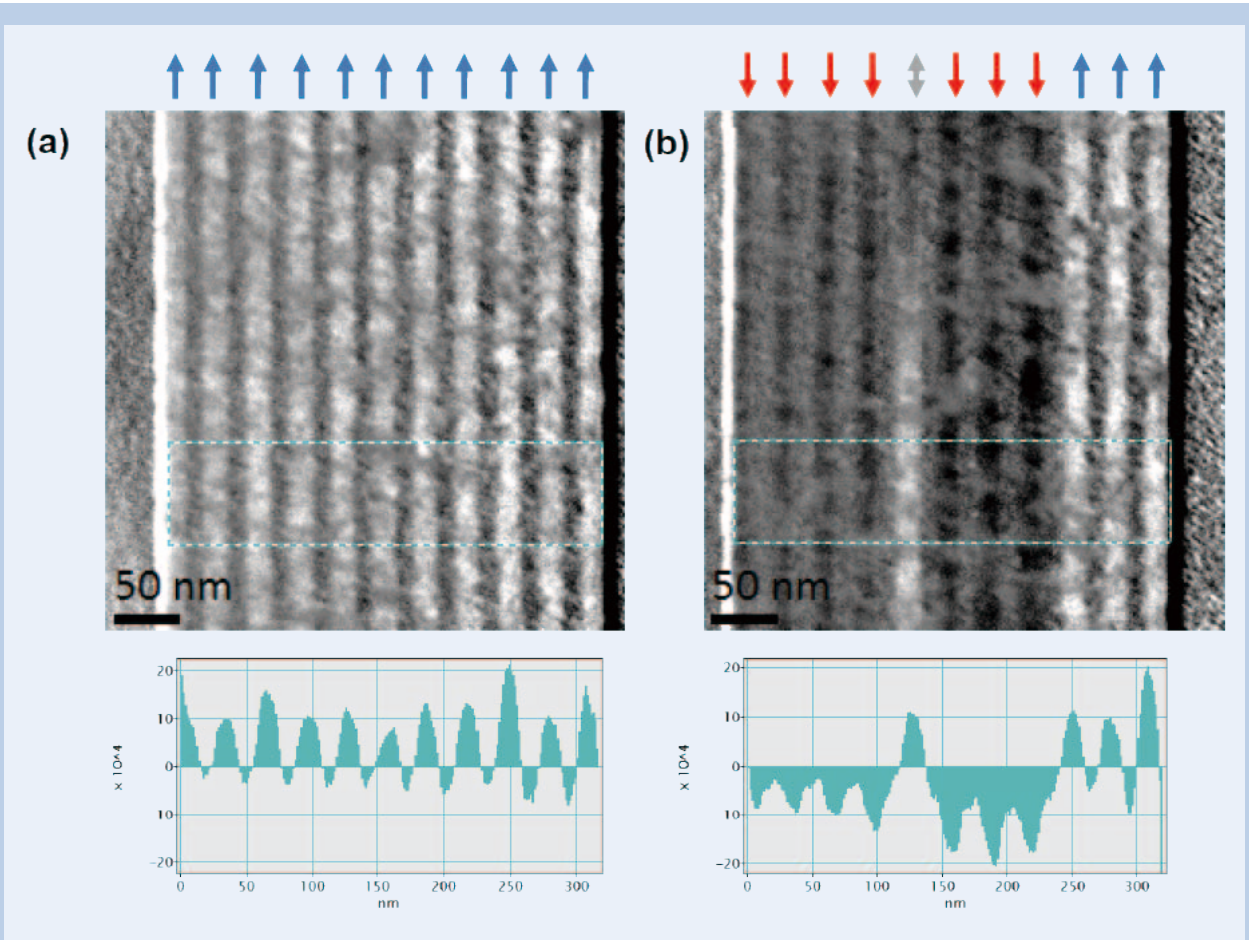

Fig. 7 DPC component images showing in cross-section, the orientation of magnetisation in a multi- ferromagnetic layer sample. (a) corresponds to the fully saturated state, (b) some layers have become oppositely magnetised by application of a magnetic field.

University, Belfast, UK; tri-layered Cr/$Ni_{80}Fe_{20}$/Cr samples from the group of C. H. Marrows, University of Leeds, UK.

We also acknowledge funding support from the UK EPSRC, grant number EP/I013520/1, which funded one of the authors (M-J.B.) and enabled much of the development work.

References

[1] J.N. Chapman and M. R. Scheinfein, *J. Magn. Magn Mater.* **200**, 729 (1999).
[2] P. A. Midgley, R. E. Dunin-Borkowski, *Nature Materials* **8**, 189 (2009).
[3] Y Aharonov and D Bohm, *Phys. Rev* **115** (1959) 485.
[4] J. N. Chapman, I. R. McFadyen, and S. McVitie, *IEEE Trans. Magn.* **26**, 1506 (1990).
[5] M. Takeguchi, M. Shimojo, K. Furuya, *Nanotechnology* **16**, 1321 (2005).
[6] M. Gavagnin, H. D. Wanzenboeck, D. Belic, E. Bertagnolli, *ACS Nano* **7**, 777 (2013).
[7] M. Bode, O. Pietzsch, A. Kubetzka, W. Wulfhekel, D. McGrouther, S. McVitie, J. N. Chapman, *Physical Review Letters* **100**, 029703 (2008).
[8] J. H. Franken, M. A. J. van der Heijden, T. H. Ellis, R. Lavrijsen, C. Daniels, D. McGrouther, H. J. M Swagten, B. Koopmans, accepted for publication in Advanced Functional Materials doi:10.1002/adfm.201303540.
[9] M. A. Basith, S. McVitie, D. McGrouther, J. N. Chapman, *Applied Physics Letters* **100**, 232402 (2012).
[10] M. J. Benitez, M. A. Basith, D. McGrouther, S. McVitie, in preparation.

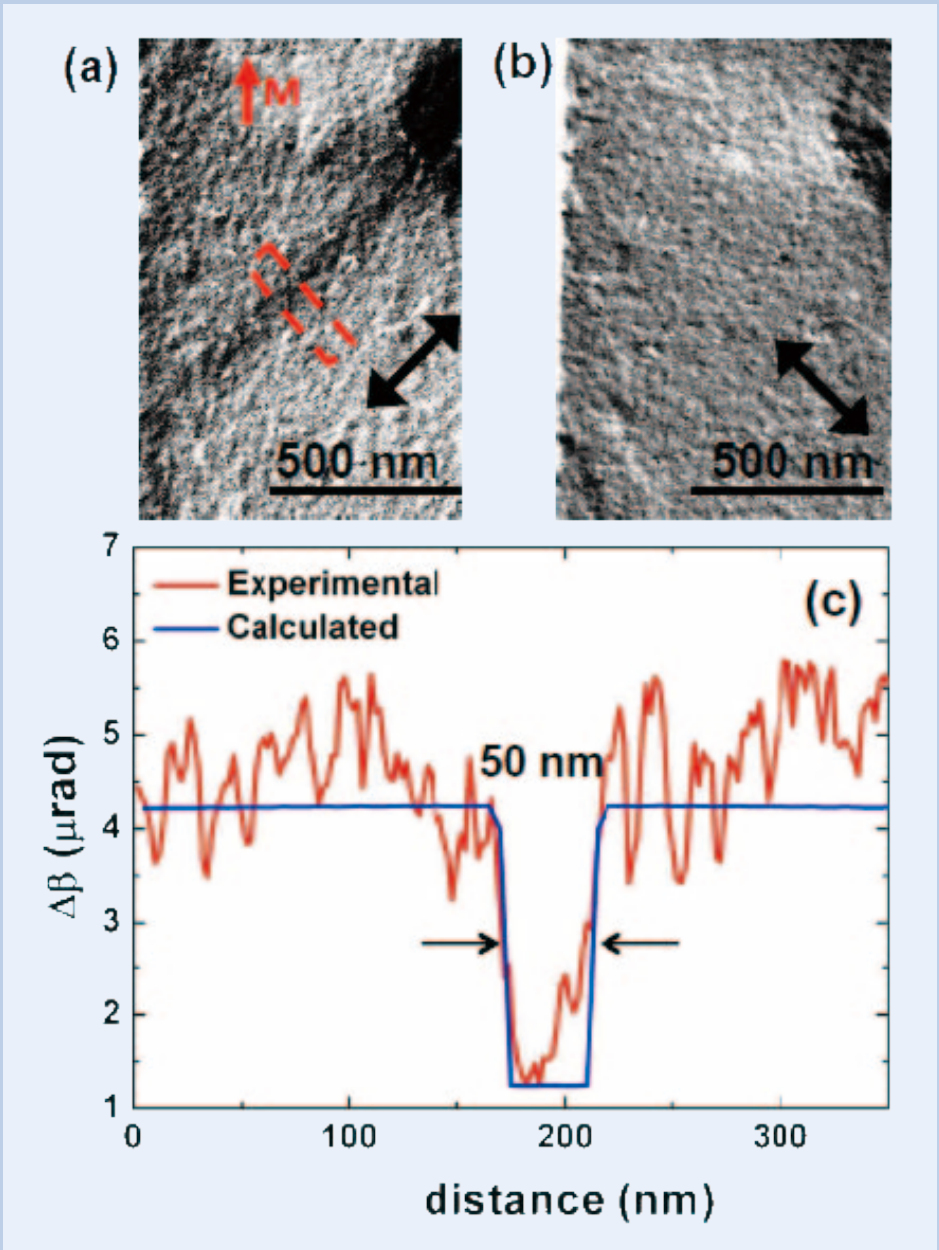

Fig. 8 DPC analysis of FIB irradiated lines in a Cr/$Ni_{80}Fe_{20}$/Cr multi-layer. (a) & (b) Component images showing the irradiated line, (c) a quantitative plot of beam showing the variation of beam deflection and width of the irradiated line.

Atomic-Resolution Characterization Using the Aberration-Corrected JEOL JEM-ARM200CF at the University of Illinois – Chicago

Robert F Klie, Ahmet Gulec, Arijita Mukherjee, Tadas Paulauskas, Qiao Qiao, Xue Rui, Runzhe Tao, Canhui Wang, Tad Daniel, Patrick J. Phillips, Alan W. Nicholls

University of Illinois at Chicago

Modern aberration-corrected scanning transmission electron microscopes (STEM) provide a multitude of characterization techniques that can be applied across a wide-range of length and temperature scales. At the University of Illinois at Chicago, the aberration-corrected, cold-field emission JEOL JEM-ARM200CF is capable of atomic-resolution imaging, electron energy-loss (EEL) as well as energy-dispersive X-ray (XEDS) spectroscopy in a temperature range between 80 – 1,300 K. The capabilities of this instrument will be demonstrated using a number of studies focusing on both structural and chemical properties of materials including NbH, $SrTiO_3$, CdTe and ferritin protein. The central theme of these studies is microscope versatility, which is realized through the ability to perform atomic-scale chemical characterization while retaining high spatial imaging resolution. Of particular interest to many studies is the visualization of light elements, such as N, O or H, using simultaneous high-angle annular dark field (HAADF) and annular bright field (ABF) imaging. Novel in-situ capabilities will be demonstrated using graphene liquid cells. Finally, we will demonstrate the effects of a new silicon drift detector, the Oxford X-MaxN 100TLE on performing atomic-column resolved XEDS mapping at varying length scales and energy resolution.

Introduction

A better understanding of the mechanisms that influence a material's property on the atomic level is essential for developing new functional nano-devices for electronics, energy and biological applications, it is essential that we gain an understanding. Even more so than on the macroscopic level, when a component has been miniaturized for use in nano-devices, surfaces, interfaces, and individual defects dominate its properties by changing the material's structural, compositional and bonding behavior. If working and reliable devices are to be successfully fabricated, it is imperative that we understand the structure-property relationships of these defects, interfaces and surfaces.

Over the last decade, analytical transmission electron microscopy (TEM) and scanning TEM (STEM) have emerged as the primary tools for exploring the structure-property relationships of novel nano-materials [1-15], in particular the atomic and electronic structures of defects, interfaces, or nano-particles [16-20]. The scanning transmission electron microscope (STEM) fitted with a probe-side aberration corrector, such as the JEOL JEM-2200FS or the JEOL JEM-ARM200F [21-24] yields unparalleled spatial resolution of both heavy and light chemical species. With spatial resolution of aberration-corrected high-resolution phase contrast imaging (HRTEM) and high angle annular dark field, HAADF, (or Z-contrast) imaging in aberration-corrected STEMs now reaching the fundamental limit of the Bohr radius, a_0~ 50 pm, the focus is shifting to increasing the chemical resolution and visualizing all constituent atomic species, while retaining spatial resolution. To that end, electron energy loss spectroscopy (EELS) and energy-dispersive X-ray spectroscopy (XEDS) are being pushed to the point where atomically-resolved chemical maps are possible with both techniques [25, 26]. The implementation of silicon drift detectors (SDD) with larger active detector areas in XEDS have greatly aided this advancement, leading to the demonstration of single atom sensitivity [27].

Many material systems are utilized in devices under conditions (i.e. temperatures, pressures or fields) that are substantially different from those present inside an electron microscope column. In a conventional atomic-resolution transmission electron microscope, atomic-resolution studies have previously been limited to ambient temperatures and under high vacuum ($P_{O2}=10^{-5}$ Pa) due to the inability to get in-situ holders into the small gap of an ultra-high-resolution objective lens pole-piece. Over the

845 W Taylor Street, Chicago, IL

E-mail: rfklie@uic.edu

last decade, the field has advanced significantly, and in-situ capabilities are now available to study the dynamic behavior of materials in environments other than the high-vacuum of the TEM column. Novel sample stage designs have enabled in-situ heating up to 1,300 K with atomic resolution, in-situ gas and liquid experiments with nano-meter resolution, as well as time-resolved imaging with better than nanosecond resolution.

This paper will demonstrate the capabilities of the JEOL JEM-ARM200CF at the University of Illinois at Chicago, a probe aberration-corrected STEM equipped with a cold-field emission electron source, a post-column EEL spectrometer and the new Oxford X-MaxN 100TLE SDD-XEDS detector. We will demonstrate that atomic-resolution imaging of light elements, including N, O and H is possible using ABF imaging, while the cold-field emission electron source allows for EELS with an energy resolution of better than 400 meV. In addition, we will highlight our newly developed graphene liquid cell approach of encapsulating biological samples, such as ferritin proteins in a liquid between two single layers of graphene.

Experimental

The JEOL JEM-ARM200CF installed in the Research Resources Centre (RRC) at the University of Illinois at Chicago (**Fig. 1**) is equipped with a cold field emission gun, 5 annular detectors, a Gatan Enfina EELS spectrometer and the new Oxford X-MaxN 100TLE SDD EDS detector and was installed in our laboratory in late 2011. The spatial resolution that can now be routinely achieved using the JEOL JEM-ARM200CF exceeds 70 pm at 200 kV primary energy (see **Fig. 2**(a)) and 100 pm at 80 kV primary energy. The energy resolution of the EEL spectra at any energy between 80 and 200 kV is 350 meV (see Fig. 2(b)). The stability of the instrument was measured using a long-exposure HAADF image without drift correction, and was determined to better than 150 pm/min. In addition to the double tilt holders, we also took delivery of a Gatan double-tilt liquid He cooling stage, a Protochips Aduro double tilt heating stage, a Fischione tomography stage, as well as a Nanofactory STM-TEM stage and a Protochips Poseidon liquid flow cell. In addition, we have still access to the Gatan double tilt heating and the double tilt LN_2 cooling stage, which were purchased in 1998 for use in the UIC JEM-2010F.

In this paper, we will show results from several of these in-situ stages, including the Gatan LN_2 cooling stage and the home-made graphene liquid cell. These results are meant to demonstrate the wide range of experiments that can be conducted on a daily basis in the ARM200CF. At this point, it is important to note that switching between TEM and STEM mode can be done without disturbing the alignment or stability of the instrument significantly. For example, when switching from TEM to STEM mode, it is possible to achieve atomic resolution nearly immediately after the coma and astigmatism have been manually corrected. At the highest imaging resolution, we notice that during the first 60-120 minutes after entering STEM mode, some adjustment of the focus and stigmator is necessary. Once the ARM200CF has been in STEM mode for two hours, the instrument is completely stable.

The UIC JEOL JEM-ARM200CF is located in an open-access user-facility, which allows qualified users to use the instrument 24 hours, 7 days per week on an hourly user-charge basis [28]. It is, therefore, crucial that any of the experimental setups required by the user are not affecting the performance of the instrumentation for the subsequent users. To date, we have not experienced any significant influence of any in-situ experiments or

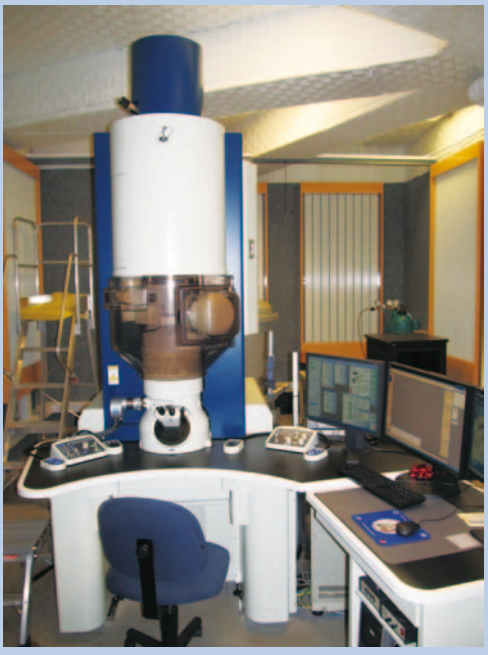

Fig. 1 The JEOL JEM-ARM200CF at the University of Illinois at Chicago.

low-voltage measurements on the vacuum column or energy-stability performance for more than a few hours after the completion of the experiments.

Results and Discussion

Here, we will discuss the results from several experiments conducted using the JEOL ARM200CF at the University of Illinois at Chicago. The materials that were characterized include $SrTiO_3$ thin films on GaAs, ß-NbH, polycrystalline CdTe and ferritin proteins in a graphene liquid cell.

Low voltage characterization of $SrTiO_3$/GaAs interfaces

Over the past few years, ultrathin metal-oxide films on polar semiconductor surfaces have received much attention due to the occurrence of novel interfacial properties, including ferroelectricity, superconductivity and the presence of an interfacial 2-dimensional electron gas [29-34]. The first successful growth of $SrTiO_3$ thin films on Si was reported more than two decades ago, and various techniques have been used to assemble a layer-by-layer crystalline oxide film and avoid the formation of the amorphous layer at the interface [35, 36].

The $SrTiO_3$/GaAs interfaces were studied experimentally and theoretically with various techniques in order to develop a fundamental understanding of the structure property relationships and it has been reported that the $SrTiO_3$ film prefers to be SrO terminated at the interface, regardless of the growth condition, and a submonolayer of Ti, hereafter referred to as a Ti pre-layer, between the oxide and semiconductor can release the Fermi level pinning after the thin film deposition.[37-39] However, due to the oxygen deficiency of the film, it was not possible to perform atomic resolution electron energy-loss spectroscopy (EELS) on the highly beam sensitive $SrTiO_3$/GaAs interface [40].

Using the JEOL ARM200CF at UIC, we conducted a detailed study of the atomic and electronic structures of the $SrTiO_3$/GaAs interface with and without a Ti pre-layer using HAADF imaging and EELS at 80 kV primary electron energy [41]. **Figure 3** shows atomic-resolution Z-contrast images of a 4 monolayer thin $SrTiO_3$ film on GaAs (001), where the epitaxy is apparent with $SrTiO_3$(001) || GaAs (001) and $SrTiO_3$[110] || GaAs[100]. The interface between the $SrTiO_3$ film and the GaAs-support in Fig. 3 appears sharp with no obvious interfacial diffusion. Moreover, the images suggest that the oxide films start with a SrO layer at the As terminated GaAs interface, regardless of the fact that 0.5 ML of a Ti pre-layer was deposited on the GaAs surface prior to $SrTiO_3$ growth for the sample shown in Fig. 3(a)). As opposed to the experiments

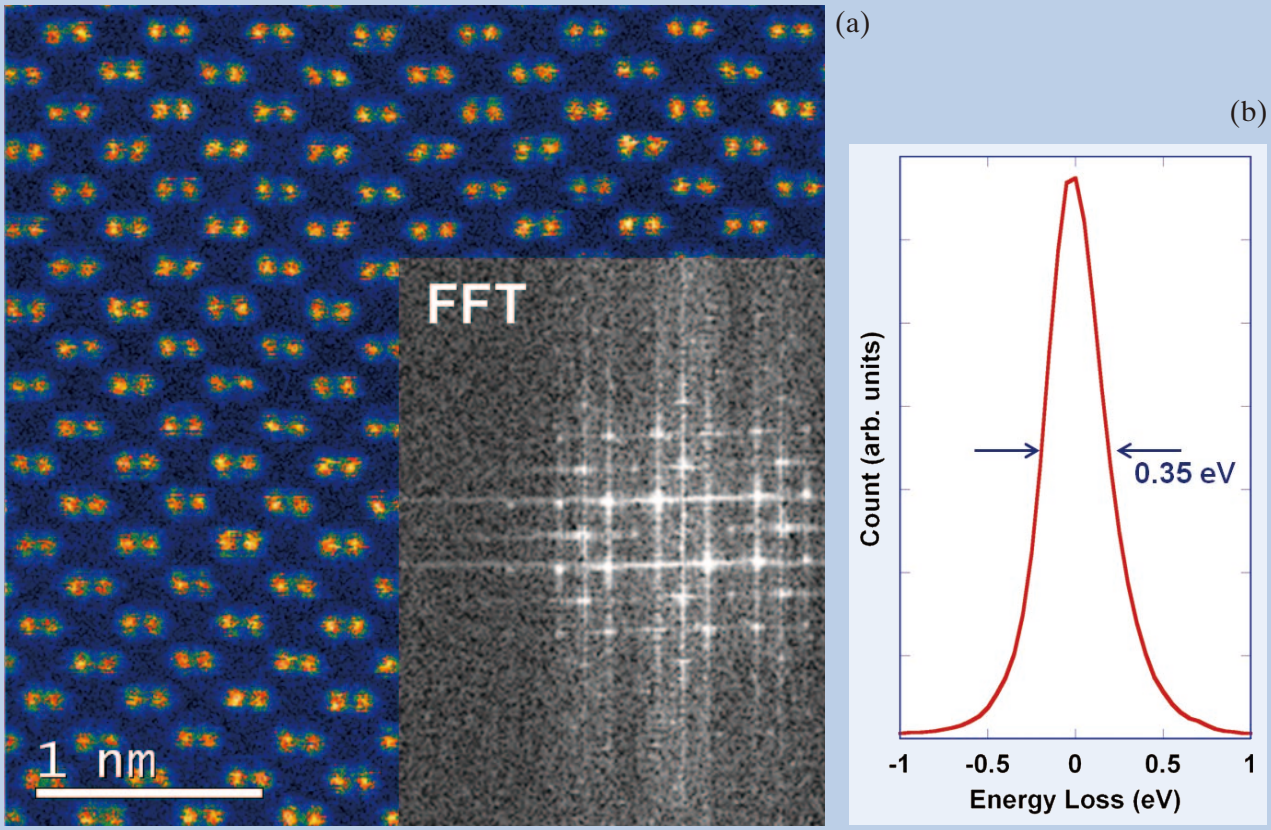

Fig. 2 a) HAADF image at 200 kV of Si (110) with Fourier transform shown as insert. b) Zero-loss peak with indicated full width at half maximum.

conducted at 200 kV primary electron energy, the $SrTiO_3$/GaAs interfaces are now sufficiently stable to withstand atomic resolution imaging and spectroscopy for extended periods of time. Even several hours of analysis on a particular region of a sample has so far not shown any signs of beam damage, neither in Z-contrast imaging nor in spectroscopy.

The acquired Ti L- and O K-edges are shown in **Fig. 4** and **Fig. 5**, respectively acquired using a convergence semi-angle of 30 mrad, a collection semi-angle of 35 mrad, with a 0.1 eV/pxl dispersion and a 3s dwell time. The top spectrum in Fig. 4 and Fig. 5 is taken from a $SrTiO_3$ bulk specimen thus providing a Ti^{4+} fine structure as a reference. In Fig. 4, the crystal field splitting of Ti L_3 and L_2 edges can be clearly resolved in all the spectra taken from the $SrTiO_3$ thin film, which indicates that the Ti valence is close to 4+ throughout the films in both films with and without the Ti prelayer.[42] To further assess the Ti valence state, and thereby the oxygen stoichiometry of the films, the energy scale has been calibrated using the O K-edge onset, as shown in Fig. 4.

It can now be seen that in the film without the Ti pre-layer, the Ti L-edges for each location in the film are slightly shifted towards lower energy, again indicating a slight decrease in the Ti. More specifically, both L_3 and L_2 edges shift to lower energies as the electron probe approaches to the $SrTiO_3$/GaAs interface, indicating a decrease of the Ti valence from 4+ to a mixture state of 3+ and 4+ [42]. Such phenomena could be caused by oxygen vacancies, or because the Ti-O bonding state on the TiO_2 columns in the thin film changed to Ti-As on the surface of the substrate. In addition, it is interesting to note here that a Ti signal is noticeable at least 2 layers into the GaAs support, indicating that some of the Ti has diffused into the GaAs support during the film synthesis.

In Fig. 5, the acquired O K-edges are fitted to their 5^{th} nearest neighbors and compared with the reference spectrum taken from bulk $SrTiO_3$. The colored spectra correspond to the colored rectangles in Fig. 3. It is immediately noticeable that the O K-edge fine-structure in the $SrTiO_3$ thin films is significantly different from the bulk $SrTiO_3$, especially for the film grown without the Ti prelayer. More specifically, the pre-peak, which strongly scales, with the presence of oxygen vacancies, is suppressed in the spectra taken from the films [43, 44], indicating the presence of oxygen vacancies. Furthermore, near the $SrTiO_3$/GaAs interface, the fine-structure of the O K-edge exhibits several peaks that were not found in the bulk $SrTiO_3$, nor in the films $SrTiO_3$ spectra. These additional peaks indicate the oxygen bonding with arsenic on the GaAs surface during the initial steps of the thin film synthesis. Finally, the integrated O K-edge intensity disappears completely in the GaAs support, even in the locations where a Ti signal was found. This further indicates that only the Ti diffuses into the support, while the oxygen remains in the $SrTiO_3$ film and on the GaAs surface.

Our low-kV imaging and spectroscopy study, therefore, shows, that while the atomic structure of the interfaces does not reveal any evidence of the Ti prelayer at the $SrTiO_3$ interface, the electronic structure of the films appears significantly different. The films grown without the Ti pre-layer appears to be more oxygen deficient, and exhibit stong interaction between the GaAs support and the interfacial oxygen, potentially forming As_2O_3. The deposition of the Ti pre-layer appear to alleviate the oxidation of the substrate and consequently lift the

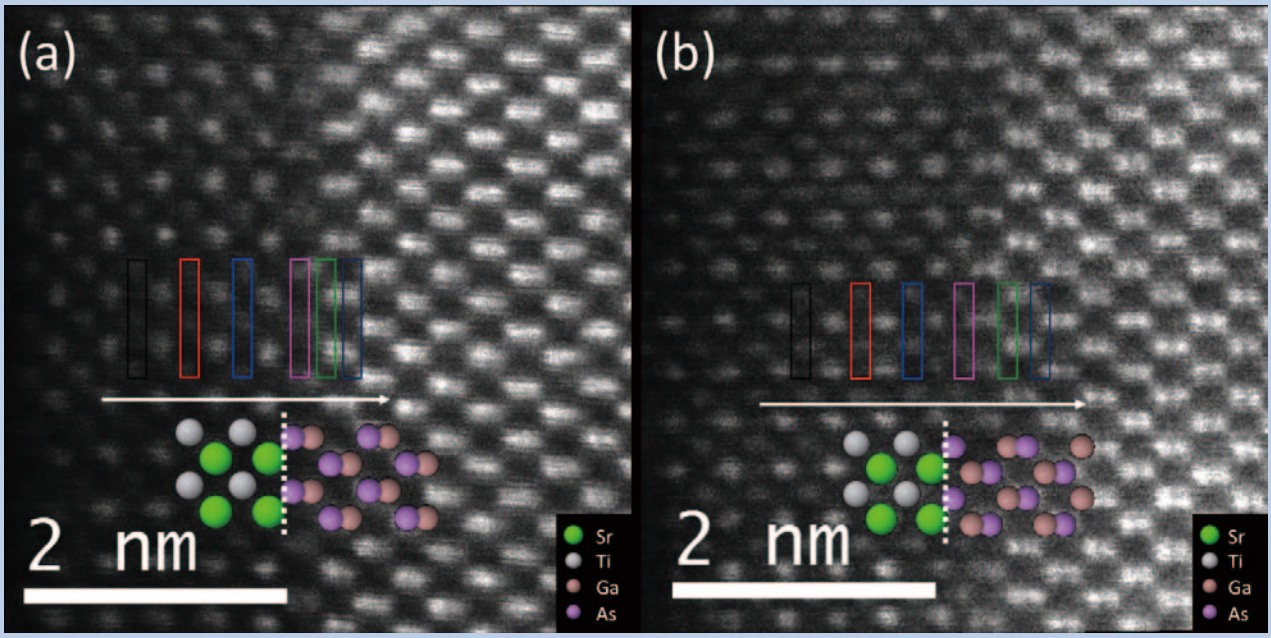

Fig. 3 Atomic resolution HAADF image at 80 kV of $SrTiO_3$/GaAs a) with and b) without the Ti pre-layer. The colored rectangle highlight the area where EEL spectra where acquired. An atomic model is superimposed on the images and the interface is indicated by the dotted line.

Fermi-level pinning [41].

Direct imaging of hydrogen in ß-NbH

Niobium, a *4d* transition metal, has found many applications including hydrogen storage, heterogeneous catalysis, dielectric coatings, and superconducting devices, such as superconducting radio-frequency (SRF) cavities [45]. In the next generation accelerators, the performance of SRF cavities at moderate (i.e. 16-19 MVm^{-1}) and high electric (i.e. >35 MVm^{-1}) field gradients are critical [46]. Nevertheless, even after decades of research, a solid understanding of the microstructural defects limiting the medium and high field performance is still missing. What appears clear, however, is that Niobium hydride, if present, can be a major contributor to the degradation of the quality factor, Q, since hydride precipitates can only be superconducting by proximity effect, and their premature transition to the normal state will lead to strong losses [47, 48].

Here, we present an atomic-resolution study of the formation of ß-NbH precipitates at room temperature in Nb grains near the cavity surfaces.[49] In addition, we demonstrate that atomic-resolution imaging is still possible at LN_2 temperatures, although spatial drift limits the dwell time per pixel to around 16 μs/pixel.

Figure 6 shows a pair of HAADF and ABF

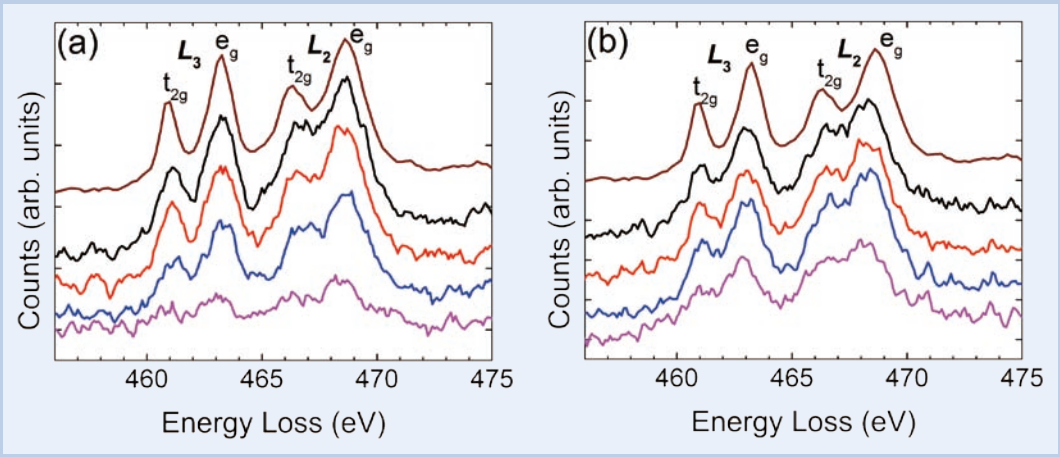

Fig. 4 EELS at 80 kV of the Ti L-edges after background subtraction for the sample a) with and b) without the Ti pre-layer.

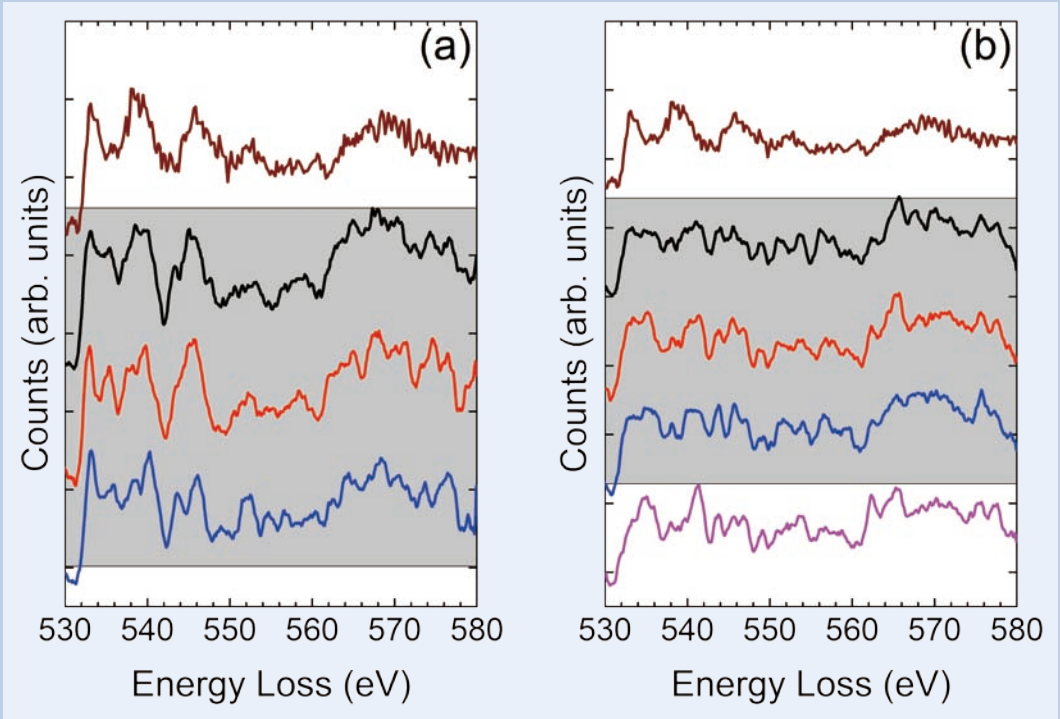

Fig. 5 EELS spectra of the O K-edges for the samples a) with and b) without the Ti pre-layer. The shaded area indicates spectra taken from the $SrTiO_3$ film, while the top spectrum is taken from bulk $SrTiO_3$ as a reference.

images, acquired simultaneously, of a ß-NbH precipitate in the [110] orientation. While the HAADF image appears very similar to that of pure Nb, the ABF image reveals additional atomic columns, which can be identified as hydrogen atomic columns. The insert in Fig. 6 shows the proposed structure of ß-NbH [110] as well as the calculated image contrast using the multi-slice method. The contrast in the image calculations agrees with that measure in the experimental ABF images. Using a combination of ABF imaging, selective area electron diffraction and EELS, we confirmed that the phase image is ß-NbH [110].

According to the phase diagram for Nb-hydride, there exist several other phases depending on the local hydrogen concentration and temperature. Therefore, in order to fully understand the role of hydride precipitates on the mid and high field gradient performance of Nb based SRF cavities, an imaging method capable of atomic-resolution at low temperature (e.g. LN_2 temperature) is needed. Using the Gatan double tilt LN_2 stage, we imaged bulk Nb [110] (**Fig. 7**(b)) and show that achieving atomic-resolution is possible at that temperature. However, due to the increase mechanical vibrations as a result of the nitrogen boiling off, we had to decrease the pixel dwell time to 16 μs/pixel and average over several images to achieve a presentable signal to noise ratio. If necessary, more sophisticated noise reduction procedures can be employed if repeated acquisition of short-exposure time images is not possible.

XEDS analysis of defects in poly-crystalline CdTe

Polycrystalline CdTe thin film based photovoltaic devices are present leaders in thin film solar technology ([50], [51]). Commercial success of CdTe based devices stems from the nearly ideal band gap of the material which very effectively couples to our sun's light spectrum as well as ease of manufacturing and low cost of the modules. However, to improve the conversion efficiency beyond 20%, it is critical to minimize the harmful effects of grain boundaries and lattice defects in CdTe. Direct atomic-scale structural and chemical investigation is desirable in order to identify atomic configurations which can act as carrier recombination centers. Likewise, it is necessary to confirm that passivants introduced into CdTe are able to diffuse and bind to the target defects.

Besides arbitrarily oriented grain boundaries, stacking faults and Σ3 twin boundaries, both lying on

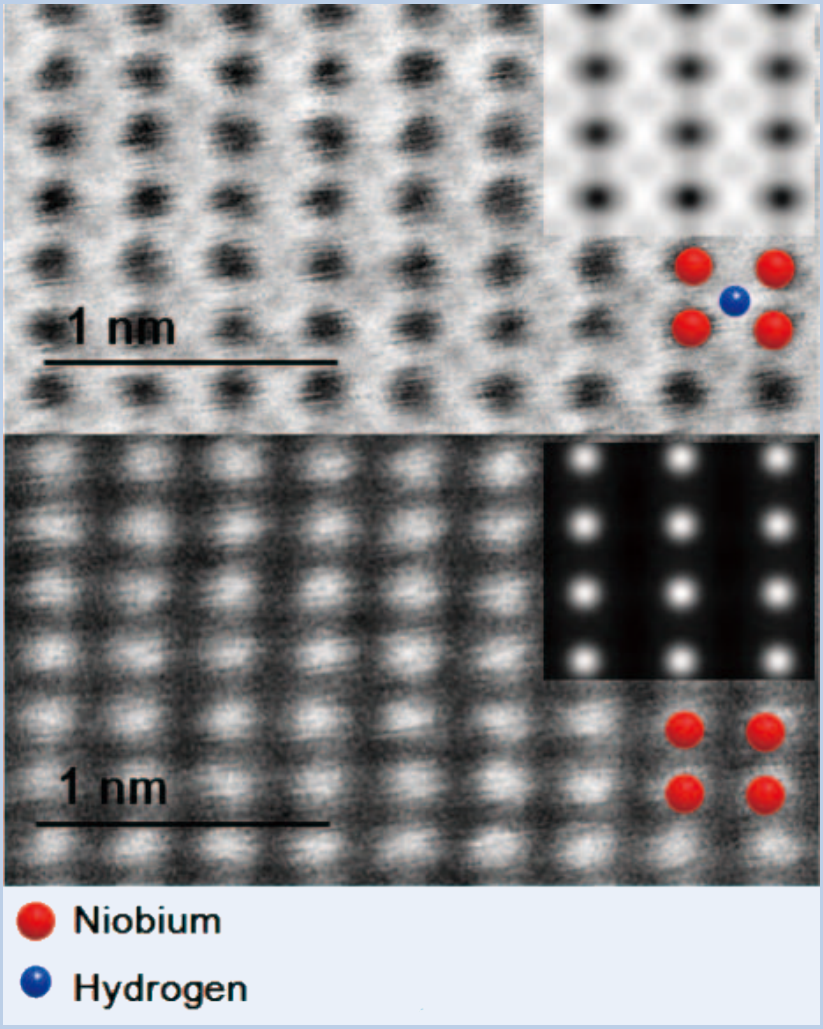

Fig. 6 Simultaneous HAADF and ABF images at 200 kV of ß-NbH [110] clearly showing the hydrogen atomic columns in the ABF image.

{111} planes, are very common planar defects in CdTe. These defects have the correct nearest-neighbor bonding, however stacking disorder becomes apparent in second (and beyond) nearest neighbors. While these interfaces have been deemed benign as far as carrier recombination centers are concerned, their role in attracting impurities and anti-site point defects remains unknown. In **Fig. 8**, we show an HAADF image and XEDS image of a stacking fault in CdTe along [110]. In this projection, Cd and Te atomic columns form a dumbbell-like structure with 162 pm column separation. The XEDS data clearly shows atomic resolution and the polarity of the planar defect can be readily identified. More precisely, the direction of the dumbbells at the stacking fault is rotated by 250° about [110]. Figure 8 shows that the terminating column of the left side of the interface is Te, followed by Cd. Such data will allow us to quantify possible changes in stoichiometry across twin boundaries and stacking faults, detect the presence of dopants, and determine the atomic structure of dislocation cores terminating such defects.

HAADF image and atomic-column resolved XEDS map of a Lomer-Cottrell dislocation along [-1-10] zone-axis in CdTe are presented in **Fig. 9**. More specifically, two intrinsic stacking faults are seen in the HAADF image and the XEDS spectrum image shows the integrated intensity of the Cd and Te L-peaks in the stacking faults. The dislocation core is located at the vertex of two intersecting stacking faults, and is composed of three Cd atomic columns and a single Te column (Cd_3Te), as can be seen from the spectrum image map shown in Fig. 8. It should be pointed out here that without the availability of the XEDS spectrum image, the identification of the atomic columns in the dislocation core would not be possible, since the atomic numbers (Z) for Cd and Te are too close to be distinguished using HAADF imaging alone.

Ferritin in a graphene liquid cell

Nanoparticle growth, chemical reactions or biochemical activity often occur in the presence of a liquid. To study liquid sample in an electron microscope, several liquid cell designs have become commercially available in recent years that enable materials to be imaged in a carefully controlled liquid environment within the vacuum of a TEM. However, all suffer from a few key limitations that do not allow for ultra high-resolution imaging or spectroscopy:[52] 1) two Si_3N_4 layers (50-500 nm thick) used as electron transparent windows and 2) the thickness of the

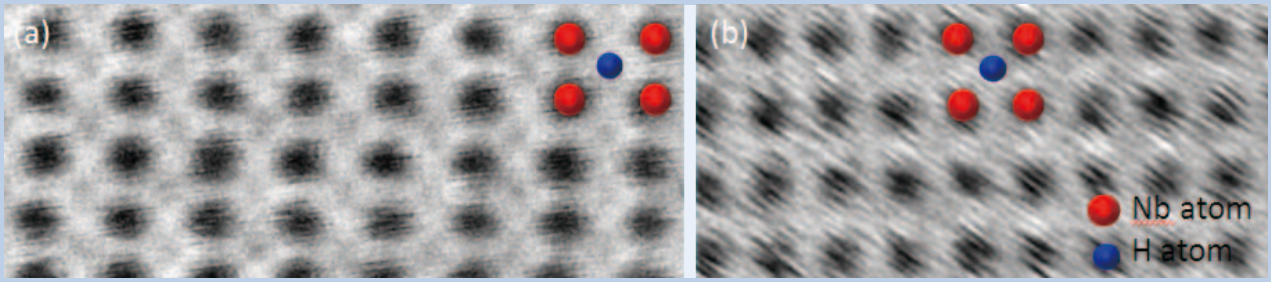

Fig. 7 200 kV atomic-resolution ABF images at a) room and b) LN_2 temperature. Both images show the Nb atomic columns, but the Hydrogen columns are not very visible in the low temperature image due to the increased sample vibration.

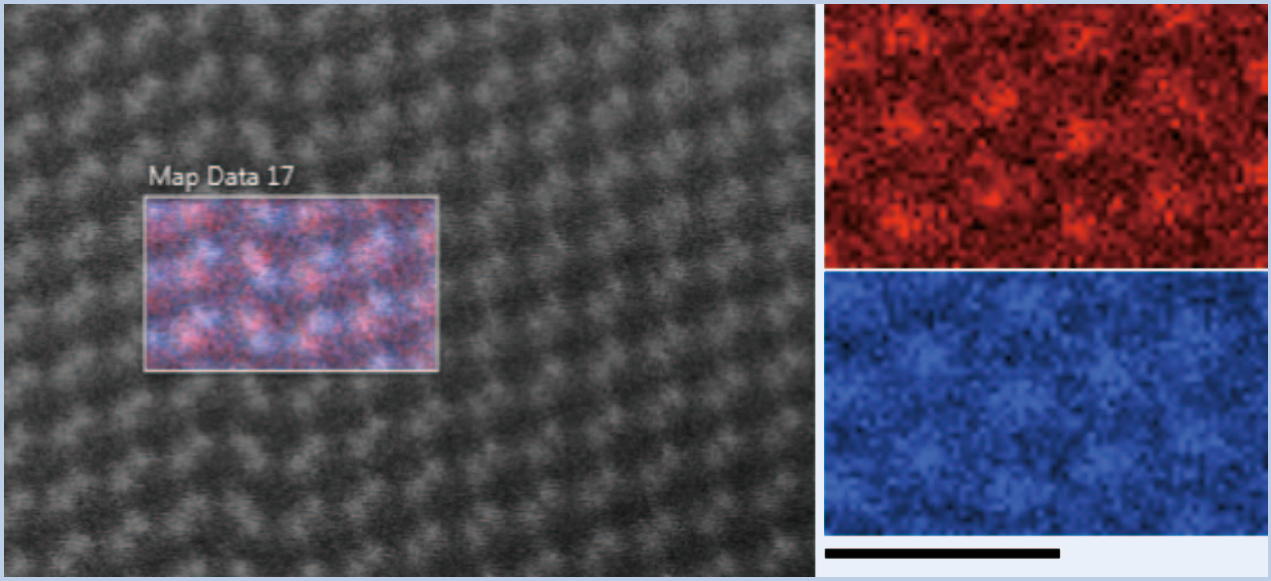

Fig. 8 An HAADF STEM image acquired across a twin boundary, viewed with the Cd L (red) and Te L (blue) series overlaid. The scale bar is 1 nm and applies to the individual element maps.

liquid surrounding the sample. In these liquid cells, the imaging resolution is usually limited to nanometers. Electron energy-loss spectroscopy (EELS) is degraded by multiple scattering events in the thick window layers, and the strong core-loss signals associated with the presence of Si and N [53]. In addition to the increased sample thickness, radiation damage is a fundamentally limiting factor when examining beam sensitive materials and /or hydrous samples in TEM. It has been shown that coating the specimen with carbon, metal or grapheme [54-58], or lowering the temperature [57] have positive effects against radiation damage by reducing electrostatic charging, mass loss, loss of crystallinity, or defect formation rate [54-58]. These studies suggest that it is possible to reduce radiation damage to below breakage of covalent bonds. However, further reduction of radiation damage is needed for characterization of biological samples, since many biological structures and functions are related to the much weaker hydrogen bonds.

We have developed a biocompatible approach of encapsulating liquid containing samples in monolayers of graphene. This not only allows biological samples to be directly imaged at atomic resolution in a native liquid state without limitations from the window thickness (see **Fig. 10**), but also enables nm-scale analysis using EELS to quantify reactions in an aqueous environment [59]. It has to be pointed out here that any imaging or chemical analysis of graphene liquid cells required that the electron beam energy is lowered below 100 kV, and the images shown in Fig. 10 are taken at 80 kV.

Further, we have shown that the energy deposited by the incoming electrons is dissipated by graphene from the area irradiated at a rate equivalent to the beam current of several electrons per $Å^2$ per second [59]. This would therefore provide a reduction of radiation damage, allowing for high resolution imaging and spectroscopy of beam sensitive materials. Details, such as individual Fe atoms (see Fig. 10) or polypeptide of unstained protein, are resolved in a liquid environment. By carefully controlling the induced electron dose rate, we have shown that reactions, such as liquid/ gas phase transition (bubble formation and condensation), or nanoparticle/ nanowire growth can be initiated at selected locations in GLC, and recorded at nm resolution. This technique also allows us to perform a quantitative study of radiation damage effect on different encapsulated samples, such as water or protein, by observing local reaction processes.

Conclusion

Nearly two years after the delivery of the new JEOL ARM200CF to UIC, we have demonstrated the capabilities of the instrument to perform with sub-Å and sub-eV resolution in a variety of environments using a 200 kV primary energy electron beam. The spatial resolution is decreased in 1.0 Å for low energy imaging at 80 kV without any loss in the analytical capabilities of the instrument. In addition, the ARM200CF is capable of imaging samples in a liquid environment, at elevated or cryogenic temperatures in either TEM or STEM mode.

Acknowledgments

The authors acknowledge support for this work from the National Science Foundation [DMR-0846748] and the US Department of Energy (DOE-EE0005956). The acquisition of the UIC JEOL JEM-ARM200CF is supported by a MRI-R^2 grant from

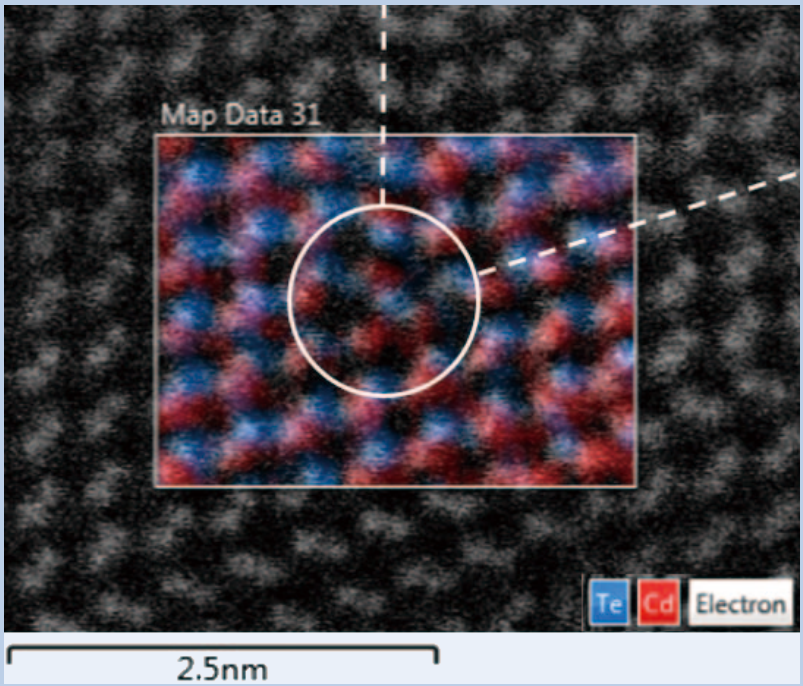

Fig. 9 a) Atomic-column resolved XEDS map overlaid on top of the Z-contrast image in the <110> projection. L-C dislocation core (circled) is associated with the two dashed intrinsic stacking faults.

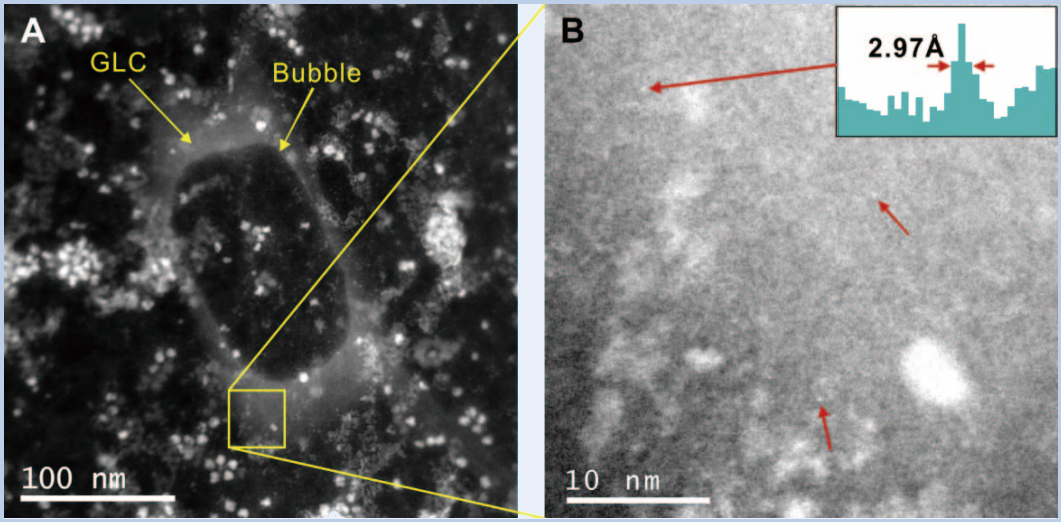

Fig. 10 HAADF (A and B) images of ferritin in a graphene liquid cell (GLC). Bubbles in (A) were formed in advance using the Ronchigram mode to confirm the presence of a liquid. In STEM mode, electron dose rate and pixel dwell time is optimized so that no further bubbles are formed during scanning. Single iron atoms are resolved in a liquid environment in image (B) near the edge of a GLC. A line profile across the upper left atom is shown as an inset of (B), with each pixel corresponds to 0.99 Å. The resolution of these images is optimized by taking images under the corresponding threshold area averaged dose rate of bubble formation at each magnification.

the National Science Foundation [DMR-0959470]. Support from the UIC Research Resources Center is also acknowledged.

References

[1] Hashimoto, A., et al., Direct evidence for atomic defects in graphene layers. *Nature*, **430**(7002): p. 870-873 (2004).
[2] Regan, B.C., et al., Carbon nanotubes as nanoscale mass conveyors. *Nature*, **428**(6986): p. 924-927 (2004).
[3] Cumings, J., P.G. Collins, and A. Zettl, Materials - Peeling and sharpening multiwall nanotubes. *Nature*, **406**(6796): p. 586-586 (2000).
[4] Iijima, S., Helical Microtubules of Graphitic Carbon. *Nature*, **354**(6348): p. 56-58 (1991).
[5] Wang, Z.L. and Z. Kang, C., Functional and Smart Materials.: Plenum Press (1998).
[6] Ohtomo, A., et al., Artificial charge-modulation in atomic-scale perovskite titanate superlattices. *Nature*, **419**(6905): p. 378-380 (2002).
[7] Zuo, J.M., et al., Atomic resolution imaging of a carbon nanotube from diffraction intensities. *Science*, **300**(5624): p. 1419-1421 (2003).
[8] Bell, A.T., The impact of nanoscience on heterogeneous catalysis. *Science*, **299**(5613): p. 1688-1691 (2003).
[9] McKee, R.A., F.J. Walker, and M.F. Chisholm, Crystalline oxides on silicon: The first five monolayers. *Physical Review Letters*, **81**(14): p. 3014-3017 (1998).
[10] McKee, R.A., F.J. Walker, and M.F. Chisholm, Physical structure and inversion charge at a semiconductor interface with a crystalline oxide. *Science*, **293**(5529): p. 468-471 (2001).
[11] Yan, Y., S.J. Pennycook, and A.P. Tsai, Direct imaging of local chemical disorder and columnar vacancies in ideal decagonal Al-Ni-Co quasicrystals. *Physical Review Letters*, **81**(23): p. 5145-5148 (1998).
[12] Shan, Z.W., et al., Grain boundary-mediated plasticity in nanocrystalline nickel. *Science*, **305**(5684): p. 654-657 (2004).
[13] Gai, P.L. and K. Kourtakis, Solid-State Defect Mechanism In Vanadyl Pyrophosphate Catalysts - Implications For Selective Oxidation. *Science*, **267**(5198): p. 661-663 (1995).
[14] Gai, P.L., B.C. Smith, and G. Owen, Bulk Diffusion Of Metal Particles On Ceramic Substrates. *Nature*, **348**(6300): p. 430-432 (1990).
[15] Gai, P.L. and E.M. McCarron, Direct Observation And Analysis Of Cuo2 Shear Defects In La2-Xsrxcuo4. *Science*, **247**(4942): p. 553-556 (1990).
[16] Jia, C.L. and K. Urban, Atomic-resolution measurement of oxygen concentration in oxide materials. *Science*, **303**(5666): p. 2001-2004 (2004).
[17] Jia, C.L., M. Lentzen, and K. Urban, Atomic-resolution imaging of oxygen in perovskite ceramics. *Science*, **299**(5608): p. 870-873 (2003).
[18] Nellist, P.D., et al., Direct sub-angstrom imaging of a crystal lattice. *Science*, **305**(5691): p. 1741-1741 (2004).
[19] Nellist, P.D. and S.J. Pennycook, Atomic resolution Z-contrast imaging of ultradispersed catalysts, in Electron Microscopy And Analysis 1997. p. 399-402 (1997).
[20] Varela, M., et al., Spectroscopic imaging of single atoms within a bulk solid. *Physical Review Letters*, **92**(9): p. 095502 (2004).
[21] Haider, M., et al., A spherical-aberration-corrected 200 kV transmission electron microscope. *Ultramicroscopy*, **75**(1): p. 53-60 (1998).

[22] Dellby, N., et al., Progress in aberration-corrected scanning transmission electron microscopy. *Journal of Electron Microscopy*, **50**(3): p. 177-185 (2001).
[23] Lupini, A.R., et al., Developments in Cs-corrected STEM, in Electron Microscopy And Analysis 2001. p. 31-34 (2001).
[24] Batson, P.E., N. Dellby, and O.L. Krivanek, Sub-angstrom resolution using aberration corrected electron optics. *Nature*, **419**(6902): p. 94-94 (2002).
[25] Klie, R.F., et al., Examining the structure and bonding in complex oxides using aberration-corrected imaging and spectroscopy. *Physical Review B*, **85**(5): p. 7 (2012).
[26] D'Alfonso, A.J., et al., Atomic-resolution chemical mapping using energy-dispersive x-ray spectroscopy. *Physical Review B*, **81**(10) (2010).
[27] Lovejoy, T.C., et al., Single atom identification by energy dispersive x-ray spectroscopy. *Applied Physics Letters*, **100**(15) (2012).
[28] ; Available from: http://www.rrc.uic.edu/ems.
[29] Pertsev, N.A., A.K. Tagantsev, and N. Setter, Phase transitions and strain-induced ferroelectricity in $SrTiO_3$ epitaxial thin films. *Physical Review B*, **61**(2): p. R825-R829 (2000).
[30] Ahn, C.H., K.M. Rabe, and J.M. Triscone, Ferroelectricity at the nanoscale: Local polarization in oxide thin films and heterostructures. *Science*, **303**(5657): p. 488-491 (2004).
[31] Haeni, J.H., et al., Room-temperature ferroelectricity in strained $SrTiO_3$. *Nature*, **430**(7001): p. 758-761 (2004).
[32] Woicik, J.C., et al., Anomalous lattice expansion of coherently strained $SrTiO_3$ thin films grown on Si(001) by kinetically controlled sequential deposition. *Physical Review B*, **73**(2) (2006).
[33] Warusawithana, M.P., et al., A Ferroelectric Oxide Made Directly on Silicon. *Science*, **324**(5925): p. 367-370 (2009).
[34] Ohtomo, A. and H.Y. Hwang, A high-mobility electron gas at the $LaAlO_3/SrTiO_3$ heterointerface. *Nature*, **427**(6973): p. 423-426 (2004).
[35] Tarsa, E.J., et al., Growth And Characterization of (111) And (001) Oriented MgO Films On (001) GaAs. *Journal of Applied Physics*, **73**(7): p. 3276-3283 (1993).
[36] Blamire, M.G., et al., The Materials Science of Functional Oxide Thin Films. *Advanced Materials*, **21**(38-39): p. 3827-3839 (2009).
[37] Klie, R.F., et al., Atomic structure of epitaxial $SrTiO_3$-GaAs(001) heterojunctions. *Applied Physics Letters*, **87**(14): p. 143106 (2005).
[38] Liang, Y., J. Curless, and D. McCready, Band alignment at epitaxial $SrTiO_3$-GaAs(001) heterojunction. *Applied Physics Letters*, **86**(8) (2005).
[39] Liang, Y., et al., Hetero-epitaxy of perovskite oxides on GaAs(001) by molecular beam epitaxy. *Applied Physics Letters*, **85**(7): p. 1217-1219 (2004).
[40] Klie, R.F., et al., Atomic structure of epitaxial SrTiO[sub 3]–GaAs(001) heterojunctions. *Applied Physics Letters*, **87**(14): p. 143106 (2005).
[41] Qiao, Q., et al., Atomic and electronic structures of $SrTiO_3$/GaAs heterointerfaces: An 80-kV atomic-resolution electron energy-loss spectroscopy study. *Physical Review B*, **85**(16): p. 165406 (2012).
[42] Muller, D.A., et al., Atomic-scale imaging of nanoengineered oxygen vacancy profiles in $SrTiO_3$. *Nature*, **430**(7000): p. 657-661 (2004).
[43] Klie, R.F. and N.D. Browning, Atomic scale characterization of oxygen vacancy segregation at $SrTiO_3$ grain boundaries. *Applied Physics Letters*, **77**(23): p. 3737-3739 (2000).
[44] Browning, N.D., et al., Correlation Between Hole Depletion And Atomic-Structure At High-Angle Grain-Boundaries In $YBa_2Cu_3O_{7-\delta}$. *Physica C*, **212**(1-2): p. 185-190 (1993).
[45] Padamsee, H., The science and technology of superconducting cavities for accelerators. *Superconductor Science & Technology*, **14**(4): p. R28-R51 (2001).
[46] Phinney, N., N. Toge, and Walker, International Linear Collider Reference Design Report. 2007 (2007).
[47] Romanenko, A., et al., Proximity breakdown of hydrides in superconducting niobium cavities. *Superconductor Science & Technology*, **26**(3) (2013).
[48] Halbritter, J., P. Kneisel, and K. Saito. 6th Workshop on RF Superconductivity 1993 (1993).
[49] Kim, Y.J., et al., Direct Atomic-Scale Imaging of Hydrogen and Oxygen Interstitials in Pure Niobium Using Atom-Probe Tomography and Aberration-Corrected Scanning Transmission Electron Microscopy. *ACS Nano*, **7**(1): p. 732-739 (2013).
[50] Triboulet, R. and S. P., CdTe and Related Compounds; Physics, Defects, Hetero- and Nano-structures, Crystal Growth, Surfaces and Applications ed. Elsevier (2010).
[51] Chen, L., et al., From atomic structure to photovoltaic properties in CdTe solar cells. *Ultramicroscopy*, **134**: p. 113-125 (2013).
[52] de Jonge, N. and F.M. Ross, Electron microscopy of specimens in liquid. *Nature Nanotechnology*, **6**(11): p. 695-704 (2011).
[53] Holtz, M.E., et al., In Situ Electron Energy-Loss Spectroscopy in Liquids. *Microscopy and Microanalysis*, **19**(4): p. 1027-1035 (2013).
[54] Salih, S.M. and V.E. Cosslett, *REDUCTION IN ELECTRON-IRRADIATION DAMAGE TO ORGANIC COMPOUNDS BY CONDUCTING COATINGS*. Philosophical Magazine, 1974. **30**(1): p. 225-228 (1974).
[55] Fryer, J. and F. Holland, *Ultramicroscopy*, **11**: p. 67-70 (1983).
[56] Fryer, J.R. and F. Holland, HIGH-RESOLUTION ELECTRON-MICROSCOPY OF MOLECULAR-CRYSTALS .3. RADIATION PROCESSES AT ROOM-TEMPERATURE. Proceedings of the Royal Society of London Series a-Mathematical Physical and Engineering Sciences, **393**(1805): p. 353-& (1984).
[57] Zan, R., et al., Control of Radiation Damage in MoS_2 by Graphene Encapsulation. *Acs Nano*, **7**(11): p. 10167-10174 (2013).
[58] Algara-Siller, G., et al., The pristine atomic structure of MoS2 monolayer protected from electron radiation damage by graphene. *Applied Physics Letters*, **103**(20) (2013).
[59] Wang, C., et al., High-Resolution Electron Microscopy and Spectroscopy of Ferritin in Biocompatible Graphene Liquid Cells and Graphene Sandwiches. *Advanced Materials*, **26**: p. 3410–3414 (2014).

Quantitative Characterization of Magnetic Materials Based on Electron Magnetic Circular Dichroism with Nanometric Resolution Using the JEM-1000K RS Ultra-High Voltage STEM

Shunsuke Muto[1], Jan Rusz[2], Kazuyoshi Tatsumi[1], Roman Adam[3], Shigeo Arai[1], Vancho Kocevski[2], Peter M. Oppeneer[2], Daniel E. Bürgler[3] & Claus M. Schneider[3]

[1]Division of Green Materials, EcoTopia Science Institute, Nagoya University, Japan
[2]Department of Physics and Astronomy, Uppsala University, Sweden
[3]Peter Grünberg Institut, Forschungszentrum Jülich GmbH, Germany

Electron magnetic circular dichroism (EMCD) allows the quantitative, element-selective determination of spin and orbital magnetic moments in a manner similar to its better-established X-ray counterpart, X-ray magnetic circular dichroism (XMCD). As an advantage over XMCD, EMCD measurements are performed using transmission electron microscopes, which are routinely operated at sub-nanometer resolution. However, because of the low signal-to-noise ratio of the EMCD signal, it has not yet been successful to obtain quantitative information from EMCD signals at the nanometer scale. In the present article, we demonstrate a new approach to EMCD measurements that takes most of the higher accelerating voltage of the incident electrons, which considerably enhances the applicability of the technique. The statistical analysis introduced here yields robust quantitative EMCD signals. In the present scheme, quantitative magnetic information can be routinely obtained using electron beams of only a few nanometers in diameter, without imposing any restrictions on the crystalline order of the specimen.

Introduction

Electron microscopy, when used in combination with several types of spectrometers, provides not only magnified images with spatial resolutions down to the atomic scale but also local chemical information such as chemical composition and electronic states. In particular, electron energy-loss spectroscopy (EELS), which analyzes electrons transmitted through a sample, can be used to explore a rich variety of material properties. Its emerging significance in nanometric analysis is growing further, in competition with its counterpart, the X-ray absorption spectroscopy, measured at synchrotron X-ray sources.

Modern synchrotron X-ray sources capable of delivering intense radiation with a well-defined polarization have provided insight into not only the structural and chemical but also magnetic aspects of solids [1]. The usefulness of synchrotron X-rays in magnetism can be attributed to the discovery of an important phenomenon called as X-ray magnetic circular dichroism (XMCD) [2-4]. XMCD originates from the dependence of the absorption cross-section on the sample magnetization with respect to the photon helicity. Spin and orbital magnetic moments can be quantitatively determined in an element-specific manner using a simple integration of the XMCD spectra employing sum rules [5,6]. An analog to XMCD is the electron magnetic circular dichroism (EMCD) technique, in which electrons are transmitted through a magnetic sample in a transmission electron microscope (TEM) [7,8]. EELS measured at core levels in different positions in the diffraction plane can then be employed to extract element-selective magnetic information.

Since the possible existence of EMCD was first outlined in 2003 [7] using methods reminiscent of symmetry-selected EELS [9], recent theoretical and experimental progress in the EMCD technique has led to improvements in its spatial resolution [10,11], facilitated theoretical understanding [12-16], and also given rise to the first quantitative studies [17-19] of spin and orbital magnetic moments. Although TEM has been expected to offer a much higher spatial resolution than that currently obtainable with XMCD, high-resolution quantitative EMCD has not yet been achieved, because of its inherent low net

Division of Green Materials, EcoTopia Science Institute, Nagoya University, Furo-cho, Chikusa-ku Nagoya 464-8603, Japan

E-mail: s-mutoh@nucl.nagoya-u.ac.jp

signal strength. Because EMCD is measured at core-level edges, the signal strength exhibits a power-law decay as a function of energy loss. Another challenge is the necessity to measure EMCD at diffraction angles that do not coincide with Bragg spots in the diffraction plane, which reduces the signal strength even further. Moreover, beam and sample instabilities, coupled to a potential damage of the sample by an intense electron beam, limit the acquisition time. In most experiments performed to date, a large beam current was used in an optimized geometry—namely, the 2-beam [8,14,17,20,21] or 3-beam [11,17,19,22] Bragg condition—which in turn necessitates the use of a single-crystalline specimen in a precise and stable orientation.

In our recent article [23], we had introduced a new scheme for measuring EMCD by utilizing an ultra-high voltage scanning transmission electron microscope (UHV-STEM) equipped with EELS. The conventional procedure of optimizing the signal-to-noise ratio (SNR) in a fixed geometry is inherently prone to beam damage and stability issues. Therefore we rapidly collected a large number of independent spectra and, in addition, introduced a new statistical technique for the analysis, efficiently overcoming the aforementioned restrictions and reducing the lateral resolution of quantitative EMCD to the nanometer range. The power of the technique was demonstrated by analyzing a polycrystalline iron sample [23].

Theoretical background and simulation

The underlying idea for the measurement scheme involves the decomposition of the inelastic transition matrix elements (mixed dynamic form-factor; MDFF) using a dipole approximation into a linear combination of non-magnetic and magnetic terms, including their anisotropies [15]. In a material with a cubic crystal structure, such as bcc iron, the anisotropic terms are negligible, and a simple expression for the MDFF $S(\mathbf{q}, \mathbf{q}', E)$ remains:

$$S(\mathbf{q}, \mathbf{q}', E) \propto \mathbf{q}.\mathbf{q}' N(E) + i(\mathbf{q} \times \mathbf{q}')_Z M_Z(E), \cdots\cdots\cdots (1)$$

where $\mathbf{q}$ and $\mathbf{q}'$ are momentum transfer vectors, E is the energy loss, and $N(E)$, $M_Z(E)$ are the white-line non-magnetic signal and magnetic EMCD signal, respectively. In this equation, it has been assumed that the sample is magnetically saturated along the z-axis in the magnetic field of the objective lens.

At an arbitrary relative orientation of the crystalline axes, incoming beam, and detector, the scattering cross-section $\partial^2\sigma(E,\Omega) / \partial E \partial \Omega$ will be a weighted sum, as given below:

$$\frac{\partial^2\sigma(E,\Omega)}{\partial E \partial \Omega} \propto A(\Omega)N(E) + B(\Omega)M_Z(E), \cdots\cdots\cdots (2)$$

where $A(\Omega)$ and $B(\Omega)$ are coefficients that depend on the diffraction angle Ω. Consequently, we establish that for a bcc-iron polycrystalline sample with sufficiently large grains, every spectrum is a linear combination of a white-line non-magnetic signal $N(E)$ and a magnetic EMCD signal $M_Z(E)$, albeit with *a priori* unknown coefficients $A(\Omega)$ and $B(\Omega)$.

On the basis of the theoretical method outlined above, we performed simulations to obtain the dichroic signal distribution in the diffraction plane for a randomly oriented polycrystalline sample. A bcc iron supercell of 4 × 4 × 18 lattice dimensions (approximately 1 nm × 1 nm × 5 nm) containing 576 iron atoms was melted, annealed, and slowly cooled in accordance with classical molecular dynamics, considering the interatomic potential proposed by Mendelev et al. [24]. The procedure was repeated multiple times, and in some cases, we obtained a model structure with several crystalline grains of different orientations (**Fig.1**(a)). The corresponding electron diffraction pattern is presented in Fig. 1(b). We calculated the electronic structure of this model structure using density functional theory and estimated an average magnetization of 2.19 μ_B per atom. For calculations of the dynamical diffraction, this model structure was periodically

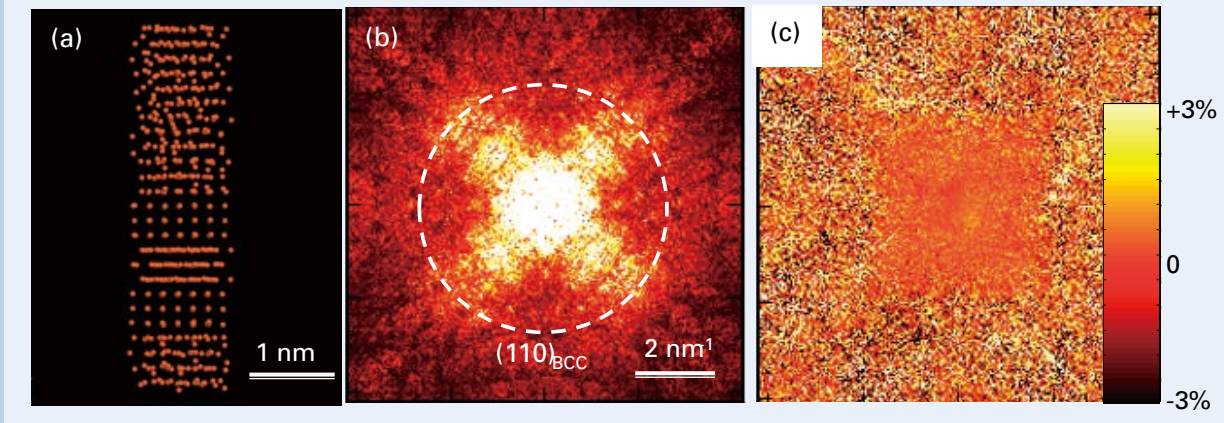

Fig. 1 (a) Model bcc Fe polycrystalline supercell produced by a classical molecular dynamics simulation. (b) Calculated electron diffraction pattern of the cell. (c) The theoretical EMCD signal intensity distribution (along z-direction [18]) in the diffraction plane (1 mrad ~ 0.25 g_{110} ~ 1.25 nm^{-1}).

repeated in the x, and y dimensions and illuminated by a plane wave. The calculated Fe-L_3 edge energy-filtered diffraction pattern of the magnetic signal along the z-direction [16] is presented in Fig. 1(c). Approximately 600 beams were considered in the simulation [12,25]. The approach proposed in this article has been inspired by simulated distributions of dichroic signals in the diffraction plane [12,15], which suggest that EMCD is present almost everywhere in the diffraction plane, despite non-trivial variations in strength and sign.

Experimental

A 30-nm-thick bcc iron layer and a 3-nm-thick Al cap layer (to prevent the oxidation of Fe) were deposited on 50-nm-thick Si_3N_4 membranes by thermal evaporation in an ultra-high vacuum molecular beam epitaxy (UHV-MBE) system. The disordered structure of the membranes (nanocrystalline or amorphous) led to a polycrystalline morphology of the metallic Fe/Al films. Air exposure after the deposition oxidized the Al cap layer to a depth of 1.5 to 2 nm. Because the Al layer was 3-nm thick, a closed AlO_x layer was maintained even in the presence of surface roughness, as is likely for a polycrystalline film. The grain size was ~30 nm, which is comparable to the thickness of the iron layer (**Fig. 2**(a)).

Because oxidation of the iron film could have substantial effects on the intensity ratio of the L_3 and L_2 edges [26], the film was examined with EELS to probe if any oxidation of the iron occurred before or after the EMCD measurements. This was achieved by taking advantage of the fact that the oxygen K edge can be easily distinguished between aluminum and iron oxides. Nevertheless, no iron oxides were observed within the detection limit of EELS (< 1 at %).

The measurements were performed using EELS spectral imaging with an ultra-high voltage scanning transmission electron microscope (UHV-STEM), the JEOL JEM-1000K RS of Nagoya University (Fig. 2(b)). The STEM was operated at 1 MV, and it was equipped with an equivalent Gatan Image Filter (GIF) Quantum specially designed for this accelerating voltage. The sample was heated to 200 °C during the experiment so that measurements were contamination-free. The full width at half maximum (FWHM) of the zero-loss peak (ZLP) was ~2.6 eV because the beam current had been increased to ensure an increase in spectral counts.

A schematic diagram of our experimental setup is presented in **Fig. 3**. The electron beam was focused to ~5 nm, and the sample was scanned with 15 × 15 pixels with a scan step of 20 nm. This configuration ensured that the electron beam illuminated random grains, typically one or a few grains at each scanned position. The convergence semiangle of the probe was ~1 mrad. EELS spectra were recorded with a dispersion of 0.5 eV/channel, exposure time of 30 s for each spot, and a collection semiangle of ~1 mrad. The detector aperture was placed adjacent to the transmitted beam in the diffraction plane to avoid including the intense transmitted beam. Under these conditions, the Fe-L_3 peak intensities ranged between 8,000 and 12,000 counts per spectrum. The same experiment was repeated independently for three different areas.

Results

The acquired dataset forms the starting point for our statistical procedure leading to the extraction of the EMCD spectrum. In the measurement, we use an ultra-high-voltage (1 MV) electron beam to significantly reduce the effect of multiple scattering, which could otherwise distort the EMCD signal [18,19,27]. Our theoretical simulations indicate that the net EMCD signal at an accelerating voltage of 1 MV is ~20% larger than that obtained at 200 kV for a specimen thickness between 25 and 40 nm [28], as shown in **Fig. 4**.

The obtained spectral image data-cubes were

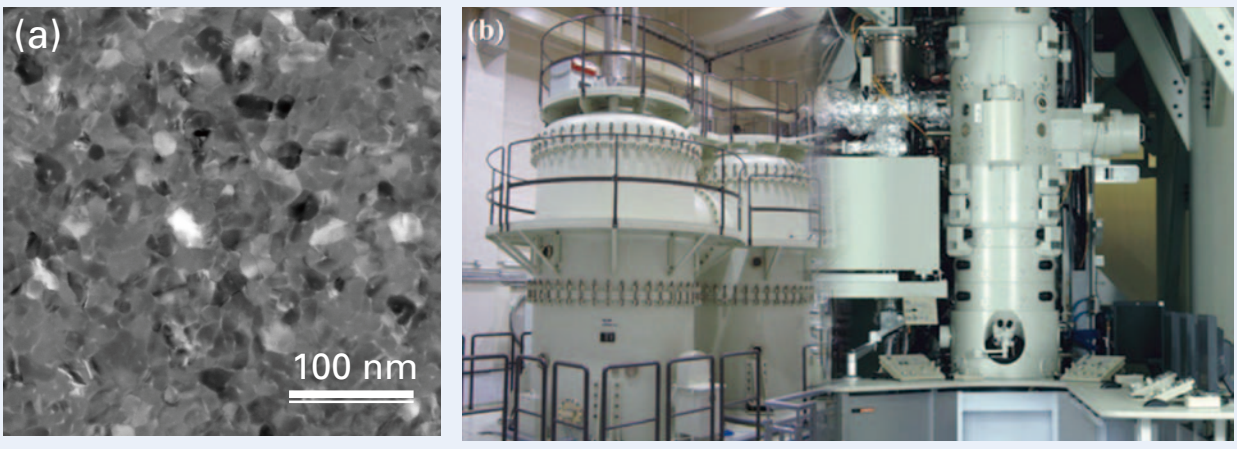

Fig. 2 (a) TEM image of the present polycrystalline Fe film. (b) Photograph of the UHV-STEM JEM-1000K RS at Nagoya University.

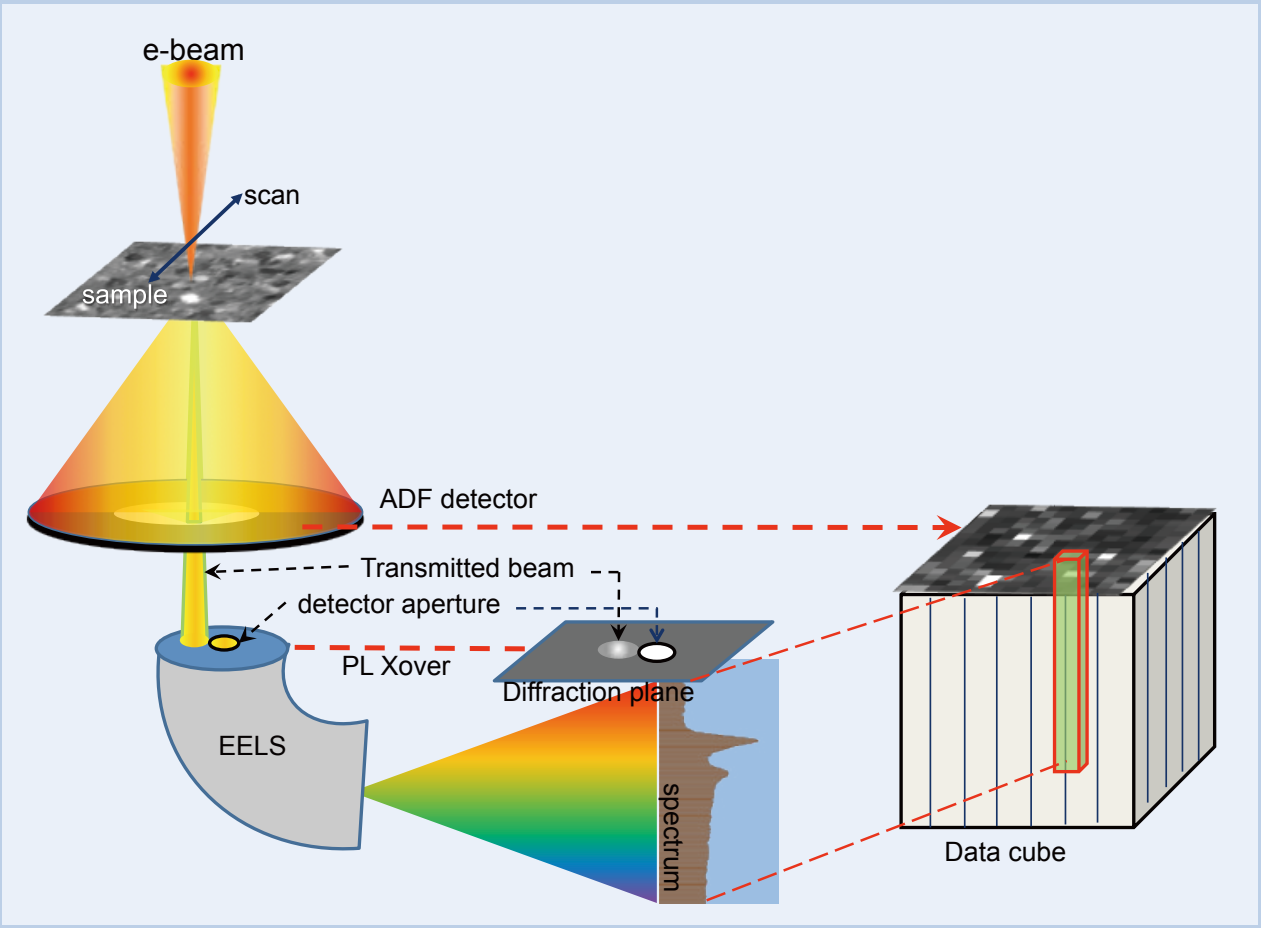

Fig. 3 Schematic drawing of the present experimental setup and the data obtained (ADF: annular dark field, PL: projector lens).

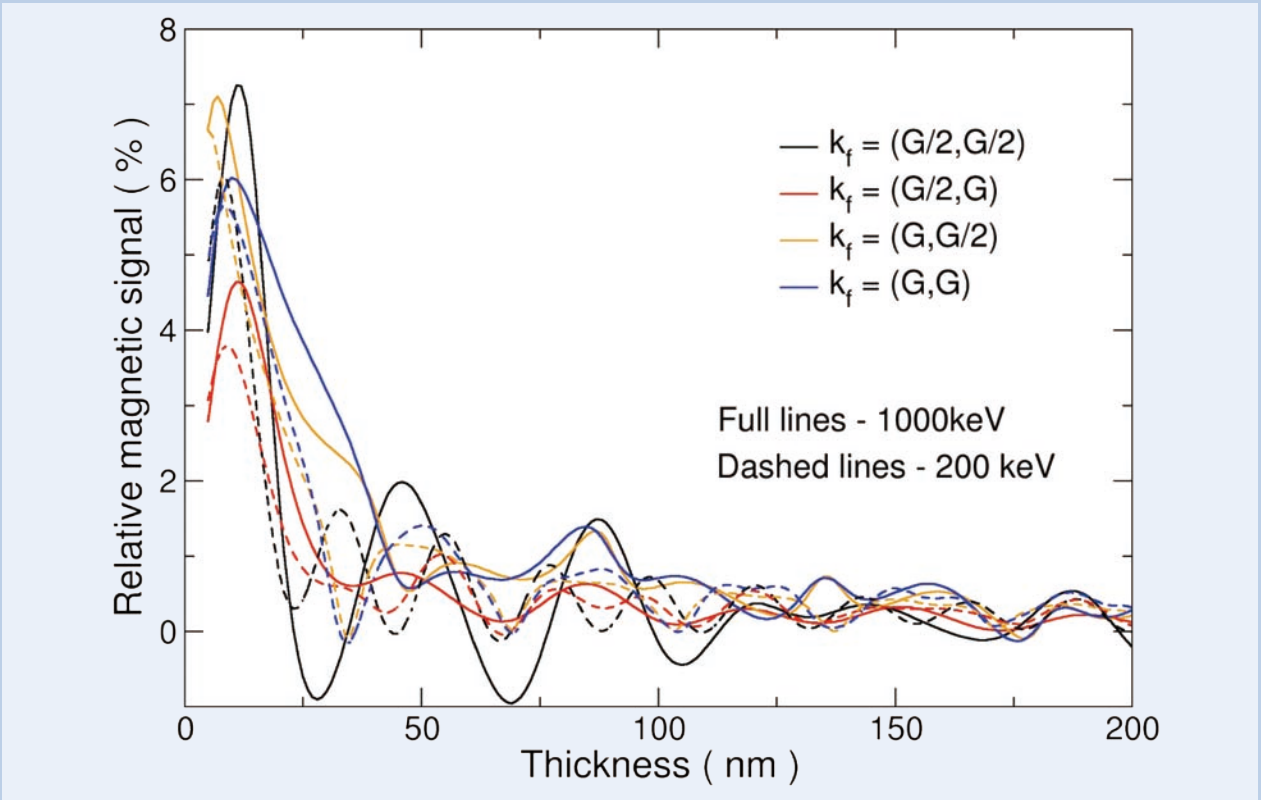

Fig. 4 Calculated net EMCD signal at accelerating voltages of 200 kV and 1 MV on the Fe-L_3 peak, with respect to its peak height, for a bcc single crystal Fe. Here, the incident beam is parallel to the <$\bar{1}$1 8> and the 110 systematic row is excited. Each solid line corresponds to the case of the center of the Laue circle indicated in the legend, in units of G, where G = (110) is a Bragg reflection defining the systematic row orientation.

first treated by aligning the drifted peak positions and removing X-ray spikes (very bright/dark spots). We then applied the pre-edge background subtraction to extract the Fe-$L_{2,3}$ peaks, after which we applied a low-pass filter with a window width that was variable from 3.5 to 10 eV.

We did not apply the Fourier-ratio deconvolution to remove the plural scattering effect, because the plasmon peak-to-zero loss peak intensity ratio was less than 6%, causing only a negligible difference to the final m_L/m_S ratio within the experimental accuracy [18]. The reduced size of the error, attributed to the multiple scattering, is another advantage of using a megavolt-STEM in addition to the improved strength of the EMCD signal compared with lower acceleration voltages, as more explicitly discussed in [28].

Each measured spectrum was normalized by scaling the post-edge intensity, integrated over the range 740–750 eV, to one. The effect of this normalization on the quantitative analysis was discussed in a previous study [29]. In the first step, we examined the difference spectra for all pairs of the spectra in the dataset. As described above, each spectrum can be considered as consisting of two components, a magnetic one (the EMCD) and a nonmagnetic one. When a spectrum is acquired in a random orientation, the weight of each component is also random; however, once the spectra are background-subtracted and normalized post-edge (where the magnetic component is always zero), the nonmagnetic component will be identical in every spectrum and will therefore be eliminated by taking the difference spectrum.

After pre-processing the 225 measured spectra in each dataset, we calculated a difference spectrum for every pair of spectra present in the dataset, which yielded a total of 25,200 difference spectra per dataset. Each of the difference spectra were subsequently examined for the presence of an EMCD signal using criteria that probe the relative signs of intensity around the L_3 and L_2 edges:

$$\int_{L_3} \Delta\sigma\, dE \cdot \int_{L_2} \Delta\sigma\, dE < 0 \text{ and}$$
$$I_{\Delta\sigma}(\text{at } L_3 \text{ peak}) \cdot I_{\Delta\sigma}(\text{at } L_2 \text{ peak}) < 0, \quad \cdots\cdots (3)$$

where $\int_{L_3} \Delta\sigma\, dE$ represents the EMCD signal intensity integrated over the Fe-L_3 peak region and $I_{\Delta\sigma}$ (at L_3 peak) denotes the EMCD signal value at the L_3 peak position. All the difference spectra that met our selection criteria were first adjusted in sign such that the L_3 signal was positive (cf., **Fig. 7**(a)) and then summed. Of the entire set, approximately 20–25% of the pairs always displayed signs of the EMCD signal and thus met our selection criteria. The selected subset (~ 5,000 difference spectra) originated from more than 100 independent raw spectra among the entire set of 225 spectra, which ensures that the statistical noise is reduced by a factor of 10 compared to the average noise of individual raw spectra.

The final summed signal intensities and profiles for the three datasets were nearly identical (see **Fig. 5**(a)). Minor differences were observed in the pre-edge and post-edge background regions, which were related to varying fluctuations between individual datasets. These differences can be attributed to inaccuracies in the extraction of the power-law background signal, which is caused by extrapolation from a noisy pre-edge signal.

We averaged the three accumulated EMCD signals to obtain the final EMCD spectrum, which is presented in **Fig. 6**. The EMCD signal intensity fraction was estimated to be 2–2.3% of the Fe-$L_{2,3}$ signal intensity (Fig. 5(b)), which is consistent with the theoretical estimate (see Fig. 4). The final EMCD signal is a result of averaging over ~15,000 different spectra and was thus observed to be statistically robust.

After extraction of an EMCD signal with a good SNR, the EMCD sum rules [12] were applied to the signal to evaluate the orbital moment/spin moment ratio, which is given by [13,14]:

$$\frac{m_L}{m_S} = \frac{2}{3}\frac{\int_{L_3}\Delta\sigma(E)dE + \int_{L_2}\Delta\sigma(E)dE}{\int_{L_3}\Delta\sigma(E)dE - 2\int_{L_2}\Delta\sigma(E)dE} = \frac{2q}{9p - 6q} \quad \cdots (4)$$

where q is an energy integral of the EMCD spectrum $\Delta\sigma(E)$ over both edges and p is an energy integral over the L_3 edge only. Without loss of generality, we can rescale the EMCD spectrum or its integral such that $p = 1$ (Fig. 6(a)). Thus, the orbital to magnetic moment ratio m_L/m_S becomes a function of q only. The application of the low-pass filter can possibly lead to the overlap and cancellation of the EMCD signals of the L_3 and L_2 peaks, which could equally reduce the magnitude of both peaks and consequently enhance the effect of their difference. Moreover, the application of the low-pass filter can affect the post-edge normalization [29]. The latter could alter the m_L/m_S ratio determined using the sum rules. The m_L/m_S ratio was hence plotted as a function of the low-pass filter window width, as illustrated in Fig. 6(b). The minimal and maximal q values were extracted from the post-edge region between 740-750 eV energy loss, from which the minimal and maximal m_L/m_S were calculated. In Fig. 6(b), the m_L/m_S values with error bars are plotted as the middle points of these upper and lower bounds. The shaded area is bounded by linear regression lines (grey solid lines) at the lower and upper bound values. The final m_L/m_S was evaluated to be the intercept of the linear regression line (grey broken line) of the middle points +/- half of the interval defined by the intercepts of the bound lines. By linear extrapolation to zero filter width, we finally obtained $m_L/m_S = 0.0429 \pm 0.0075$, which is in good agreement with the value obtained by XMCD for bcc iron, 0.043 [3]. To our knowledge, this result is the first quantitative EMCD detection performed on a polycrystalline film.

Discussion

The main error source for our extraction method of the EMCD spectrum stems from the imperfection of the employed detectors: the recorded raw spectra may include significant fractions of systematic errors that originate from instrumental instabilities and concomitant intrinsic limitations, in addition to statistical random noise.

For the reasons stated above, we observed that

conventional statistical signal extraction methods, such as the one based on multivariate curve resolution technique [29], were not efficient. It was rather essential that the data are first sorted so that only the data sets containing significant signal levels are selected on the basis of the selection criteria (Eq. (3)) applied to the difference spectra.

To eliminate the possibility that our procedure might lead to a fake EMCD-like signal profile extracted from a random noisy data array, we performed an equivalent set of measurements on an antiferromagnetic NiO film, from which no EMCD signal was expected because of the cancellation of magnetic signals from symmetrically equivalent atoms with antiparallel moments. The sample was a NiO polycrystalline film (grain size ~ 30 nm, film thickness ~ 30 nm), and the measurements were performed under the same conditions (at 165°C, which is below the Néel temperature) as for the bcc iron film. Subsequently, the same data processing procedure was applied to the Ni $L_{2,3}$ white-line spectra.

The noise level was estimated by taking the square-root of the sum of squares of the difference spectra between the raw and median filtered (averaged over every 10 channels) spectra divided by the number of channels used for the analysis. Then, the SNR was estimated by dividing the intensity at the L_3 peak position of the averaged EMCD signal by the noise level. The estimated SNR was 2-3 for bcc iron, whereas it was less than 0.5 for NiO. The averaged signal extracted from the NiO data was

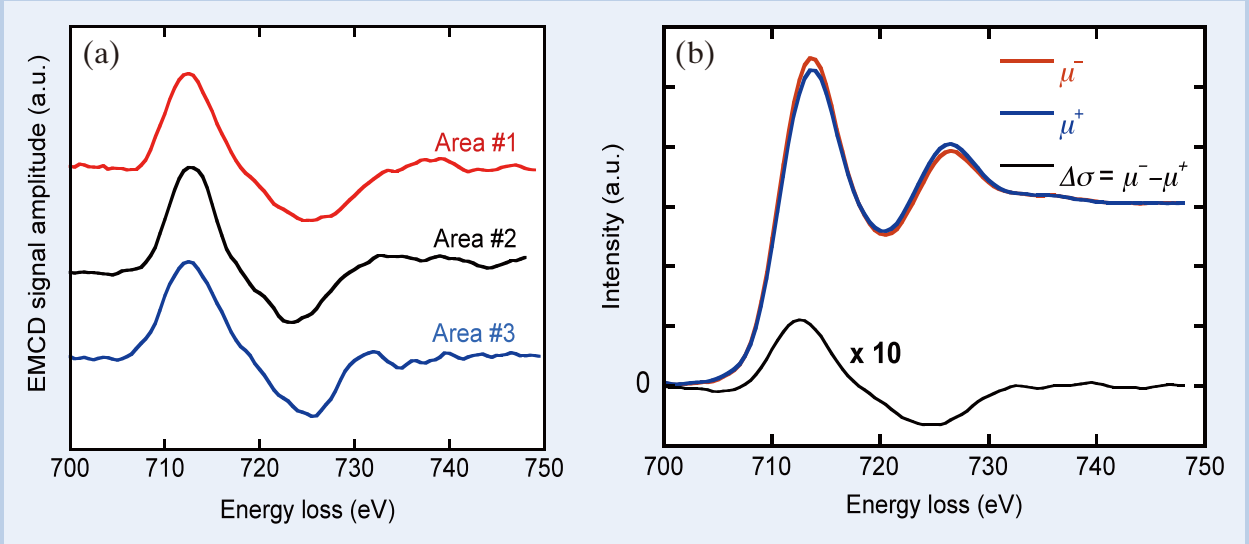

Fig. 5 Representative EMCD spectra measured on a fine-grain polycrystalline Fe film by STEM-EELS at an accelerating voltage of 1 MV, in the case where a 5-eV low-pass filter is applied to the original spectra. (a) EMCD signals extracted during three independent trials, from different areas of the sample. (b) A pair of Fe-$L_{2,3}$ spectra (μ^+ and μ^-) extracted from the dataset and the difference spectrum (EMCD signal) $\Delta\sigma = \mu^- - \mu^+$.

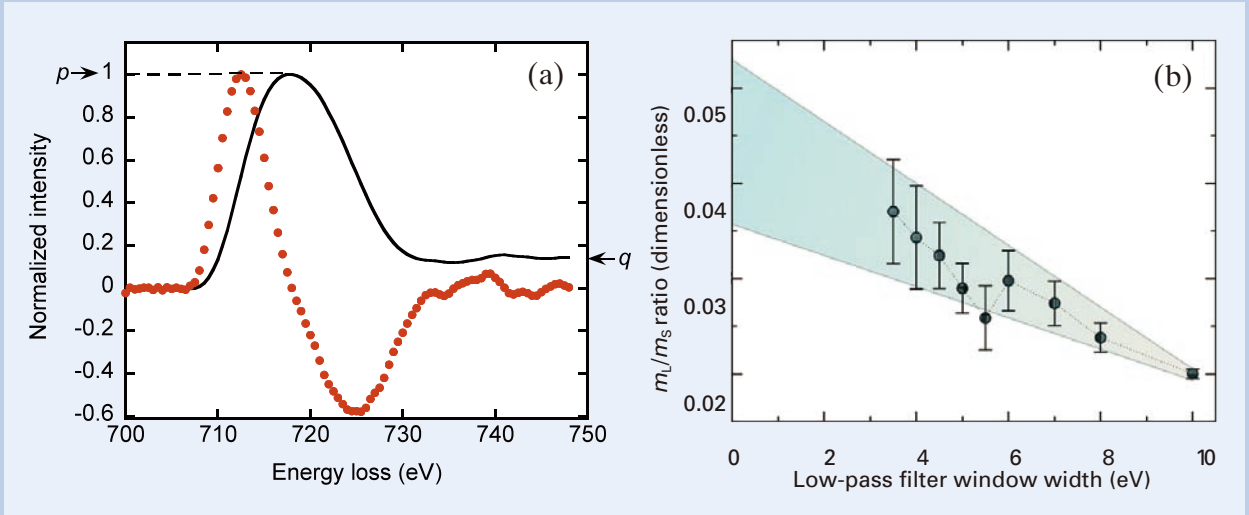

Fig. 6 (a) The averaged EMCD signal (red dots) and its cumulative sum (black line), evaluated, in order to apply the sum rule. (b) Plot of m_L/m_S estimated by the sum rule, as a function of the window width of the low-pass filter used for data smoothing.

actually observed to exhibit a bimodal EMCD-like profile; however, the profile significantly varied upon changing the integration width for the first selection criterion. Additionally, the q-value from the sum rule was sometimes positive and sometimes negative, without a clear trend with respect to the filter width. The bimodal profile is a result of the selection requirements (Eq. (3)), which extract all EMCD-like difference-spectra naturally occurring in the set of completely random difference-spectra. However, the signal profiles extracted from the iron film exhibited a stable feature. The situation can be best observed from the overlaid typical difference spectra meeting the selection criteria for the two cases, as shown in Fig. 7(a) and (b). For the iron film, one can clearly recognize an approximate EMCD signal profile, whereas for the NiO film, the spectra visually differ only slightly from random noise.

As an additional test of the statistical robustness of the polycrystalline iron EMCD result, in contrast to the averaged NiO signals originating from noise, we varied the $L_{2,3}$ peak energies in the neighborhood of their experimental values in our extraction procedure. At every combination of the $L_{2,3}$ peak energies, an averaged EMCD-like signal was constructed. For every extracted signal, we calculated its norm as a sum of squares within the edge integration intervals. If a true EMCD signal was present in the data, this sum of squares would have a local maximum near the physically correct values of

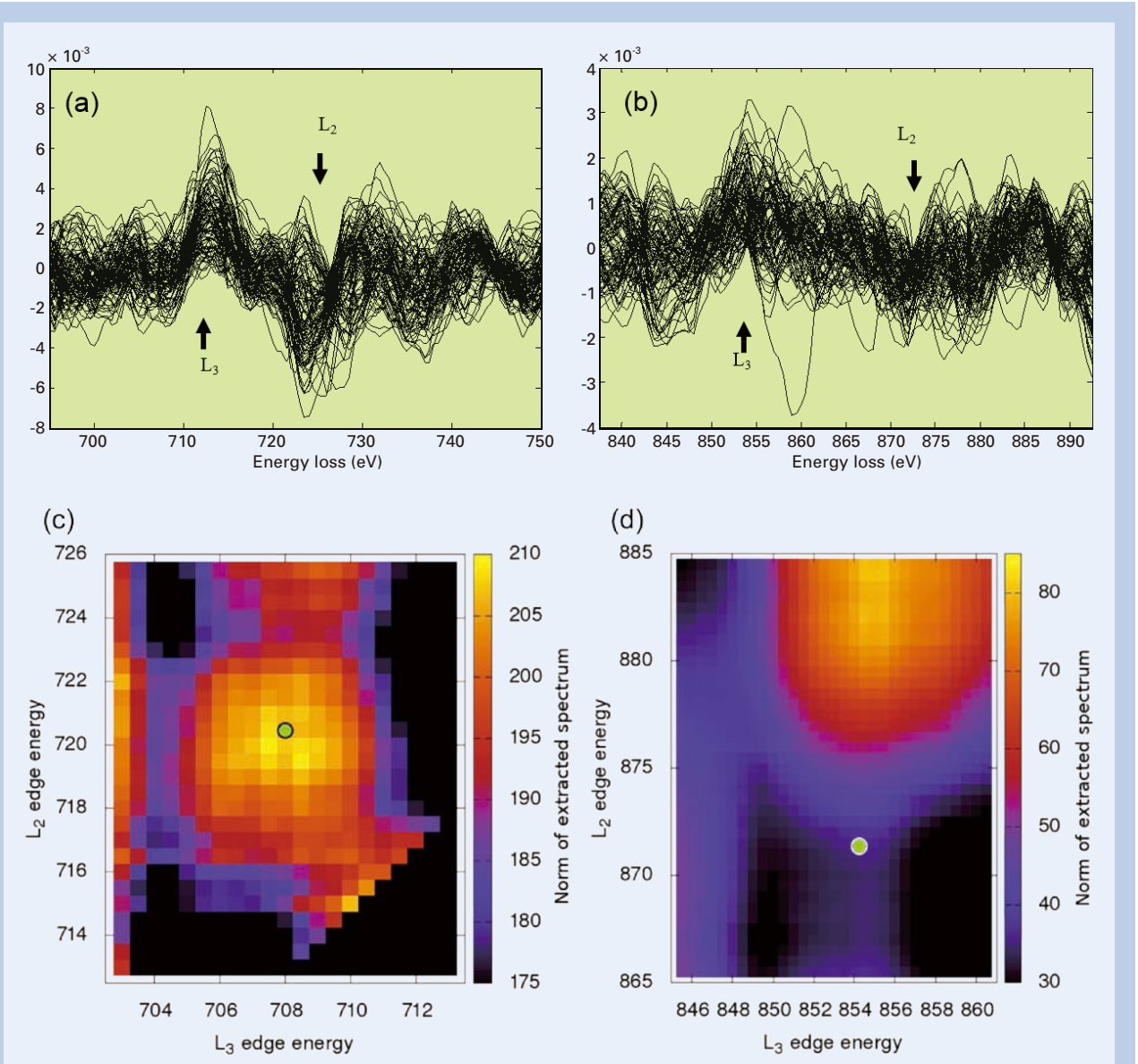

Fig. 7 (a) Example of the difference spectra for a polycrystalline bcc iron film. Only spectra that met the criteria (Eq. (3)) are shown, after being aligned in sign. (b) Same as (a) but for a polycrystalline NiO film. The arrows indicate the L_3 and L_2 peak positions of the raw spectra. Note the different scale of the vertical axes relative to the post-edge normalized spectra, considering that all raw spectra were normalized to 1 in the post-edge region. (c) Maps of the norm of the extracted averaged spectrum, as a function of the L_2 and L_3 edge energies for the polycrystalline bcc iron sample (see Discussion). (d) Same as (c) but for the antiferromagnetic NiO film. The green circles indicate experimental edge energies. Note again the different scale of the norms.

the peak energies.

Fig. 7(c) and (d) present maps of the norms calculated for a median filter of 7 eV and an integration range ±5 eV around the assumed peak energies, with the L_3 energy as its abscissa and the L_2 energy as its ordinate. A green circle denotes the position of the L_3/L_2 peak energies, where the experimental white-line spectra exhibit maximal counts. The striking difference between the two plots clearly demonstrates the validity of our method. The polycrystalline iron data reveal a distinct peak around the expected values of the peak energies, with a maximum within 1 eV of the experimental values. Conversely, the NiO spectra do not exhibit any such feature around the expected peak energies.

Conclusion

In this article we demonstrated a method utilizing UHV-STEM-EELS, that leads to statistically significant EMCD spectra. We emphasize that, even though a 5-nm nanoprobe was used, the spectral differences were computed from the entire data stack, rendering the effectively sampled area to be of the order of 100 nm. This area could be reduced by changing the scanning pattern, provided that sufficiently random orientations were included in each dataset. Consequently, our approach allows quantitative EMCD studies of non-single crystalline samples at the nanoscale, and hence paves the way for a wide range of applications of EMCD experiments in the field of nano-magnetism.

Acknowledgments

We are very grateful to the engineers, in particular Drs. M. Ohsaki and S. Ohta, of JEOL Ltd. for their dedicated efforts in building the new UHV-STEM at Nagoya University. A part of this work was supported by a Grant-in-Aid on Innovative Areas "Nano Informatics" (grant number 25106004) from the Japan Society of the Promotion of Science, Swedish Research Council, and STINT.

References

[1] Stöhr, J. & Siegmann, H., Ch. Magnetism: From fundamentals to Nanoscale Dynamics. Springer, ISBN 978-3-540-30283-4 (2006).
[2] Erskine, J. L. & Stern, E. A., *Phys. Rev. B* **12**, 5016-5024 (1975).
[3] Schutz, G., Wagner, W., Wilhelm, W., Kienle, P., Zeller, R., Frahm, R. & Materlik, G., *Phys. Rev. Lett*. **58**, 737-740 (1987).
[4] Chen, C. T., Idzerda, Y. U., Lin, H-J., Smith, N. V., Meigs, G., Chaban, E., Ho, G. H., Pellegrin, E. & Sette, F., *Phys. Rev. Lett*. **75**, 152-155 (1995).
[5] Thole, B T., Carra, P., Sette, F. &. van der Laan, G., *Phys. Rev. Lett*. **68**, 1943-1946 (1992).
[6] Carra, P., Thole, B. T., Altarelli, M. & Wang, X., *Phys. Rev. Lett*. **70**, 694-697 (1993).
[7] Hebert, C. & Schattschneider, P., *Ultramicroscopy* **96**, 463-468 (2003).
[8] Schattschneider, P., Rubino, S., Hébert, C., Rusz, J., Kunes, J., Novák, P., Carlino, E., Fabrizioli, M., Panaccione, G. & Rossi, G., *Nature* **441**, 486-488 (2006).
[9] Batson, P., *Phys. Rev. Lett*. **70**, 1822-1825 (1993).
[10] Schattschneider, P., Hébert, C., Rubino, S., Stoeger-Pollach, M., Rusz, J. & Novák, P., *Ultramicroscopy* **108**, 433-438 (2008).
[11] Schattschneider, P., Stoeger-Pollach, M., Rubino, S., Sperl, M., Hurm, Ch., Zweck, J. & Rusz, J., *Phys. Rev. B* **78**, 104413 (2008).
[12] Rusz, J., Rubino, S. & Schattschneider, P., *Phys. Rev. B* **75**, 214425 (2007).
[13] Rusz, J., Eriksson, O., Novák, P. & Oppeneer, P. M., *Phys. Rev. B* **76**, 060408(R) (2007).
[14] Calmels, L., Houdellier, F., Warot-Fonrose, B., Gatel, C., Hÿtch, M. J., Serin, V., Snoeck, E. & Schattschneider, P., *Phys. Rev. B* **76**, 060409(R) (2007).
[15] Rusz, J., Rubino, S., Eriksson, O., Oppeneer, P. M. & Leifer, K., *Phys. Rev. B* **84**, 064444 (2011).
[16] Rubino, S., Schattschneider, P., Rusz, J., Verbeeck, J. & Leifer, K., *J. Phys. D: Appl. Phys.* **43**, 474005 (2010).
[17] Lidbaum, H., Rusz, J., Liebig, A., Hjörvarsson, B., Oppeneer, P. M., Coronel, E., Eriksson, O. & Leifer, K., *Phys. Rev. Lett*. **102**, 037201 (2009).
[18] Rusz, J., Lidbaum, H., Rubino, S., Hjörvarsson, B., Oppeneer, P. M., Eriksson, O. & Leifer, K., *Phys. Rev. B* **83**, 132402 (2011).
[19] Warot-Fonrose, B., Gatel, C., Calmels, L., Serin, V. & Schattschneider, P., *Ultramicroscopy* **110**, 1033 (2010).
[20] Warot-Fonrose, B., Houdellier, F., Hÿtch, M. J., Calmels, L., Serin, V. & Snoeck, E., *Ultramicroscopy* **108**, 393 (2008).
[21] Zhang, Z. H., Wang, X. F., Xu, J. B., Muller, S., Ronning, C. & Li, Q., *Nat. Nanotech*. **4**, 523 (2009).
[22] Stoeger-Pollach, M., Treiber, C. D., Resch, G. P., Keays, D. A. & Ennen, I., *Micron* **42**, 456-460 (2011).
[23] Muto, S., Rusz, J., Tatsumi, K., Adam, R., Arai, S., Kocevski, V., Oppeneer, P. M., Bürgler, D. E. & Schneider, C. M., Nat. Commun. 5, 3138 (2014): doi: 10.1038/ncomms4138.
[24] Mendelev, M. I., Han, S., Srolovitz, D. J., Ackland, G. J., Sun, D. Y. & Asta, M., *Phil. Mag.* **83**, 3977 (2003).
[25] Rusz, J., Muto, S. & Tatsumi, K., *Ultramicroscopy* **125**, 81 (2013).
[26] Stöger-Pollach, M., *Scripta Materialia*, **69**, 820-822 (2013).
[27] Rusz, J., Novák, P., Rubino, S., Hébert, C. & Schattschneider, P., *Acta Phys. Polonica A* **113**, 599 (2008).
[28] Tatsumi, K., Muto, S., Rusz, J., Kudo, T. & Arai, S., *Microscopy*, in press (2014): doi: 10.1093/jmicro/dfu002.
[29] Muto, S., Tatsumi, K. & Rusz, J., *Ultramicroscopy* **125**, 89 (2013).

Photonic Crystal Lasers

Susumu NODA

Department of Electronic Science and Engineering, Kyoto University

In this article, recent progress in broad-area photonic-crystal lasers based on photonic band-edge effect is described. It is shown that unique beam patterns can be generated by designing photonic crystal structures. Moreover, it is demonstrated that watt-class high-power, high-beam-quality, surface-emitting, lasing oscillation has been successfully achieved. These results represent an important milestone for innovation in the field of lasers because it provides a route towards overcoming limitations in applications that suffer from low beam quality, which opens the door to a wide range of applications in material processing, laser medicine, nonlinear optics, sensing and so on.

Introduction

It is well known that semiconductor distributed feedback lasers possess a one-dimensional lattice, and that the forward-propagating wave undergoes Bragg reflection due to this grating, being diffracted to the opposite direction. The resulting forward and backward-propagating waves couple with each other to generate a standing wave, forming a cavity. This is equivalent to the fact that in a one-dimensional photonic crystal the cavity loss is smallest at the band edges, which are at both ends of the photonic bandgap, giving rise to a state that causes oscillation. When this idea is extended to photonic crystals with two-dimensional periodicity, one can make use of the coupling of optical waves due to Bragg reflection within the two-dimensional plane in order to form a standing wave state that covers the entire surface of the plane [1,2]. As a result, it becomes possible to obtain an oscillation mode with an electromagnetic field distribution that is perfectly defined at each lattice point in the two-dimensional crystal. The optical output can be diffracted in the direction perpendicular to the plane of the crystal, thus realizing a surface-emitting characteristic. Two-dimensional photonic crystals hence enable the construction of surface-emitting lasers in which not only the longitudinal mode of lasing is defined, but also the beam pattern, usually referred to as the transverse mode. Furthermore, it becomes possible to realize a novel laser that oscillates in a single longitudinal and transverse mode, no matter how large the surface area is, which surpasses a conventional concept in the field of laser research.

The first semiconductor laser to be based on this principle was realized in 1999 [1]. Since then, in addition to the demonstration of room-temperature continuous lasing, it has been shown that two-dimensional photonic crystals can generate beams with controlled polarization and patterns; for example, a doughnut-shaped beam can be formed, which is expected to be focusable to sizes smaller than the wavelength [2-6]. The other notable recent developments using this principle are the realization of a current-injection-type blue-violet surface-emitting operation and electronically beam-steering operation [7, 8]. We discuss the current state of the art in the following sections.

Kyoto 615-8510, Japan,

E-mail: snoda@kuee.kyoto-u.ac.jp

Basic Device Structure and Operation Principle

Figure 1 shows an example of a laser based on the two-dimensional photonic crystal band-edge effect. This laser consists of two wafers, A and B; wafer A includes an active layer for the injection of electrons and holes, and a photonic crystal as the upper-most layer. The integration of wafers A and B results in the photonic crystal being sandwiched to complete the device. As shown in the insert of Fig. 1, this photonic crystal has a square lattice structure and is designed such that the periodicity in the Γ-X direction matches the emission wavelength in the active layer. In this design, light propagating in a certain Γ-X direction is Bragg diffracted to the opposite (-180°) direction, as well as to the -90° and 90° directions; the four equivalent light waves propagating in the Γ-X direction then couple to form a two-dimensional cavity. More precisely, higher-order Bloch waves in addition to these fundamental four waves are involved for the construction of two-dimensional cavity mode (see **Fig. 2**(a)). Figure 2(b) shows the photonic band structure of this cavity. The lasing mode occurs at the band edges indicated by the red dots at the Γ-points of the four bands, A, B, C and

D. Detailed analysis [9] indicates that either of band edges in bands A and B yields the highest Q factor, and that lasing oscillation most readily occurs there. The output beam can be coupled out to the direction normal to the photonic crystal surface.

Broad Area Coherent Oscillation and Beam Pattern Control

To construct the device shown in Fig.1, the photonic crystal was fabricated by electron beam lithography and dry etching technique and embedded in the device by a wafer bonding technique. The device successfully oscillated coherently in the broad area as shown in **Fig. 3**. It is apparent that a single-wavelength operation was achieved across the device despite the large lasing area of 150 × 150 μm.

Such an ability to realize broad-area coherent oscillation enables us to produce very unique beam patterns, which cannot be realized by conventional semiconductor lasers. Because the pattern of the surface-emitted beam from a photonic crystal laser can be determined by the Fourier transformation of its two-dimensional electromagnetic distribution, the beam pattern can be tailored by varying the electromagnetic distribution in the two-dimensional plane, that is, by changing the coupling state of the light that propagates in various directions in the two-dimensional plane. One effective method of achieving this is to vary the shapes and spacing of the lattice points in the photonic crystal. **Figure 4**(a) and (b) show the electromagnetic field distribution in the unit lattice of a crystal when the holes placed at the lattice points are circles and equilateral triangles, respectively. Changing the shape of the holes from circular to triangular removes the four-fold rotational symmetry in the electromagnetic field distribution; there is no symmetry in the x-direction for triangular holes. Figure 4(c) – (g) show the electromagnetic field distributions over the entire crystal in cases where shifts of the lattice points were introduced in order to increase the lattice spacing in either the longitudinal or transverse directions. Figure 4(c) represents the case with no shift, whereas Fig. 4(d) – (g) represent increasing numbers of shifts. It is apparent that shifting the lattice spacing reverses the polarity of the electromagnetic field distribution at the position

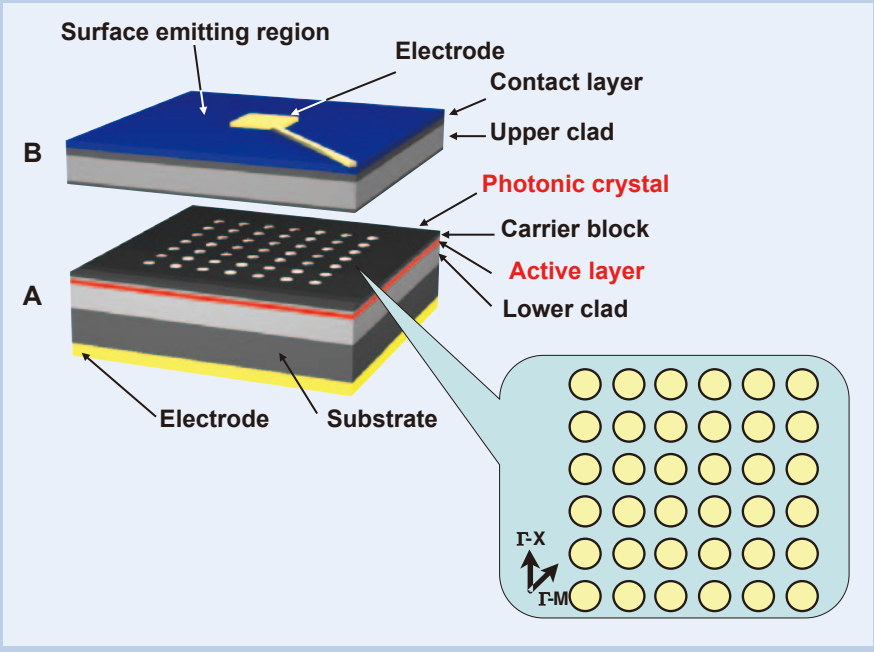

Fig. 1 Schematic of an example of a laser based on the two-dimensional photonic crystal band-edge effect. The inset shows the photonic crystal with a square lattice structure.

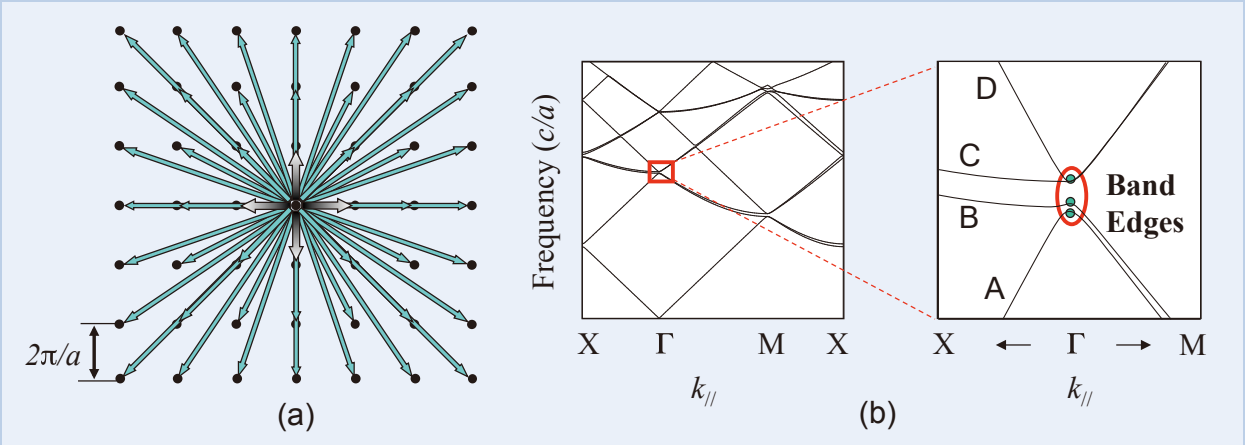

Fig. 2 (a) Bloch waves which construct a two-dimensional cavity mode, and (b) photonic band structure.

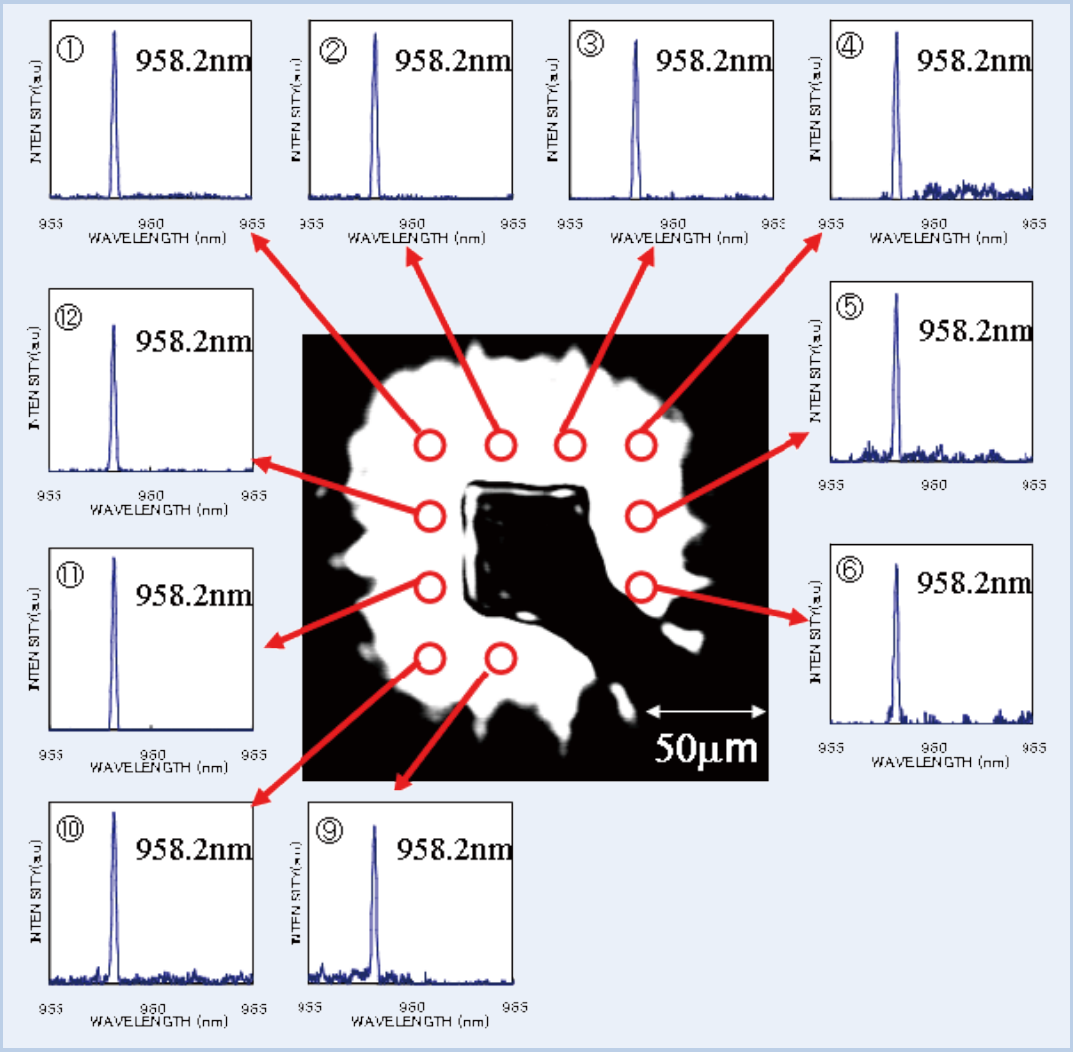

Fig. 3 Near-field pattern with lasing spectra at various points of the device.

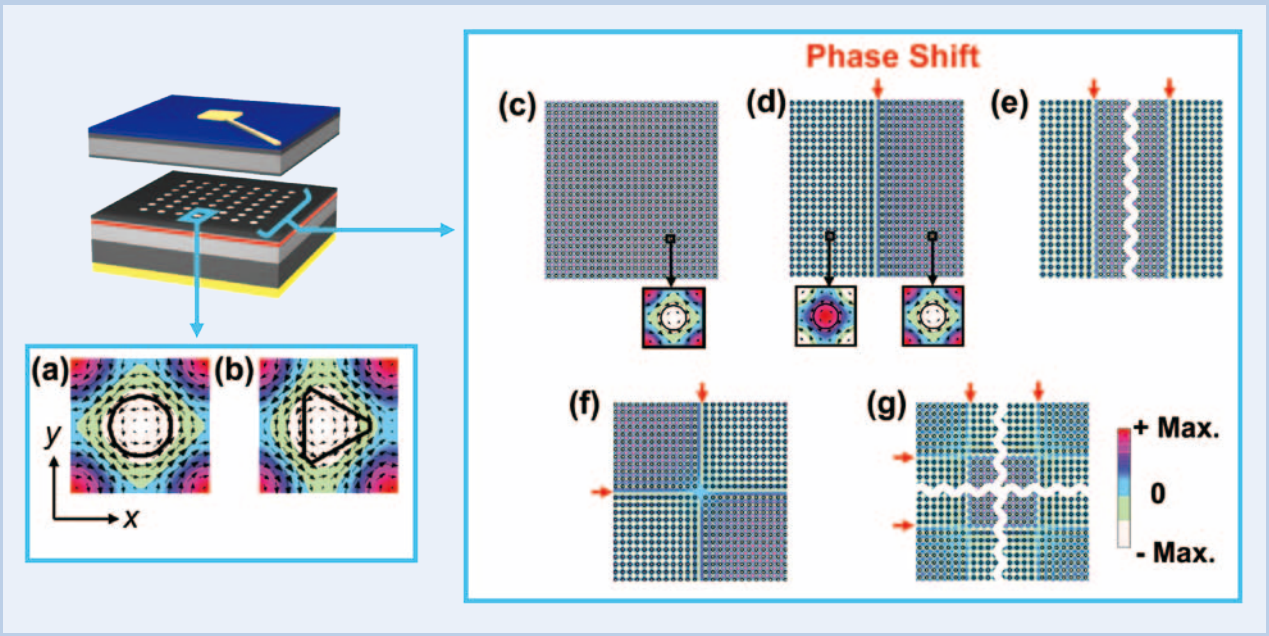

Fig. 4 Electromagnetic field distribution in various photonic crystal lasers. Black arrows represent the electric field, and shading indicates the magnetic field in the direction perpendicular to the paper. Field distributions around the lattice points are shown for (a) circular lattice points and (b) triangular lattice points. Field distributions over the entire crystal are shown for circular lattice points with (c) no phase shift, (d) one phase shift in the x-direction, (e) two phase shifts in the x-direction, (f) one phase shift in both directions, and (g) two phase shifts in both directions. The phase in each region was shifted by π across the boundary where the phase shift was introduced.

of the shift. Further increasing the number of shifts repeats the reversal of the electromagnetic field. It is clear that the electromagnetic field distribution in the plane can be controlled in various ways by appropriate design of the photonic crystal.

We fabricated devices with various different photonic crystal structures, as shown in **Fig. 5**(a)–5(f). All of these devices exhibited lasing oscillation at room temperature with a stable single mode. The right-hand panels of Fig. 5(a)–9(f) show the corresponding measured beam patterns. An interesting array of patterns was obtained ranging from a single doughnut shape to twofold doughnut, fourfold doughnut, and regular circular shapes. The beam divergence was extremely narrow, reflecting the fact that these are large area coherent laser oscillations. The device in Fig. 5(a) has regular circular holes, and the corresponding electromagnetic field distribution exhibits well-defined rotational symmetry as shown in Fig. 4(a). When the laser light corresponding to this electromagnetic field distribution is output to free space, the electromagnetic field at the center of the beam cancels out to yield a doughnut-shaped beam. On the other hand, triangular lattice holes (Fig. 5(f)) remove the rotational symmetry of the electromagnetic field distribution, as shown in Fig. 4(b). The cancellation effect at the center of the beam in Fig. 4(a) is also lost, yielding a clean circular pattern. In this case, the polarization is also different, being linear. Introducing such a nonsymmetrical effect is a key factor in achieving high optical output power by enabling a greater optical extraction efficiency in the perpendicular direction as described in the next section. Note that in the next section, a significantly asymmetric structure in the form of right-isosceles-triangle-shaped air holes was employed for much higher power operation.

Watt-class high-power, high-beam-quality photonic-crystal lasers

In the previous section, the photonic crystal was embedded in the device by a wafer-bonding technique, where bonded interface may contain many defect states which absorb the lasing light and make it difficult to realize high power operation. To avoid such degradation of performance, we changed the method to introduce the photonic crystal into the device from a wafer bonding to a crystal growth technique such as organometallic vapor phase epitaxy (OMVPE) [10,11], and found that the air holes of photonic crystal can be retained even by the crystal growth technique. **Figure 6** (a) shows the schematic of the device fabricated by two-step OMVPE. Note that the growth direction was downward. Figure 6 (b) shows a plan-view scanning electron microscope (SEM) image of the photonic crystal with right-isosceles-triangle-shaped air holes before the crystal growth. A typical cross-sectional SEM image of a row of air holes embedded by OMVPE is shown in Fig. 6(c). It is clearly seen that the air holes were successfully embedded in the device, where the air holes become narrower towards the lower side of the device, whereas the upper parts of the air holes maintain an almost uniform shape with vertical side walls.

I then describe the lasing characteristics of the

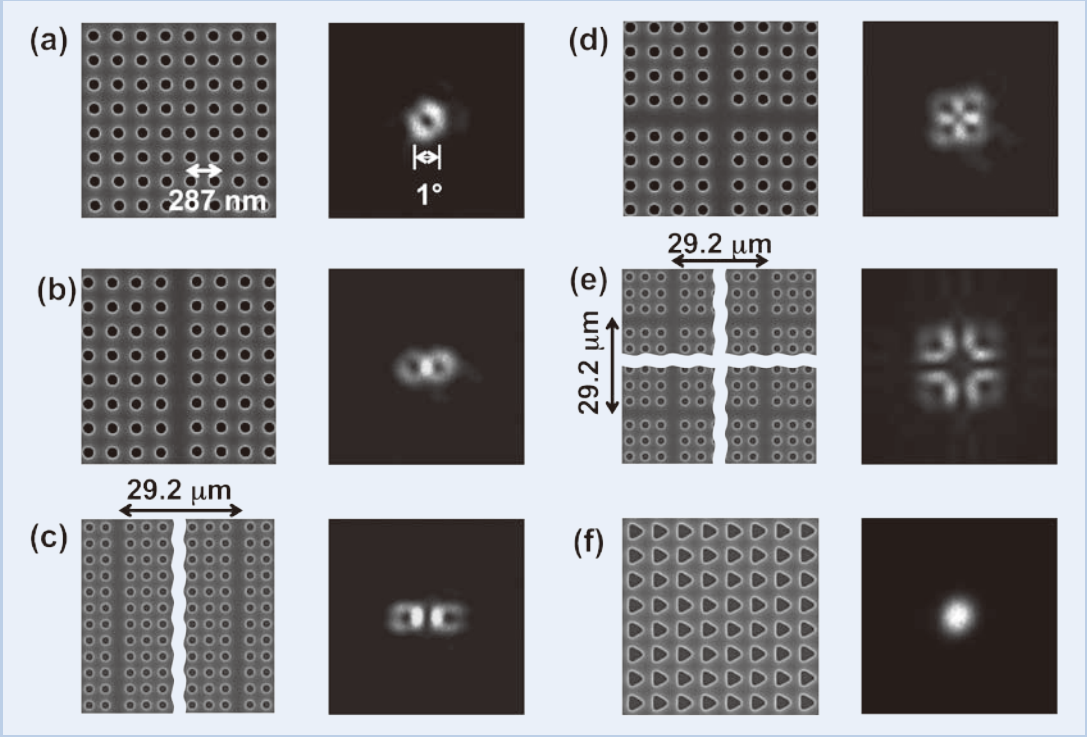

Fig. 5 Electron micrographs (left-hand panels) and obtained beam patterns (right-hand panels) of fabricated photonic crystals used to construct lasers. Photonic crystals with circular lattice points are shown with (a) no shift of the lattice period, (b) one lattice shift in one direction, (c) two lattice shifts in one direction, (d) one lattice shift in both directions, and (e) two lattice shifts in both directions. (f) Triangular lattice points with no phase shift.

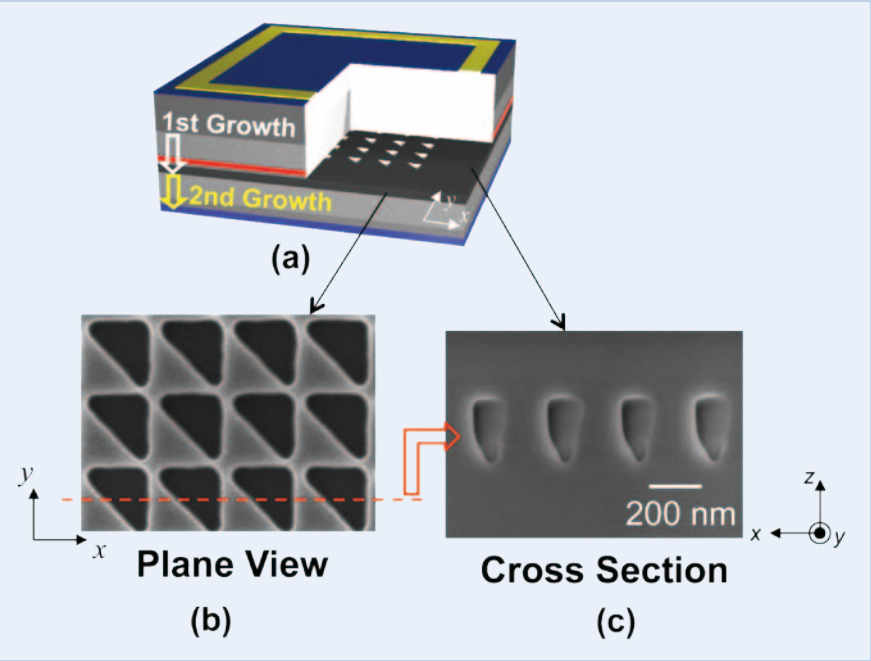

Fig. 6 (a) Schematic of the device fabricated by two-step OMVPE. (b) plan-view SEM image of the photonic crystal with right-isosceles-triangle-shaped air holes formed by electron beam lithography (JEOL JBX-6300FS) and dry etching. (c) A typical cross-sectional SEM image of a row of air holes embedded by OMVPE.

fabricated device [12] under the room-temperature (RT) continuous-wave (CW) condition. The corresponding experimental results are shown in **Fig. 7**(a) – (c). A maximum CW output power of 1.5 W at 2.5 A was achieved with a narrow, single-lobed beam of low divergence. When the output power was less than 0.5 W, the beam quality was quantitatively evaluated by measuring the value of M^2. For an ideal Gaussian beam, M^2 is known to be unity, but it increases when the beam quality is degraded due to the transverse multimode. Measurements of M^2 were performed under room-temperature CW conditions, and we found that M^2 was kept almost at ~1.0 in both the x- and y-directions up to a power up to 0.5 W, indicating that a fundamental single transverse mode is maintained. Note that the beam divergence angle was less than 3° even at 1.5W power level.

Lasers with such a narrow beam divergence should enable unique applications that do not require any lens. We examined the direct irradiation of a sheet of paper placed 8.5 cm from the PCSEL to demonstrate such lens-free potential under CW operation at 25 °C. The light output was set to 0.86 W at a current of 1.7 A. The paper was burnt, forming a small hole immediately after radiation, as shown in **Fig. 8**. Although this is just a simple demonstration, it shows the potential of lens-free applications.

Conclusion (or Summary)

I have described the current status and recent developments in the field of photonic-crystal lasers. It has been shown that the band-edge effect of two-dimensional photonic crystals enables large-area single longitudinal and transverse mode lasing oscillation, as well as complete control over the beam patterns obtained. It has been also described that a device with an output power exceeding 1.5 watt under CW condition at RT. Our work represents an important milestone for innovation in the field of lasers because it provides a route towards overcoming limitations in applications that suffer from low beam quality, which opens the door to a wide range of applications in material processing, laser medicine, nonlinear optics, sensing and so on.

Acknowledgments

The author thanks members of Noda's Lab., Kyoto University, and Rohm and Hamamatsu Photonics for the collaboration. This work was supported in part by JST, ACCEL & CREST, C-PhoST, MEXT, Japan.

References

[1] M. Imada, S. Noda, A. Chutinan, T. Tokuda, M. Murata, and G. Sasaki: "Coherent two-dimensional lasing action in surface-emitting laser with triangular-lattice photonic crystal structure," *Appl. Phys. Lett.*, **vol.75**, pp.316-318 (1999).

[2] S. Noda, M. Yokoyama, M. Imada, A. Chutinan, M. Mochizuki, "Polarization Mode Control of Two-Dimensional Photonic Crystal Laser by Unit Cell Structure Design," *Science*, **vol.293**, pp. 1123-1125 (2001).

[3] M. Imada, A. Chutinan, S. Noda, and M. Mochizuki, "Multidirectionally distributed feedback photonic crystal lasers", *Physical Review B*, **Vol.65, No.19**, pp.195306 (2002).

[4] K. Sakai, E. Miyai, T. Sakaguchi, D. Ohnishi, T. Okano, and S. Noda, "Lasing band edge identification for a surface-emitting photonic-crystal laser," *IEEE Journal of Selected Area in Communications*, **vol.23, no.7**, pp.1330-1334 (2005).

[5] D. Ohnishi, T. Okano, M. Imada, and S. Noda, "Room Temperature Continuous Wave Operation

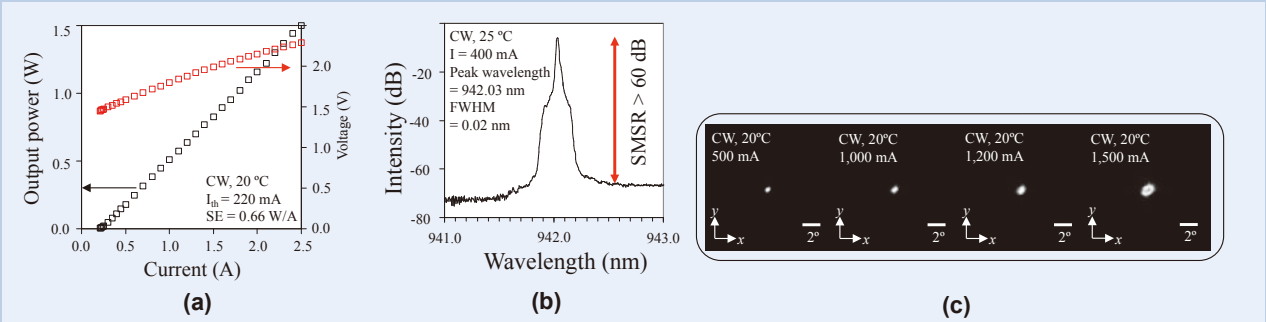

Fig. 7 Lasing characteristics of the device fabricated by two-step OMVPE. (a) I-L characteristics, (b) lasing spectra, and (c) far-field patterns at various current injection levels.

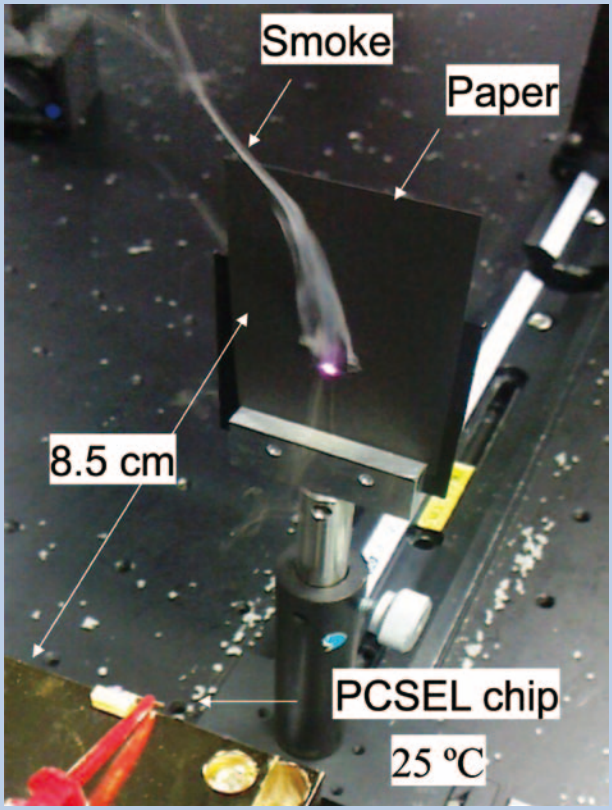

Fig. 8 Photograph taken immediately after direct radiation of the laser on a sheet of black paper placed 8.5 cm from the device.

of a Surface-Emitting Two-Dimensional Photonic Crystal Diode Laser," *Optics Express*, **vol.12**, pp.1562-1568 (2004).

[6] E. Miyai, K. Sakai, T. Okano, W, Kunishi, D. Ohnishi, and S. Noda, "Lasers producing tailored beams", *Nature*, **Vol.441, No.7096**, pp.946-946 (2006).

[7] H. Matsubara, S. Yoshimoto, H. Saito, Y. Jianglin, Y. Tanaka, and S. Noda, "GaN photonic-crystal surface-emitting laser at blue-violet wavelengths", *Science*, **Vol. 319, No. 5862**, pp. 445-447, (2008).

[8] Y. Kurosaka, S. Iwahashi, Y. Liang, K. Sakai, E. Miyai, W. Kunishi, D. Ohnishi, and S. Noda, "On-chip beam-steering photonic-crystal lasers", *NATURE PHOTONICS*, **Vol.4, No. 7**, pp. 447-450 (2010).

[9] Y. Liang, P. Chao, K. Sakai, S. Iwahashi, and S. Noda, "Three-dimensional coupled-wave model for square-lattice photonic crystal lasers with transverse electric polarization: A general approach", *Physical Review B*, **vol. 84, no. 19**, 195119 (2011).

[10] T. Sakaguchi, W. Kunishi, S. Arimura, K. Nagase, E. Miyai, D. Ohnishi, K. Sakai, S. Noda, "Surface-Emitting Photonic-Crystal Laser with 35W Peak Power," The Conference on Lasers and Electro-Optics and the International Quantum Electronics Conference 2009, CTuH1 (2009).

[11] K. Hirose, Y. Kurosaka, A. Watanabe, T. Sugiyama, Y. Liang, and S. Noda, "High power Photonic-Crystal Surface-Emitting Lasers," The 10th Conference on Lasers and Electro-Optics Pacific Rim (CLEO-PR 2013), ThI1-4 (2013).

[12] M. Nishimoto, K. Ishizaki, K. Maekawa, K. Kitamura, and S. Noda, "Air-Hole Retained Growth by Molecular Beam Epitaxy for Fabricating GaAs-Based Photonic-Crystal Lasers", *Applied Physics Express*, **vol. 6, no. 4**, 042002, (2013).

[13] K. Hirose, Y. Liang, Y. Kurosaka, A. Watanabe, T. Sugiyama, and S. Noda, "Watt-class high-power, high-beam-quality photonic-crystal lasers", *Nature Photonics*, **vol.8**, pp.406-411 (2014).doi: 10.1038/ncomms4138.

Electron Microprobe Study of the Yinxu (Anyang) Bronze of Academia Sinica Collection

Yoshiyuki Iizuka[1] and Junko Uchida[2]

[1]Institute of Earth Sciences, and [2]Institute of History and Philology, Academia Sinica

To understand bronze casting technology in ancient China, a series of electron microprobe study has been carried out on bronze objects from the Yinxu (Anyang) in the Academia Sinica collection. Because oxidation parts of bronzes do not preserve the original structures and chemical compositions, non damaged bronze's interior in polished cross-sections were carefully selected, and then their micro-structure and chemical compositions were investigated. Observed metallurgical structures of bronze are divided in two types; dendrite and granular (annealed) structures. Although the granular structured bronze is not common, it suggests that the heat treatment technique has already been applied in the Yinxu Period. Oxygen was also measured to confirm its condition of the oxidation by EPMA, and 73 samples of arms and vessels were discriminated as well-preserved samples. Most of the Yinxu bronzes are tin (Sn)-bronze with a little amount of lead (Pb). An overall result indicates that the bulk Cu/(Cu+Sn) ratios of the bronzes range from 0.79 to 0.89, and chemical compositions are rather different in type of usages. It indicates that the chemical compositions (mixture ratios of Cu:Sn) of the bronzes were already intentionally controlled for their usages in the Yinxu Period.

Introduction

Institute of History and Philology, Academia Sinica, which was established in 1928 for modern archaeological studies, performed excavation works for 15 times in Yinxu (殷墟) of Anyang, Henan Province, the Central Plain in China. Excavation programs were suspended in 1937 due to chaotic situations. The most of excavated materials were transferred, and a large quantity of bronze objects from Yinxu has been stored in the Institute since 1949, now at Taipei.

Yinxu is the place where the oracle bone scripts were discovered and is thought to be an ancient capital in the Late Shang Dynasty (*ca*. 14c.BC-11c.BC), in the Bronze Age of China. The Yinxu bronzes of the Academia Sinica collection were excavated from aristocratic tombs in the Xiaotun palace area, and royal tombs in the Xibeigang area and the collection contains all kinds of bronze objects from all phases of time sequences through the Yinxu Period. Although the collection is one of the most precious and variable for study of the Bronze culture, only little amount of bronze was studied by scientific approaches. To understand technological innovation of bronze casting in the East Asia, the Yinxu's materials are extremely important because it used to be the center of bronze manufacture at early Bronze Age in the East Asia. Information from the Yinxu bronzes and further comparison study of other ages, areas and technology would indicate evolution of the Bronze culture. Since 2007, the authors have launched a series of investigation of the Yinxu bronze collection using electron microprobe techniques to reveal bronze casting technology in Anyang of the Shang Dynasty. Here we report on analytical methods of ancient bronze and implications of bronze culture in the Shang Dynasty.

No. 128, Sec. 2, Academia Road, Nangang, Taipei, Taiwan

E-mail: yiizuka@earth.sinica.edu.tw

Ancient bronzes and sample preparations

The bronze, the first alloy of human kind, is composed of two metallic elements of copper (Cu) and tin (Sn). Bronze object was manufactured by pouring molten alloy into a mold. Melting points of Cu and Sn are approx. 1085ºC and 232ºC, respectively, and melting points decrease with increasing of Sn content in bronze. **Figure 1**a shows the phase diagram of Cu-Sn (tin-bronze) system. Of molten bonze within 90-80 wt.% of Cu (10-20 wt.% of Sn), the primary solid phase of bronze is α-phase when it reached the liquidus temperature. The α-phase generates segregation-solidification (dendrite: Fig. 1b-d) during temperature falling and then secondary δ-phase appears in cooling rate of normal casting. In normal casting, crystallization of Sn-enriched phases, ε and η, does not occur because temperature falls too low to react. In other words, only

dendrite α-phase and $\alpha+\delta$ eutectic phases are observed normally in ancient bronze's interiors as reported by Gettens[1] and Wan[2], and any phase contain less than 77 wt.% of Cu (>33 wt. % of Sn) does not exist in normal casting bronze.

It is well known that a green patina forms on bronze surface for long time of burial. The patina is composed of copper-, tin- and lead oxides and their carbonates. Without exception, the surface of ancient bronzes was oxidized. Although various analytical approaches have been applied for study of bronze chemistry such as X-ray fluorescence (XRF), XR-EDS and chemical dissolution method on the surfaces, only surface analysis is impossible to investigate its original chemistry and casting technology.

The Yinxu collection contains a large quantity (probably more than 20,000) of bronze fragments but many are not able to apply for conservation work. It is, however, still valuable and is able to choose some appropriate samples to investigate metallurgical microstructure and chemistry from cross-sections. The studied samples were selected from entire phases of the Yinxu Period (Middle Shang to Late Shang) and various usages. At least in the Han Dynasty, six kinds of usages are recognized in bronze objects, namely, vessels, instruments, arms, tools, ornaments and chariot items. To understand their chemical character of the Yinxu bronzes, ritual vessels (*Jue, Ding, Zun, Gu, Pou,* and *Hu*), arms (helmets, daggers, knives, arrow- and spear-heads) and chariot ornaments were selected for this study. Excavated helmets were only from HPKM1004 tomb in the Yinxu.

Analytical procedure of the Yinxu bronzes

Sample preparation

To observe a cross section of bronze object, the selected fragments were sliced out a small piece (less than a few cm in size with few mm in thickness) by a

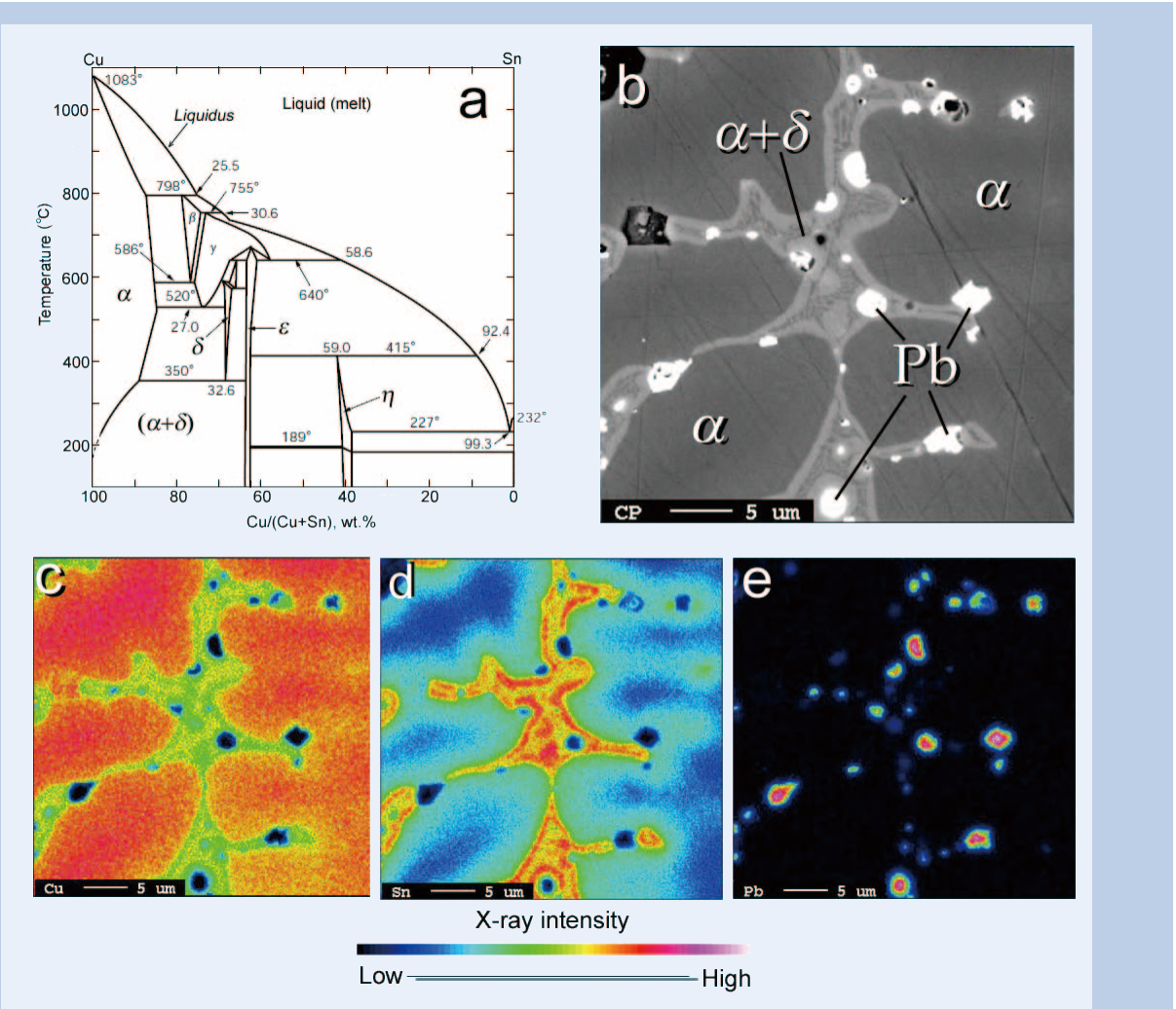

Fig. 1 Bronze system and a representative micro-structure of bronze helmet from the HPKM1004.
a) Phase diagram of copper (Cu) – tin (Sn) system in the condition of equilibrium[9].
b) Back-scattered electron micrograph. Segregated lead (Pb) particles are observed as bright (white on the image) spots (less than few μm) in structures of $\alpha+\delta$ eutectic phases of bronze, shown as dendrite which are surrounding the primary α phases of bronze (shown as darker area).
c) d) and e). Elemental distribution maps of copper, tin and lead, respectively. Scale bars: 5 μm.

micro-diamond saw. To avoid thermal and mechanical damages for metallurgical structure, slow rotation speed of the diamond saw was operated in 100 r.p.m. with distilled water for cooling during the cutting. Cleaned samples by ethanol were mounted in a cold-mounting (room temperature cured for eight hours) epoxy resin with 1-inch diameter mold and exposed surfaces were polished with diamond paste, and then finished by colloidal silica solution.

SEM

Polished cross section was initially observed by an optical microscope with the reflecting light. Then Scanning Electron Microscopes (JEOL W-SEM JSM-6360LV and FE-SEM JSM-7100F) were used to observe metallurgical structure by back-scattered electron images, which represent mean atomic abundance by contrast in black and white images. Semi-quantitative analyses were conducted by an energy dispersive spectrometer (Oxford Instruments Ltd) used under the beam conditions of 15 kilo Volt (kV), and 0.1 nano Ampere (nA) for the acceleration voltage and beam current, respectively, in the vacuum condition of 25 Pa (Pascal). Bulk chemical compositions were determined by mean value of 10 to 20-areas of 120 μm × 90 μm (1000 times in the magnification of SEM image). X-ray counting time was for 100 seconds. The quantitative data were corrected by ZAF method with chemical-known pure metals and synthetic alloys for Cu (copper metal), Sn (tin metal), Sb (antimony metal), Ag (silver metal), As (gallium arsenide: GaAs), Zn (zinc metal), Pb (crocoite: $PbCrO_4$), Bi (bismuth metal), Fe-Co-Ni (NBS868 metal standard) and S (pyrite: FeS_2).

EPMA

In the X-ray energy dispersive analysis on bronze, tin (Sn-*L* lines) is interference element for oxygen (O-*kα*) analysis. Then, quantitative chemical analysis of copper, tin, lead and oxygen was made by EPMAs (JEOL W-EPMA JXA-8900R and FE-EPMA JXA-8500F) which equipped wave-length dispersive spectrometers (WDS). Operated beam conditions were 20 kV, 10 nA, and 5 μm de-focused beam for the acceleration voltage, beam current and beam size, respectively. The measured X-ray intensities were corrected by metal PRZ method using the standard calibration of chemical-known standard metals and oxides with the following diffracting crystals: copper metal for Cu-*Kα* with LiF crystal, tin-metal for Sn-*Lα* with PETH crystal, crocoite ($PbCrO_4$) for Pb-*Mβ* with PETH crystal and tin-oxide (SnO_2) for O-*ka* with LDE1H crystal. X-ray peaks are their both upper and lower baseline X-rays which are counted for 20 and 10 s, respectively. To obtain bulk chemistry from each sample, analyzed points were randomly selected 100 to 225 points at 50 μm intervals with X-Y directions by the mapping point table conversion. Both secondary- and back-scattered electron images were used to avoid damaged and weathered areas. Then the bulk chemistry, especially bulk Cu/(Cu+Sn) ratios (Cu#), were calculated as mean values. Chemical distribution (mapping) analysis of Cu, Sn, Pb, O and some others (As and Sb) was also performed by FE-EPMA at the condition of 20 kV and 30 nA for the acceleration voltage and beam current, respectively.

Results

Metallurgical structure of the bronze's interior

The thickness of studied Yinxu bronzes is mostly 2 to 3 mm. Many of bronzes were seriously oxidized not only at their surfaces but also in their interiors occasionally. Such samples were not appropriate to investigate their metallurgical structure. We attempted near 200 bronze fragments, but 95 samples were able to study their cross sections.

Figure 1 (b-e) shows a representative dendrite structure in the Yinxu bronze object (helmet F1 from HPKM1004) with back-scattered electron micrograph and its chemical distributions of Cu, Sn and Pb. Lead (Pb) is segregated from the bronze phases which are composed of *α* phase, the primary crystal phase, and *α*+*δ* eutectic phases. Pb is a fusing agent and is conducting melting point to be lowered. Pb was in molten bronze at the high temperature, but is not distributed in solid bronze.

The bronze micro-structures are divided into two types, such as dendrite and granular structures (**Fig. 2**). The dendrite is substantially present but granular structure is observed only 5 cases so far. For structure comparison, we study experimental bronze objects simultaneously. The dendrite is observed in normal casting bronzes, whereas granular or chemical homogeneity structure is obtained from experimental products after thermal treatment such as annealing or tempering. The results indicate that at least a kind of thermal treatment method has already applied in the Yinxu Period of the Shang Dynasty, it is very uncommon though.

Chemical composition of the Yinxu bronzes

Accuracy of bulk Cu/(Cu+Sn) ratios (Cu#) of bronzes was confirmed by chemical known bronze alloys. **Figure 3** shows performed results by 4-type of analysis methods. Some standards were leaded bronzes (3 to 10 wt.% in original weights). Lead (Pb) is fusing agent and behaves as volatile gas during the experiments. Thus Pb contents were expected to be decrease from the originals. However, the Cu# in the leaded bronzes were well maintained. Over all results are acceptable within 0.02 in the Cu#[3].

Figure 4 shows Pb content with the Cu# of the studied 95 bronzes by the usages. The most of bronzes are ranging between 0.77 and 0.89 in the Cu#, and do not contain much Pb (less than 2 wt.%). The bronzes, contained more than 0.9 in Cu#, are four (4) arsenic (As) bronzes (**Fig. 5**a), one (1) antinomy (Sb) bronze from the arms (Fig. 5b), and Pb-bronze (2-ornaments: R014314 and R007306) which show less Sn were identified. Excluding such bronzes (> 0.9 in Cu#), the most of studied Yinxu bronzes are shown less-content of Pb and more than 75% of the studied bronzes are shown less than 2 wt% in Pb. The mean value of the Cu# and Pb of helmets from the HPKM1004 are 0.838 and 1.56 wt.%, respectively, in the studied 30

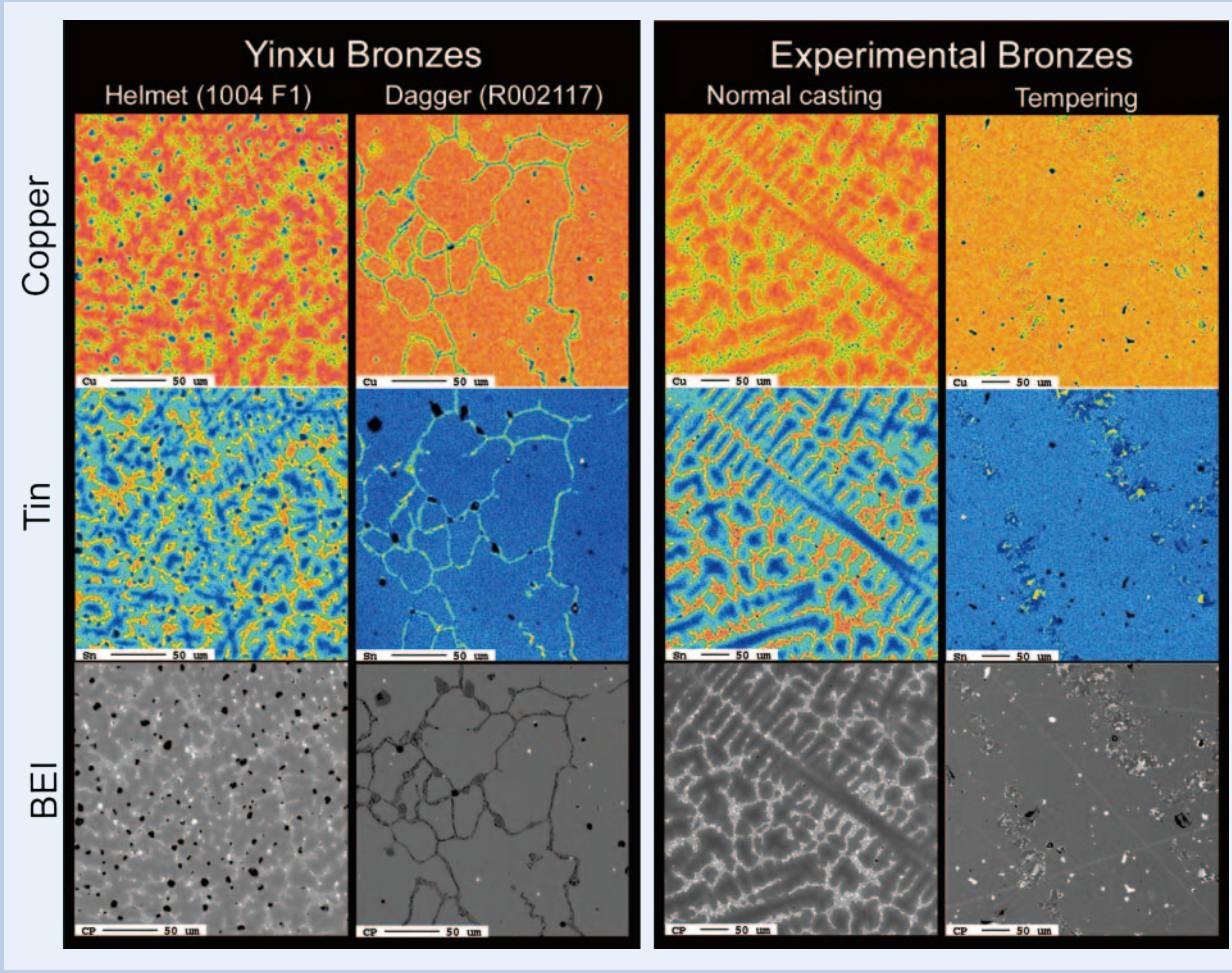

Fig. 2 Representative metallurgical structure of bronzes objects from Yinxu (left) and experimental products (right). Dendrite structure and chemical heterogeneities of Cu (tops) and Sn (middles) are observed from a Yinxu bronze object (helmet: HPKM1004 F1) and normal casting experiment (JY-4: Cu:Sn:Pb = 80:15:5, the Cu# = 0.158), on the other hand, granular structure and chemical homogeneity are observed from the interiors of dagger (R002117) and run product after tempering (JY6T: Cu:Sn:Pb = 80:15:5, the Cu# = 0.158; heat-treatment experiment: kept at 600 ºC for 24 hrs and then processed a slow-cooling). BEI: back-scattered electron micrographs. Colder (blue) and warmer (red) colors indicate lower and higher concentration of each element, respectively. Scale bars: 50 μm.

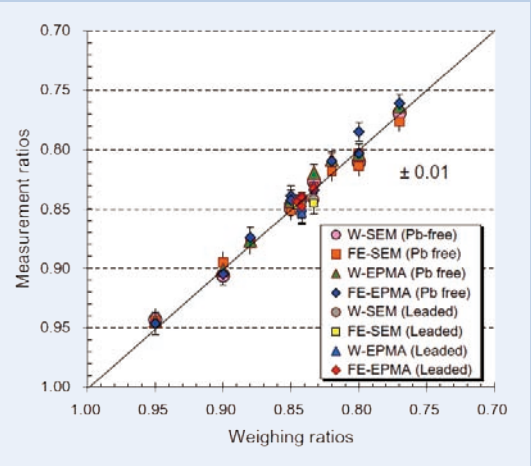

Fig. 3 Analytical results of chemical-known bronze standard materials. X- and Y- axes represent weighing and measurement ratios of bulk Cu/(Cu+Sn). W-SEM: JEOL JSM-6360LV with Oxford Si[Li] EDS; FE-SEM: JEOL JSM-7100F with Oxford SDD-EDS; W-EPMA: JEOL JXA-8900R; FE-EPMA: JEOL JXA-8500F.

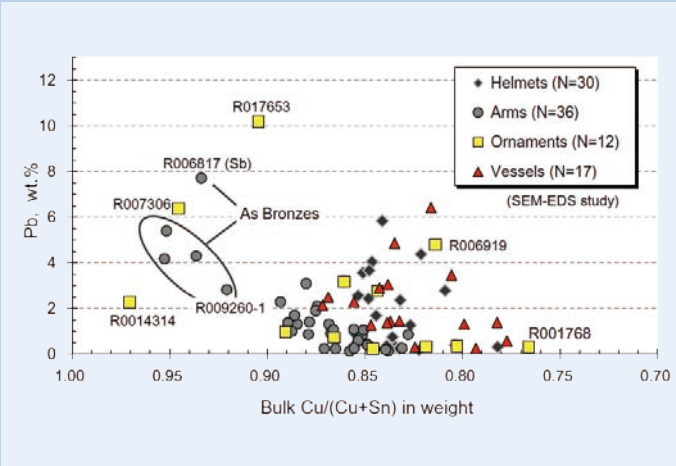

Fig. 4 Distributions of Pb contents with the bulk Cu/(Cu+Sn) ratios of studied Yinxu bronze objects shown by the usages. Diamonds: helmets from only the HPKM1004; circles: weapons: four (4) of them are identified as As-bronzes and one is As-Sb bronze (R006817); squares: decorations such chariot ornaments (3 of them are high-Cu bronzes); triangles: pots and cups with fine relieves on the surface. N: numbers of studied samples by SEM-EDS.

samples. On the other hand, the #Cu of the ritual vessels ranges 0.78-0.88 which is relatively lower Cu (or higher Sn) range. Most of the vessels contain some amounts of Pb (up to 7 wt.%). In the ornaments, Cu# ranges widely from 0.77 to 0.98. A sample which highly decorated with inlaid of turquoise (R017653) shows the highest Pb content (10.5 wt.%) in this series of analysis.

In the chariot items, sample R006919 contains rather high Pb as 4.8 wt.%, and the #Cu is similar to the other ritual vessels as 0.814. On the other hand, so called a bow-shaped ornament (R001768), contains less Pb (0.3 wt.%), and the #Cu is only 0.766. It is so far the lowest value of #Cu and differs from the ratio of other arms. This is thought to be a kind of arms, but its chemical composition indicates different concern to categorize the objects. Cavities or void spaces were well observed in the interior of high-Pb bronzes generally. Less cavities are observed in the interior of low-Pb bronzes. It seems that condition of preservation is relatively better in lower Pb bronzes.

EPMA results with Oxygen analysis

Presence of oxygen in bronzes' interior indicates condition of preservation. Thus inspection of oxygen is useful to discriminate their original chemistry for further discussion. **Figure 6** shows representative results of mapping analysis on two samples, an oxidized and a well-preserved bronze helmet of helmets, from the HPKM1004. It is obviously impossible to indicate their state of the oxidation from the back-scattered images (BEI) on both sections because the dendrites were clearly identified. However, oxygen mappings demonstrate the micro-dendrite structure was oxidized in the helmet-07. Quantitative spot analysis results are shown in **Fig. 7**. Oxidized helmets (Hel-06 and -07) shows scattered O range up to 25 wt.% and the Cu/(Cu+Sn) ratios from 1.0 to 0.3 which are inconsistent with normal casting bronze, whereas well-preserved helmets (Hel-05 and -08) does not contain O and all Cu# range are consistent with α-phase and $\alpha+\delta$ eutectic phase (from 94 to 72 wt.% of Cu: see Fig. 1a). The results indicate that oxidation process vary its Cu# from the original.

In the EPMA overall results, 73 bronze objects were confirmed as well-preserved samples and keep reliable chemistry to discuss its original bulk Cu:Sn ratios. **Figure 8** shows distributions of the Cu# (bulk Cu/[Cu+Sn] ratio) by usages. Each Cu# was calculated by 100-225 spots analysis by EPMA.

The helmets from the HPKM1004 (grey) are ranging between 0.80 and 0.89, and most of the helmets are between 0.83 and 0.86, and mean value is 0.843 in the Cu#. The arms (green) are also wide in range from 0.82 to 0.89 in the Cu#. The data contains various types of arms though. On the other hand, the Cu# of the ritual vessels (red) are ranging from 0.80 to 0.86. Differences in the bronze chemistry seem not clear in the variation of the time sequence through the Yinxu Period.

Discussion

It is well studied about physical properties of Cu-Sn alloy in the modern metallurgy that the color, the Brinell hardness, the tensile strength, and the elongation of bronze vary with ratios of Cu:Sn (**Fig. 9**). In general, bronze is getting harder with increasing of Sn content from 15 wt.% but it is getting brittle because the tensile strength and the elongation are significantly decreasing with Sn content more than 20 wt.%. It seems that bronze gains most toughness around 85-80 wt.% of Cu (15-20 wt.% Sn). Estimated viscosity of molten bronze is also shown in Fig. 9 that viscosity is decreasing with increasing of Sn content[4].

So far we obtained 73 bronze chemistries and 46 data of them were helmets from the HPKM1004. As shown in Fig. 8, the #Cu of helmets shows relatively

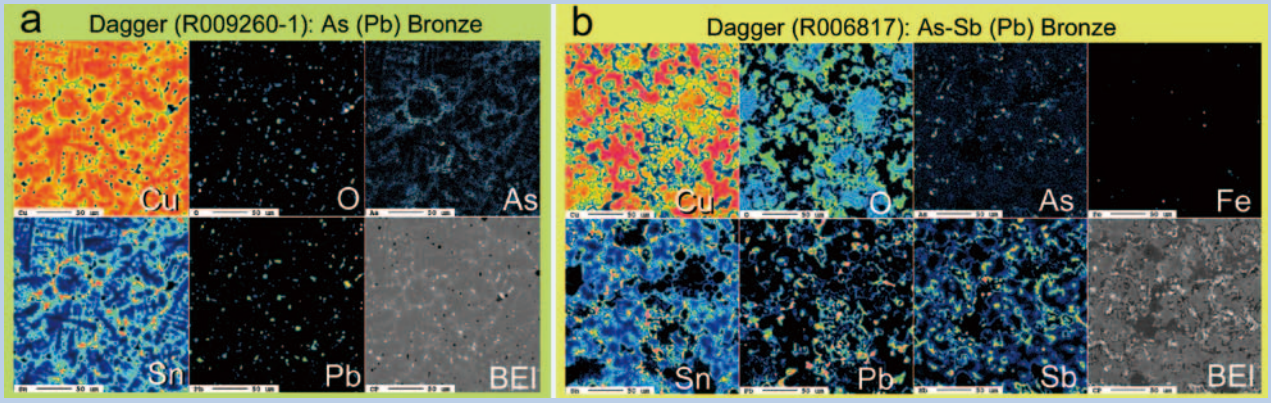

Fig. 5 a) Mapping result of As (Pb) bronze (dagger: R009260-1). Arsenic (As) distributes mostly in δ-phase of bronze but not exists in δ-phase because the solidus of Cu-Sn α-phase is too high to form Cu-As alloy. Highest value of As in δ-phase is approx.3 wt.% and bulk content of As is approx. 1wt. %. We suppose that As might be derived from copper ore mineral in nature instead of an addition because shape this dagger is expected to be the northern warriors type.
b) Mapping result of Sb-As (Pb) bronze (dagger: R006817). Antimony (Sb) is observed as segregated phase, such similar behavior as Pb and Fe (iron). As distributes mostly in δ-phase of bronze Colder (blue) and warmer (red) colors indicate lower and higher concentration of each element, respectively. BEI: electron back-scattered micrographs. Scale bars: 50 μm.

uniformed and most of helmets distribute between 0.83 and 0.86, and mean value is 0.843. Their #Cu ratios seem comparable to high toughness range of bronze. On the other hand, the Cu# range of the ritual vessels is slightly Sn-enriched and Pb as well (see Fig. 4). The vessels are usually decorated with fine relieves on the surface. These phenomena indicate that the Sn and Pb were added intentionally in order to increase the viscosity of molten bronze for casting, which might be easy to pour into fine decoration molds. Various kinds of arms were studied but some of arms seem ritual objects with surface decoration instead of real weapons. It might be the reason that the Cu# of arms distributes in wider range from 0.82 to 0.89. From these circumstances, it is likely that craftsmen already understood characters of bronze at the time.

In the ancient Chinese classic of the Zhou Dynasty of Rites of Zhou < 周礼考工記 *Zhou Li Kao Gong Ji*>, *the Six Formula* of mixture ratios < 金有六斉 *Liu Qi*> were standardized for different usages of bronze. It has debated that description was in the 4th to the 3rd Century BC on the basis of the knowledge of the 9th to the 7th Century BC which is represented of the period of Zhou Dynasty. According to the description, it is thought that difference of the bronze alloy components (ratios of Cu:Sn) might be controlled since long time ago in China. However it has not been confirmed with chemical compositions of ancient bronzes.

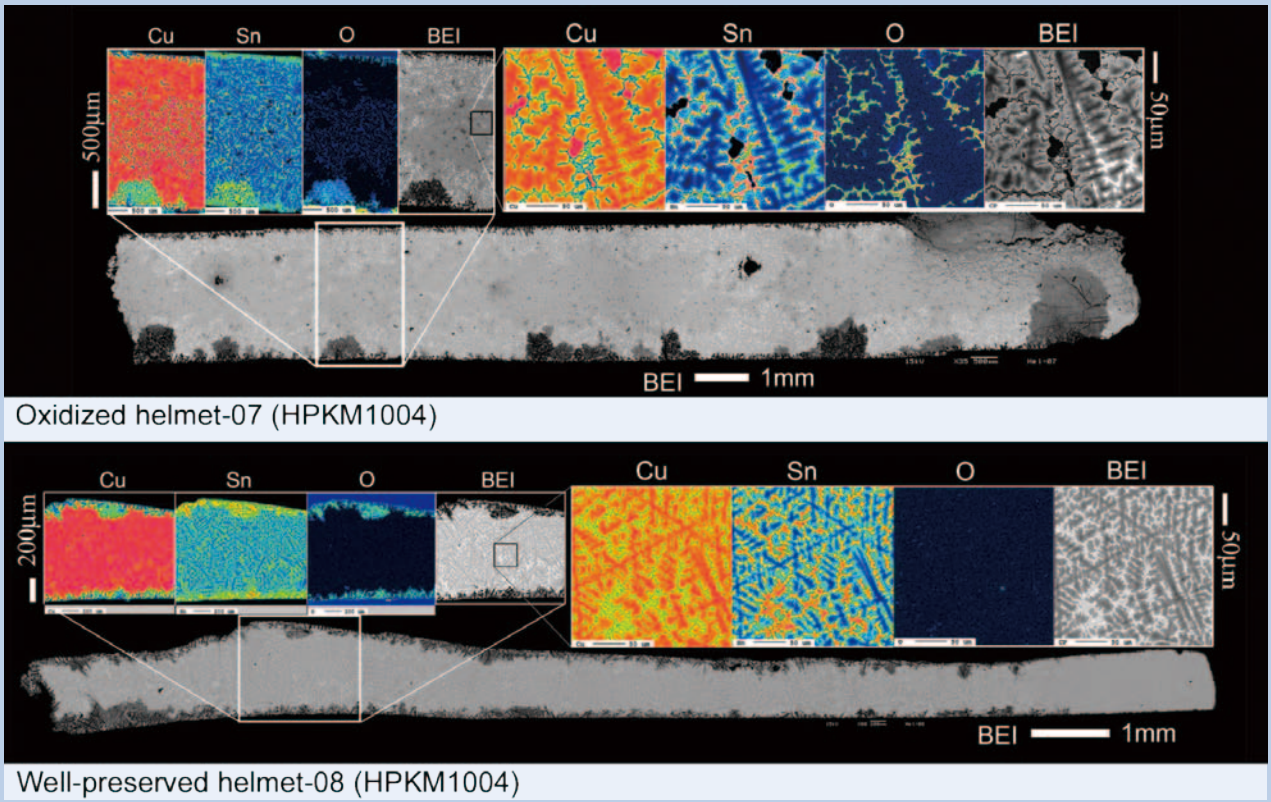

Fig. 6 Back-scattered electron micrographs (BEI) and elemental distribution maps of copper (Cu), tin (Sn) and oxygen (O). An oxidized- (upper: helmet-07: thickness 3 mm) and a well-preserved (bottom: helmet-08: thickness 1mm) bronzes from the HPKM1004. X-ray intensities were counted for 0.04 sec and 0.025 sec at intervals of 2 μm and 0.5 μm with the X-Y stage driving in wide (sections) and small (250 × 250 μm) area maps, respectively.

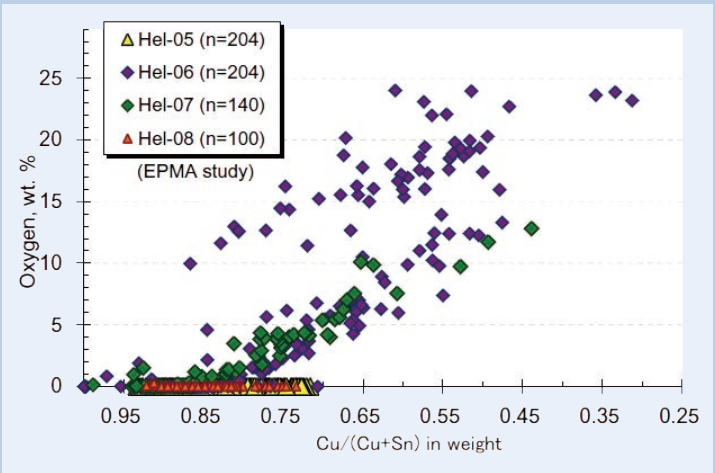

Fig. 7 Representative results of oxygen contents with the Cu/(Cu+Sn) ratios from the interiors of the bronze helmets from the HPKM1004 by EPMA spot (quantitative) analysis. Diamonds: oxidized bronzes (Helmets-06 and -07). Triangles: well-preserved bronzes (helmets-05 and -08). n: numbers of analytical spots.

Wan[2] proposed 2-ways interpretation of *the Six Formula* based on weighing ratios, shown as cases -A and -B in **Table 1**. Because a term of copper was not present at the time, the ancient sentences in *the Six formula* were described bronze mixture ratios with "Metal" and "Tin". He assumed "metal" in case of bronze (case-A) and copper (case-B) and estimated the six mixture ratios in weight in the Cu# from 83.3 to 50 wt.% in case-A, and from 85.7 to 66.7 wt.% in case-B.

In modern metallurgy, it is well known that bronze which contained less than 66.7 wt.% of Cu (more than 33.3 wt.% of Sn) is unable to cast. In the metallurgical point of view, a bronze which is composed of only δ phase (68.2-66.8 wt.% of Cu) is also not exist. The world most highest Sn (lowest Cu) bronze object has been recorded as 32.6 wt.% of Sn (67.4 wt.% of Cu) from Kerala, South India[5]. As shown in the results, most of the Yinxu bronzes are constructed by α and α+δ phases. The lowest Cu# is 0.783. On the other hand, the highest Cu# of 83.3 and 85.7 wt.% in case -A and -B, respectively. However there are not reliable because the well-preserved bronzes are dispersed up to the range of 0.89 in the Cu#. Therefore it is suggested that Wan's 2-hypotheses are inconsistent in reality.

Hori[6] investigated the ancient balance-weights from the Ancient Central Asia and it was confirmed that the Central Asian weight system was established around 4000BC and is the oldest in the world. On the other hand, Chinese weight system might be established in later than 1000BC which might be comparable to Post-Shang Dynasty. Qiu *et al.* [7] interpreted ancient Chinese articles that volume unit by the decimal system was already established in the Pre-Qin Period (by 221BC). They also pointed out in historical point of view that the appearance of the weight unit is later than the establishment of units of length and volume. Two Pb ingots were excavated from the Xiaotun E-16 pit at Yinxu [8] but any weighing and balance-weights tool were not discovered yet from Anyang. It is supposed that, therefore, weighing system was not established yet in the Yinxu Period.

Volumetric system is another measurement way. The density of Cu and Sn (β-Sn) are 8.94 and 7.365 (g/cm^3) respectively. Thus the mass (or weight) of Cu and Sn are different in even the same volume.

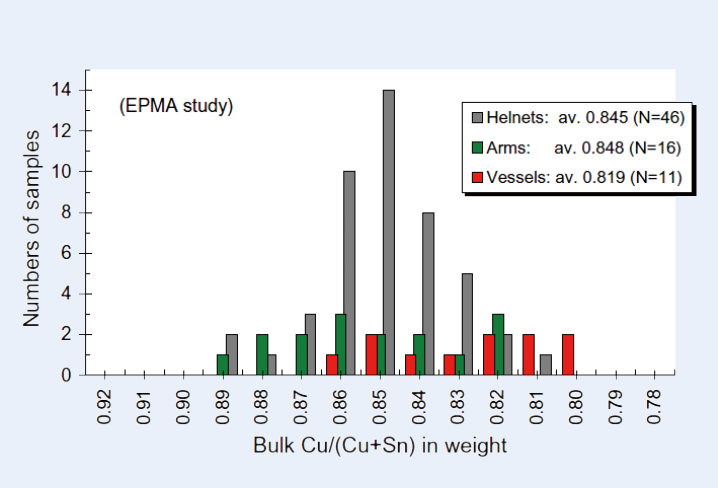

Fig. 8 Distributions of the bulk Cu/(Cu+Sn) ratios by usages. Grey: helmets from only the HPKM1004; green: arms include daggers, knives, arrow- and spear-heads); red: vessels. av.: average in the bulk Cu/(Cu+Sn) ratios in weight. N: numbers of studied samples by EPMA.

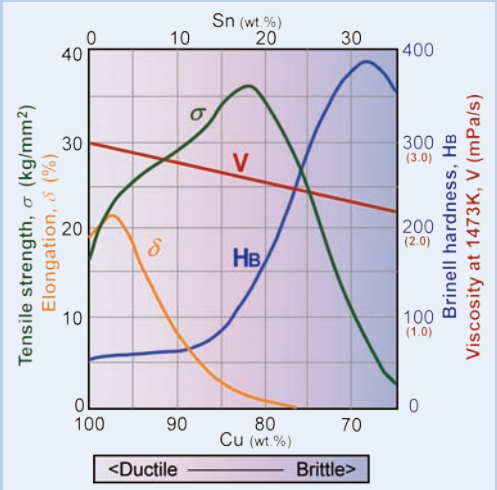

Fig. 9 Physical properties of bronze as functions of chemistry. σ : tensile strength [2]; δ : elongation; H_B: hardness (Brinel Number) [10], and V: estimated viscosity of molten bronze at temperature of 1470K[4].

Table 1 Suggesting Cu:Sn ratios from hypothetical interpretations for *the Six Formula* of bronze casting.

金有六斉 <*Liu Qi*> *the Six Formula*			Mixture ratios		Weight ratios		Volumetric ratios
					『金 Metal』 as Bronze	『金 Metal』 as Copper	『金 Metal』 as Copper
					Case-A (Wan [2])	Case-B (Wan [2])	Case-C (this study)
Type			<Metal>	Tin	(<Bronze>-Sn)/<Bronze>	Cu/(Cu+Sn), wt.%	Cu/(Cu+Sn), wt.%
I	鐘鼎	Bells & Cauldrons	6	1	83.3	85.7	87.9
II	斧斤	Axes	5	1	80.0	83.3	85.9
III	戈戟	Daggers & Halberds	4	1	75.0	80.0	82.9
IV	大刃	Blades	3	1	66.7	75.0	78.5
V	削殺矢	Arrows	5	2	60.0	71.4	75.2
VI	鑒燧	Mirrors	2	1	50.0	66.7	70.8
					impossible to cast	*possible to cast*	*Exist in the Yinxu*

Assuming that mixture ratios of *the Six Formula* are based on the volumetric ratios, their weight ratios are suggested from 88 to 71 wt. % within few % steps in the Cu# (case-C in Table 1). From the analytical results, the #Cu of helmets from the HPKM1004 are relatively uniformed within 3 wt.% and these ranges are also reflected to the physical property of bronze. Further the suggested range of the Cu# from 88 to 71 wt.% of Cu might be reliable for casting. Thus it is likely that volumetric hypothesis is probable.

In types I and III of *the Six Formula* instruct the ratio for Bells & Cauldrons (Cu6:Sn1=88 wt.% of Cu), and daggers (Cu4:Sn1=83 wt.% of Cu), respectively, which are represented vessels and arms. Thus it indicates that the vessels are enriched in Cu than the arms, however, the analytical results showed contradiction that the arms are enriched in Cu than the vessels. It is also inconsistent with physical property of bronze.

Conclusion

We attempted near 200 bronze objects from the Yinxu (Anyang) in the Academia Sinica collection to investigate their metallurgical structure and chemistry. Most of the Yinxu bronzes are tin (Sn)-bronze with a little amount of lead (Pb). Bulk Cu/(Cu+Sn) ratios (Cu# in weight) of each bronze fragment were calculated by average of 100 to 225 EPMA quantitative (spots) analysis with oxygen and lead, followed by semi-quantitative analysis by SEM-EDS . The Cu# from non-oxidized interior represents its original Cu#, whereas the ratios could significantly be shifted after oxidation. We confirmed that 73 samples of arms (helmets, daggers, arrow- and spear-heads) and vessels were well preserved. An overall result indicates that the original Cu# ranges from 0.79 to 0.89. No variation is verified in time sequence during the Yinxu Period. By the usages, the Cu# of helmets are between 0.84 and 0.89, and 0.845 in average, and it is relatively uniformed when compared with other various usages. The most of helmets do not contain much Pb (< 2 wt. %), and less cavities are observed in the interior. Physical property of bronze is varied by their Cu#, and helmet chemistries are fit its toughness chemical range. The vessels show relatively lower in Cu# (high-Sn bronze) and contain some amount of Pb (up to 5-6 wt. %). In the contrast with the helmets, the vessels are usually decorated with fine relieves on the surface. Since lower Cu# (or higher Sn content) and addition of Pb reduce viscosity of molten bronze, it might be easy to cast with fine decoration molds. It is suggested from the results of chemical analysis that the Cu# of bronzes was intentionally controlled by purpose of usages within few % in the Yinxu Period. Based on this series study of the Yinxu bronzes, we proposed a hypothetical interpretation of *the Six Formula* by volumetric ratios might be probable, instead of the weight-base interpretation. However, the Cu# of the Yinxu bronzes are inconsistent with the ratios which were described in the ancient Chinese classic.

Acknowledgments

We thank Dr. Kwang-tzuu Chen and Ms. Yu-yun Lin of Institute of History and Philology for their kind support. Professors Haruhisa Mifune and Takekazu Nagae of University of Toyama are appreciated to provide experimental bronze samples and valuable discussion. We thank Ms. Ya-ting Hsu, Mr. Yu-shiang Wang and Ms. Hui-ho Hsieh of Institute of Earth Sciences for their technical support of bronze analysis. This study is supported by National Science Council (Taiwan) and the Institute of History and Philology of Academia Sinica.

References

[1] Gettens R.J. 1969 The Freer Chinese Bronzes Volume II Technical Studies. Smithsonian Institution Freer Gallery of Art, Oriental Studies, **No.7**. Washington DC.

[2] Wan Chia-pao (1970) A preliminary report on the metallographic examinations of Shang bronze helmets. Institute of History and Philology Academia Sinica Special Publications, **No.60**. pp.48. Taipei (in Chinese with an English summary).

[3] Iizuka Y., J. Uchida (2013) Chemical compositions of Yinxu (Anyang) bronze objects in the Academia Sinica collection and its implications for Ancient Chinese Casting techniques. Bulletin of Japan Society of Chinese Archaeology, **13**:23-47 (in Japanese with Chinese abstract).

[4] Kozlov L.Y., L.M. Romanov, N.N. Petrov (1983) Prediction of multicomponent metal melts viscosity. Izvestiya Vyssh. Uch. Zav., Chernaya Metallurgiya, **3**:7-11.

[5] Mifune H. (2010) Comparison of the manufacturing technology of high-tin bronze tools in modern Asia. In *Asian high-tin bronzes: Production technology and regional characteristic.* pp.125-135 (ISBN 978-4-9905066-1-2).

[6] Hori A. (2007) Reconsideration of the Weight System of the Ancient Central Asia. Bulletin of the Society for Near Eastern Studies in Japan (Nippon Oriento Gakkai), **50(1)**:30-32 (in Japanese with English abstract).

[7] Qiu Guangming, Qiu Long, Yang Ping (2001) Unit of Weight (Chapter 4) in *History of Chinese Technology.* Science and Technology Press, pp.25-31. Beijing (in Chinese).

[8] Chen Kwang-tzuu (1991) Analysis and study on Lead Ingots from Yinxu. In *Archaeology and Historical Culture. Commemoration of the Eightieth Anniversary of Kao Ch'u-hsun*, pp.355-388. Cheng-Chung Book. Taipei (in Chinese).

[9] Massalski B.T. (Editor-in-chief) (1990) Binary Alloy Phase Diagram: Second edition. National Institute of Standards and Technology, Library of Congress Cataloging in Publications Data, USA (ISBN-10: 0-87170-405-6).

[10] Scott D.A. (1991) Metallography and microstructure of ancient and historic metals. The J. Paul Getty Museum, pp.155. Los Angels (ISBN 0-89236-195-6).

Elucidation of Deterioration Mechanism for Organic Solar Cells
– Toward Highly Efficient Solar Cells –

Kazuhiro Marumoto

University of Tsukuba

We report on an electron spin resonance (ESR) study of polymer solar cells to investigate accumulated charge carriers in these devices under device operation from a microscopic viewpoint. Light-induced ESR (LESR) signals and device characteristics were simultaneously measured using the same device under simulated solar irradiation. From the ESR analysis, the molecules where photogenerated hole carriers were accumulated are clearly identified as poly(3-hexylthiophene) (P3HT). Moreover, the simultaneous measurements of ESR and device characteristics demonstrate a clear correlation between the increased LESR intensity and deteriorated device performance. The ESR study reveals that the deep trapping sites for photogenerated hole carriers are located at interfaces between a hole buffer layer poly(3,4-ethylenedioxythiophene):poly(4-styrenesulfonate) (PEDOT:PSS) and an active layer P3HT:[6,6]-phenyl C_{61}-butyric acid methyl ester (PCBM), which can be ascribed as the main mechanism for the reversible deterioration of the device performance of polymer solar cells.

Introduction

Organic thin-film solar cells are a promising alternative source of electrical energy because of their printable and flexible device structure, light weight, and low-cost production.[1-3] Solar cells have been investigated using a variety of methods with the aim of improving their performance.[4-10] There has been a significant amount of interest in the high power conversion efficiency (PCE) of more than 10% that was recently obtained in organic thin-film solar cells due to their potential practical applications.[11,12] In addition to device performance, the durability of solar cells is an important problem for the practical use of solar cells. For durability studies, degradation of solar cells due to extrinsic factors such as oxygen and water has been reported, where materials and device structures were irreversibly degraded.[13-15] Moreover, in addition to the irreversible degradation, the reversible initial deterioration of device performance without material degradation has been reported for a polymer solar cell using methods that employ thermal stimulated current (TSC) and current density (J)-voltage (V) measurements.[16,17] The studied polymer solar cell was a bulk-heterojunction (BHJ) thin-film solar cell with blend films of a conducting polymer regioregular poly(3-hexylthiophene) (P3HT) and a soluble fullerene [6,6]-phenyl C_{61}-butyric acid methyl ester (PCBM), which has been widely studied as a typical polymer solar cell.[1-10,16,17] The polymer solar cell has a device structure of indium-tin oxide (ITO)/poly(3,4-ethylenedioxythiophene):poly(4-styrenesulfonate) (PEDOT:PSS)/P3HT:PCBM/Al, where PEDOT:PSS is a typical hole buffer layer and has been widely used to improve device performance.[1-13,16,17] The previous studies reported that the device performance gradually deteriorated during device operation and that the deterioration could be recovered via thermal annealing.[16,17] In other words, the deterioration has been ascribed to an accumulation of photogenerated charge carriers during device operation rather than to the degradation of organic materials and/or device structures.[16,17] The TSC study indicated that the accumulation sites were located at interfaces between active layers and electrodes with various trapping levels.[16] However, a more detailed study clarifying molecules and these sites where charge carriers are accumulated (trapped) without molecular degradation has not yet been conducted, which will be extremely important for further device performance and durability improvements.

Electron spin resonance (ESR) is one promising method for such a microscopic characterization of charge-accumulation sites because it is a highly sensitive and powerful approach that is capable of investigating organic materials at the molecular level.[18-21] This method has the advantage of being able to directly observe accumulated charge carriers without detrapping carriers via thermal stimulation, as used in

1-1-1 Tennodai, Tsukuba, Ibaraki 305-8573, Japan

E-mail: marumoto@ims.tsukuba.ac.jp

the TSC method. This ESR method has successfully clarified the microscopic properties of charge-carrier states in organic devices, including spin states and their spatial extent of wave function in pentacene,[18] fullerene (C_{60}),[19] and P3HT[19,21] at device interfaces. The ESR method has also been applied to pentacene/C_{60} heterojunction organic thin-film solar cells and their organic layered films; these studies directly observed charge formation in pentacene layers during device fabrication under dark conditions.[22,23] However, the accumulation of photogenerated charge carriers in polymer solar cells under device operation has not yet been investigated using the ESR method. Such an investigation from a microscopic viewpoint would be useful in clarifying the accumulation sites, which would help to improve device durability and performance.

In this news, we report on an ESR study of P3HT:PCBM polymer solar cells to investigate accumulated charge carriers in these devices under device operation.[24] We measured light-induced ESR (LESR) signals and device characteristics (short-circuit current and open-circuit voltage) simultaneously using the same device under simulated solar irradiation. From the ESR analysis, the molecules where photogenerated hole carriers were accumulated are clearly identified as P3HT. Moreover, the simultaneous measurements of ESR and device characteristics demonstrate a clear correlation between the increased LESR intensity and deteriorated device performance. With the use of organic layered films of PEDOT:PSS/P3HT:PCBM, the ESR study reveals that the deep trapping sites for photogenerated hole carriers are located at PEDOT:PSS/P3HT:PCBM interfaces, which can be ascribed as the main mechanism for the reversible initial deterioration of the device performance of polymer solar cells.

Experimental

Commercially available P3HT (Sigma-Aldrich, Plexcore OS 1100, regioregularity: 98.5%), PCBM (Frontier Carbon, nanom spectra E100, purity: 99.2%), and PEDOT:PSS (Clevios PAI4083) were used to fabricate the solar cells. The chemical structures of P3HT, PCBM, PEDOT, and PSS are provided in **Fig. 1**. The device structure was ITO/PEDOT:PSS (≈40 nm)/P3HT:PCBM (≈160 nm)/Pd (1.2 nm)/LiF (0.6 nm)/Al (100 nm). PEDOT:PSS films were fabricated by spin-coating an aqueous solution onto ITO-coated quartz substrates, followed by annealing at 140 °C for 10 min under an Ar atmosphere. Solutions of P3HT and PCBM (1:0.8 w/w) dissolved in *o*-dichlorobenzene (3.4 wt.%) were stirred with a magnetic stirrer for 30 min at 70 °C, and were spin coated on top of the PEDOT:PSS films at 1000 rpm for 75 s to form P3HT:PCBM films. The area of the interface between P3HT:PCBM and PEDOT:PSS was 3 mm × ≈14 mm. Then, Pd, LiF, and Al layers were deposited onto the P3HT:PCBM blend film to form the anode using a conventional vacuum sublimation technique under vacuum conditions below 2×10^{-4} Pa. Finally, the devices were annealed at 140 °C for 30 min under an Ar atmosphere and vacuum-sealed after wiring in an ESR sample tube. The device performance was confirmed to improve by the use of Pd on the anode side. We also obtained similar ESR results to those of the present study by using devices without Pd and LiF.

The *J*-*V* characteristics were evaluated using an Agilent Technology B1500A semiconductor device analyzer under simulated solar irradiation (AM 1.5G) with a 100 mW cm^{-2} intensity at 290 K under an Ar atmosphere. ESR measurements were performed using a JEOL RESONANCE JES-FA200 X-band spectrometer under vacuum conditions at 290 K. The number of spins, *g* factor, and linewidth of the ESR signal were calibrated using a standard Mn^{2+} marker sample. The absolute value of the number of spins was calculated using a solution (220 µl) of 4-hydroxy-2,2,6,6-tetramethylpiperidin-1-oxyl (TEMPOL) as a standard. The calibration of the *g* factor was performed by using a software program of the JEOL RESONANCE ESR system considering higher order correction to the effective resonance field. Its correctness was also confirmed by using 2,2-diphenyl-1-picrylhydrazyl (DPPH) as another standard sample. Simultaneous measurements of LESR and the device characteristics J_{sc} and V_{oc} were performed using a Keithley 2612A source meter under simulated solar irradiation (AM 1.5G) with a 100 mW cm^{-2} intensity with a Bunkoukeiki OTENTOSUN-150BXM solar simulator at 290 K. The simultaneous measurements under the open-circuit

condition were performed immediately after performing simultaneous measurements under the short-circuit condition using the same device.

Results and Discussion

Firstly, we describe the device characteristics of our solar cells. When we fabricated solar cells with an active area of 2 mm × 2 mm using an ITO substrate with a conventional size of 20 mm × 20 mm, our devices had the following typical parameters: a short-circuit current density (J_{sc}) of ≈7.1 mA cm^{-2}, an open-circuit voltage (V_{oc}) of ≈0.66 V, a fill factor (FF) of ≈0.60, and a PCE of ≈2.8%. These values are equivalent to those reported by other groups.[3-9,16,17] Thus, we have confirmed standard device operation using our device fabrication method. However, the device parameters of the cells for the ESR experiments deteriorated, compared with those of the above cells because of the following difficulties. Firstly, the use of a narrow ITO substrate with a size of 3 mm × 20 mm (see Fig. 1c of Ref. 22) was necessary because we needed to insert the device into an ESR sample tube with an inner diameter of 3.5 mm. Secondly, to overcome the low signal-to-noise (SN) ratio of the LESR signal due to device operation, we needed to fabricate a device with a large active area; we adopted an active area of 2 mm × 10 mm in this study. Thus, the film quality of the asymmetric active area deteriorated because of the variation in film thickness, which was caused by the difficulties of spin coating using the narrow ITO substrate. As a result, the device characteristics deteriorated; J_{sc} and V_{oc} decreased to approximately 2.2 mA cm^{-2} and 0.35 V, respectively. Despite this decreased device performance, our devices for the ESR experiments exhibited similar performance deterioration under device operation as that reported by other groups.[16,17] Therefore, the present microscopic characterization by ESR analysis is considered to be useful for clarifying the essential problems of performance deterioration under device operation, as demonstrated below.

Next, we present the light-induced ESR (LESR) signals of the devices under device operation. **Figure 2** demonstrates the dependences of the LESR signals of the same device on the duration of simulated solar irradiation under: a) short-circuit condition, and b) open-circuit condition. Here, the LESR signals were obtained by subtracting the ESR signal under dark conditions from that under simulated solar irradiation. The vertical axis is plotted using a unit of peak-to-peak ESR intensity of the ESR signal for a

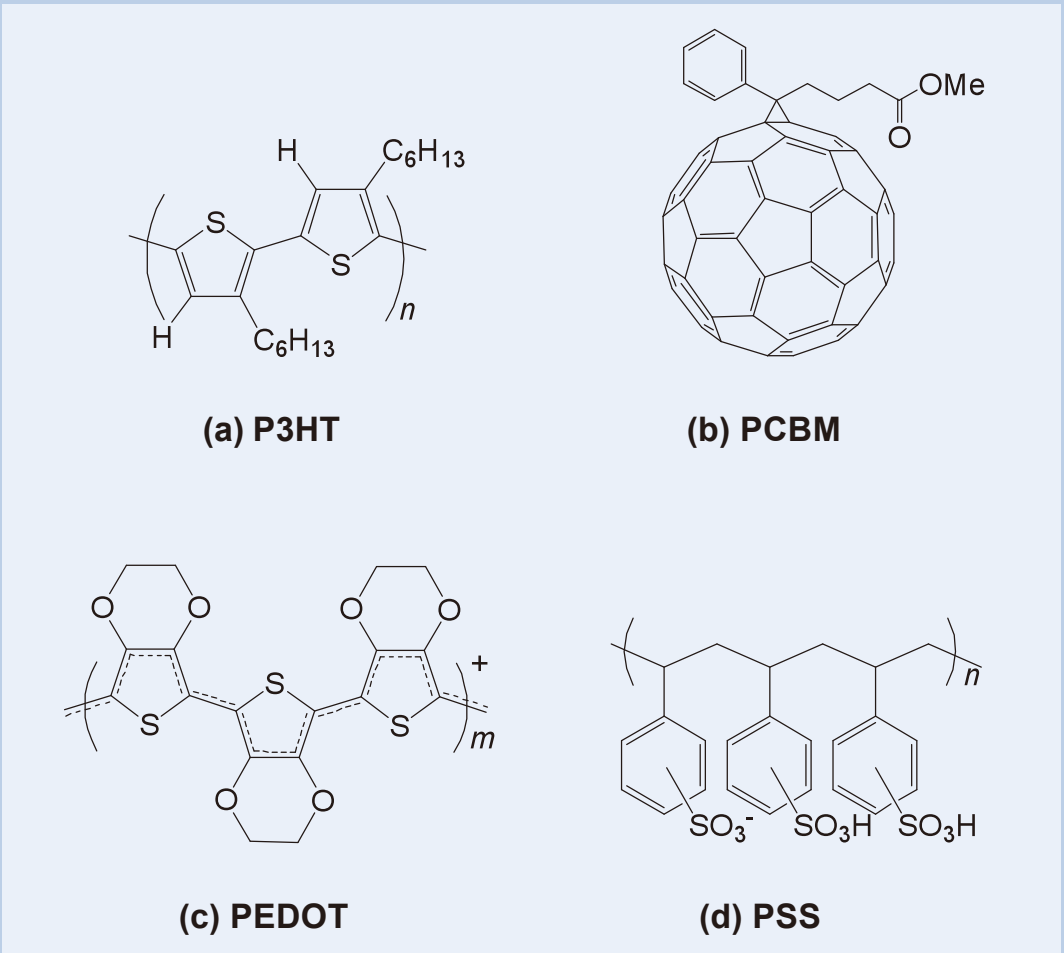

Fig. 1 Chemical structures of: a) regioregular poly(3-hexylthiophene) (P3HT), b) [6,6]-phenyl C_{61}-butyric acid methyl ester (PCBM), c) poly(3,4-ethylenedioxythiophene) (PEDOT), and d) poly(4-styrenesulfonate) (PSS).

standard Mn^{2+} marker sample, I_{Mn}, which is attached to the inside wall of the ESR cavity of the JEOL RESONANCE ESR system. In our experiment, we used a continuous-wave method with a modulation frequency of 100 kHz for the external magnetic field. Thus, the photogenerated charge carriers with short lifetimes less than 10 μs cannot be observed using the present ESR method. Freely diffusive charge carriers to electrodes contribute the standard operation of the device. Therefore, the observed LESR signals are due to the accumulation of photogenerated charge carriers with lifetimes longer than 10 μs, namely, trapped photogenerated carriers. As revealed in Fig. 2a,b, gradual increases in the LESR intensities are clearly observed under both operation conditions. The increased rate of the LESR signal under the short-circuit condition is larger than that under the open-circuit condition. The g factor and peak-to-peak ESR linewidth, ΔH_{pp}, are determined to be: a) g = 2.0022 and ΔH_{pp} = 0.25 mT, and b) g = 2.0023 and ΔH_{pp} = 0.24 mT. These values are consistent with those of hole carriers (positive polarons) in P3HT films in organic field-effect devices.[19,21] Therefore, the LESR observation directly demonstrates that the observed spin species are photogenerated hole carriers accumulated in P3HT molecules.

To clarify the locations of accumulated holes further, we performed LESR measurements for organic layered films of ITO/P3HT:PCBM, ITO/PEDOT:PSS, and ITO/PEDOT:PSS/P3HT:PCBM. For the ITO/P3HT:PCBM and ITO/PEDOT:PSS/P3HT:PCBM films, we observed the same LESR signal as that observed in Fig. 2a,b. However, for the ITO/PEDOT:PSS films, we did not observe such a LESR signal. Moreover, the ESR signal of PCBM has been reported to have g-tensor values of 1.9982 - 2.00058,[25-27] which differ radically from that observed in Fig. 2a,b. Furthermore, the ESR signals of PEDOT:PSS and PEDOT have been reported to exhibit a broader ESR linewidth than that observed in Fig. 2a,b.[28,29] Therefore, we can ascribe the LESR signals observed in Fig. 2a,b to accumulated hole carriers in P3HT. We here comment that the reason for the absence of LESR signal from radial

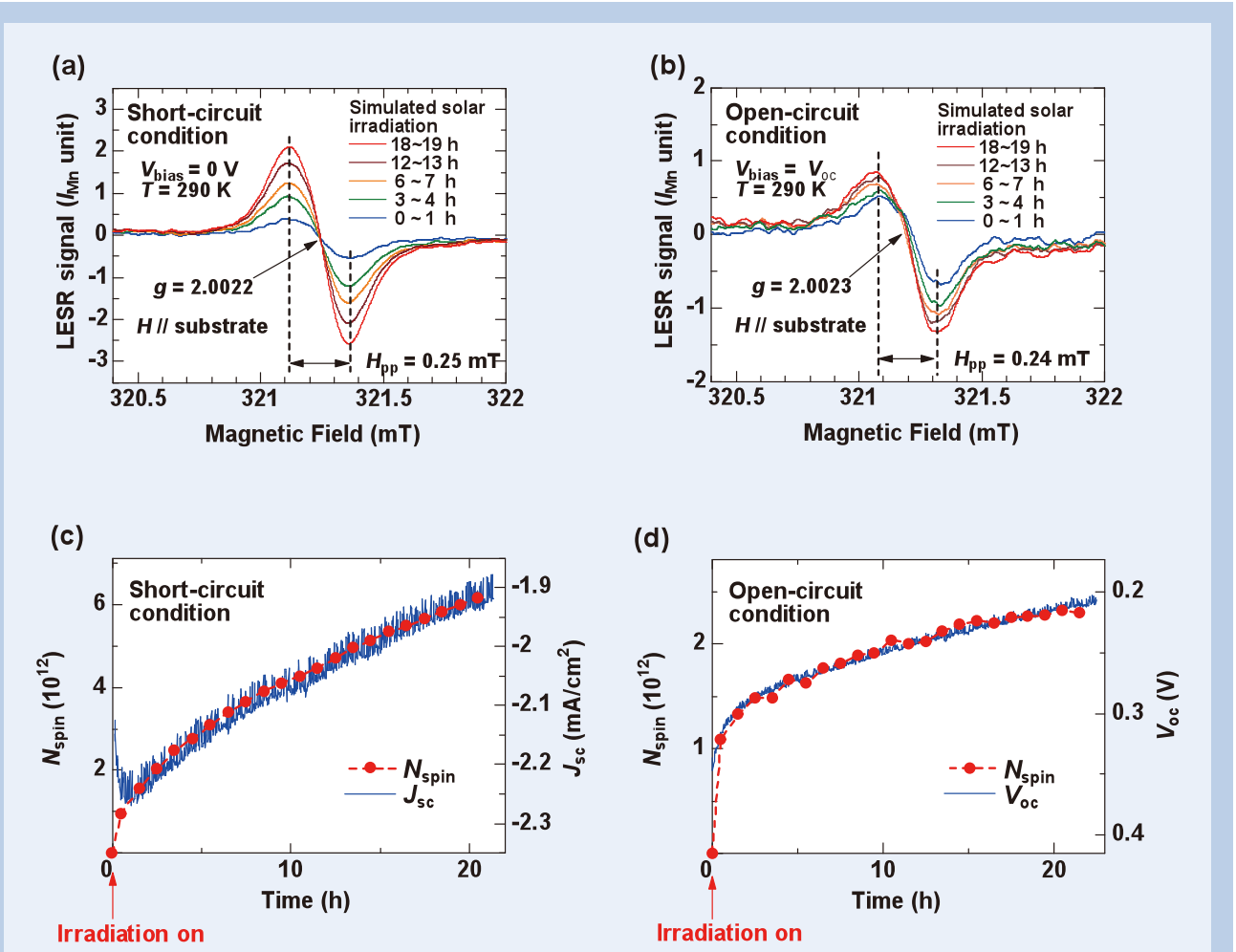

Fig. 2 a,b) LESR signals of ITO/PEDOT:PSS/P3HT:PCBM/Pd/LiF/Al at approximately 320.4-322 mT for various exposure times to simulated solar light (AM 1.5G) with a 100 mW cm^{-2} intensity at 290 K under short-circuit condition (a) and open-circuit condition (b), respectively. The external magnetic field H is parallel to the substrate. The vertical axis is plotted using a unit of peak-to-peak ESR intensity of the ESR signal of a standard Mn^{2+} marker sample, I_{Mn}. The data were obtained by averaging LESR signals measured under irradiation during 1 h. c,d) The dependences of N_{spin} and the device parameters J_{sc} (c) and V_{oc} (d) on the duration of simulated solar irradiation at 290 K, respectively. The N_{spin} is obtained from the averaged LESR signal of P3HT under irradiation for 1 h, and is plotted at each averaged time over 1 h.

anion (electron) on PCBM is ascribed to the rapid spin relaxation of fullerene's electron at room temperature.[19,27]

Next, we present the results of simultaneous measurements of LESR and device characteristics using the same device. To present the ESR results, we use the number of spins, N_{spin}, due to the accumulation of photogenerated hole carriers in P3HT varied from that before irradiation at each experiment, which was obtained by integrating the LESR signal twice at approximately 320.5-322 mT and comparing this value with the standard Mn^{2+} marker sample. Fig. 2c,d illustrate the dependences of N_{spin} and the device parameters J_{sc} and V_{oc} on the duration of the simulated solar irradiation, respectively. These results indicate that an increase in N_{spin} clearly correlates with the deterioration of the device performance. That is, N_{spin} monotonically increases and J_{sc} and V_{oc} concomitantly decrease as the duration of simulated solar irradiation increases. This clear correlation demonstrates that the accumulation of photogenerated hole carriers in P3HT deteriorates the device parameters J_{sc} and V_{oc}. To the best of our knowledge, this is the first instance in which such a clear correlation between the microscopic ESR characteristics and macroscopic device parameters has been observed. The charge accumulation affects an internal electric field in the device, which prevents current flow and creates additional potential in the cells, as disscussed later.

The influence of the increased charge accumulation (carrier density) on J_{sc} and V_{oc} were investigated in detail by other groups.[16,17] The studies showed the decreases in J_{sc} and V_{oc} during device operation, which are consistent with those of our device. Note that the reversibility of the charge accumulation and the device parameters J_{sc} and V_{oc} was confirmed from ESR and J-V characteristics after irradiation off, which is consistent with that of the previous works.[16,17] We comment that the long-lived accumulated charge carriers in polymer films have been reported by several groups, which were caused by deep trappings due to low temperatures[30] or extrinsic factors such as oxygen under irradiation.[27] The influence of traps due to such extrinsic factors on J_{sc} and V_{oc} have been also studied.[13,14] The influence is an interesting problem for the present results because our device is vacuum sealed in an ESR sample tube, which is beyond the present research scope and is open for further study.

Next, we discuss the accumulation sites of the photogenerated hole carriers in more detail. As presented in Fig. 2c,d, the accumulation rate of the photogenerated hole carriers under the short-circuit condition is larger than that under the open-circuit condition. Under the short-circuit condition, an internal electric field exists in the BHJ active layer in the device, which causes the migration of photogenerated hole carriers to ITO electrodes through the interface between the PEDOT:PSS and P3HT:PCBM layers. Thus, one can consider that the difference for the accumulation rates between the short- and open-circuit conditions can be ascribed to the effect of the PEDOT:PSS/P3HT:PCBM interfaces. To clarify the effect of the PEDOT:PSS/P3HT:PCBM interfaces on hole accumulation, we examined the transient response of LESR for layered thin films of ITO/P3HT:PCBM and ITO/PEDOT:PSS/P3HT:PCBM upon simulated solar irradiation. **Figure 3**a,b present the transient responses of N_{spin} for: a) ITO/P3HT:PCBM, and b) ITO/PEDOT:PSS/P3HT:PCBM. For ITO/P3HT:PCBM, N_{spin} monotonically increases under simulated solar irradiation. When irradiation ceases, N_{spin} sharply decreases to a small value, and then, the small remaining component gradually decreases (see Fig. 3a). However, for ITO/PEDOT:PSS/P3HT:PCBM, a different behavior was observed compared with that of ITO/P3HT:PCBM. That is, a large remaining component was clearly observed after turning off the irradiation (see Fig. 3b). The lifetime of the remaining component is extremely long, more than 40 h, even at room temperature. Therefore, this result demonstrates that PEDOT:PSS insertion between ITO and P3HT:PCBM causes the hole accumulation sites with deep trapping levels in P3HT at PEDOT:PSS/P3HT:PCBM interfaces. Using this hole accumulation, the different rates of increase for N_{spin} observed in Fig. 2 can be reasonably explained because hole carriers are easily accumulated at the PEDOT:PSS/P3HT:PCBM interfaces due to the flow of short-circuit currents. We here comment on the sharply increasing and decreasing components upon irradiation on and off, respectively, in Fig. 2c,d, and 3a,b. These LESR signals are due to shallowly trapped photogenerated holes in P3HT, which accumulation sites are probably located at bulk materials.

The findings from the ESR study are summarized in Fig. 3c, which helps to explain the hole accumulation at the interfaces under simulated solar irradiation. Firstly, the hole accumulation sites with deep trapping levels are formed by depositing P3HT:PCBM films on a PEDOT:PSS layer (see left-hand side in Fig. 3c). Secondly, photogenerated hole carriers are accumulated at deep trapping sites in P3HT molecules at the PEDOT:PSS/P3HT:PCBM interfaces (see the right-hand side of Fig. 3c). This hole accumulation is enhanced by the current flow at the interfaces because of the internal electric field under the short-circuit condition. We here explain an energy-level shift in the highest occupied molecular orbital (HOMO) of P3HT at the interfaces shown in Fig. 3c. This energy-level shift is related to the interfacial electric dipole layer, which can be caused by an electron transfer from P3HT to PEDOT because of the energy difference between the HOMO of P3HT (4.7-5.1 eV)[31,32] and the work function of PEDOT:PSS (5.3 eV).[8,22] This electron transfer forms holes in P3HT under the dark condition, as discussed in a previous ESR study on pentacene/C_{60} heterojunction solar cells with PEDOT:PSS hole-buffer layers.[22] We confirmed this additional hole formation in the present study by measuring ESR signals of layered films of quartz/P3HT:PCBM and quartz/PEDOT:PSS/P3HT:PCBM under dark conditions before simulated solar irradiation. That is, the number of spins of P3HT under dark conditions for quartz/PEDOT:PSS/P3HT:PCBM was measured to be 3.2×10^{12}, which is larger than that of 4.6×10^{11} for quartz/P3HT:PCBM. This result demonstrates the additional hole formation in P3HT due to the electron

transfer from P3HT to PEDOT:PSS under dark conditions. Note that this hole formation under dark conditions is not presented in Fig. 3c to present the hole accumulation in P3HT clearly under simulated solar irradiation mentioned above.

In the following, we discuss the correlation shown in Fig. 2c,d in more detail. Firstly, we explain the decrease in V_{oc} using an interfacial electric dipole layer due to accumulated holes at the PEDOT:PSS/P3HT:PCBM interfaces. When an interfacial electric dipole layer due to accumulated charges is formed, a vacuum-level shift occurs at the interface.[33] Such vacuum-level shift decreases V_{oc} of solar cells because of the energy-level shift for molecules at the interface.[34] We here evaluate the interfacial electric dipole length (d) due to the hole accumulation at PEDOT:PSS/P3HT:PCBM interface using the capacitance formula $Q = CV$. Let S be the area at the interfaces, ΔN_{spin} and ΔV_{oc} be the increase in N_{spin} and the decrease in V_{oc} due to the hole accumulation at the interfaces, respectively, e be the elemental charge, ε_0 be the permittivity in vacuum, ε_r be the dielectric constants of P3HT:PCBM materials,[35] then, d may be expressed as follows:

$$d = \varepsilon_0 \varepsilon_r \frac{S}{e\Delta N_{spin}} \Delta V_{oc} \quad \cdots\cdots (1)$$

Using the experimental values of S = 0.4 cm^2, $\Delta N_{spin} = 1.2\times10^{12}$, and ΔV_{oc} = 0.11 V, d is evaluated to be approximately 1 nm. This length probably corresponds to the length of alkyl-side chains in P3HT;[36] the alkyl-side chains are insulators without π electrons. It should be noted that ΔV_{oc} is proportional to ΔN_{spin}, which well explains the experimental result shown in Fig. 2d.

Next, we explain the decrease in J_{sc} using charge-carrier scattering due to the hole accumulation. Such

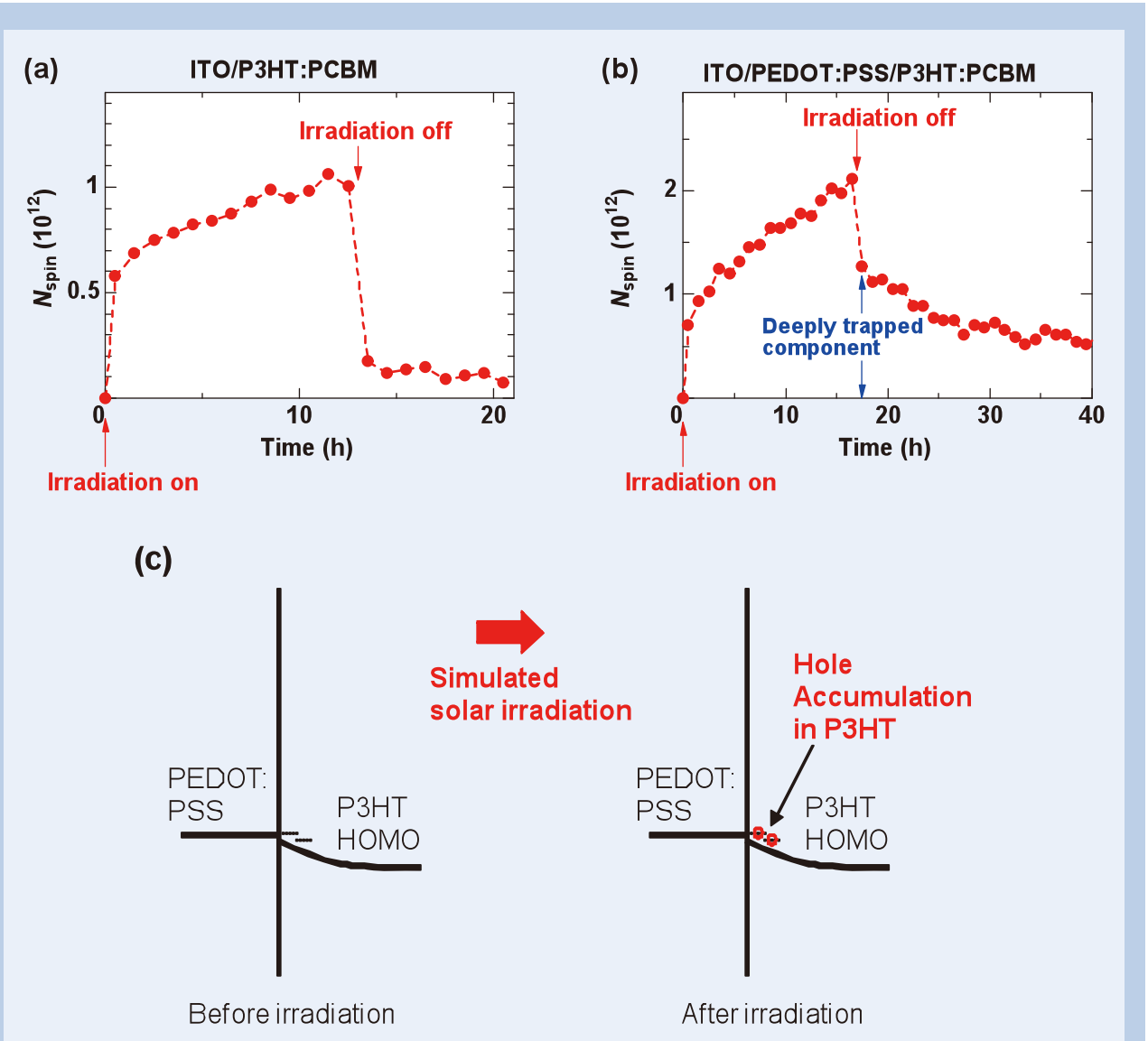

Fig. 3 Transient responses of N_{spin} for organic layered thin films of: a) ITO/P3HT:PCBM, and b) ITO/PEDOT:PSS/P3HT:PCBM upon simulated solar irradiation at 290 K. The N_{spin} is obtained from the averaged LESR signal of P3HT under irradiation for 1 h at 290 K, and is plotted at each averaged time over 1 h. c) Energy diagrams at the PEDOT:PSS/P3HT interfaces, which schematically explain the accumulation of photogenerated hole carriers in P3HT molecular sites after simulated solar irradiation.

scattering is considered to be independent of other charge-carrier scattering mechanisms in solar cells, and then we may use the Matthiessen's rule for the mobility μ in the cells as follows:[37]

$$\frac{1}{\mu} = \frac{1}{\mu_{SC}} + \frac{1}{(c/N_{spin})\mu_{HA}} \quad \cdots\cdots (2)$$

Here, we use two mobility constituents, μ_{SC} and μ_{HA}, related to the charge-carrier scattering in solar cells without and with the hole accumulation, respectively. The latter depends on N_{spin} with a proportionality constant c. Using Equation (2), we may express the current density j in solar cells using charge density n and internal electric filed E in the cells as follows:

$$j = ne\mu E = ne\frac{\mu_{SC}\mu_{HA}}{\mu_{HA}+(\mu_{SC}/c)N_{spin}}E \quad \cdots\cdots (3)$$

Equation (3) shows that j decreases as N_{spin} increases. This behavior well explains the experimental result shown in Fig. 2c. Therefore, the charge-carrier scattering induced by the accumulated holes in the cells decreases J_{sc} during device operation under simulated solar irradiation.

Finally, we comment on the disordered molecular orientation for the hole-accumulation sites. **Figure 4** shows the ESR and LESR signals of P3HT in an organic layered thin film of ITO/PEDOT:PSS/P3HT:PCBM under dark condition and simulated solar irradiation, respectively. These signals were obtained by subtracting the ESR signal of PEDOT:PSS from that of ITO/PEDOT:PSS/P3HT:PCBM to present the ESR signal of P3HT clearly. Under dark condition, the ESR signal of P3HT was observed, which can be ascribed to the hole formation due to the charge transfer between P3HT and PEDOT:PSS, as mentioned above.[22] The obtained g value of 2.0018 means that the hole-formation sites are attributable to P3HT molecules in ordered lamella structures from the anisotropy of the g values for P3HT molecules.[21] However, the LESR signal of P3HT after simulated solar irradiation shows the different g value of 2.0022 from that for ordered P3HT molecules. This finding clearly demonstrates that the molecular orientation for the hole-accumulation sites is disordered and is different from that in the ordered lamella structures. Note that the disordered molecular orientation is further confirmed by the detailed anisotropy for the LESR signal.

Conclusion

We have fabricated polymer solar cells of ITO/PEDOT:PSS/P3HT:PCBM/Pd/LiF/Al and performed simultaneous measurements of LESR and device characteristics under simulated solar irradiation to clarify the deterioration mechanism

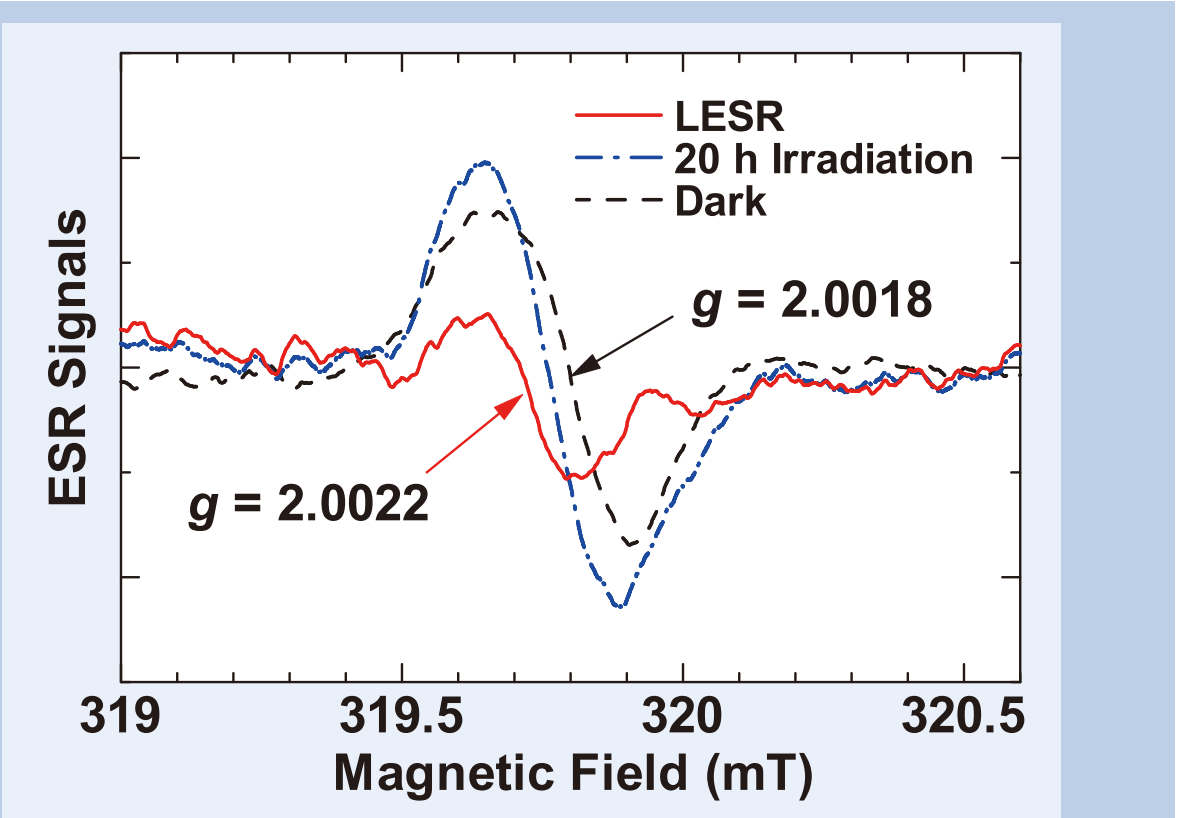

Fig. 4 The ESR and LESR signals of P3HT in ITO/PEDOT:PSS/P3HT:PCBM under dark condition and simulated solar irradiation at 290 K, respectively. The external magnetic field is parallel to the substrate. Dashed line shows the ESR signal under dark condition. Dashed-dotted line shows the ESR signal after 20 h simulated solar irradiation. Solid line shows the LESR signal, which is obtained by subtracting the ESR signal under dark conditions from that under simulated solar irradiation.

of device performance during device operation at the molecular level. We observed a monotonic increase in LESR signals under simulated solar irradiation, which is ascribed to the accumulation of photogenerated hole carriers in P3HT of the device under operating condition from the microscopic viewpoint for the first time. We also observed a clear correlation between the increase in N_{spin} due to the hole accumulation and the deterioration of the device parameters J_{sc} and V_{oc}. This correlation demonstrates that the hole accumulation in P3HT causes the initial deterioration of the device performance. The sites of hole accumulation with deep trapping levels were identified as being formed in P3HT at the PEDOT:PSS/P3HT:PCBM interfaces from the study of organic layered films, which explains the more rapidly increasing rate of LESR for the devices under the short-circuit condition than under the open-circuit condition. Thus, modifications at the PEDOT:PSS/P3HT:PCBM interfaces are recommended to improve device durability by preventing hole accumulation under device operation. For other solar cells, we also propose improvements in device durability by reducing the charge accumulation in the cells during device operation based on the microscopic information obtained from this and future ESR studies.

Acknowledgments

The author thanks T. Nagamori and M. Yabusaki for their collaboration. This research was partly supported by Grants-in-Aid for Scientific Research (24560004 and 22340080) from the Japan Society for the Promotion of Science (JSPS) and by JST, PRESTO.

References

[1] C. J. Brabec, *Sol. Energy Mater. Sol. Cells*, **83**, 273 (2004).
[2] P. Kopola, T. Aernouts, R. Sliz, S. Guillerez, M. Ylikunnari, D. Cheyns, M. Valimaki, M. Tuomikoski, J. Hast, G. Jabbour, R. Myllylä , A. Maaninen, *Sol. Energy Mater. Sol. Cells*, **95**, 1344 (2011).
[3] M. Kaltenbrunner, M. S. White, E. D. Głowacki, T. Sekitani, T. Someya, N. S. Sariciftci, S. Bauer, *Nat. Commun*. **3**, 770 (2012).
[4] G. Li, V. Shrotriya, J. Huang, Y. Yao, T. Moriarty, K. Emery, Y. Yang, *Nat. Mater.* **4**, 864 (2005).
[5] W. Ma, C. Yang, X. Gong, K. Lee, A. J. Heeger, *Adv. Funct. Mater.* **15**, 1617 (2005).
[6] S. Günes, H. Neugebauer, N. S. Sariciftci, *Chem. Rev*. **107**, 1324 (2007).
[7] E. Ahlswede, J. Hanisch, M. Powalla, *Appl. Phys. Lett*. **90**, 163504 (2007).
[8] Y. Kim, A. M. Ballantyne, J. Nelson, D. D. C. Bradley, *Org. Electron*. **10**, 205 (2009).
[9] G. Dennler, M. C. Scharber, C. J. Brabec, *Adv. Mater.* **21**, 1323 (2009).
[10] J. S. Kim, J. H. Lee, J. H. Park, C. Shim, M. Sim, K. Cho, *Adv. Funct. Mater.* **21**, 480 (2011).
[11] R. F. Service, *Science* **332**, 293 (2011).
[12] M. A. Green, K. Emery, Y. Hishikawa, W. Warta, E. D. Dunlop, *Prog. Photovoltaics*: *Res. Appl*. **21**, 1 (2013).
[13] M. Jørgensen, K. Norrman, F. C. Krebs, *Sol. Energy Mater. Sol. Cells*, **92**, 686 (2008).
[14] A. Seemann, T. Sauermann, C. Lungenschmied, O. Armbruster, S. Bauer, H.-J. Egelhaaf, J. Hauch, *Sol. Energy*, **85**, 1238 (2011).
[15] V. Singh, S. Arora, P. K. Bhatnagar, M. Arora, R. P. Tandon, *J. Polym. Res*. **19**, 9899 (2012).
[16] K. Kawano, C. Adachi, *Adv. Funct. Mater.* **19**, 3934 (2009).
[17] T. Yamanari, H. Ogo, T. Taima, J. Sakai, J. Tsukamoto, Y. Yoshida, in *2010 35th IEEE Photovoltaic Specialist Conf. (PVSC),* IEEE, p.001628 (2010).
[18] K. Marumoto, S. Kuroda, T. Takenobu, Y. Iwasa, *Phys. Rev. Lett*. **97**, 256603 (2006).
[19] K. Marumoto, T. Sakamoto, S. Watanabe, H. Ito, S. Kuroda, *Jpn. J. Appl. Phys*. **46**, L1191 (2007).
[20] K. Marumoto, M. Kato, H. Kondo, S. Kuroda, N. C. Greenham, R. H. Friend, Y. Shimoi, S. Abe, *Phys. Rev. B* **79**, 245204 (2009).
[21] S. Watanabe, H. Tanaka, S. Kuroda, A. Toda, S. Nagano, T. Seki, A. Kimoto, J. Abe, *Appl. Phys. Lett*. **96**, 173302 (2010).
[22] K. Marumoto, T. Fujimori, M. Ito, T. Mori, *Adv. Energy Mater*. **2**, 591 (2012).
[23] M. Ito, K. Marumoto, *Chem. Lett*. **41**, 696 (2012).
[24] T. Nagamori, K. Marumoto, *Adv. Mater.* **25**, 2362 (2013).
[25] J. De Ceuster, E. Goovaerts, A. Bouwen, J. C. Hummelen, V. Dyakonov, *Phys. Rev. B* **64**, 195206 (2001).
[26] O. G. Poluektov, S. Filippone, N. Martín, A. Sperlich, C. Deibel, V. Dyakonov, *J. Phys. Chem. B* **114**, 14426 (2010).
[27] A. Aguirre, S. C. J. Meskers, R. A. J. Janssen, H.-J. Egelhaaf, *Org. Electron*. **12**, 1657 (2011).
[28] J. Ouyanga, Q. Xu, C.-W. Chu, Y. Yang, G. Li, J. Shinar, *Polymer* **45**, 8443 (2004).
[29] R. Jalili, J. M. Razal, P. C. Innis, G. G. Wallace, *Adv. Funct. Mater.* **21**, 3363 (2011).
[30] N. A. Schultz, M. C. Scharber, C. J. Brabec, N. S. Sariciftci, *Phys. Rev. B* **64**, 245210 (2001).
[31] M. C. Scharber, D. Mühlbacher, M. Koppe, P. Denk, C. Waldauf, A. J. Heeger, C. J. Brabec, *Adv. Mater.* **18**, 789 (2006).
[32] R. J. Davis, M. T. Lloyd, S. R. Ferreira, M. J. Bruzek, S. E. Watkins, L. Lindell, P. Sehati, M. Fahlman, J. E. Anthony, J. W. P. Hsu, *J. Mater. Chem*. **21**, 1721 (2011).
[33] H. Ishii, K. Sugiyama, E. Ito, K. Seki, *Adv. Mater.* **11**, 605 (1999).
[34] D. Cheyns, J. Poortmans, P. Heremans, C. Deibel, S. Verlaak, B. P. Rand, J. Genoe, *Phys. Rev. B* **77**, 165332 (2008).
[35] J. W. Jung, W. H. Jo, *Adv. Funct. Mater.* **20**, 1 (2010).
[36] M. Brinkmann, J.-C. Wittmann, *Adv. Mater.* **18**, 860 (2006).
[37] K. Harada, F. Li, B. Maenning, M. Pfeiffer, K. Leo, *Appl. Phys. Lett*. **91**, 092118 (2007).

Super High Resolution Imaging with Atomic Resolution Electron Microscope of JEM-ARM300F

H. Sawada, N. Shimura, K. Satoh, E. Okunishi, S. Morishita, T. Sasaki, Y. Jimbo, Y. Kohno, F. Hosokawa, T. Naruse, M. Hamochi, T. Sato, K. Terasaki, T. Suzuki, M. Terao, S. Waki, T. Nakamichi, A. Takano, Y. Kondo, T. Kaneyama

EM Business Unit, JEOL Ltd.

Through the technology evolved in the R005 project and the JEM-ARM200F, we developed an atomic resolution electron microscope of the JEM-ARM300F as a new platform for a super high-resolution instrument. The developed microscope is equipped with an ultra-stable cold field emission gun and spherical aberration correctors for probe and image forming systems. The stability of the microscope in TEM was tested by a lattice fringe of a crystal specimen and Young's fringe for a thick specimen showing beyond (50 pm)$^{-1}$ spatial information in these images. Ga-Ga dumbbells separated by 63 pm for a GaN [211] specimen was resolved in high angle annular dark field STEM imaging. Sub-50 pm imaging was demonstrated in STEM using a Ge [114] specimen.

Introduction

Since an aberration correction system has been practically established [1-3], electron microscopes with the system drastically enhanced analysis capability in a scanning transmission electron microscopy (STEM) and structural study in transmission electron microscopy (TEM). During the R005 project (Project leader: Prof. Kunio Takayanagi 2004-2009), Tokyo Institute of Technology and JEOL Ltd. realized resolution of 0.05 nm [4,5], with a developed 300 kV high resolution electron microscope equipped with probe- and image-forming aberration correctors [3]. For an electron source, a cold field emitter was used to achieve high-brightness and narrow energy spread. 63-pm resolution was demonstrated using a GaN crystalline specimen observed from the [211] orientation [6]. Sub-50 pm resolution was demonstrated [7] using 47-pm separated atomic columns of Ge-Ge with Ge[114] specimen [8,9]. Li atomic column was detected with annular bright field (ABF) imaging technique for a sample of LiV_2O_4 [10].

For 200 kV microscopes, spherical aberration correctors of CESCOR and CETCOR (CEOS GmbH) were installed into the JEM-2100F and the JEM-2200FS in 2003 [11]. And the JEM-2100F with a STEM aberration corrector imaged atomic structures of segregations at grain boundaries [12]. Next, we developed a 200 kV high-end microscope for commercial use in 2009; it is the JEM-ARM200F, which is equipped with a spherical aberration corrector for a probe-forming system in the standard configuration. The microscope demonstrated sub-Ångström imaging with Ge and Si specimens observing from the [112] orientation. Light elements were visualized by ABF with a developed STEM detecting system using a bright field aperture [13]. Atomic resolution analysis by electron energy loss spectroscopy (EELS) and energy dispersive spectroscopy (EDS) were also demonstrated.

Refining these technologies cultivated in the R005 project and the JEM-ARM200F, we developed a new atomic resolution microscope of 300 kV JEM-ARM300F. In this paper, the features and the performances of the microscope are introduced.

Instrumental features

Appearance of JEM-ARM300F

Figure 1 shows appearances of the JEM-ARM300F. There are four types of configurations depending on corrector equipment; basic version which has no corrector, STEM corrector version [Fig.1(a)], TEM corrector version, and double corrector version [Fig.1(b)]. The width of an operation table is same as that of the JEM-ARM200F, whereas the JEM-ARM300F is higher than JEM-ARM200F; the height of the STEM-version of the JEM-ARM300F is 3.16 m and that of the double version is 3.44 m. The JEM-ARM300F is usable at a higher accelerating voltage up to 300 kV and better resolution is attainable, as shown later. Then, we name the microscope "GRAND ARM"

3-1-2 Musashino, Akishima, Tokyo, 196-8558, Japan.

E-mail: hsawada@jeol.co.jp

as a nickname, presenting the highest class of the ARM series.

6-SIPs & TMP pumping system and high performance cold field emission gun

To achieve high quality vacuum at the specimen stage, we employed a differential pumping system composed of six sputter ion pumps (SIP) and a turbo molecular pump (TMP), as shown in **Fig. 2**(a). The specimen stage is pumped with a 150 L/s SIP, the intermediate lens (IL) and the condenser lens (CL) systems are pumped with two individual 20 L/s SIPs. The pre-evacuation of a specimen holder is performed with the TMP, whereas the TMP is

Fig. 1 Appearance of JEM-ARM300F (GRAND ARM).
(a) STEM corrector version (b) Double corrector version.

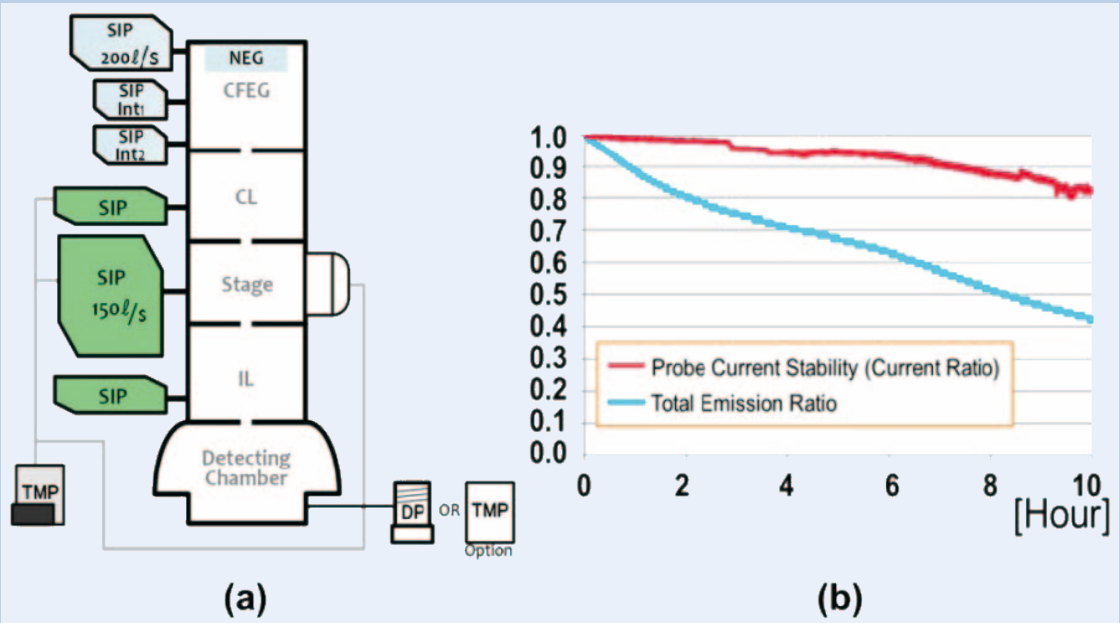

Fig. 2 (a) Schematic of the pumping system in JEM-ARM300F. (b) Emission stability for the cold field emission gun.

stopped during observation. The TMP is also used to pump the column during the baking of column and/or a liquid nitrogen tank for anti-contamination. With this pumping system, a pressure level of 2~10×10^{-6} Pa is typically achievable at the stage measured with the ion current of the 150 L/s SIP.

The developed CFEG is evacuated with non evaporable getters (NEG), a 200 L/s SIP (with noble pump) and two 20 L/s SIPs. NEG pumps the gas around the emitter, and the 200 L/s SIP pumps the accelerating tube, and the 20 L/s SIPs pumps the 1st and 2nd intermediate chambers [14]. The pumping system enables achieving an ultimate current stability of the CFEG. Figure 2(b) shows current stability, after a flashing of the emitter and a setting an emission current to be 10 μA. Total time for the procedures of flashing and auto-emission takes approximately 1 min. Owing to an ultra-high vacuum of 4~10×10^{-9} Pa measured at the accelerating tube, the probe current keeps 90 % of initial current even after four hours. Thus, the 6-SIPs & TMP pumping system is very effective to keep a specimen stage vacuum clean and stabilize the emission current from the electron source well.

Corrector system

The JEM-ARM300F is equipped with an aberration corrector, which was developed in the R005 project [3]. The spherical aberration is compensated by two three-fold astigmatism fields [1] generated in two dodeca-poles (**Fig. 3**(a)). As a further optical innovation, an electron trajectory is expanding toward a specimen in the corrector and largely expanding between the condenser-mini lens and the transfer condenser-mini lens (CM-CMT) or between the objective-mini lens and the transfer objective-mini lens (OM-OMT) [3]. The expanding trajectory enables us to reduce disturbance in above elements resulting that extra chromatic aberration and noise from the corrector can be reduced. We call the system as ETA (Expanding Trajectory Aberration) optical system (Fig. 3(b), (c)).

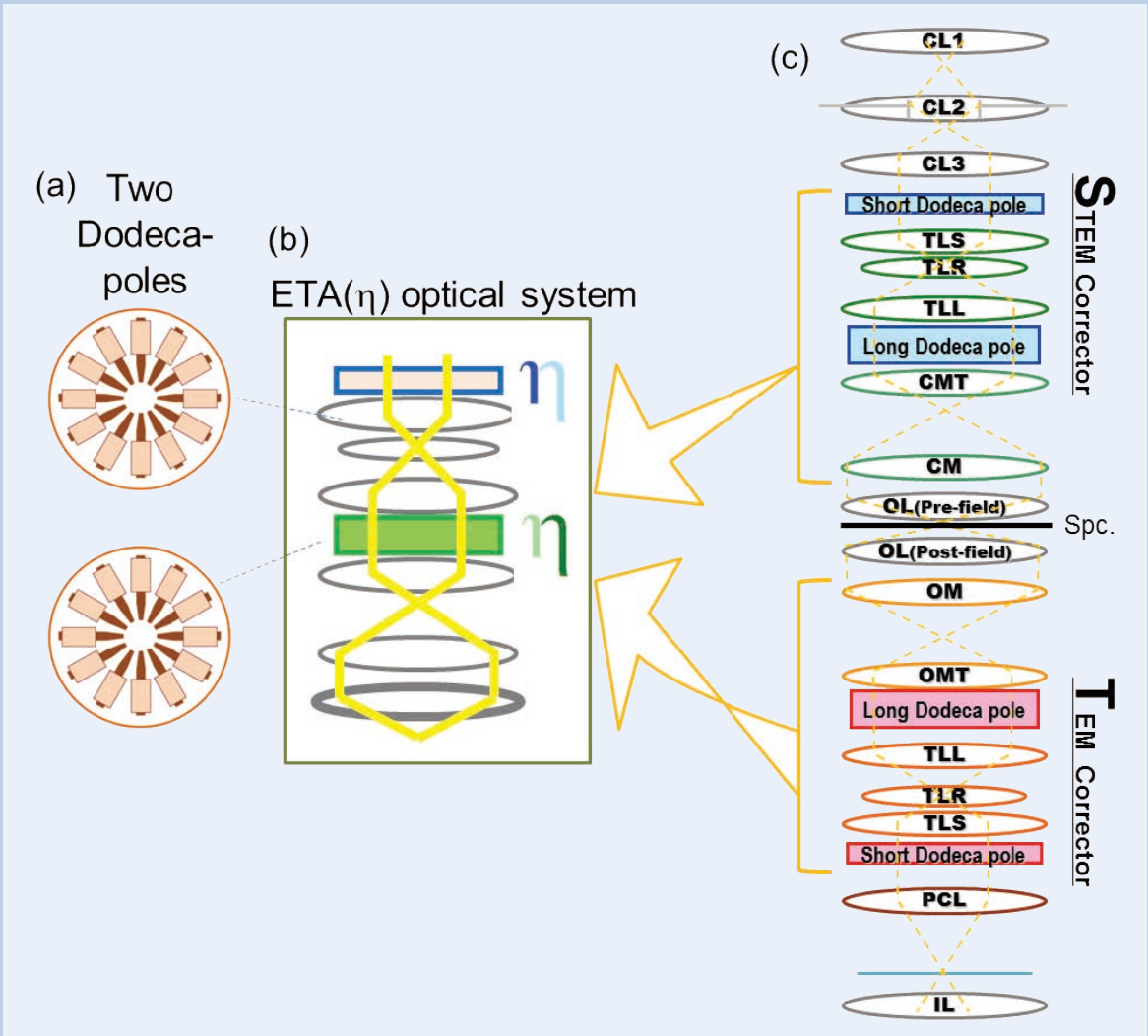

Fig. 3 (a) Schematic of dodeca-poles. (b)ETA (Expanding Trajectory Aberration Correction) optical system. (c) Schematic drawings of STEM and TEM ETA correctors.

Corrector system module

For a corrector control software, we developed the corrector system module (JEOL COSMO: corrector system module), which measures aberrations up to 5th order. For tuning of a probe-forming lens system, under and over defocused Ronchigrams are recorded to measure aberrations by the segmented Ronchigram auto-correlation function matrix (SRAM) method [15] (**Fig. 4**(a-d)). For tuning of an image-forming lens system, diffractogram tableau [16] are used for aberration measurement (Fig.4(e,f)).

Highly stabilized column

Figure 5(a) shows a power spectrum of Fourier transform from the TEM image of a Si [110] specimen at an accelerating voltage of 300 kV, where lattice information beyond 50 pm can be confirmed. Young's fringe test including non-linear term using a thick specimen of gold particles on a carbon film is shown in Fig. 5(b). Fringes are extended to spatial information better than $(50\ pm)^{-1}$. These results indicated that the mechanical and electric stability of the microscope realized the capability of 50 pm resolution.

Figure 5(c) is a high-resolution HAADF STEM image of Si [110] at 300 kV with an acquisition time of 10 s and Fig. 5(d) is one with an acquisition time of 80 s. A high-resolution image with a long acquisition time in Fig. 5(d) shows little distortion, indicating that the scanning system and the stage are highly stabilized against not only high frequency disturbance but also low frequency fluctuation.

Detecting System

The microscope is equipped with a viewing chamber and a detecting chamber (**Fig. 6**(a) and (b)), where four STEM detectors can be attached totally: high-angle annular dark field (HAADF), low-angle annular dark field (LAADF), annular bright field (ABF),

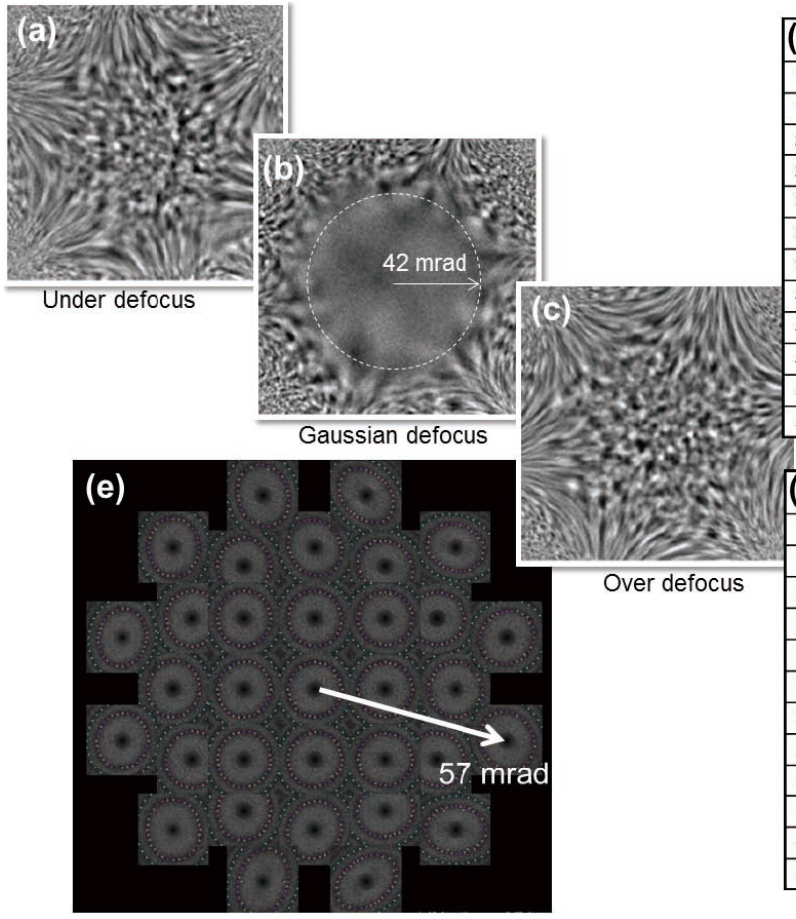

(d)

	Geometrical Aberrations	Amplitude(Azimuth)
1st	Defocus	- 1.903 nm
1st	2-fold astigmatism	4.125 nm(28.39°)
2nd	Axial coma	39.109 nm(-92.47°)
2nd	3-fold astigmatism	34.953 nm(3.66°)
3rd	Spherical aberration	-0.128 μm
3rd	Star aberration	0.707 μm(-74.02°)
3rd	4-fold astigmatism	0.201 μm(-29.32°)
4th	Axial coma	11.911 μm(42.75°)
4th	Three-lobe	7.690 μm(-56.17°)
4th	5-fold astigmatism	12.516 μm(-9.51°)
5th	Spherical aberration	0.354 mm
5th	6-fold astigmatism	0.732 mm(19.05°)

(f)

	Geometrical Aberrations	Amplitude(Azimuth)
1st	Defocus	- 282.628 nm
1st	2-fold astigmatism	5.299 nm(81.05°)
2nd	Axial coma	35.978 nm(-125.30°)
2nd	3-fold astigmatism	83.664 nm(5.61°)
3rd	Spherical aberration	1.828 μm
3rd	Star aberration	0.726 μm(-63.33°)
3rd	4-fold astigmatism	0.563 μm(-2.22°)
4th	Axial coma	18.942 μm(-101.30°)
4th	Three-lobe	87.234 μm(-6.09°)
4th	5-fold astigmatism	47.311 μm(-35.88°)
5th	Spherical aberration	-0.424 mm
5th	6-fold astigmatism	0.539 mm(24.74°)

Fig. 4 (a-c) Under and over defocused Ronchigrams at 300 kV. (d) Measurement values for a probe-forming lens by SRAM at an accelerating voltage of 300 kV. (e) Diffractogram tableau for aberration measurement at 300 kV. (f) Measurement values for the image-forming lens by diffractogram tableau at an accelerating voltage of 300 kV.

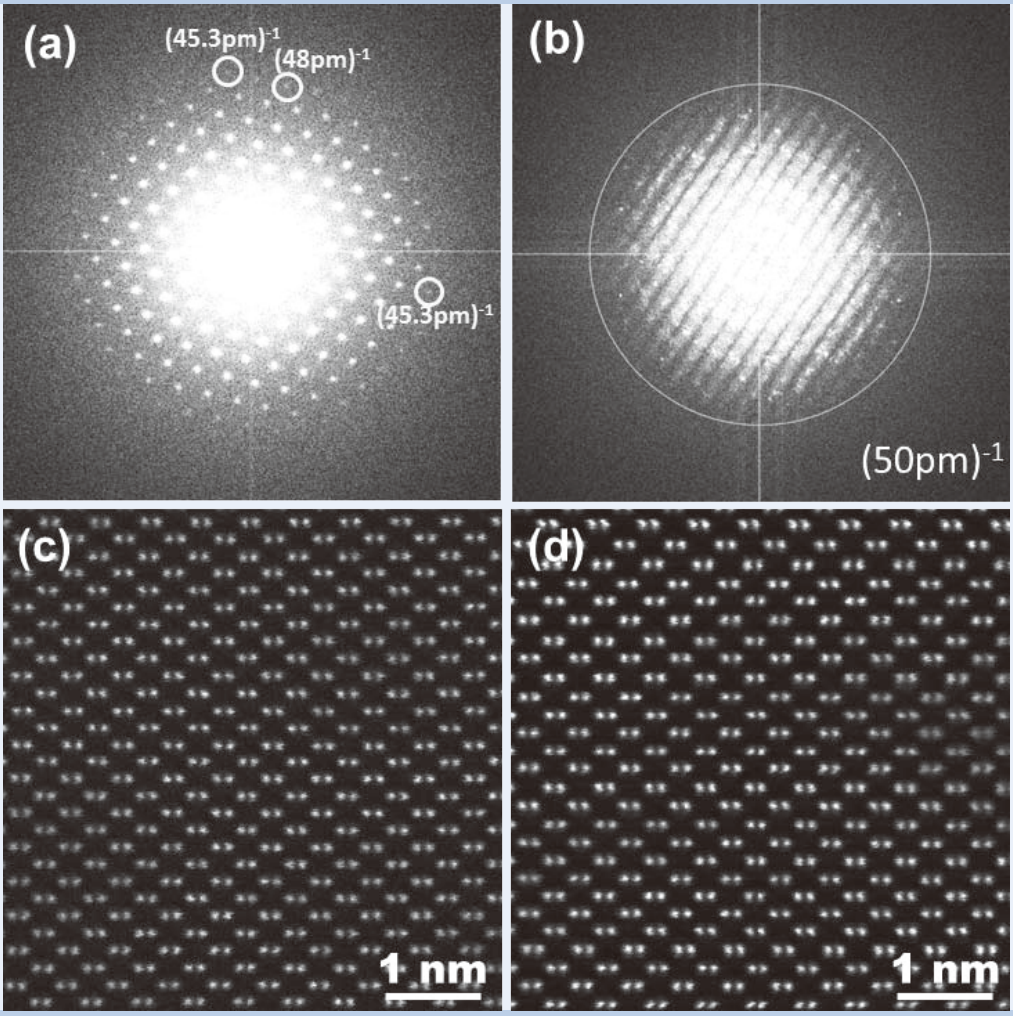

Fig. 5 (a) The power spectrum of Fourier transform from a high-resolution TEM image of Si [110]. (b) Young's fringe test using gold particles on a carbon thick film. (c,d) Si [110] high-resolution HAADF images with an acquisition time of (c) 10 s and (d) 80 s.

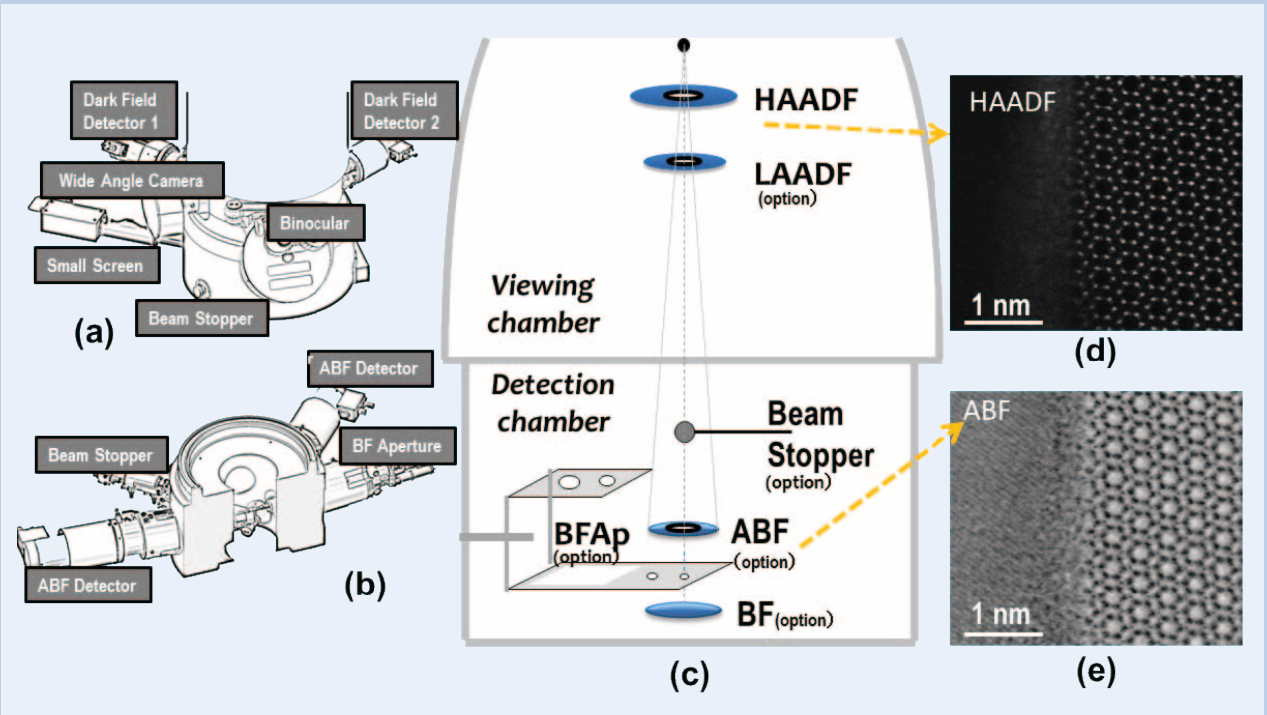

Fig. 6 Schematics of (a) a viewing chamber and (b) a detecting chamber with detectors. (c) Schematic of STEM detector configuration. (d) High-resolution HAADF image of a grain boundary in a β-Si_3N_4 polycrystalline specimen at 300 kV. (e) High-resolution ABF image.

and bright field (BF) detectors (Fig.6(c)). Four images by these detectors can be obtained, simultaneously. Figure 6(d) and (e) respectively show an example of a HAADF image and a simultaneously acquired ABF image for a specimen of β-Si_3N_4. Nitrogen atomic columns are detectable in the image of ABF.

Wide range of accelerating voltage

The microscope can be operated at wide range accelerating voltages from 80 to 300 kV. **Figure 7**(a-c) show high-resolution HAADF images of a Si [110] crystalline specimen. Observation at 300 kV can image a sub-Ångström structure, as shown later, and 80 kV imaging is useful for soft materials to reduce the specimen damage. At 80 kV, 136 pm imaging is achievable, as shown in Fig. 7 (c). Operation at 160 kV is optionally available (Fig. 7(b)), and 160 kV imaging is useful for a semiconducting material because of high-resolution and relatively small damage compared with higher voltage. Lower voltage operation at 60 kV is optionally available.

Developed two objective pole pieces and ultra-high resolution imaging

We newly developed two types of pole pieces of an objective lens for the JEM-ARM300F. They are FHP (full high resolution pole piece) for the ultra-high resolution configuration and WGP (wide gap pole piece) for the high resolution analytical configuration. FHP is designed [3] for ultra-high resolution observation with a small chromatic aberration; a chromatic aberration coefficient value of 1.35 mm in STEM/TEM at 300 kV is significantly small. WGP is useful for a high-sensitive EDS analysis with a large solid angle of the detection, for a thicker special holder owing to a large space inside a pole piece gap, and for a higher tilt angle of a specimen holder compared with FHP.

Ultra-high resolution STEM images were obtained using GaN and Ge crystalline specimen using the developed STEM ETA corrector. 63 pm separation was clearly detected in a raw image (**Fig.8**(a)) and an intensity line profile of HAADF at 300 kV using the FHP pole piece (Fig.8(d)). Spots smaller than $(63\ pm)^{-1}$ information were detected in the power spectrum in Fig.8 (b).

As a further challenging, a sub-50 pm resolution was imaged in HAADF using the FHP (**Fig. 9**). 47-pm separation was confirmed in the intensity line profile in Figure 9(f) and a spatial information of $(47\ pm)^{-1}$ was detected in the power spectrum in Fig.9 (d). The microscope of "GRAND ARM" has a capability to image sub-50 pm resolution. The stability must be effective in not only ultra-high-resolution imaging but also robust data acquisition for analysis and structure study.

Summary

We developed a new atomic resolution microscope of the JEM-ARM300F. The developed cold field emission gun showed ultra-high emission stability due to an ultra-high vacuum around the emitter. Stability of the microscope was confirmed using the power spectrum of TEM images and an atomic-resolution STEM image with a long acquisition time. Ultra-high resolution STEM images were demonstrated, by using the developed corrector and objective lens. The microscope will be new platform for an atomic resolution study.

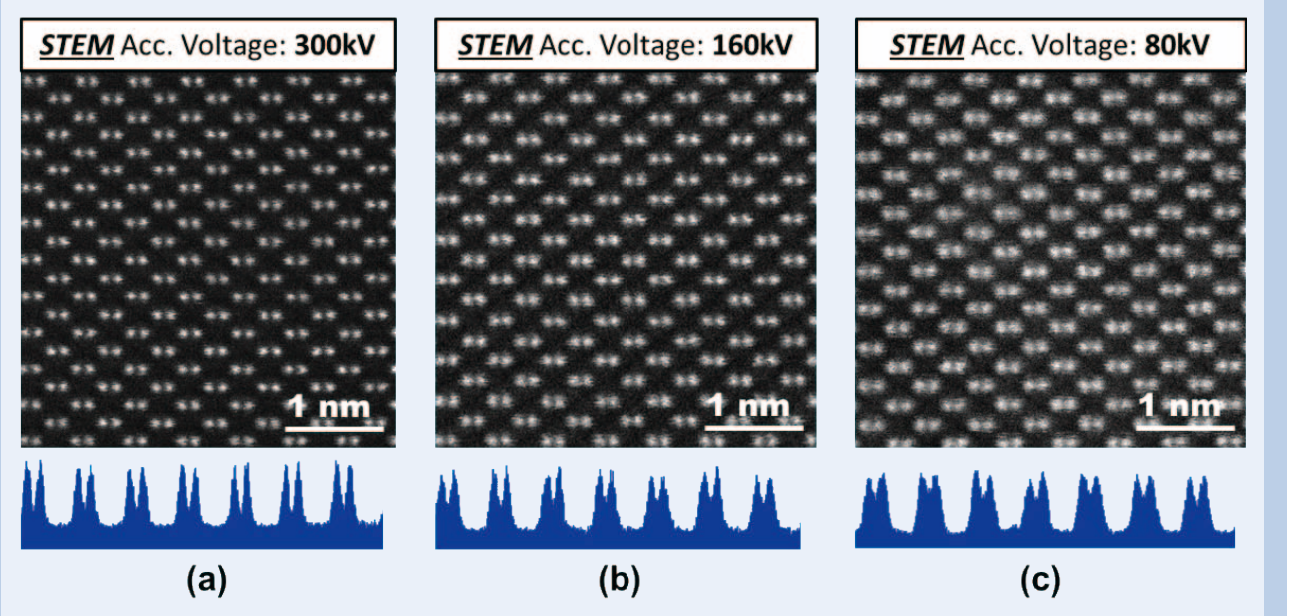

Fig. 7 High resolution HAADF imaging of Si [110] at (a) 300 kV, (b) 160 kV, and (c) 80 kV with their intensity line profiles, as shown at the lower parts.

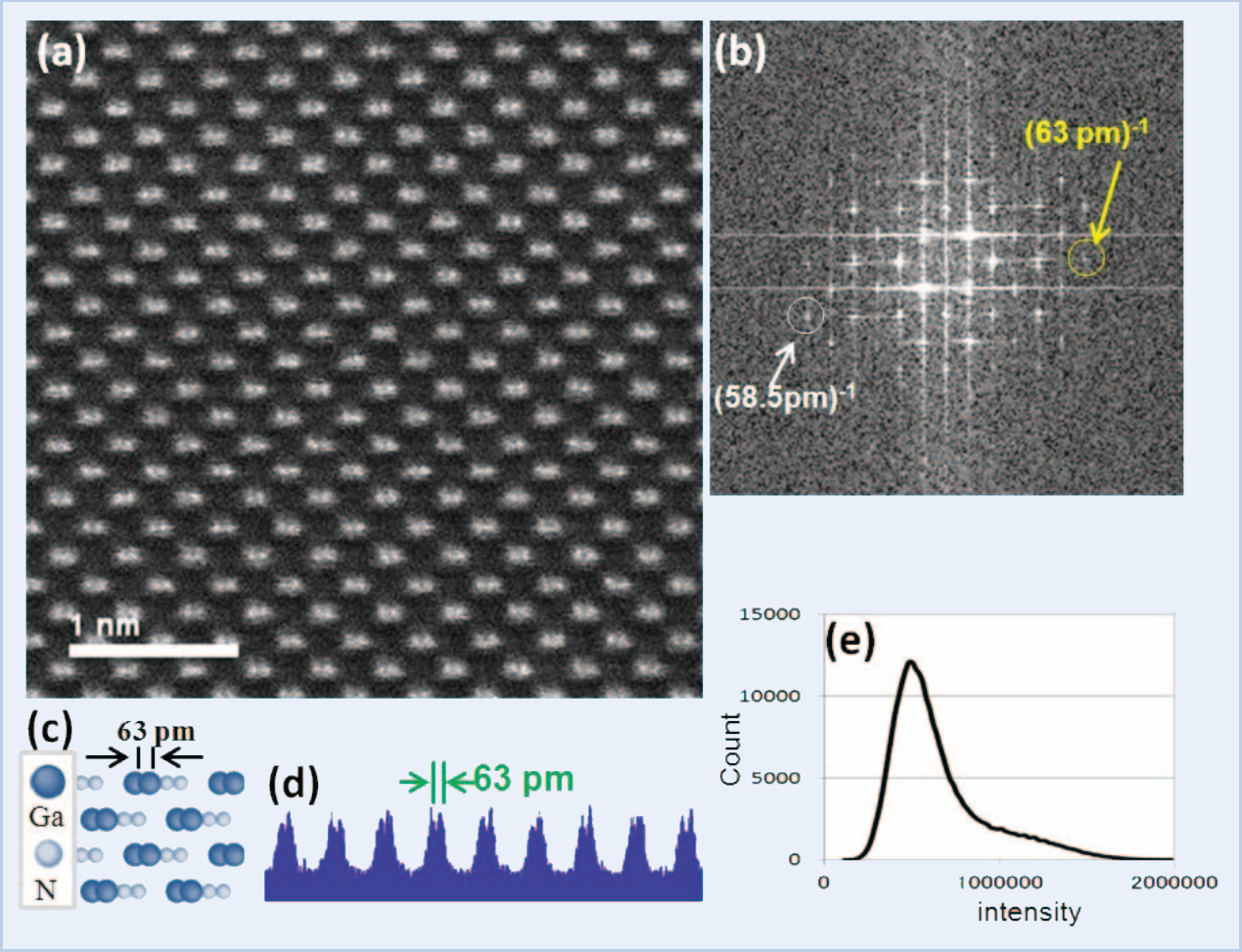

Fig. 8 (a) Raw HAADF image of a GaN [211]. (b) The power spectrum from Fig.8(a). (c) Atomic structure model of a GaN[211]. (d) Intensity line profile of a GaN[211] raw image. (e) Intensity histogram of Fig.8(a).

Acknowledgments

The authors thank Prof. K. Takanayagi, Y. Tanishiro of Tokyo Institute of Technology and other members of JST CREST R005 project for advice to establish the R005 microscope and develop the elements of ETA correctors, ultra-high-stabilized cold field emission gun, and FHP. The authors appreciate Emeritus Prof. M. Tanaka of Tohoku University for organizing of the CREST project. The authors thank Prof. Y. Ikuhara and N. Shibata of the University of Tokyo for collaboration of the development of the GRAND ARM.

References

[1] Haider, M., Uhlemann, S., Schwan, E., Rose, H., Kabius, B., and Urban, K. ; Electron microscopy image enhanced. *Nature*, **392**, 768-769 (1998).

[2] Krivanek, O. L., Dellby, N., and Lupini, A. R. ; Towords sub-angstrom beams. *Ultramicroscopy*, **78**, 1-11 (1999).

[3] Hosokawa, F., Sawada, H., Kondo, Y., Takayanagi, K., Suenaga, K. ; Development of Cs and Cc correctors for transmission electron microscopy. *Microscopy*, **62**, 23-41 (2013).

[4] Takayanagi, K., Oshima, Y., Tanaka, T., Tanishiro, Y., Sawada, H., Hosokawa, H., Tomita, T., Kaneyama, T., and, Kondo, Y. ; Lithium Atom Microscopy at Sub-50 pm Resolution. *JEOL News*, **45**, 2-7 (2010).

[5] Takayanagi, K., Kim, S., Lee, S., Oshima, Y., Tanaka, T., Tanishiro, Y., Sawada, H., Hosokawa, F., Tomita, T., Kaneyama T., and Kondo Y. ; Electron microscopy at a sub-50 pm resolution. *J. Electron Microsc.*, **60**, S239-S244 (2011).

[6] Sawada, H., Hosokawa, F., Kaneyama, T., Ishizawa, T., Terao, M., Kawazoe, M,, Sannomiya, T., Tomita, T., Kondo, Y., Tanaka, T., Oshima, Y., Tanishiro, Y., Yamamoto, N., and Takayanagi, K. ; Achieving 63 pm resolution in scanning transmission electron microscope with spherical aberration corrector. *Jpn. J. Appl. Phys.*, **46**, L568-570 (2007).

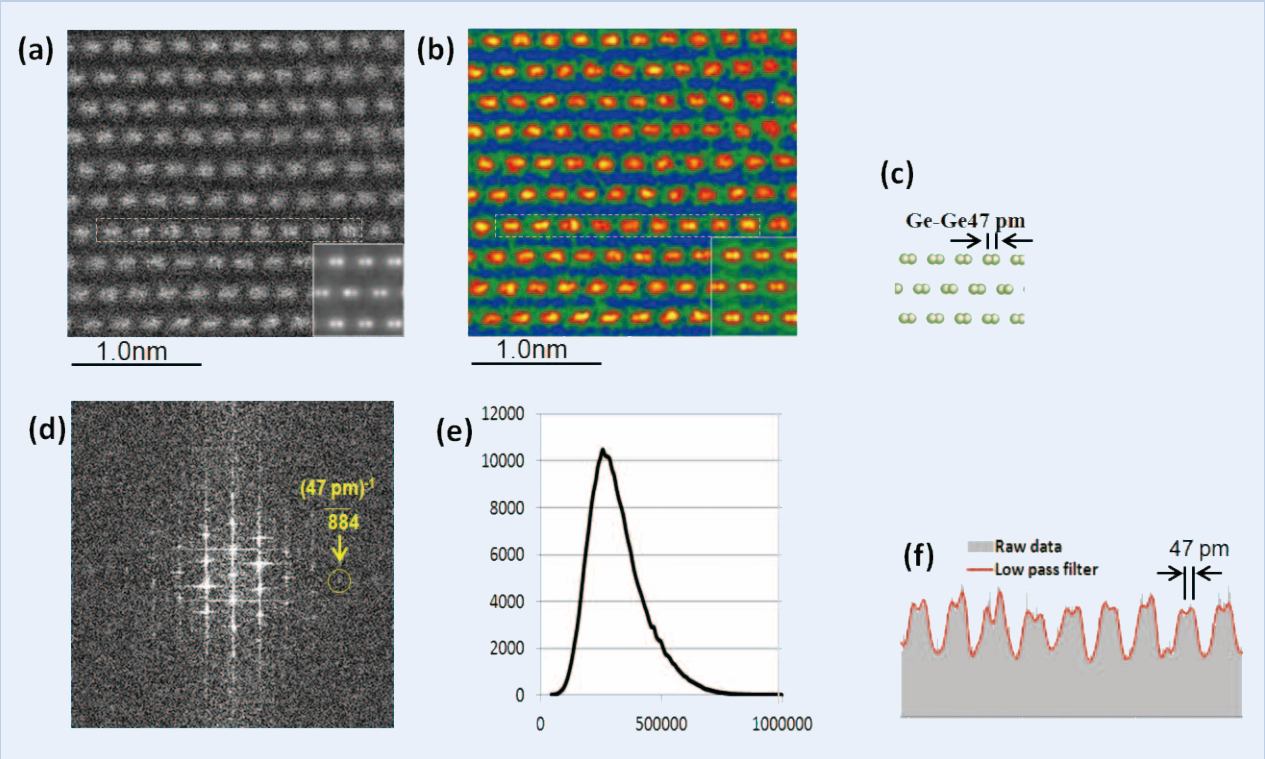

Fig. 9 (a) Raw HAADF image of Ge [114]. (b) Low pass filtered image of Fig.9(a). Simulated images are inserted at the lower right part in Fig. 9 (a) and 9 (b). (c) Atomic structure model of a Ge[114]. (d) The power spectrum from Fig.9(a). (e) Intensity histogram of Fig.9(a). (f) Intensity line profile of a dotted rectangle area in Fig.9 (a) and Fig.9(b).

[7] Sawada, H., Tanishiro, Y., Ohashi, N., Tomita, T., Hosokawa, F., Kaneyama, T., Kondo, Y., and Takayanagi, K. ; STEM Imaging of 47-pm Separated Atomic Columns by Spherical Aberration-Corrected Electron Microscope with 300 kV Cold Field Emission Gun. *J. Electron Microsc.*, **58**, 357-361 (2009).

[8] O'Keefe, M., Allard, L., Blom, D. ; HRTEM imaging of atoms at sub-Angstrom resolution. *J. Electron Microsc.*, **54**, 169-180 (2005).

[9] Erni, R., Rossell, M. D., Kisielowski, C., and Dahmen, U. ; Atomic-resolution imaging with a sub-50-pm electron probe. *Physical Review Letter*, **102**, 096101 (2009).

[10] Oshima, Y., Sawada, Hosokawa, F., Okunishi, E., Kaneyama, T., Kondo, Niitaka, S., Takagi, H., Y., Tanishiro, Y., and Takayanagi, K. ; Direct imaging of lithium atoms in LiV_2O_4 by spherical aberration-corrected electron microscopy. *J. Electron Microsc.*, **59**, 457-461 (2010).

[11] Sawada, H., Tomita, T., Naruse, M., Honda, T., Hambridge, P., Hartel, P., Haider, M., Hetherington, C. J. D., Doole, R.C., Kirkland, A.I., Hutchison, J. L., Titchmarsh, J.M., Cockayne, D. J. H. ; Experimental evaluation of a spherical aberration-corrected TEM and STEM. *J. Electron Microsc.*, **54**, 123-126 (2005).

[12] Sato, Y., Buban, J.P., Mizoguchi, T., Shibata, N., Yamamoto, T., and Ikuhara, Y. ; Role of Pr segregation in acceptor-state formation at ZnO grain boundaries. *Phys. Rev. Lett.*, **97**, 106802 1-4 (2006).

[13] Okunishi, E., Sawada, H., and Kondo, Y.; Experimental study of annular bright field (ABF) imaging using aberration-corrected scanning transmission electron microscopy (STEM). *Micron*, **43**, 538-544 (2012).

[14] Kohno, Y., Okunishi, E., Tomita, T., Ishikawa, I., Kaneyama, T., Ohkura, Y.,Kondo, Y., Isabell, T. ; Development of a cold field-emission gun for a 200 kV atomic resolution electron microscope. *Microsc. Anal.* **24**, S9–S13 (2010).

[15] Sawada, H., Sannomiya, T., Hosokawa, F., Nakamichi, T., Kaneyama, T., Tomita, T., Kondo, Y., Tanaka, T., Oshima, Y., Tanishiro, Y., and Takayanagi, K. ; Measurement method of aberration from Ronchigram by autocorrelation function. *Ultramicroscopy* **108**, 1467-1475 (2008).

[16] Zemlin, F., Weiss, K., Schiske, P., Kunath, W., and H.Herremann, K. ; Coma-free alignment of high resolution electron microscopes with the aid of optical diffractograms. *Ultramicroscopy* **3**, 49-60 (1978).

Advanced Analysis of Active Materials in Li-Ion Battery by XPS and AES

Kenichi Tsutsumi, Masahide Shima and Akihiro Tanaka

SA Business Unit, JEOL Ltd.

Introduction

Auger Electron Spectroscopy (AES) and X-ray Photoelectron Spectroscopy (XPS) are widely used as analytical methods that perform elemental analysis of the specimen surface down to only a few-nanometer region. In particular, these two methods enable direct detection of lithium which is a light element and furthermore, provide both quantitative evaluation and chemical bonding-state evaluation. Thus, the methods have been used for research and development of various materials in a Li-ion battery. However, when examining the number of books and papers covering the topics of a Li-ion battery using the Internet literature searching systems (ex. http://scholar.google.com), documents which present research achievements by the use of XPS reach as many as 2000, but those by AES are issued only 500 under the same searching conditions. This may be partly due to the difference between the number of the XPS users and the AES users. But one essential reason is that the AES users misunderstand AES to be difficult to analyze Li and hard to be used for the Li investigation. In fact, the kinetic energy of an Auger electron of Li KVV is about 50 eV. This means that an Auger spectrum of Li is located at a large background consisting of secondary electrons and also it overlaps with Auger peaks of the other elements. Thus, depending on the specimen, it may be difficult to identify the Li peak from Auger spectrum. Another reason is that the escape depth of an Auger electron of Li is very short. The intensity of Li KVV peaks decreases drastically when a small volume of contaminants (only 1 to 2 nm thickness) covering a specimen (containing Li), thus making it difficult to detect Li. On the other hand, in the case of XPS, the kinetic energy of a photoelectron emitted from Li is approximately 1200 to 1400 eV, which is much higher than that of the corresponding Auger electron. For this reason, Li1s is easily detected in XPS spectrum even if the specimen surface is rather contaminated. Furthermore in XPS, the overlap of the Li peak with the other peaks is less, thus facilitating the detection of Li. Lithium peak overlaps especially with that of transition metal such as Mn, Fe, Co, Ni, etc., which are frequently-used transition metals for the Li-ion battery. However in the case of XPS, only a Fe3p peak overlaps with a Li1s peak. That is, in the case of AES, preventing deposition of contaminants onto the specimen surface is of prime importance at the process of pre-treatment of the specimen. If a pre-treatment technique is improper, even if the same specimen is analyzed by XPS and AES, there happen many cases where Li is detected by XPS but is not detected by AES.

In this context, Li seems to be an unsuitable element to be observed by AES. But we emphasize the following points. If the operator understands and gains a proper specimen pre-treatment technique and precautions to be taken during AES analysis, the detection intensity of Li itself is higher than that analyzed by XPS. In addition, AES has capacity to measure the Li distribution in a single particle of Li-ion battery materials even at magnifications of several tens of thousands of times to several hundreds of thousands of times. That is, AES and XPS have advantages and disadvantages in Li analysis to each other. Thus, a creative use of AES and XPS, which is based on the full understanding of the features of the two analytical methods, will play an effective role in Li analysis. In this article, we focus on analysis techniques for Li-ion battery and report on our analysis results.

Pre-Treatment Technique for Lithium Detection in Surface Analysis

Precautions when handling materials containing Lithium

Due to its characteristics, a Li ion in Li-ion battery material moves easily toward materials (irrespective of solid and liquid) which are located near the Li-ion battery materials. Therefore, precautions have to be taken when performing pre-treatment of the specimen.

The following example describes a $LiCoO_2$ particle, one of Li-ion battery material. When the AES analysis is applied to a clean particle surface, it is possible to clearly observe the Li peak in the differential spectrum as shown in **Fig. 1**. But when ultrasonic cleaning (by ethyl alcohol, etc.) is applied

3-1-2 Musashino, Akishima, Tokyo, 196-8558, Japan.

E-mail: tsutsumi@jeol.co.jp

to the specimen aimed at removing contaminations on the specimen surface, the Li peak becomes hardly detected from the surface of $LiCoO_2$ particles. This is considered to arise from the decrease of Li concentration on the surface, as a result of the fact that Li elements in the region of the particle surface are eluted into an ethyl alcohol solvent during the cleaning. As shown in Fig. 1, the Li peak disappears and this substance is found to be cobalt oxide. There is high possibility that this phenomenon arises for not only water but also the other organic solvents; therefore, AES and XPS which analyze the top surface of the specimen require special precautions. Consequently, in surface analysis by AES or XPS, we point out that it is not recommended to clean the particle surface with inorganic or organic solvents except for special cases.

If the $LiCoO_2$ particle surface has contamination, we recommend the following way. Do not clean the specimen surface with a solvent and expose a new clean surface by grounding $LiCoO_2$ powders with a pestle in a mortar for analysis.

Pre-treatment technique and precautions for powder specimen at Auger analysis

Concerning specimen pre-treatment techniques and the tips for analysis when surface analysis is applied to a powder specimen, we explained in 2009 JEOL EPMA/Surface analysis Users' Meeting document [1]. Thus in this article, we introduce "Method for spraying a powders onto a carbon-specimen stub".

The carbon-specimen stub presented here is the carbon specimen stub (Parts No. : 600154386) that is sold by JEOL Ltd., shown in **Fig. 2**. The dimensions of this stub are 10 mm in diameter and 5 mm in height. In the pre-treatment process, this specimen stub is polished with sandpaper with its grit number about 1000 to expose a relatively flat surface. After that, grooves with a little small depth are fabricated on the surface with a head-pointed tool (precision screwdriver, etc.). After spraying the powder onto this carbon-specimen stub, slightly scrub the carbon-specimen stub surface for filling the powders into the groove with paper (medical paper, etc.). The remaining powders on the stub surface must be removed with a blower.

After mounting the carbon-specimen stub on the standard specimen holder without spring inside the standard specimen holder (shown in shown in **Fig. 3** left), preparation for AES is completed.

This specimen pre-treatment enables particles with various configurations to be placed on the carbon-specimen stub. For example, as is shown in the

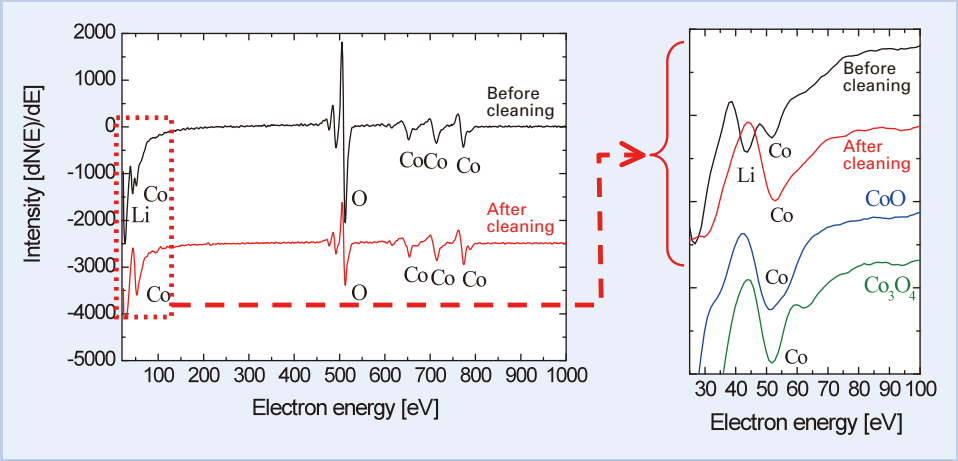

Fig. 1 Difference of the lithium peak intensity from the $LiCoO_2$ surface (before and after ultrasonic cleaning).

①Lightly polish the surface with sandpaper.

②Make grooves on the mount with a head-pointed tool.

③Rub a powder specimen into the grooves and remove extra powders.

Fig. 2 Placing a powder specimen onto the carbon-specimen stub.

right-side secondary electron image of shown in Fig. 3 right, a large surface area is seen where powders are permeated with high particle density in the fabricated grooves. In addition, on the surface that is polished by sandpaper with its grit number about 1000, fine surface irregularities or fine polished marks are produced. In this state, single particles and clusters exist in the irregularities or the polished marks. Since various-shape particles exist on the specimen stub, it becomes possible to perform analyses at several states with only one specimen stub. For example, a single particle is selectively analyzed and the average composition of a region with high particle density is also analyzed.

Pre-treatment technique and precautions for powder specimen at XPS analysis

When an insulating powder specimen is measured by XPS, there arise several problems that the insulating specimen is influenced by charging and a difficulty in fixing the specimen on the specimen holder. For comparison with the other fixing methods, we reported in 2006 JEOL EPMA/Surface Analysis Users' Meeting document [2]. The most suitable pre-treatment method for XPS is to mold a specimen into a pellet (**Fig. 4**). To perform pellet molding, a relatively large volume of powder specimen is required; however, the specimen surface molded by this method is flat, thus leading to advantages that XPS measurement sensitivity is high and it is easy to suppress the influence of charging.

Detection and Quantification of Lithium in Surface Analysis

Detection and sensitivity of lithium

In AES, rather surprisingly, the sensitivity of Li is not so low, enabling us to complete the analysis in a short period of time for not only point analysis but also Auger mapping. We compared the detection sensitivity for Li in AES with that in XPS. As is shown in **Fig. 5**, when the peak intensities in the standard spectra acquired by AES is compared between C (carbon) and Li under the same measurement conditions, the peak intensity of Li is approximately 4 times higher than that of C. In the case of XPS as well, the peak intensities of pure materials should directly be compared in principle; however, it is hard to acquire the Li standard spectrum in XPS. Due to this limitation, we performed comparison of the difference in ionization cross sections excited with an AlKα (1486.6 eV) X-ray source as the difference in the sensitivity between C and Li (right to Fig. 5). As is indicated in Fig. 5, compared to the peak intensity of C, Li provides a very low sensitivity, approximately 1/18 that of C. That is, when the Li intensity is compared between AES and XPS based on the C intensity as the standard peak intensity, it is revealed that AES has much higher sensitivity than XPS, approximately 72

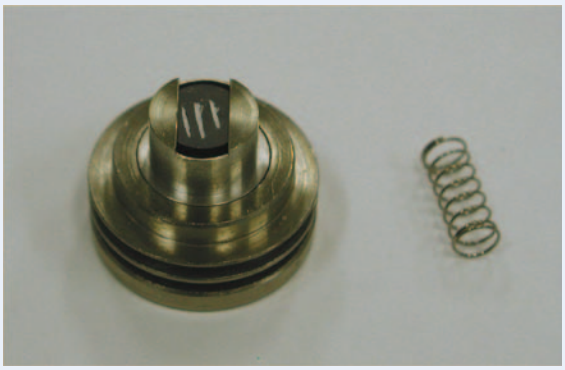

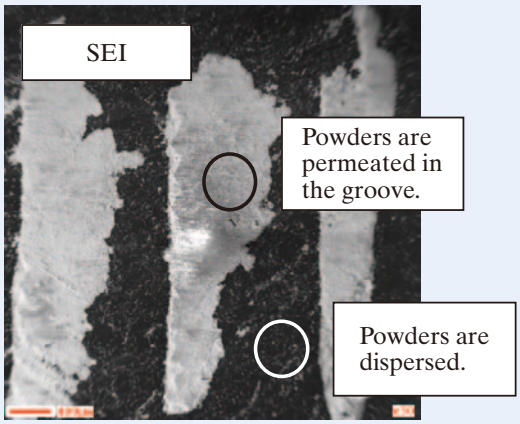

Fig. 3 State where the carbon-specimen stub is mounted on the standard specimen holder and a secondary electron image (SEI) of the specimen surface.

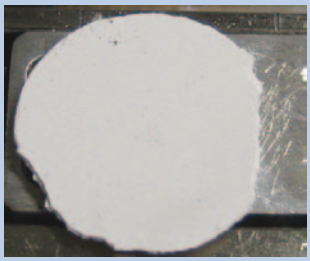

Fig. 4 Powder specimen molded into a pellet.

times.

However in general, it is likely to be recognized that XPS allows easier detection of Li than AES does. This misunderstanding leads to the fact that XPS is frequently used for surface analysis of Li compared to AES as mentioned in "Introduction" in this article. This fact is owing to the difference of escape depth between AES and XPS, which is largely due to the difference of kinetic energy between the Li Auger electron and the Li photoelectron. **Figure 6** shows the energy dependence of the mean free path of an electron in a solid. The Li KVV Auger electron only possesses a kinetic energy of approximately 50 eV. On the other hand, On the other hand, the kinetic energy of Li peak obtained using the AlKα line in XPS provides more than 1400 eV. This result leads to a large difference of the mean free path between the Auger electron (in AES) and the photoelectron (in XPS). When the escape depth of the electron is estimated to be approximately 3 times the mean free path, the escape depth of the Li KVV Auger electron is less than 2 nm. This implies that the escape depth of Auger electron in AES is approximately 1/3 times that of photoelectron in XPS. Thus, it is found that deposition of very small amount of contaminations onto the specimen surface gives rise to a large

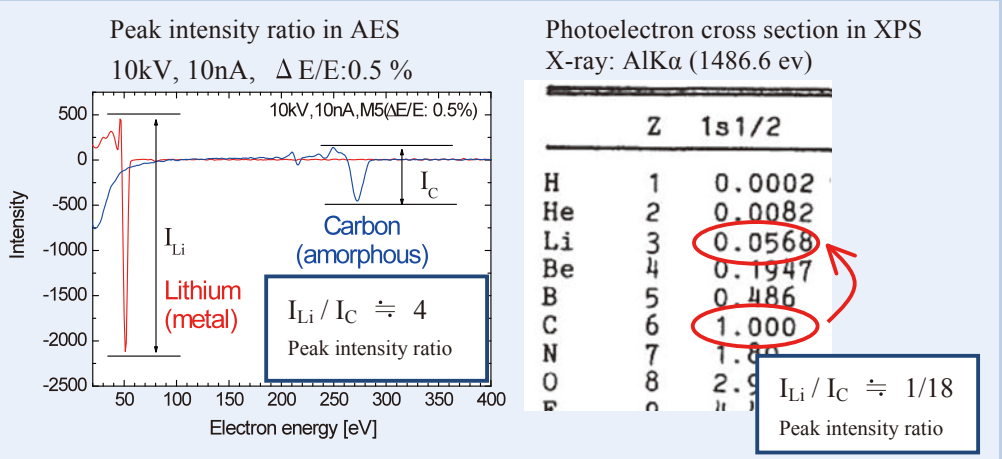

Fig. 5 Comparison of lithium sensitivity between AES and XPS.

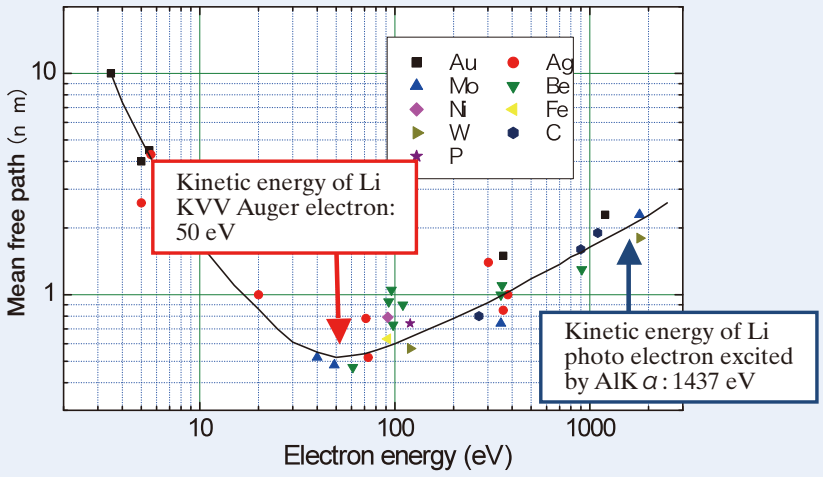

Fig. 6 Mean free path of an electron in a solid specimen.

Fig. 7 Images of lithium metal (left: before cutting, right: immediately after cutting).

decrease in the peak intensity and there is high possibility that Li cannot be detected. That is, when performing AES for Li, specimen pre-treatment is prime importance in addition to the analysis itself, and sufficient care is required for the specimen pre-treatment.

Next, we show spectra of Li chemical compounds obtained by actual measurement with an XPS instrument [3]. First, a measurement result of metal Li is presented. Normally, to avoid oxidation of metal Li, this material is preserved by immersing it in paraffin oil. However, Li reacts with water even at room temperature and transform to lithium hydroxide; finally transforms to lithium carbonate by absorbing CO_2 in the air. As a result, when preserved Li is extracted to the air, the color of the surface of Li turns to white (**Fig. 7**). Cutting Li using a razor at this state enables a surface which contains metal glaze to be exposed. However in the air, a portion showing metal glaze changes its color to black within several 10 s and further changes to white.

For the white portion where Li transformed to lithium carbonate, even after the specimen surface was etched by ion sputtering in a long period of time, oxygen and carbon did not vanish; therefore metal Li spectra were unable to be acquired. **Figure 8** shows the spectra acquired from the lithium carbonate portion by XPS measurement.

Since Li metal reacts with water in the air to transform to oxide, a bulk of Li is cut in a glove bag filled with dry nitrogen and the cut Li bulk is subject to XPS with Li metal glaze kept. After this process, a spectrum corresponding to metal Li and lithium oxide were obtained. **Figure 9** shows Li1s acquired from three kinds of chemical compounds including lithium oxide, lithium carbonate and lithium phosphate. **Table 1** lists spectral peak positions of those chemical compounds. As presented here, the use of XPS enables us to clearly observe Li spectra and also to obtain the change of chemical bonding states of Li itself.

Lithium quantification (relative sensitivity factor method and absolute intensity quantification method)

Up to the previous sections, we explained about the specimen pre-treatment and precautions about detecting Li. If the above-explained precautions are taken into consideration, a relatively skilled operator for AES does not have a difficulty in analyzing Li by not only XPS and but also AES. However for the next challenge, that is, Li quantification and its accuracy, there is no established method at present. In this section, as the quantification method of Li, the relative sensitivity factor method and the absolute intensity quantification method are described.

Li has only two occupied orbitals of 1s and 2s. In particular, the 2s orbital forms a covalent bond orbital with the bonded-counterpart element, thus depending on the bonding state, the peak position and the peak shape of the Auger spectrum changes greatly. Furthermore, the Li KVV peak around 50 eV exists on the large background of secondary electrons, the valence-electron peak of the other elements overlap with the Li KVV peak. Therefore, the use of the relative sensitivity factor method, which has been used as a quantitative analysis method for AES, makes it very difficult to correctly estimate concentration of elements contained in the specimen.

The peak intensities of AES appear as peak-to-peak in the differential spectrum (**Fig. 10**). In the relative sensitivity factor method for AES, the atomic concentration ratio is obtained in the following way. A measured peak intensity is multiplied by the relative peak intensity ratio (relative sensitivity factor) among pure substances, then the intensity correction is executed. After that, the summation of those corrected values is normalized to 100%. Finally, the resultant normalized value is regarded to be the atomic concentration ratio. If only the relative sensitivity factor is obtained, simple calculation of the peak intensities enables us to obtain a quantitative analysis result easily. This method is a widely-recognized, general quantitative analysis method for surface analysis. However in AES, the differential peak intensity is significantly sensitive to the change of peak shape. This is due to the change of the chemical states and the overlap of the peaks of the other elements, which gives rise to a large error in the quantitative analysis result. These large errors cause very serious problem when quantifying Li, typically in the case of a very low concentration Li (atomic concentration ratio: 5 % or less), thus the peak of Li cannot be detected as an independent peak. The existence of Li in the specimen is not often discovered without a curve fitting which shows Li peak buried in the peaks of the other elements.

In this context, we propose that when performing quantitative analysis of Li, instead of using the relative sensitivity factor method, it is reasonable to use the absolute intensity quantification method for the quantitative analysis of Li. The procedure of this method is described in Steps (1) to (4) below.

(1) Measure the Auger spectra of the specimen with taking care about pretreatment.
(2) Deconvolute the measured spectra into the respective components based on curve-fitting calculations using the standard spectra.
(3) Convert the spectral intensities of the respective components into the corresponding atomic concentrations with the intensity ratio between the spectral intensities of the respective components at the corresponding chemical states and those of the standard spectra acquired under the same measurement conditions.
(4) Examine the quantification accuracy with the calculated total atomic concentration.

In Step (1), it is not always necessary to select a high energy resolution for the Auger spectra. It is possible to calculate the quantification results even with the energy resolution of 0.5% with the standard spectra of the same measurement condition. Off course, it is effective to calculate with high energy resolution spectra in the case of containing different chemical states species [4]. It is important to measure the Auger spectra with the energy resolution suitable for the purpose of analysis and to perform measurement by taking care about the specimen damage due to electron-beam irradiation or Ar-ion irradiation.

In Step (2), curve fitting calculation is performed

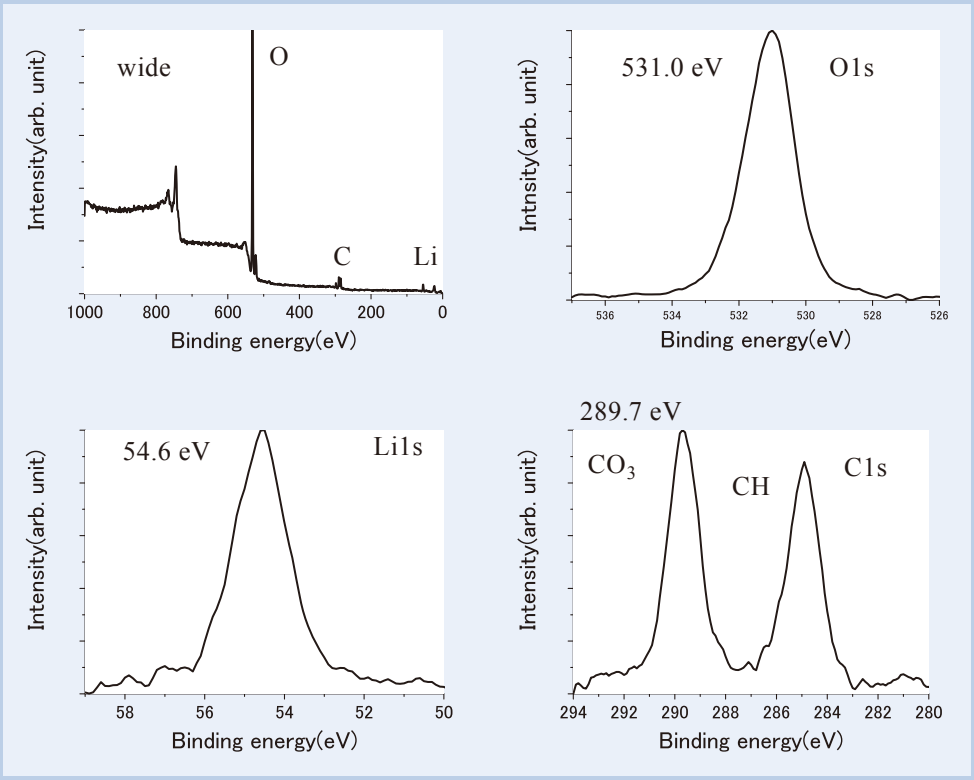

Fig. 8 XPS measurement result of the lithium white portion.

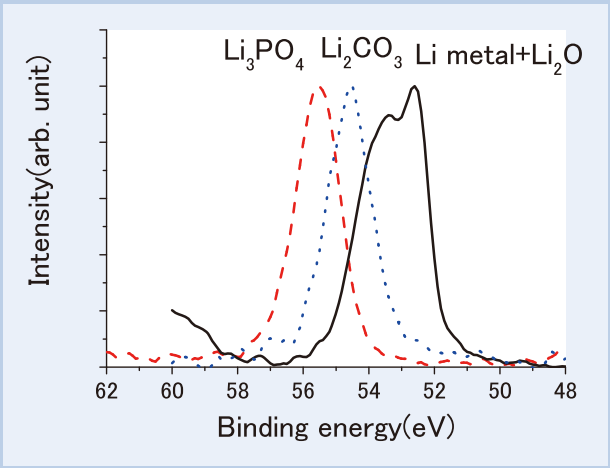

Table 1 Spectral peak positions of lithium related substances.

	Li1s	O1s	P2p	C1s
Li	52.6			
Li_2O	53.5	528.3		
Li_2CO_3	54.6	531.0		289.7
Li_3PO_4	55.5	531.0	133.9	

Fig. 9 Photoelectron peak of Li1s at different chemical bonding states.

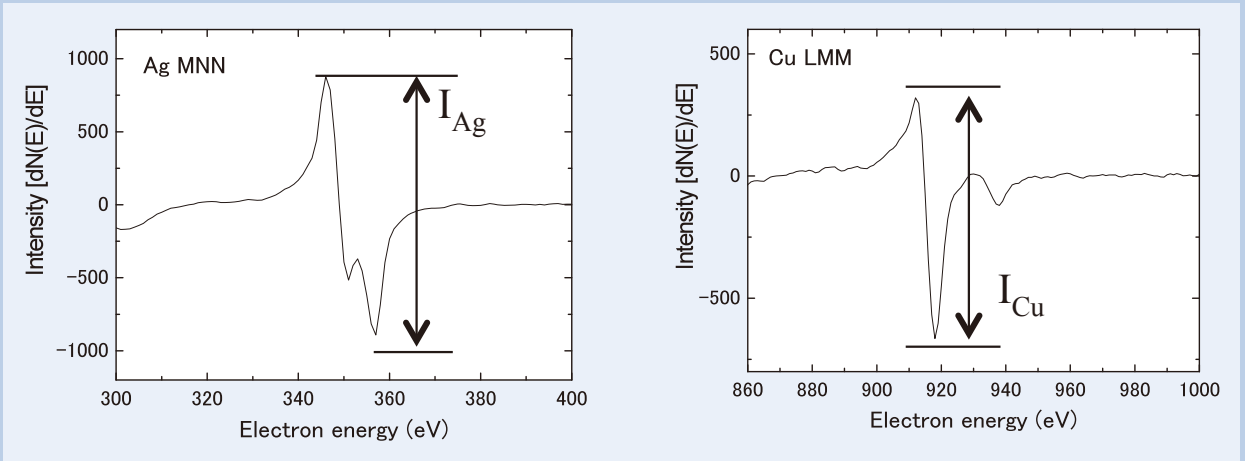

Fig. 10 Definition of peak intensity for the relative sensitivity factor method.

by using the least squares method based on the standard spectra. In this article, we omit to show the detailed calculation method, so please refer to Reference [5] "Peak Deconvolution Analysis in Auger Electron Spectroscopy". An important issue that should be noted here is to surely differentiate the spectra at curve fitting for subtracting the background. In the case of the Auger spectra, the Auger electron itself is one of secondary electrons; therefore, it is impossible to clearly distinguish between the background and the Auger spectra, both of them are contained in the N(E) spectra before differentiation. Execution of differentiation improves the calculation accuracy by simply subtracting the secondary-electron background, thus making it possible to perform curve-fitting calculation focused on the difference of the peak shape.

In Step (3), the absolute intensity quantitative calculation is performed by comparing the intensities of the respective components acquired in Step (2) with the intensities of the standard spectra under the same measurement conditions. Here, **Fig. 11** presents the procedure of the absolute intensity quantification method for the measured spectra of $LiCoO_2$ particles shown in Fig. 1 as an example. Here, a complex oxide of $LiCoO_2$ particles is assumed to be a mixed oxide of Li_2O and Co_3O_4.

Auger spectrum of $LiCoO_2$ particles indicated in Fig. 11 is acquired under the measurement conditions of probe current (10 nA, 10 kV) and energy resolution of 0.5%. With this energy resolution, it is difficult to distinguish the difference of the chemical states due to the Co^{2+} and Co^{3+} because Co spectra have almost the same shape. Thus, it is possible to use CoO or Co_3O_4 as the standard spectra for the absolute intensity quantification method for $LiCoO_2$. Here, the quantitative calculation was performed with the standard spectra of cobalt oxide (Co_3O_4) and lithium oxide (Li_2O).

In the region of 30 to 60 eV where the Li peak is detected, the Co peak is also detected; therefore, when curve fitting is applied using the standard spectra of Li_2O and Co_3O_4, Li_2O components are extracted. The peak intensity at the present measurement is 1078 counts and the peak intensity of the standard spectrum of Li_2O under the same measurement conditions is 3127 counts. This result shows that if the absolute intensity of Li_2O

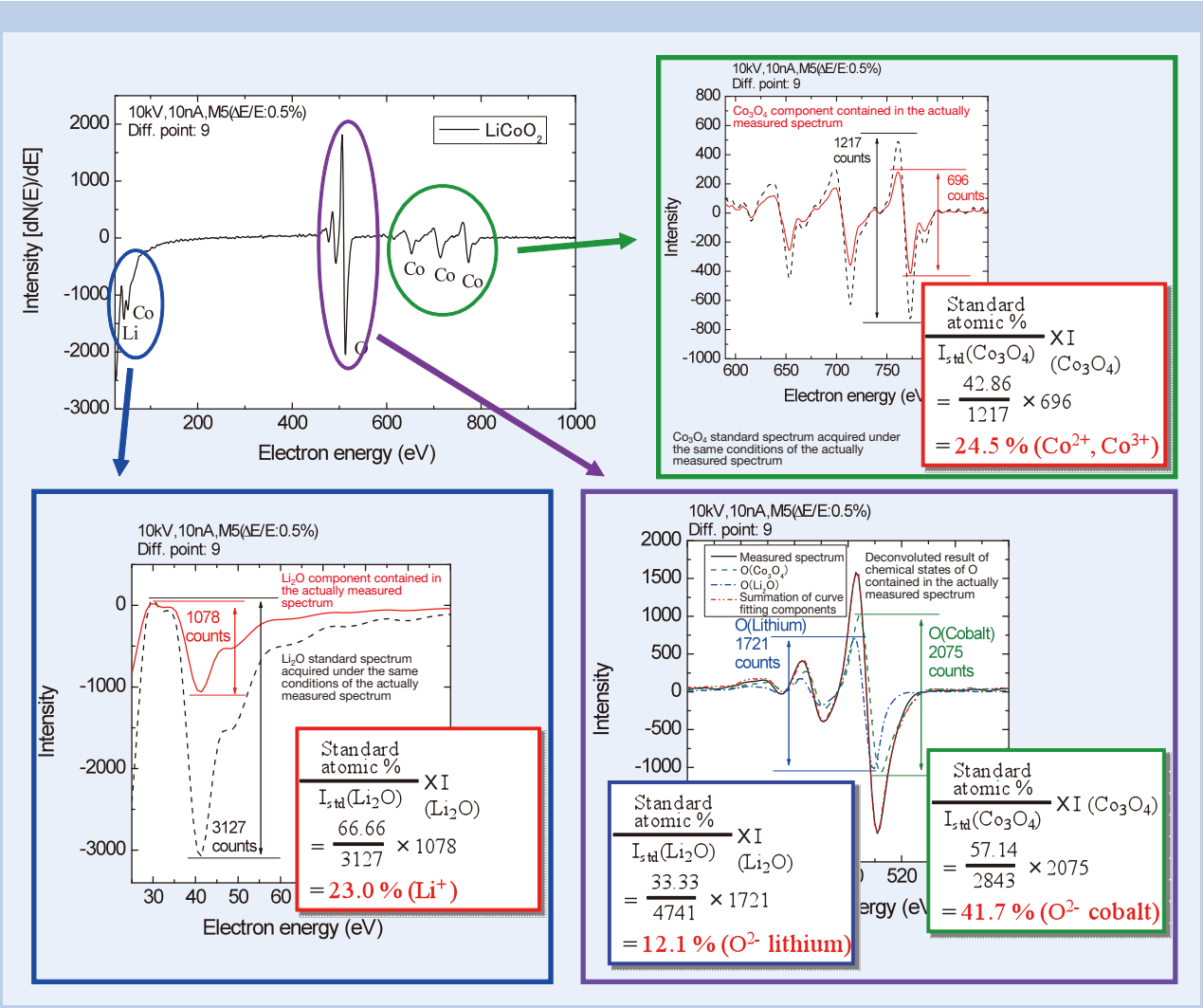

Fig. 11 Absolute intensity quantification method (example of quantitative calculation of the $LiCoO_2$ spectrum in Fig. 1).

components after curve fitting reaches 3127 counts, the intensity equals to 2/3 = 66.66…%, which is the Li atomic concentration of the standard specimen. From this result, the Li concentration measured by the absolute intensity ratio is found to be approximately 23.0%.

Similarly in this case, the energy range of 600 to 850 eV where Co is detected, allows only three peaks of Co to exist, thus the Co atomic concentration is calculated to be approximately 24.5% by comparison with the absolute intensity of the Co_3O_4 standard spectrum.

On the other hand, the O peaks around 470 to 530 eV exist in such a way that the O peak bonded to Li overlaps with the O peak bonded to Co. But the respective peak positions are different and therefore, when the corresponding two standard spectra are subject to curve-fitting calculations, the absolute intensities separated to two components can be obtained. As a result, when the atomic concentrations of the respective components are calculated from the obtained absolute intensity ratio, the concentration of O bonded to Li is calculated to be approximately 12.1%, whereas the concentration of O bonded to Co is obtained to be approximately 41.7%.

Table 2 lists the total atomic concentration and the respective atomic concentrations obtained from the absolute intensity ratio. When we see the total value of atomic concentrations, the total is approximately 100%, indicating that the error is only 1.3%. In the relative sensitivity factor method, the concentrations are inevitably normalized, thus making it difficult to discuss the error about the quantitative calculation result. To the contrary, when the absolute intensity quantification method is used, the obtained total atomic concentration enables the error to be estimated. Furthermore, the atomic concentration ratio among the respective elements is also an important point. The concentration ratio of Li to O bonded to Li is approximately 2:1, thus allowing us to estimate the formation of Li_2O. In addition, the result reveals that $LiCoO_2$ is formed because Li: Co: O (total atomic concentration) equals to 1:1:2.

As we have presented, even if the peaks of the other elements overlap with the target peak like in the case of the Li peak, it is possible to obtain the concentration of the target element by applying the absolute intensity quantification method to the

Table 2 $LiCoO_2$ atomic concentration (%) obtained by the absolute intensity quantification method.

	Li	Co	O (bonded to Li)	O (bonded to Co)	Total
Atomic concentration	23.0	24.5	12.1	41.7	101.3

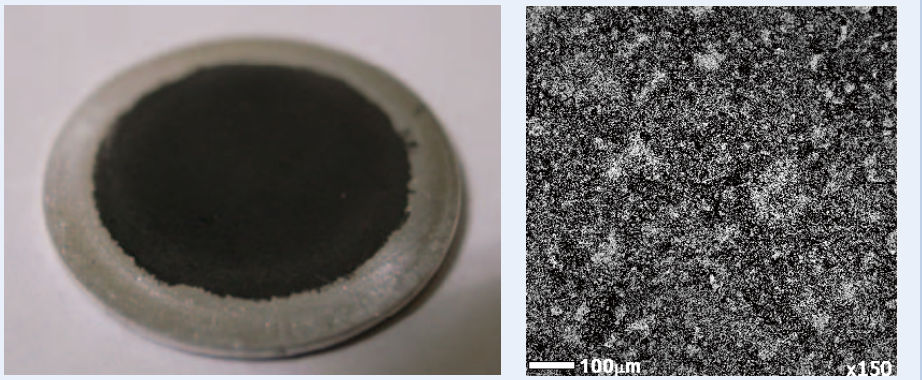

Fig. 12 Li-ion battery powder material molded into a pellet and its backscattered electron image.

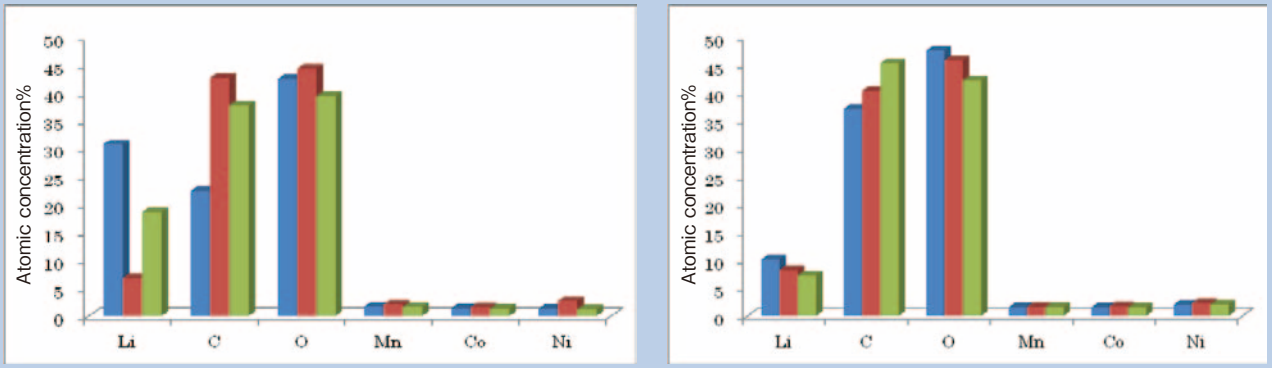

Fig. 13 (Left) Result of quantitative analysis performed by the analysis diameters of arbitrary 3 points set to 100 μm.
(Light) Result of quantitative analysis performed by the analysis diameters of arbitrary 3 points set to 3 mm.

spectra subject to curve fitting calculation.

On the other hand in the case of XPS, when the Li atomic concentration is calculated by the relative sensitivity factor method, a relatively high-accuracy result can be obtained because of the following reasons. The change of the Li spectrum, which depends on the difference of its chemical bonding states, leads only to the shift of the XPS peak as was described in the Section of "Detection and sensitivity of Li". In addition, the quantitative calculation based on the relative sensitivity factor method is applied for the area intensity of the spectra. However, it should be noted that the unevenness of the specimen has to be remind when XPS is used [6]. Also in the case of the powder specimen, there is high possibility that the specimen itself has unevenness.

As is shown in the backscattered electron image in **Fig. 12**, the powder specimen molded into a pellet is found to have an unevenness of approximately 100 μm. But, specimen observation in normal XPS is performed with an optical microscope (OM), thus making it difficult to judge the specimen unevenness which cannot be observed with OM. In such a case, it becomes possible to reduce the influence of the unevenness by sufficiently increasing the analysis diameter. **Figure 13** shows the quantitative analysis results in which quantitative analysis was performed by setting the analysis diameter to 100 μm and 3 mm for the specimen shown in Fig. 12. From Fig. 13, when the analysis diameter is set to 100 μm, it is found that the atomic concentration depends on the analysis position, thus the Li atomic concentration differs greatly. On the other hand, in the case of the analysis diameter of 3 mm, such a difference in the quantification value is not found. Thus, when analyzing the specimen by XPS, it is necessary to take account of the specimen unevenness.

Comparison of Auger analysis of powder material for Li-ion battery with the other analytical methods

In this Section, we introduce actual analysis examples of AES for Li-ion battery powder specimen and compare the AES result with the results obtained by the other analytical methods. A specimen treated in the present Section is an NMC powder specimen (hereinafter called NMC specimen) composed of Mn, Co and Ni equal to 1:1:1 (shown in **Fig. 14**). This specimen was subject to analysis after proper specimen pre-treatment was applied.

First, prior to analyzing the specimen by AES, we used an Energy-Dispersive X-ray Fluorescence Spectrometer (XRF) instrument (JEOL Element Analyzer JSX-3100RII) to examine whether or not the average composition ratio was Mn : Co : Ni = 1:1:1, which was a designated value. In general, in order to examine the average composition of Li-ion battery powder material, ICP-MS (Inductively Coupled Plasma Mass Spectrometry) or ICP-AES (Inductively Coupled Plasma Atomic Emission Spectrometry) based on the wet analysis is mainly used. The wet analysis has a big merit of high quantification accuracy, but also has a demerit that all volume of the specimen needs to be dissolved in a acid solution or an alkali solution and it requires a substantial time for solution adjustment; therefore, it is difficult to treat a number of samples. Thus, in order to examine whether or not the average composition ratio of Mn, Co and Ni in the Li-ion battery powder specimen (except for Li concentration) is correct, the XRF method is efficiently used as a primary screening technique because the XRF analyzer (Element Analyzer) enables us to obtain a high-accuracy quantitative analysis result in only a few minutes. **Figure 15** shows a spectrum acquired by the XRF method and analysis results obtained with this spectrum. The XRF analysis results reveal that the atomic concentrations of Mn, Co and Ni are approximately 13% each and those elements are contained with the ratio of 1:1:1.

Next, the specimen powders were molded into a pellet to measure the concentration of Li that averagely spreads over the surface of the powder specimen. Then, we used a JEOL JPS-9200 based on X-ray Photoelectron Spectroscopy (XPS) for performing top-surface analysis of an NMC specimen. **Figure 16** shows the quantitative analysis result. Compared to the result obtained by XRF, the detected concentration of Ni is higher than those of Mn and Co, and also it is found that as many as 14.8% Li exists at the top surface of the specimen.

Next, in order to analyze the average composition of the specimen surface using AES, we measured the

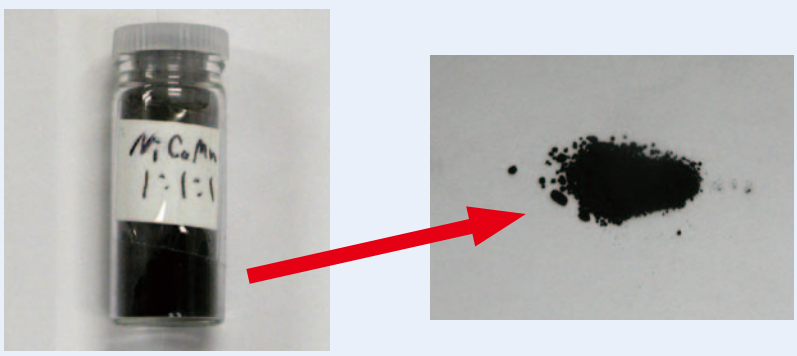

Fig. 14 NMC specimen for Li-ion battery actually used in our experiment (Mn, Co and Ni = 1:1:1).

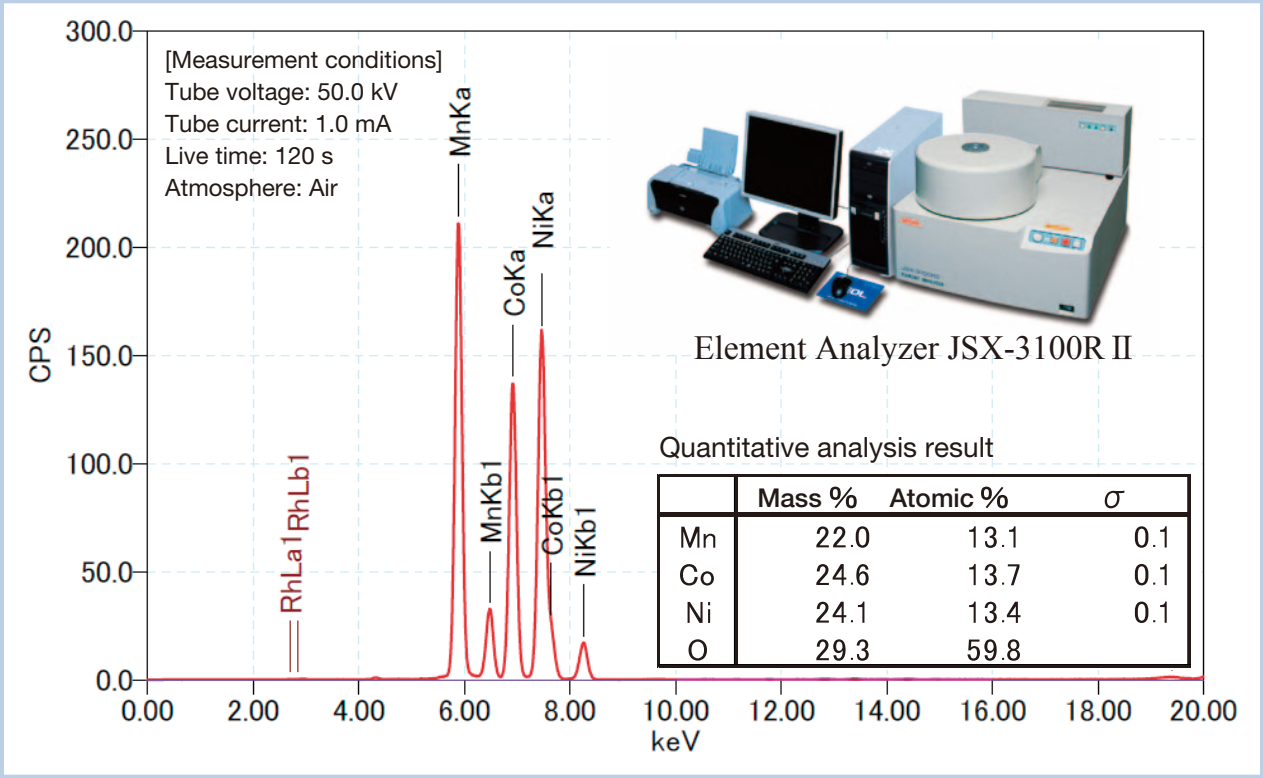

Fig. 15 Quantitative analysis result of NMC specimen acquired by X-ray Fluorescence Spectroscopy (XRF).

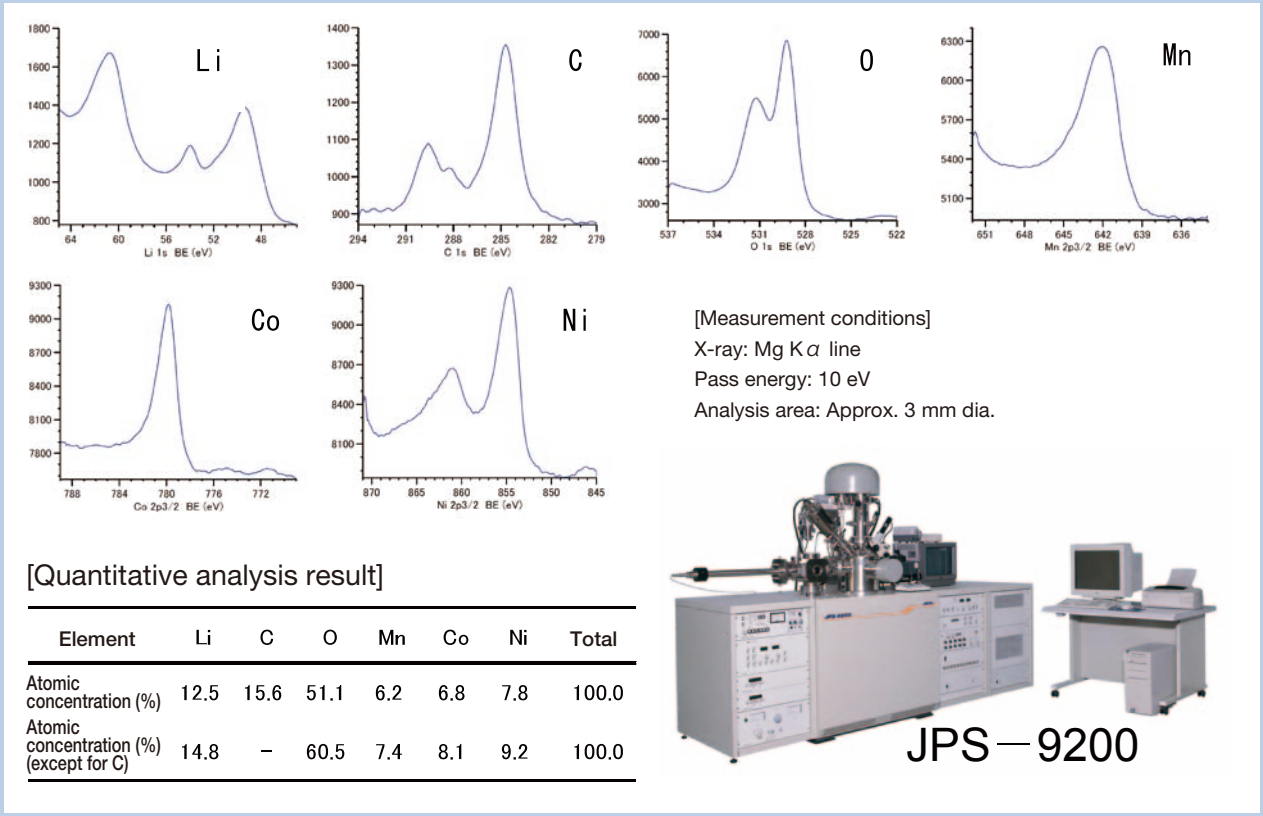

[Quantitative analysis result]

Element	Li	C	O	Mn	Co	Ni	Total
Atomic concentration (%)	12.5	15.6	51.1	6.2	6.8	7.8	100.0
Atomic concentration (%) (except for C)	14.8	–	60.5	7.4	8.1	9.2	100.0

Fig. 16 Quantitative analysis result obtained by X-ray Photoelectron Spectroscopy (XPS).

average spectrum in an area of 50 μm diameter (**Fig. 17**). Figure 17 shows the quantitative analysis result based on the absolute intensity quantification method explained in the Section of Lithium quantification in an average area. In the present result, the total value of each atomic concentration reaches 96.7 %, indicating that the error is approximately 3.3%. As a reference, **Table 3** lists a comparison result of the normalized quantification values obtained by the conventional relative sensitivity factor method and the absolute intensity quantification method, except for C originating from contamination. It is found that the Li concentration obtained by the relative sensitivity factor method is larger than that obtained by the absolute intensity quantification method because the MVV peaks of Mn, Co and Ni overlap with the Li peak.

When comparing the quantitative analysis results of XPS (Fig. 16) with AES (Fig. 17), the difference in the C concentration is remarkable. This may be due to the difference of the analysis area between XPS and AES. When the average atomic concentrations in a large area are analyzed, XPS is more advantageous because XPS can analyze a large area and this method is not likely to be influenced by localized contamination. On the other hand, AES aims to analyze a local area in principle and the analysis area is confined to several 100 μm squares at a maximum due to the input lens system. In the present experiment, we randomly measured an area which was considered to have average composition. But incidentally, an area containing many organic

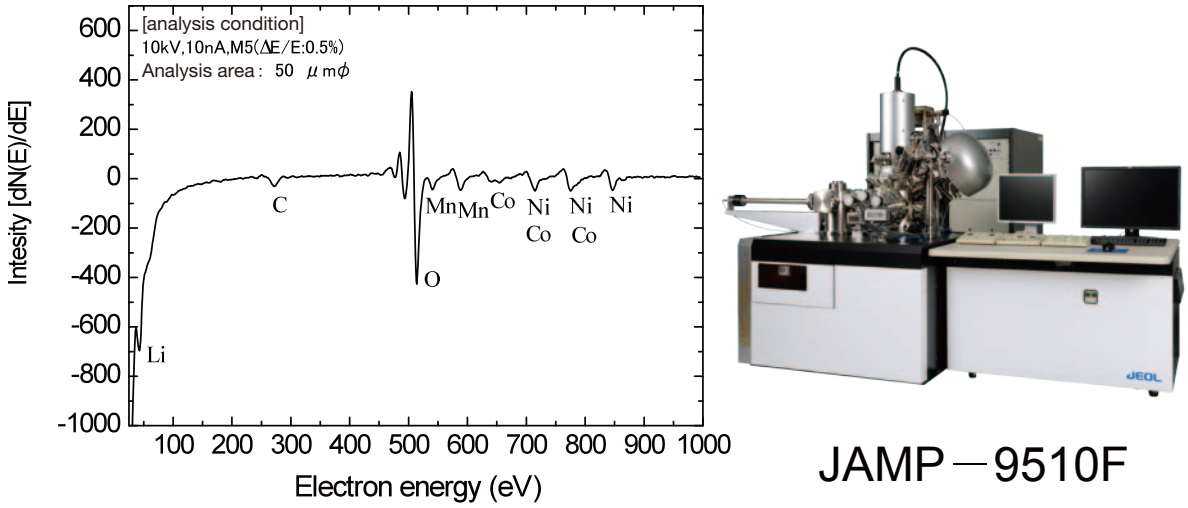

[Absolute intensity quantification result]

Element	Li	C	O	Mn	Co	Ni	Total	
Atomic concentration (%)	13.2	29.2	37.2	5.7	5.7	5.7	96.7	← Total of atomic concentrations (error: 3.3%)
Atomic concentration (%) (except for C)	19.6	–	55.0	8.5	8.5	8.4	100.0	← Normalized atomic concentration except for C

Fig. 17 Quantitative analysis result obtained by AES for NMC specimen (using the absolute intensity quantification method).

Table 3 Comparison of quantification values in AES for NMC specimen obtained by the absolute intensity quantification method and the conventional relative sensitivity factor method (normalized except for C).

Element	Li	O	Mn	Co	Ni	Total
Atomic concentration (%) obtained by the absolute intensity quantification method	19.6	55.0	8.5	8.5	8.4	100.0
Atomic concentration (%) obtained by the relative sensitivity factor method	35.4	51.7	5.9	3.4	3.6	100.0

(except for C)

substances was analyzed, thus the C concentration was considered to be high. When comparing the normalized quantification values of AES and XPS, which were obtained by the absolute intensity quantification method and excluded C element, the quantification values of the respective atomic concentrations in AES are close to those in XPS, and for Li, the difference between AES and XPS is confined to approximately 5%. Consequently, when quantification of Li is performed using AES, we recommend the use of the absolute intensity quantification method because this method enables higher accuracy quantitative analysis.

Next, as we introduced in the Section of "Pre-treatment technique and precautions for powder specimen at Auger analysis", we show the observation result of a secondary electron image (SEI) of an NMC specimen sprayed on a carbon-specimen stub in **Fig. 18**.

Figure 18 reveals the existence of many particles with different size and also, foreign particles that are confirmed to be organic substances. For convenience of analysis, particles with large diameters were defined as "point-1", those with small diameters as "point-2", and foreign particles as "point-3". Auger spectra for point-1 to point-3 are shown in Fig. 18. From the results, it was discovered that the atomic concentration ratio of Mn, Co and Ni was different between "point-1" and "point-2", and also the Li concentrations among the two points quite differed. In "point-3", no Li was detected, therefore, the powders in this area are considered to be only foreign materials. Generally, a large volume of such foreign particles are mixed in the Li-ion battery powder specimen. The present observation of SEI (secondary electron image) and BEI (backscattered electron image) accounts for the fact that a quantification value of high C concentration is obtained depending on the analysis area as shown in Fig. 17. Thus, in the case of the Li-ion battery powder specimen, the analysis results of XPS which averagely cover a wide area might be different from that of AES which performs local area analysis. Taking this fact into consideration, only either XPS or AES does not provide sufficient data for quantitatively analyzing the specimen more accurately. That is, it is necessary to obtain the data from the average area and the data from the local area for comprehensive judgment on the analysis results of the specimen.

After this experiment, we prepared a cross section of an NMC specimen with a JEOL Cross Section Polisher (CP) and performed analysis (**Fig. 19**).

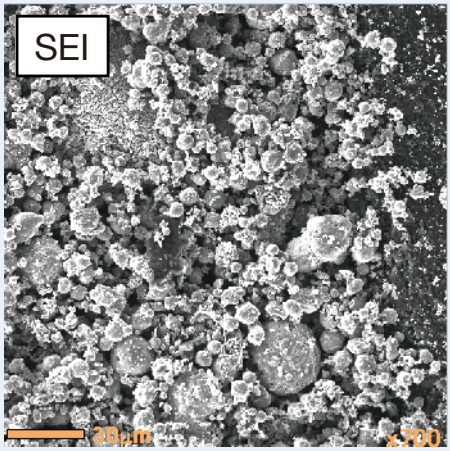

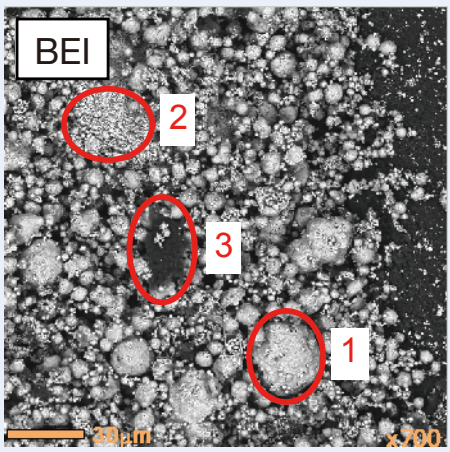

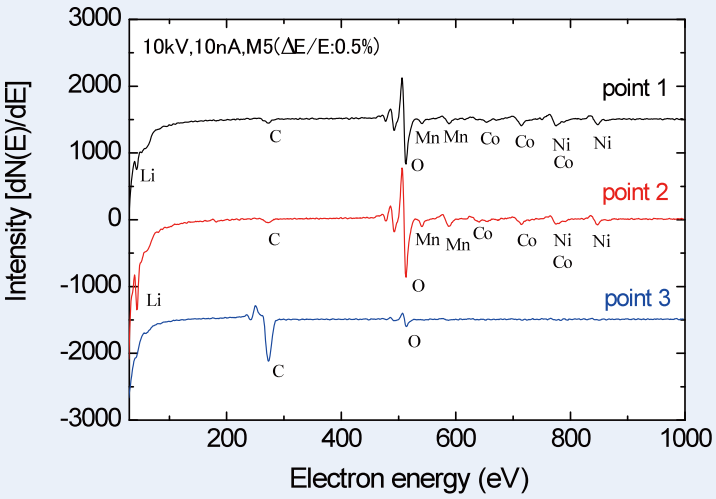

[Absolute intensity quantification result]
(atomic concentration: %)

Element	Li	C	O	Mn	Co	Ni	Total
Point 1	6.4	11.8	50.9	7.5	9.9	9.7	96.2
Point 2	16.4	11.2	49.4	12.0	6.4	9.5	104.9

Fig. 18 NMC powder specimen for Li-ion battery (containing Mn, Co and Ni). [at 10 kV, 10 nA, Magnification: ×700]

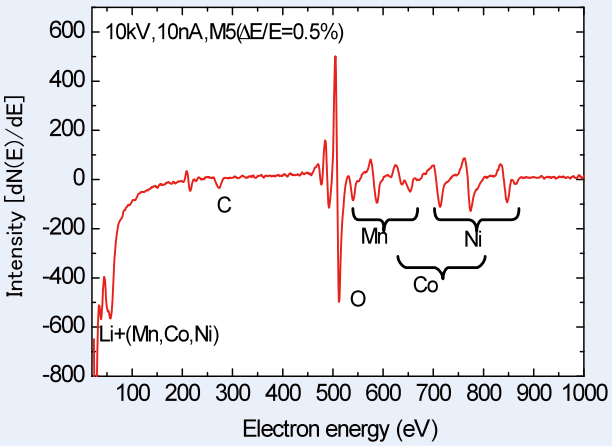

[Absolute intensity quantification result]

Element	Li	C	O	Mn	Co	Ni	Total	
Atomic concentration (%)	4.8	5.9	50.4	12.7	13.5	12.3	99.6	← Total of atomic concentrations (error: 0.4%)
Atomic concentration (%) (except for C)	5.1	–	53.8	13.6	14.4	13.1	100.0	← Normalized atomic concentration except for C

Fig. 19 AES spectrum measured from the NMC powder cross section and the absolute intensity quantification result of the cross section.

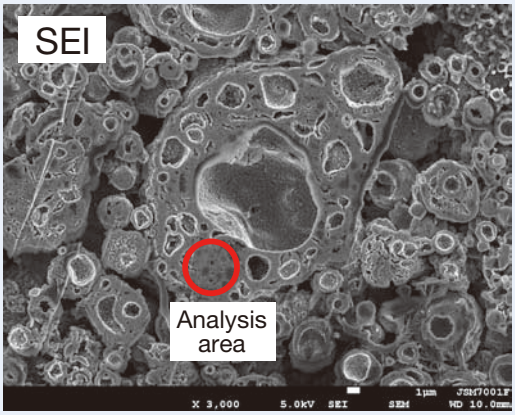

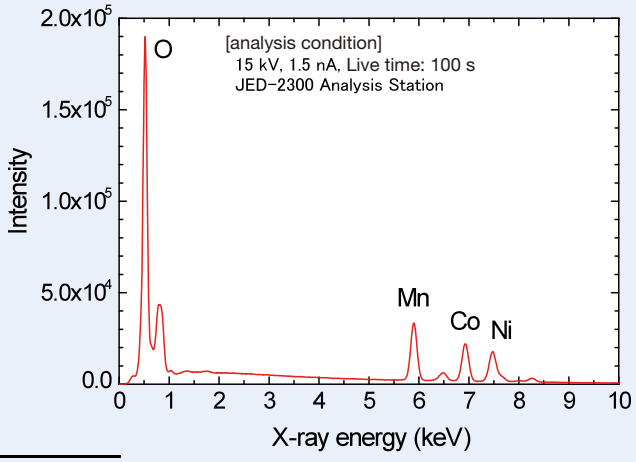

[Absolute intensity quantification result]

Element	O	Mn	Co	Ni	Total
Mass concentration (%)	33.8	19.8	23.2	23.2	100.0
Atomic concentration (%)	64.8	11.0	12.1	12.1	100.0

Fig. 20 Quantitative analysis results of NMC specimen obtained with SEM-EDS.

Table 4 Comparison of quantitative analysis results obtained with various analysis instruments.

Surface analysis (Atomic concentrations except for C are normalized.)

	Li	O	Mn	Co	Ni
AES	19.6	55.0	8.5	8.5	8.4
XPS	14.8	60.5	7.4	8.1	9.2

Bulk analysis (Atomic concentrations except for C are normalized.)

	Li	O	Mn	Co	Ni
AES	5.1	53.8	13.6	14.4	13.1
SEM-EDS	–	64.8	11.0	12.1	12.1
XRF	–	59.8	13.1	13.7	13.4

In order to prepare the cross section of a powder including Li such as Li-ion battery material for AES, several precautions need to be taken. Firstly, in order to prevent the diffusion of Li, the use of the carbon-specimen stub is a must to fix the powders (instead of the use of resin). Secondly, in order to preserve the specimen state in the powder specimen, a cross-section fabrication device must be used. Typically used devices are a CP or an Ion Slicer. These tools mill the specimen with inert gas ions which does not chemically react with the elements in the powder specimen. Thirdly, in order to prevent alteration of properties on the cross-sectioned surface, a Transfer Vessel is used, which can preserve and transfer the specimen without exposing the specimen to the air. In particular, since an AES performs elemental analysis and chemical state analysis of the specimen top surface (only a few nanometers down to the surface), much care is required.

A secondary electron image (SEI) in Fig. 19 reveals that the particles in the specimen have porous-like structures. Some Li-ion battery powder materials possess such porous-like structures in the particles (shown in Fig. 19) at the process where raw material particles are mixed and fired. CP can mill a cross section of particle even including a porous-like structure. Thus, CP is powerful and suitable for the analysis of such Li-ion battery powder materials. We acquired an Auger spectrum for an area enclosed with a red circle in Fig. 19 and performed the quantitative analysis based on the absolute intensity quantification method. As a result, it was found that Mn, Co and Ni exist with a ratio of approximately 1:1:1 and when converting the result into the atomic concentration except for C, the resultant concentration becomes approximately 13 to 14%. These concentration values are close to those obtained by XRF in Fig. 15, thus the values are considered to indicate the atomic concentrations of the particles.

Next, as is shown in an SEI in **Fig. 20**, SEM-EDS analysis was performed for the same area measured with AES shown in Fig. 19. The analysis results are indicated in the table in Fig. 20. Compared to the quantification result of AES, it is found that difference of the atomic concentrations between Mn, Co and Ni is only 2%; thus indicating the same values to each other.

The quantitative analysis results are summarized in **Table 4**. For both the surface analysis and the bulk analysis, the results obtained by AES, which are based on the absolute intensity quantification method, demonstrate high accuracy in comparison with the other analysis methods. That is, the difference in the atomic concentrations of Mn, Co and Ni is confined within approximately 2% and also, the error in the quantification value of Li is estimated to be a few %. Thus, it should be emphasized that the absolute intensity quantification method provides substantial accuracy for the quantitative analysis of Li, and the use of AES will be applied to various purposes for investigation of Li-ion battery powder material, from local area analysis to the average area analysis.

Conclusions

Nowadays, vigorous development of Li-ion battery is carried out by researchers around the world and a large number of reports have been issued. Under this circumstance, knowledge about Li behaviors and Li distributions with various chemical states at a local area in the Li-ion battery is strongly demanded, which are the basics of the development of their electrical properties. AES and XPS are only a few methods that can meet those needs. Those methods enable us to detect and quantify Li. Furthermore, commercially available AES instruments can perform mapping in a nano-area. However especially for AES, there exists misunderstanding that it is difficult to analyze Li, thus the AES instrument are not used very much for such purposes.

As the authors introduced in this article, the analysis of Li by AES is very effective like the analysis by XPS. These two instruments can detect Li with high sensitivity. In addition, when using the absolute intensity quantification method, AES enables one to obtain reliable quantitative analysis results comparable to the other analysis methods. Sufficient utilization of AES and XPS can complement the data obtained with instruments that cannot directly measure Li (TEM, SEM, EPMA, XRF, etc.). By the use of overall data with such analytical methods, the authors will expect Li distributions and Li behaviors to be revealed.

References

[1] Tsutsumi, K. ; Applications of AES for development of Li ion batteries and CIGS solar-cells , 2009 JEOL EPMA/Surface Analysis Users' Meeting document, AP100 (2009) (in Japanese).

[2] Shima, M. ; Sample Preparations and Analysis techniques of XPS of non-conductive particles, 2006 JEOL EPMA/Surface Analysis Users' Meeting document, XP41 (2006) (in Japanese).

[3] Shima, M. ; Chemical state analysis by XPS for materials in Li ion batteries 2010 JEOL EPMA/ Surface Analysis Users' Meeting document, XP45 (2010).

[4] Tsutsumi, K., Shima, M., Tanaka, A., Tazawa, T. ; Quantitative Chemical State Analysis of Tin Oxides (Sn, SnO, SnO_2) with High – Energy Resolution AES, *J. Surf.Sci. Soci. Japan*, **Vol. 33**, **No. 8**, pp. 431-436, (2012) (in Japanese).

[5] Tsutsumi, K. ; Peak Deconvolution Analysis in Auger Electron Spectroscopy, *JEOL news*, **Vol.37, No. 1**, p66 (2002).

[6] Shima, M. ; Importance of Average Large Area Analysis in XPS; oversight problems in micro area analysis, 2012 JEOL EPMA/Surface Analysis Users' Meeting document, AP92 (2012) (in Japanese).

Characteristic Features and Applications of a Newly Developed Wavelength Dispersive Soft X-ray Emission Spectrometer for Electron Probe X-ray Microanalyzers and Scanning Electron Microscopes

H. Takahashi[*1], T. Murano[*2], M. Takakura[*2], N. Handa[*3], M. Terauchi[**], M. Koike[***], T. Kawachi[***], T. Imazono[***], N. Hasegawa[***], M. Koeda[****], T. Nagano[****], H. Sasai[****], Y. Oue[****], Z. Yonezawa[****] and S. Kuramoto[****]

[*1] Global Business Promotion Division, JEOL Ltd.
[*2] SA Business Unit, JEOL Ltd.
[*3] Advanced Technology Department, JEOL Ltd.
[**] Institute for Multidisciplinary Research for Advanced Materials, Tohoku University
[***] Quantum Beam Science Directorate, Japan Atomic Energy Agency
[****] Optical Components BU Device Department, SHIMADZU Corp.

A new wavelength dispersive soft X-ray emission spectrometer (WD-SXES) consisting of a pair of newly designed varied-line-spacing gratings: JS50XL and JS200N, X-ray focusing morrors and a detector of a charge-coupled device has been developed for soft X-ray emission spectroscopy. This WD-SXES, which covers nominally the X-ray energy range between 50 and 210 eV, has successfully been installed for commercial use to electron probe X-ray microanalyzers and scanning electron microscopes. The high energy resolution Spectrum mapping software has been developed using a parallel detection system. The observed area is flexibly applied from micron square to 9 × 9 cm^2.

The energy resolution of this WD-SXES was evaluated to be 0.2 eV from the Fermi edge of the Al-L spectrum. The Li-K and Li-satellite-K emission spectra due to lithium metal and lithium fluoride were observed for the first time in EPMA. The detection limit of lithium was estimated in a 5 mass% Li-Al alloy to be 40 ppm in mass. The Li-K and Li-satellite-K emission spectra from samples of a lithium ion battery anode were measured and mapped in an area as large as 30 × 80 mm^2 under three different charging conditions. A clear distinction in spectra due to chemical states of lithium shows a high potential for the characterization of lithium ion battery anodes.

For the trace element analysis of boron, carbon and nitrogen in steel, their linear calibration curves could successfully be obtained in the composition range between 10 and 100 ppm in mass. This method could detect their concentrations as small as 10 ppm in mass. The trace element analysis of light elements in other materials than steel could possibly be performed at this level of concentrations.

Effects of compiling spectra obtained with the WD-SXES are described for fulfilling the need for comparing observed spectra with the ones compiled to identify the chemical state.

1. Introduction

A new wave-length dispersive spectrometer (WDS) to detect ultra-soft X-rays for soft X-ray emission spectroscopy (SXES) has first been designed and developed for transmission electron microscope (TEM) by Terauchi et. al. [1] This spectrometer may be called a wavelength dispersive soft X-ray emission spectrometer (WD-SXES). It consists of an aberration-corrected, concave, varied-line-spacing grating as a wavelength dispersive element, X-ray reflection mirrors and a charge-coupled device (CCD) as a detector. Terauchi and his group have successfully made a series of investigation on chemical structures of valence electrons in light elements and their compounds with this WD-SXES installed to a TEM [2, 3, 4]. Encouraged by

2-1-1 Ohtemachi, Chiyoda-ku, Tokyo 100-0004, Japan.

E-mail: takahash@jeol.co.jp

their success, we have developed a new WD-SXES installed to electron probe X-ray microanalyzers (EPMAs): JXA-8100, JXA-8500F, JXA-8230 and JXA-8530F and two scanning electron microscopes (SEMs): JSM-7800F and JSM-7100F as shown in **Fig. 1**. Characteristic features and a few applications of the WD-SXES installed to EPMAs and SEMs are briefly reported in this paper.

2. Characteristic features

Soft X-ray emission spectroscopy (SXES) has an inherent difficulty due to low efficiency of the soft X-ray emission and detection. This difficulty met in TEM-SXES can partly be overcome by installing the WD-SXES to EPMAs, which have a capacity producing far larger probe currents. In fact, the acquisition condition parameter (AQ) defined as the beam current times the acquisition time is usually expressed as a unit of nA-min for TEM whereas as a unit of μA-min for EPMA. One other difference in the acquisition conditions between TEM- and EPMA-SXES is the accelerating voltage of the electron probe. It was so far fixed at 100kV for TEM-SXES [2] whereas it can be varied at a few kV for EPMA-SXES. One of the intensity measurements of accelerating voltage dependence of soft X-ray emission spectra is shown in **Fig. 2**. In this figure, the AL-L spectrum was measured with a probe current of 100 μA for measuring time of 60 s at six accelerating voltages: 1, 2, 3, 5, 10, 15 and 20 kV. The optimum value for the Al-L spectrum was experimentally determined to be 5 kV. In the following, the accelerating voltages were selected to be a few kV depending on the spectra.

The two varied-line-spacing gratings: JS50XL and JS200N have been developed for all of TEM, EPMA and SEM. Nominally, the former JS50XL covers the X-ray energy range between 50 and 170 eV whereas the latter JS200N between 70 and 210 eV. Experimentally the energy range of JS50XL can be extended down to 46 eV. The both gratings have been set in one channel as a pair in EPMAs and SEMs so that the WD-SXES for EPMAs and SEMs covers the X-ray energy range between 50 and 210 eV. In this energy range, spectra such as Li-K (54 eV), Al-L(72eV), Si-L(92eV), P-L(119eV) and B-K (182eV) are located. Because the varied-line-spacing grating is used as a wavelength dispersive element, the X-rays with higher energy than the one in the range previously described can also be detected as the higher order spectra so that the energy range up to 700 eV can practically covered, In the case of the K emission, C (277 eV), N (392 eV), O (525 eV) and F (677 eV) can be well detected. L emission spectra of Ti, V, Cr, Mn and Fe, and M emission spectra of Zr, Nb, Mo, Ag, Cd, Sn and Sb, can be also observed. N emission spectra of Hf, Ta, W, Re, Pt, Au, Bi, a few Lanthanides such as U, can successfully be observed quite recently.

One other characteristic feature of the WD-SXES is robustness of the system and easiness of data acquisition. The varied-line-spacing grating and CCD detector are both set rigidly without any movable part, resulting in an excellent reproducibility. Furthermore, spectra within the covered energy range by the wavelength dispersive elements can be measured and acquired simultaneously, just like ordinary energy dispersive spectroscopy. This parallel detection of spectra enables to acquire a spectrum map from which elemental maps and chemical state maps can be drawn.

The size of area of analysis ranges from nanometer to micrometer in diameter in TEM. It becomes three orders of magnitude larger from micrometer to millimeter in EPMA and SEM. When the scanning stage is used in EPMA, the area as larger as 90 × 90 mm^2 can be analyzed. The installment of WD-SXES to EPMAs and SEMs makes SXES serve not only as a method of fundamental research on the chemical structure of valence electrons in elements and compounds but also as a method of the characterization of functional

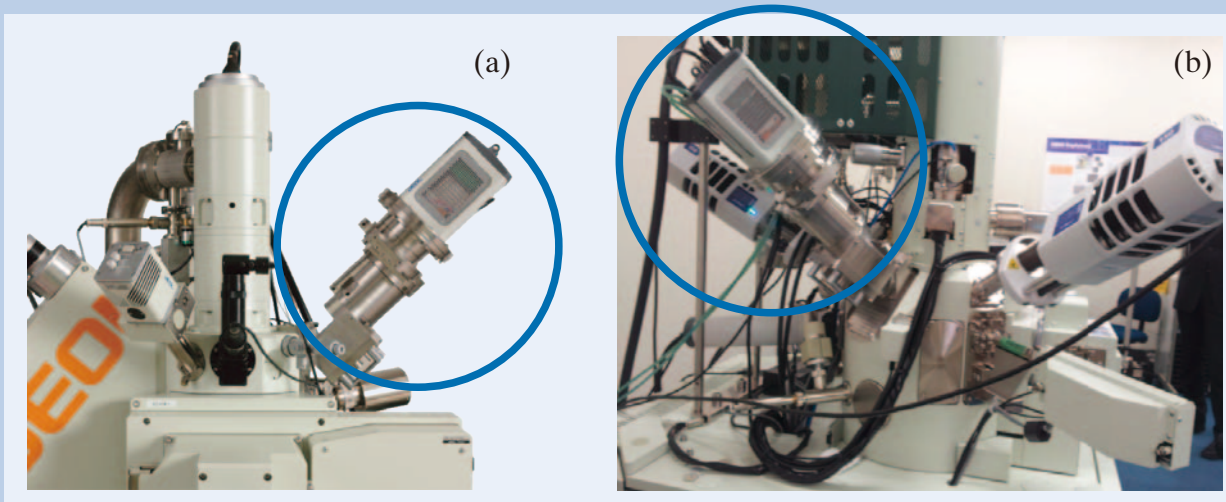

Fig. 1 External views of the wavelength dispersive soft X-ray emission spectrometer attached to EPMAs: JXA-8230 (a) and SEM: JSM-7800F (b).

materials. The latter method has a potential for being extended to quality control of functional materials in industrial products.

3. Applications

3-1. Emission Spectra of Lithium and Lithium Compounds

3-1-1. Li-K emission spectrum of lithium metal and Li-satellite- K peak obtained from lithium fluoride

Figure 3 (a) shows a Li-K emission spectrum obtained from lithium metal. This spectrum was acquired under the following condition; five different positions were measured with a probe current of 0.1 μA at an accelerating voltage of 15 kV; the measuring time at one position was 30 s so that the total time of the measurement for the spectrum was 150 s; AQ was 0.25 μA-min. The extension of the detection range down to 50 eV made the Li-K emission spectrum fully observed with its peak around 54 eV. This Li-K emission spectrum due to lithium metal was the first one observed in EPMA.

Figure 3 (b) shows a spectrum obtained from lithium fluoride in the same energy range as the one in Fig. 3(a). At present, we have not succeeded to observe a genuine Li-K spectrum due to lithium fluoride. No appreciable intensity peak was observed in the energy range shown in Fig. 3 (b) under a condition of a broad beam with a size of 30 μm in diameter even after 30 s. But once the beam was focused, the spectrum shown in Fig. 3 (b) started to be observed. Its acquisition condition was the same as the one in Fig. 3 (a), except the accelerating voltage decreased to 5 kV. In addition to the spectrum due to the Li-K emission shown in Fig. 3 (a), it shows a Li-satellite-K peak was used to monitor chemical state of lithium in a lithium ion battery anode in the following section.

3-1-2. Li-K and Al-L emission spectra of a 5mass% Li-Al alloy (Energy resolution and detection limit)

Figure 4 shows a soft X-ray emission spectrum of a 5 mass% Li-Al alloy in an energy range between 47 and 100 eV. The spectrum was acquired under the following condition, which is also shown in the figure; five different positions were measured with a probe current of 2 μA at an accelerating voltage of 5kV; the measuring time at one position was 60 s so that the total time of the measurement for the spectrum was 300 s. Under this condition, AQ was 10 μA-min. At a higher energy range around 70 eV, the Al-L emission spectrum was beautifully observed and at a lower energy range around 54 eV, the Li-K emission spectrum was also observed. Because the peak of the latter spectrum was small, an enlarged spectrum is shown at the bottom left of in the figure. The Al-L emission spectrum shows a sharp edge corresponding to the Fermi-edge (E_F) at the highest energy of the peak. The energy resolution was evaluated to be 0.2 eV from this portion of the spectrum. The left side of the profile from the Fermi-edge corresponds to the density of state of valence band. From the spectrum

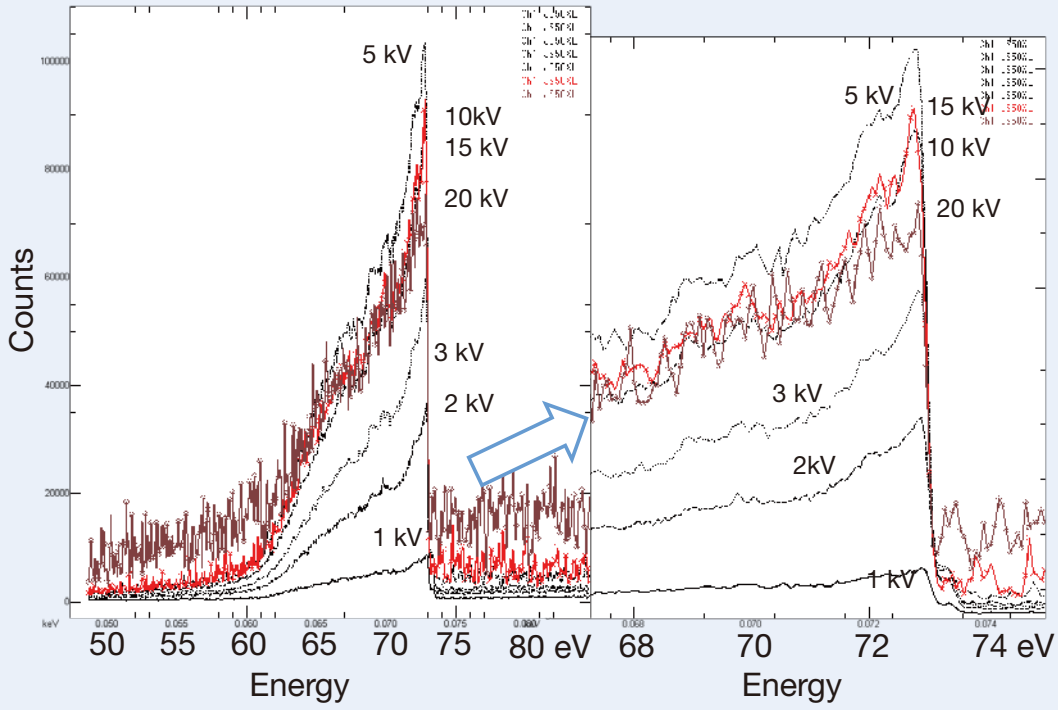

Fig. 2 The Al-L spectra measured for a time of 3 x 30 s with a probe current of 0.3 μA at five different accelerating voltages; 2, 3, 5, 10 and 15 kV.

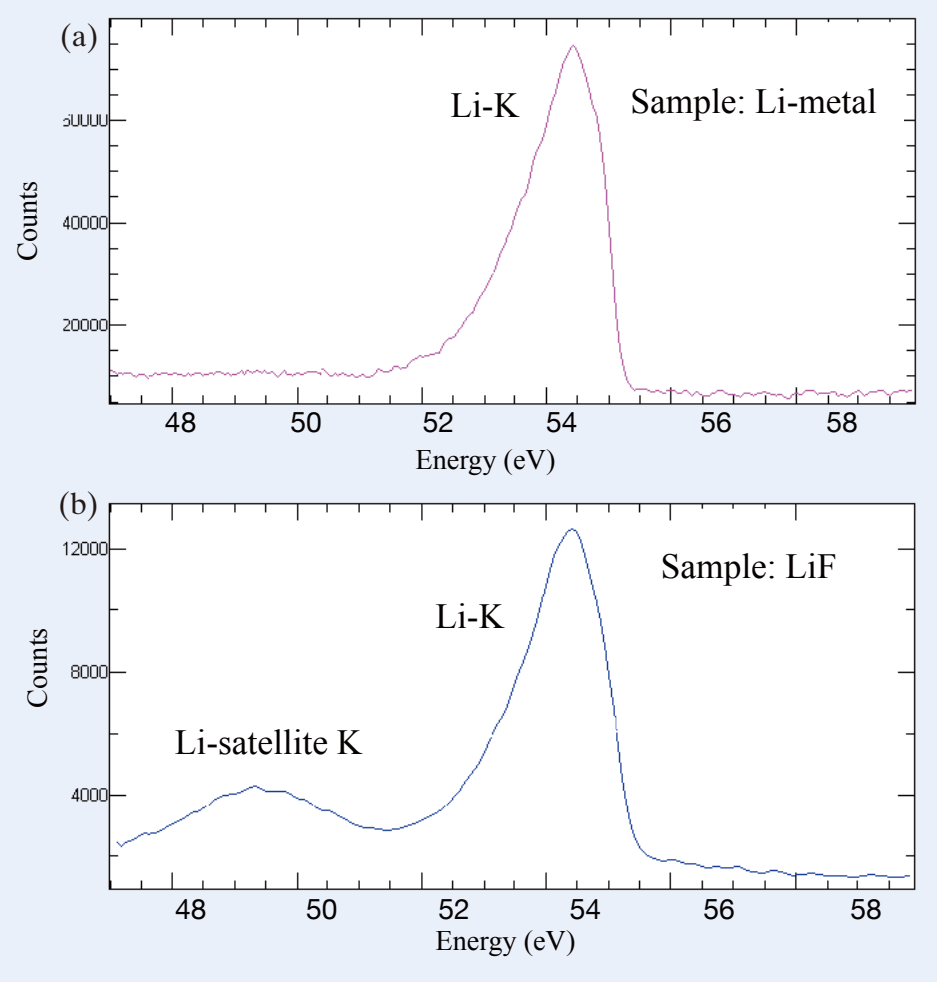

Fig. 3 (a) Li-K emission spectrum of Li metal and (b) Li-satellite-K and Li-K emission spectra from LiF.

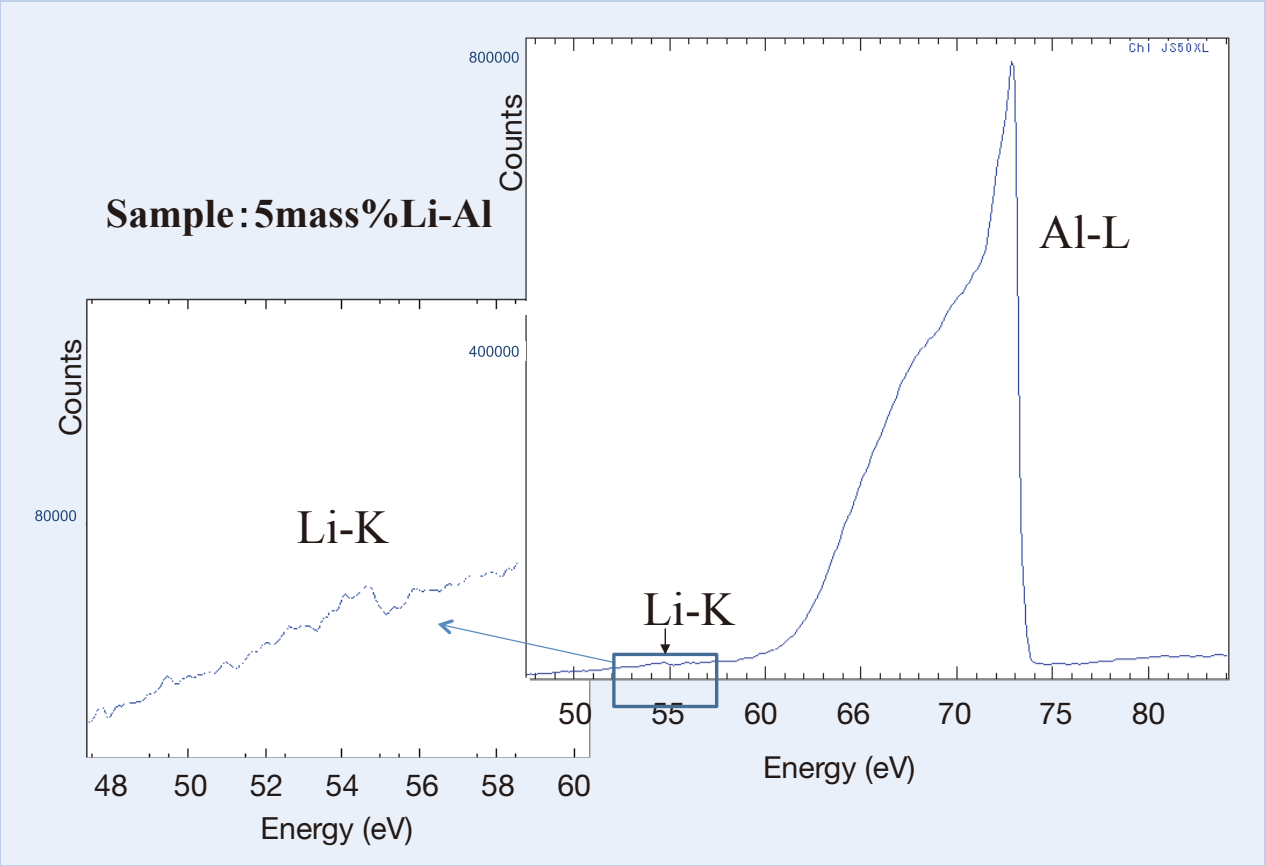

Fig. 4 A soft X-ray spectrum of 5mass%Li-Al alloy in an energy range between 47 and 100 eV.

intensity of the Li-K emission, the detection limit (C_{DL}) of lithium was estimated to be 40 ppm in mass based on the following equation:

$$C_{DL} = \frac{\sqrt{2} \times C}{\sqrt{P \times \frac{P}{B} \times t}}$$

where P and B are peak and background intensities (counts/s), t is time (s) and C is the concentration of the element [5].

3-1-3.Change of chemical states of lithium due to charging in a Lithium-ion battery anode

Three samples A, B and C of a lithium-ion battery anode with different charging conditions: 0% (A). 30% (B) and 100% (C), were supplied as sealed separately in three glove bags filled with Ar gas. They were transferred to a sample holder in a glove-bag type of wrapper filled with Ar gas, which covered both the sample holder and the insertion chamber of the EPMA as shown in **Fig. 5** (a). Though cumbersome, this precaution was necessary to avoid chemical reactions of the sample surface in the ordinary atmosphere. The three samples, each of which had a length of 50 mm and a width of 30 mm, were mounted to the sample holder side by side as shown in Fig. 5(b). A large area with a size of 16 × 50 mm^2 was selected for mapping of chemical state of lithium. The area consisted of A, B anb C was divided into 50 × 10 pixels so that the interpixel distance was 1.0 mm in the length direction and 1.6 mm in the width direction. The intensities of soft X-rays emitted by an electron probe with a diameter of 1 μm with a current of 0.8 μA at an accelerating voltage of 2 kV was acquired for 60 s/pixel in an energy range between 48 and 165 eV. Three maps constructed by using the X-rays in three energy ranges corresponding to Li-satellite-K (49 - 51 eV), Li-K (53 - 55.5 eV) and C-K of the 4th order (nominally 66 - 70 eV) are shown in **Fig. 6.** The map due to the Li-satellite-K on the left hand side apparently corresponded to the amount of charging; the intensity of Li-satellite-K emission increased with the increase in the amount of charging. The map in the middle in Fig. 6 indicated that the metallic lithium formed locally and distributed heterogeneously under the fully charged condition. The map due to C-K of the 4th order on the right hand side in Fig. 6 indicated the intensity distribution due to graphite; one other important constituent of the anode. Under the fully discharged condition, the intensity was strongest. When the amount of charging increased by 30%, it decreased substantially. But it stayed the same level, even though the amount of charging increased to 100%.

Three typical spectra corresponding to the three different conditions were shown in **Fig. 7**. Figures

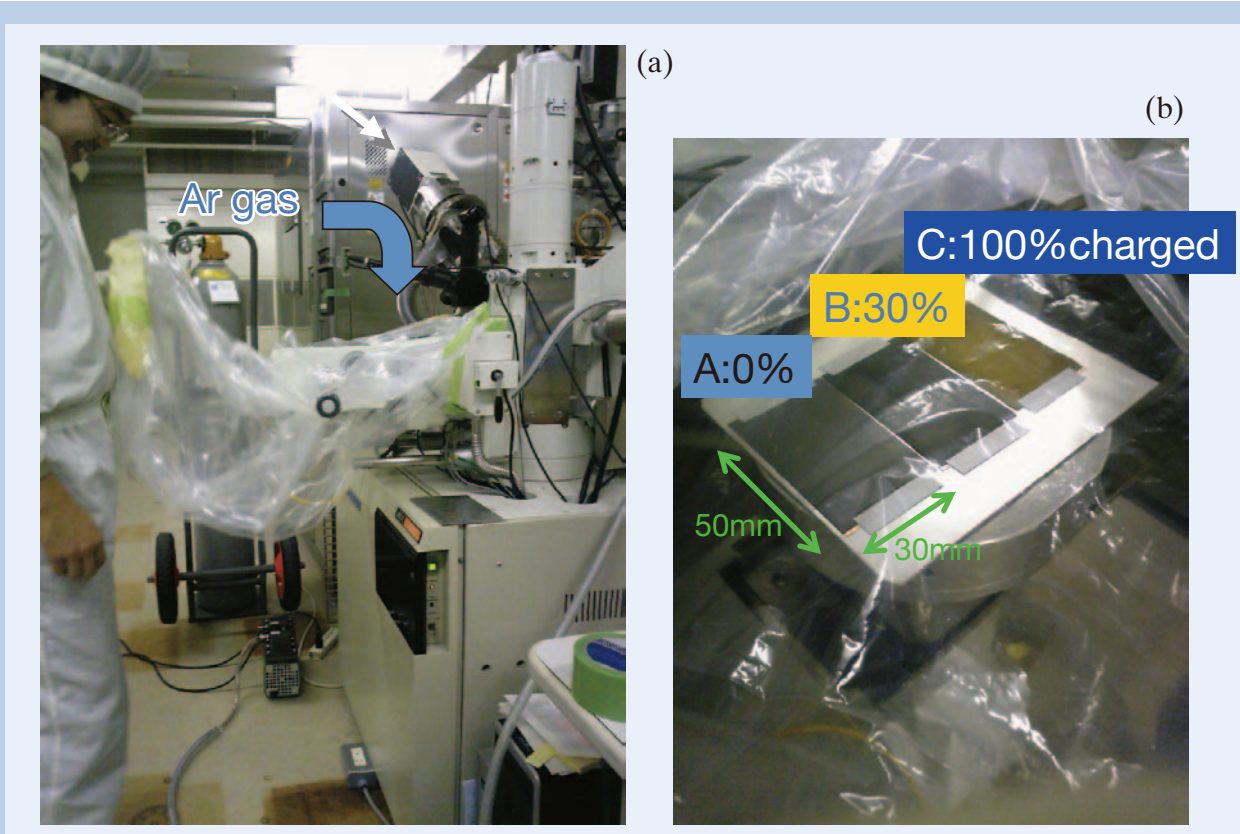

Fig. 5 Two important steps are illustrated in a procedure for transferring the samples of a lithium-ion battery anode to and mounting them on a sample holder of the EPMA. (a) Both the sample holder and the insertion chamber were covered with a wrapper to avoid the direct contact of the sample surface to the ordinary atmosphere. (b) The three samples with different amounts of charging were mounted on the sample holder side by side.

7(a) and 7(b) show the spectra in one energy range between 48.5 and 59.5 eV and in the other energy between 62 and 74.5 eV, respectively. The former energy range covered the Li-satellite-K and Li-K emission with overlapped C-K of the 5th order, whereas the latter C-K of the 4th order. They were visually selected from the typical pixels observed in the three maps shown in Fig. 6. As shown in Fig. 7(a), the Li-satellite-K and the Li-K were not observed in the fully discharged anode, whereas the Li-satellite-K was observed in the charged anodes at around 50 eV and the Li-K was clearly observed in the fully charged anode. The change in the intensity of the C-K the 4th order shown in Fig. 7(b) was the same as explained in Fig. 6. One thing to be noticed was the observed shoulder around 69.5 eV due to the π bond in the profile of the fully charged anode.

3-2. Trace element analysis of nitrogen in steel

The WD-SXES has a very high potential for analyzing trace elements in steel. Slightly extra endeavor and precaution extend the range of trace element analysis to the lower concentrations. In the ordinary EPMA, the calibration method is usually used in lower concentration ranges which need a series of reliable standard specimens. The standard deviations of calibration curves determine the concentration limit as well as the accuracy of measured concentrations. With the WD-SXES, the better intensity ratio of peak to background can be obtained. Furthermore, the better energy resolution of the WD-SXES produces a genuine target spectrum well separated from overlapped spectra often taken place, and well defined background intensities not far away from the spectrum so that the intensity of the target spectra of the element of interest very close to the genuine one can be obtained.

As preliminary experiments, calibration curves of boron, carbon and nitrogen in steels were tried to be obtained within their each concentration range between 10 and 100 ppm in mass. The signal of each characteristic X-rays from the trace elements; B-K, C-K of the 2nd order and N-K of the 2nd order, could be unambiguously observed. The calibration curves for the three trace elements were linear. These straight lines indicated that the concentration range of 10 ppm in mass could be detected with this method. The results of the present experiments strongly suggest that the similar method can also be used for the elemental analysis of trace element analysis in semiconductors.

3-3. Compilation of spectra

One of the main purposes for the development of the WD-SXES was to extend the limit of the lower energy end of the wavelength dispersive X-ray emission spectroscopy in EPMA so that in the early stage of the development attention was mainly focused on the lower energy range of spectra. One of the successful results is the detection of the Li-K spectrum and its application to monitor the chemical state of lithium in a lithium ion battery anode described in the previous section. Because of the higher energy resolution of the WD-SXES, the shapes of the spectra well reflect the detailed state of the valence electrons. Naïve approach to use the spectrum shapes for the identification of the chemical state of the element concerned is to compare the observed shapes with the ones previously obtained for the standard specimens. Tentative compilation has been published as an appendix in the leaflet prepared for the first JEOL seminar on Soft X-ray Emission Spectroscopy [6]. It contains a number of spectra of elements such as Li, Be, B, C, N, O, F, Mg, Al, Si, P and S in the states of either pure elements or compounds.

We are now trying to add more spectra in the compilation. One of the efforts is to measure and compile spectra of the standard specimens for EPMA. There are 32 pure elements commercially available as the standard specimens. Their spectra in the energy range between 50 and 210 eV have been

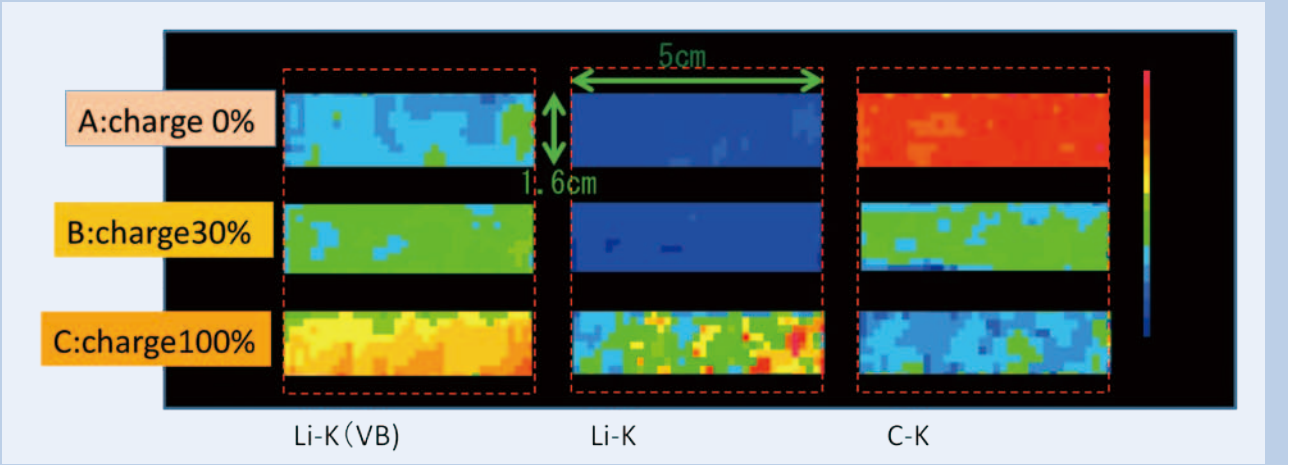

Fig. 6 Three maps constructed by using the X-rays in the three energy ranges corresponding to Li-satellite-K (left), Li-K (middle) and C-K of 4th order (right). Each map covered an area as large as 16 × 50 mm^2 consisted of three samples with different amount of charging: 0% (A), 30% (B) and 100% (C).

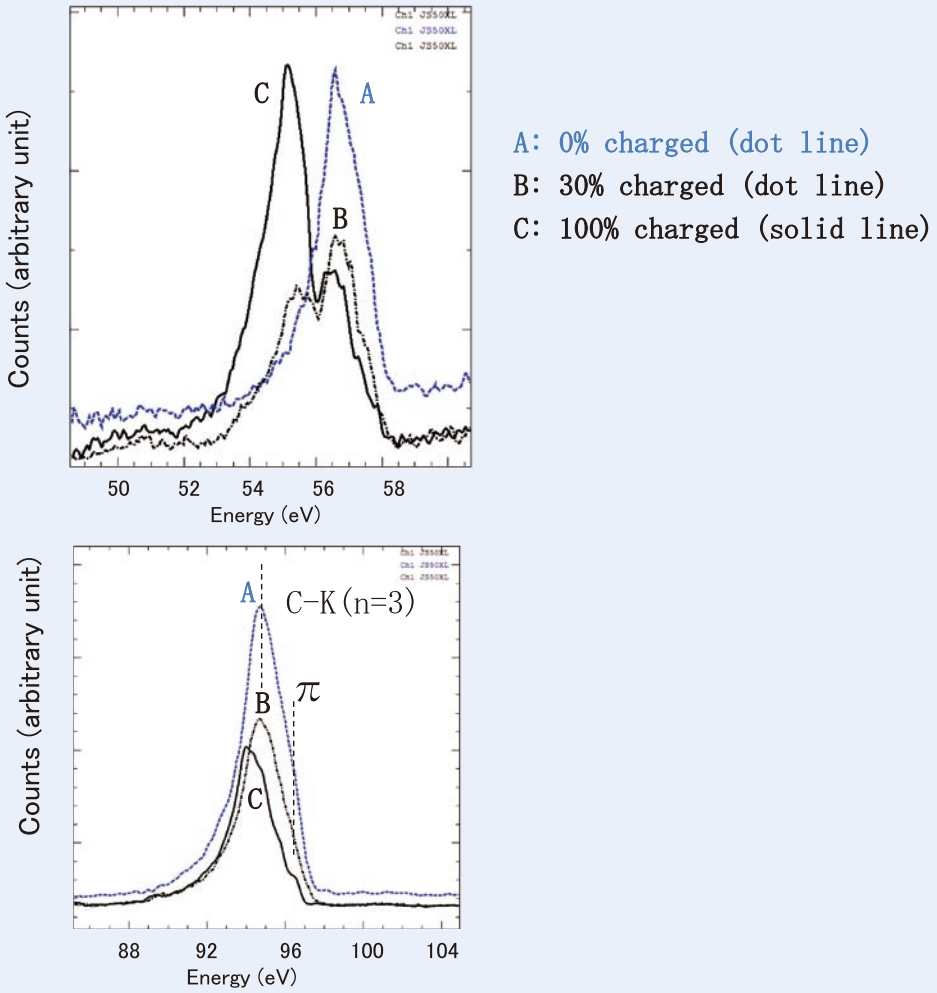

Fig. 7 Three typical spectra of a lithium ion battery anode corresponding to the three different conditions: 0% (A), 30% (B) and 100% (C). (a) The energy range between 48.5 and 59.5 eV covered the emission peaks of the Li-satellite-K, Li-K and C-K of the 5th order; and (b) between 62 and 74.5 eV covered the one of the C-K of the 4th order.

measured using both dispersion elements; JS50XL and JS200N in the following condition; accelerating voltage: 5 kV, probe current: 100 nA, and acquiring time: 5 × 60 s. One of the examples of the spectra obtained in this series of the systematic effort is shown in **Fig. 8**. Each spectrum of metal Pt and Au in the sixth row of periodic table of the elements show one distinct peak consisting of two sub-peaks in the energy range between 120 and 150 eV together with a few additional peaks in the lower energy range. As far as the present authors are concerned, these peaks have not explicitly been reported in the literature, especially in the energy range shown in the figure. Based on the table on X-ray wavelengths [7], the peaks in those spectra were assigned as shown in the figure. Roughly speaking, the shapes of two spectra look rather similar, except the shift of the peak position to higher energy by about 50 eV with increasing the atomic number from Pt to Au. The similar systematic energy shift of the peaks has been observed in spectra of a series of the sixth row elements; starting from Hf, continuing Ta, W, Re, Os, Ir, Pt until Au. Although the shapes of the peaks of Pt and Au are similar, slight difference may be noticed. Many features in these series of spectra including the peaks described above are awaited to be explained.

4. Conclusion

A newly developed wavelength dispersive soft X-ray emission spectrometer (WD-SXES) with two kinds of gratings (JS50XL and JS200N) were installed to EPMAs. It covered the energy range between 50 and 210 eV for commercial use. Experimentally the energy range could be extended down to 46 eV. The energy resolution of this WD-SXES was 0.2 eV which was evaluated from the Fermi edge of the Al-L spectrum.

The Li-K and Li-satellite-K emission spectra due to lithium metal and lithium fluoride were observed for the first time in EPMA. The detection limit of lithium was estimated in a 5 mass % Li-Al alloy to be 40 ppm in mass. The Li-K and Li-satellite-K emission spectra from samples of a lithium ion battery anode were measured and mapped in an area as large as 16 × 50 mm^2 under different charging conditions. A clear

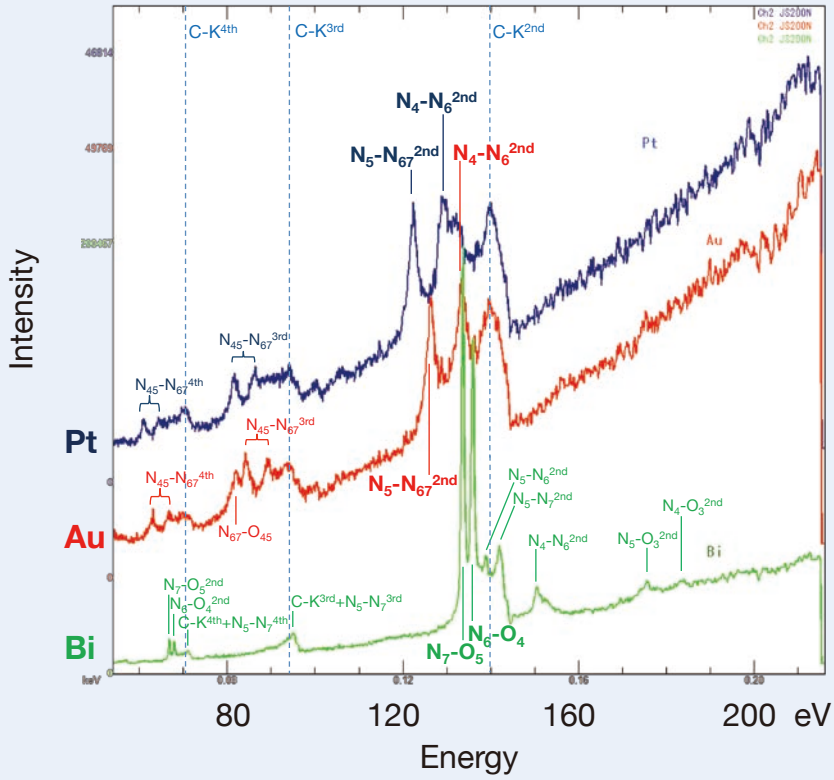

Fig. 8 Observed spectra of three elements: Pt and Au in the sixth row of the periodic table. The peaks in the energy range between 120 and 150 eV have not been reported in the literature. They are tentatively assigned as the 2nd order of N emission.

distinction in spectra due to chemical states of lithium shows a high potential for the characterization of lithium ion battery anodes.

For the trace element analysis of boron, carbon and nitrogen in steel, their calibration curves could successfully be obtained in the composition range between 10 and 100 ppm in mass. This method could detect their concentrations as small as 10 ppm in mass. The trace element analysis of light elements in other materials than steel could possibly be performed at this level of concentrations.

Efforts of compiling spectra obtained with WD-SXES are under way. The tentative compilation was published as an appendix in the leaflet prepared for the first JEOL Seminar on X-ray Emission Spectroscopy. During the present undertaking, quite a few observed peaks of heavy elements have been found that they have not been reported in the literature. It is emphasized that many aspects of spectra await explanation.

Acknowledgments

This work is supported as a program of Collaborative Development of Innovative Seeds (Practicability verification stage) by Japan Science and Technology Agency.

References

[1] M. Terauchi, H. Yamamoto and M. Tanaka, *Journal of Electron Microscopy*, **50**, 101 (2001).
[2] M. Terauchi, M. Koike, K. Fukushima and A. Kimura *Journal of Electron Microscopy*, **59**, 251 (2010).
[3] M. Terauchi, H. Takahashi, N. Handa, T. Murano, M. Koike, T. Kawachi, T. Imazono, M. Koeda, T. Nagano, H. Sasai, Y. Oue, Z. Yonezawa and S. Kuramoto, *Journal of Electron Microscopy*, **61**, 1 (2012).
[4] M. Terauchi, H. Takahashi, N. Handa, T. Murano, M. Koike, T. Kawachi, T. Imazono, M. Koeda, T. Nagano, H. Sasai, Y. Oue, Z. Yonezawa and S. Kuramoto, *JEOL News*, **Vol.47, No. 1**, 23 (2012).
[5] J. I. Goldstein, D. E. Newbury, P. Echlin, D. C. Joy, A. D. Romig, Jr., C. E. Lyman, C. Fiori and E. Lifshin, *Scanning Electron Microscopy and X-ray Microanalysis* 2nd ed. Plenum Press, New York, p.499 (1992).
[6] H. Takahashi, T. Murano, N. Handa and H. Ishikawa, Developavelength Dispersive Soft X-ray Emission Spectrometer for Section 1 Microscopes, paper presented in JEOL Seminar on Soft X-ray Emission Spectroscopy (2013).
[7] J. A. Bearden, *Review of Modern of Modern Physics*, **39**, 78 (1967).

Analysis of Organic Thin Films by the Laser Desorption/Ionization Method Using the JMS-S3000 "SpiralTOF"

Takaya Satoh

MS Business Unit, JEOL Ltd.

Laser Desorption/Ionization-Time of Flight Mass Spectrometry (LDI-TOFMS) is generally used for analysis of organic compounds because this technique generates little fragmentation of molecular ions at ionization. It makes possible to obtain information on molecular weights and molecular structures in organic compounds. In particular, a technique which uses the matrix compounds for enhancing ionization efficiency is well known as Matrix-Assisted Laser Desorption/Ionization-Time of Flight Mass Spectrometry (MALDI-TOFMS). This technique is widely used in the bio markets owing to its capability of ionizing proteins and peptides with the molecular weights of several thousands to several hundreds of thousands. The MALDI-TOFMS is also utilized for analysis of synthetic polymers. In many cases, LDI-TOFMS and MALDI-TOFMS have been used to estimate the molecular weights of organic compounds in solution. But very recently, techniques of imaging mass spectrometry, which controls the laser irradiation position by two-dimensional scan to acquire mass spectra for visualizing localization of chemical compounds with specific molecular weights, have been improved. The application of this innovative technique is increasingly spreading in the bio markets. The technology of Imaging Mass Spectrometry has been advancing for analyzing biological tissue sections, but in the future, it is expected to develop toward the material science markets. It is noted that various surface analytical techniques are already available in the material science markets. In order to study the advantages of LDI-TOFMS as one of effective surface analysis tools, it is essential to consider the complementary analysis of LDI-TOFMS with the existing surface analytical techniques. In this article, the advantages of using LDI-TOFMS for analyzing organic light-emitting diode material thin films, in accordance with comparison with Time-of-Flight Secondary Ion Mass Spectrometry (TOF-SIMS), X-ray Photoelectron Spectroscopy (XPS) and Scanning Electron Microscopy/Energy-Dispersive X-Ray Spectroscopy (SEM/EDS), have been studied. In addition, since LDI-TOFMS is a destructive analytical technique, the influence on the sample surface caused by LDI-TOFMS was also examined.

Introduction

The surface analytical techniques irradiate an electron beam, an ion beam or X-ray on the surface of the sample for investigation of its morphology and physical characteristics based on the interactions between the beam and substances existing on the sample surface. To observe the sample morphology, an optical microscope and an electron microscope are mainly used. To study the sample characteristics, a wide range of techniques is available depending on the incident particles (beam) and the signals to be detected. They include Electron Probe Microanalysis (EPMA), Auger Electron Spectroscopy (AES), X-ray Photoelectron Spectroscopy (XPS) and Time-of-Flight Secondary Ion Mass Spectrometry (TOF-SIMS). In recent years, electronic devices are frequently composed of organic compounds such as organic semiconductor, organic light-emitting diode (OLED) and organic film solar cell, and the use of them will be expected to further expand. It is increasingly important to inspect organic-compounds and their degradation mechanism in the products. Among surface analytical techniques, AES and XPS are capable of obtaining chemical bonding states or information on functional groups in chemical compounds, but those techniques have a difficulty in structural analysis of organic compounds. The TOF-SIMS is a mass spectrometry technique well known as a surface analytical technique. By using the dynamic SIMS, fragmentation of the molecular ions is likely to occur at ionization, thus making it difficult to apply SIMS to analyze organic compounds. Recently, techniques which utilize metallic clusters or gas clusters as a

3-1-2 Musashino, Akishima, Tokyo, 196-8558, Japan.

E-mail: taksatoh@jeol.co.jp

primary ion beam attached to TOF-SIMS have been succeeded to ionize more softly. These techniques are expected to expand the TOF-SIMS applications for organic compounds.

This article reports on Laser Desorption/Ionization-Time of Flight Mass Spectrometry (LDI-TOFMS). As a technique that utilizes the laser desorption mechanism, Matrix-Assisted LDI-TOFMS (MALDI-TOFMS) is in widespread use, which enables ionization of a variety of chemical compounds by properly combining a sample with matrix compounds enhancing ionization. Around 2000 year, the number of installed MALDI-TOFMS has been dramatically increased aiming to analyze proteins and peptides. Moreover in the material analysis fields, MALDI-TOFMS has been utilized for the analysis of synthetic polymers. The use of the matrix is essential for the measurement of these large-molecular weight organic compounds, thus the ionization technique using laser is generally called "MALDI". But, there are many chemical compounds which can be ionized only with laser irradiation. In this case, the used ionization technique is simply called "LDI".

Most of mass spectrometry techniques analyze samples in solution. MALDI-TOFMS also mixes the sample solvent and the matrix solvent to crystallize them by dropping on a target plate. By irradiating the co-crystal of matrix and sample compounds with the ultraviolet, MALDI-TOFMS ionizes various organic compounds contained in the sample and performs mass separation. In recent years, imaging mass spectrometry that adopts MALDI-TOFMS [1,2], which can acquire information about localization on the sample surface, is demonstrating technological improvement and therefore, the use of this unique technique is increasingly spreading. In Imaging Mass Spectrometry, the matrix is sprayed uniformly onto the sample surface and mass spectra are acquired while the laser irradiation position to the sample is two-dimensionally scanned. This process allows acquisition of information on two-dimensional distributions of specific chemical compounds. Imaging Mass Spectrometry has been expanding its applications to the bio markets from its dawn, including proteins, peptides, lipids, drugs and their metabolites. Most of the subjects for this technique are biological tissue section. On the other hand, in accordance with the establishment of biological tissue sectioning techniques, the users gradually start to study the application of Imaging Mass Spectrometry to the material analysis markets and also, this technique is expected to visualize information on localization of organic compounds on a thin film or a solid surface. In order to make Imaging Mass Spectrometry more effective in the material analysis markets, it is very important to carry out complementary analysis with the existing surface analytical techniques. In this article, the fundamental experiments using the JMS-S3000 "SpiralTOF" to examine LDI-TOFMS as one of surface analytical techniques were reported. The comparison with information obtained by XPS and TOF-SIMS and the influence of laser irradiation onto the surface of the organic thin film made of OLED material were examined.

Sample

For complementary analysis among LDI-TOFMS, TOF-SIMS and XPS, *N,N'*-Di(1-naphthyl)-*N,N'*-diphenylbenzidine (α-NPD), which is a material for a hole transport layer of an OLED, was deposited onto a Si substrate with 600 nm thick (hereinafter, called "α-NPD/Si"). In addition, in order to examine the influence of LDI on the sample surface, the author prepared a different sample of another Si substrate where a material for a hole transport layer of an organic EL (4,4',4''-Tris[2-naphthyl(phenyl)amino]triphenylamine (2-TNATA) of a thickness of 700 nm) was deposited onto the substrate and furthermore, α-NPD of a thickness of 1300 nm was deposited onto the prepared layer (hereinafter, called "α-NPD/2-TNATA/Si").

Analyses of Organic Thin Film Using LDI-TOFMS, TOF-SIMS and XPS

The JMS-S3000 "SpiralTOF" was used as an LDI-TOFMS. **Figure 1**(a) shows the external view of the SpiralTOF. The biggest feature of the SpiralTOF is adopting a JEOL originally-developed spiral ion trajectory (Fig. 1(b)) and this trajectory is formed by four hierarchical electrostatic sectors. The flight distance of 1 cycle is 2.093 m and the SpiralTOF achieves an effective flight distance of 17 m at 8 cycles. Here, the mass resolution of TOFMS is proportional to the flight distance. The general effective flight distance of the reflectron TOFMS is approximately a few meters, but the SpiralTOF which has an effective flight distance of 17 m can achieve the world-highest mass resolution among MALDI-TOFMSs. Furthermore, the electrostatic sectors which forms the spiral ion trajectory makes it possible to eliminate the fragment ions during their flight, thus a mass spectrum with little noise can be acquired. By attaching the TOF-TOF option [4], it is possible to perform structural analysis with the Tandem Mass Spectrometer (MS/MS). The high energy CID (collision-induced dissociation) could provide much structural information rather than low energy CID used in major MS/MS instruments. The SpiralTOF is equipped with a Newport Nd:YLF (349 nm) as an ionization laser source. The laser irradiation diameter onto the sample surface is approximately 20 μm and the laser intensity is 60 μJ at 100 % laser setting. α-NPD and 2-TNATA are ionized without requiring the matrix, so the experiments were performed by acquiring the mass spectra using LDI-TOFMS. **Figure 2**(a) shows a mass spectrum (*m/z* 10 to 800) acquired by fixing the laser irradiation position on the α-NPD/Si and by accumulations of 250 times. Only molecular ions of α-NPD are observed in the mass spectrum and it is found that ion fragmentation is very little at the ionization. Using the TOF-TOF option, the author acquired a product ion spectrum by selecting the observed molecular ions. Fig. 2(b) shows the observation result of the created fragment ions and the estimated fragmentation position of fragmentation. By the use of the High-Energy

CID technique, sufficiently much information was obtained to estimate the molecular structure.

The Ar gas cluster ion beam source attached to JEOL JMS-T100LP "AccuTOF LC-plus" developed in Matsuo Group at Kyoto University [5] was used for TOF-SIMS experiments. **Figure 3**(a) shows its external view. Fig. 3(b) shows a mass spectrum (*m/z* 0 to 800) which was acquired with the primary ion beam of Ar cluster ions (accelerating voltage: 10 kV) that irradiates on the "α-NPD/Si". The molecular ion peak of α-NPD ($[M]^{+\bullet}$) was observed. However, the fragment ions were also observed with noticeable abundance in low mass range, (*m/z* 100 to 500), compared to LDI-TOFMS. This may be due to two reasons. One is the fragment ions generated from α-NPD at the ionization. It was considered reasonable because the pattern of the product ion spectrum in Fig. 2(b) is relatively similar to the mass spectrum acquired with TOF-SIMS. On the other hand, the measurement region in depth direction by TOF-SIMS is confined to only 10 nm or less from the top surface of the sample, thus many chemical back ground peaks produced from surface contamination. Since Ar cluster ions are used for the primary ion beam, the mass spectrum achieves the littlest fragmentation among TOF-SIMSs. However compared to LDI-TOFMS, it should be taken into consideration the influence of the fragmentation or a remarkable influence of sample-surface contamination on the mass spectrum. TOF-SIMS makes it possible to perform high spatial resolution mapping and depth profiling by monitoring molecular ions or major fragment ions. For example during the mapping, a spatial resolution of 1 μm or less is achieved, indicating that this resolution performance is higher than that obtained by Imaging Mass Spectrometry using the present MALDI-TOFMS (typically a few tens of micrometers). But, when taking account of the fact that many fragment ions and the background originating from the surface contamination are observed, this technique is applicable only to the ions of major components. The chemical compounds deriving from the major components in degradations expected to be minor components; therefore, distinction with fragment ions or with surface contamination may become difficult.

The JEOL JPS-9010 was used for XPS experiments. **Figure 4**(a) shows its external view of the JPS-9010. The analysis area was set to be 1 mm diameter. Fig. 4(b) and (c) show the measurement result of α-NPD/Si. A spectrum shown in Fig. 4(b) is a wide spectrum (energy resolution: 1.7 eV equivalent to $Ag3d_{5/2}$) and the peaks of C and N which are constituent elements of α-NPD are clearly observed. In the spectrum obtained by XPS, which is a top-surface analysis instrument like TOF-SIMS, a Si peak originating from a substrate is not observed. Furthermore, a narrow spectrum (energy resolution: 0.5 eV equivalent to $Ag3d_{5/2}$) was acquired from the vicinity of the C peak. It was able to understand the peaks including the information on C-C

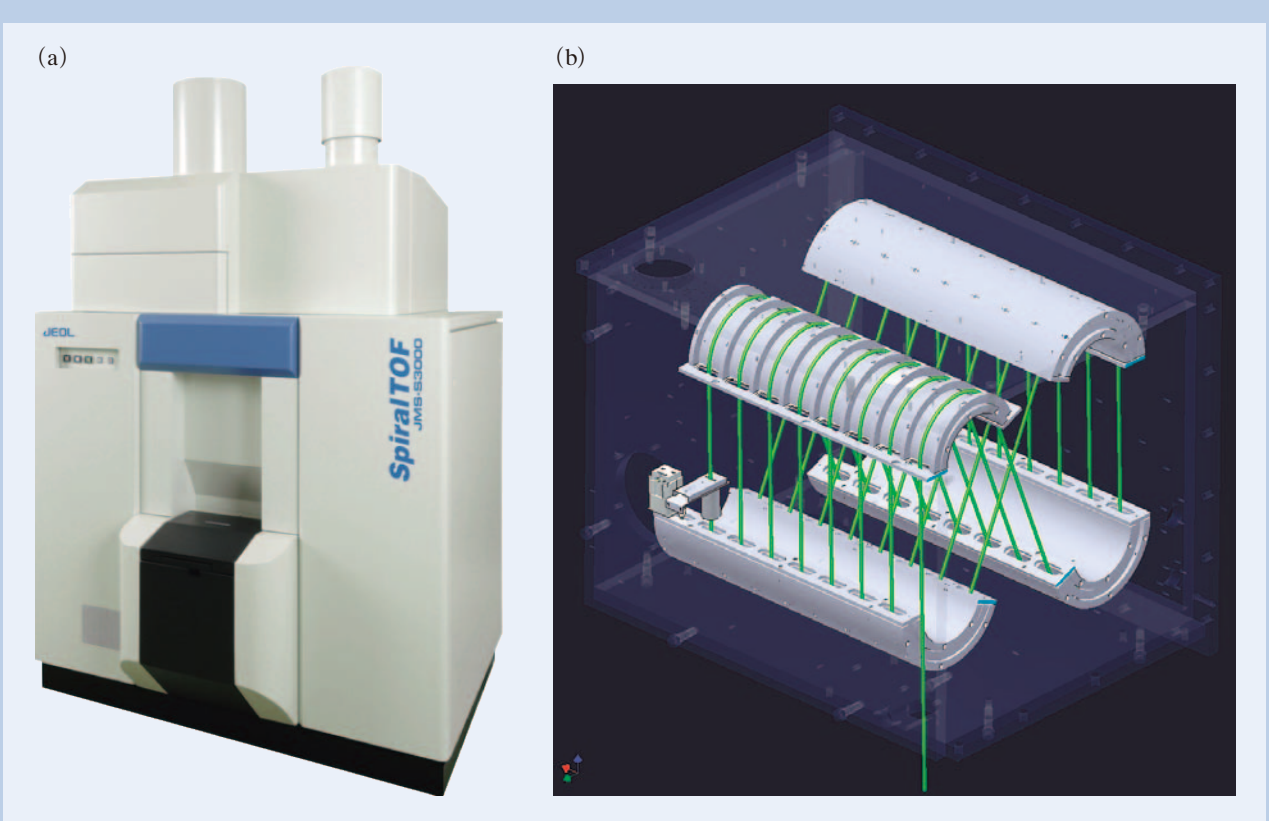

Fig. 1 (a) External view of the JMS-S3000 (when the Linear TOF option and the TOF-TOF option are attached), and (b) the schematic of the spiral ion trajectory in the JMS-S3000.

bonding and the C-N bonding. As compared to mass spectrometry techniques (LDI-TOFMS, TOF-SIMS, etc.), XPS provides non-destructive analysis and also can perform quantitative analysis which is difficult in mass spectrometry caused by ionization uncertainty. However, when the sample is an organic compound formed by a combination of limited elements, it is not easy to quantitatively analyze mixtures in the compounds with an XPS instrument. In particular, it is estimated that, when the limited elements are mixed as minor components where the composition of a degradation product does not change largely, the separation of their spectral peaks becomes more difficult.

As described above, the chemical information from LDI-TOFMS with both TOF-SIMS and XPS, which are the existing surface analytical techniques, are compared. The advantages of LDI-TOFMS in the analysis of organic compounds are the followings. LDI-TOFMS enables one to confirm mainly molecular ions from the mass spectrum and also, makes it possible to perform structural analysis through MS/MS analysis. These powerful features play a significant role especially in the analysis of

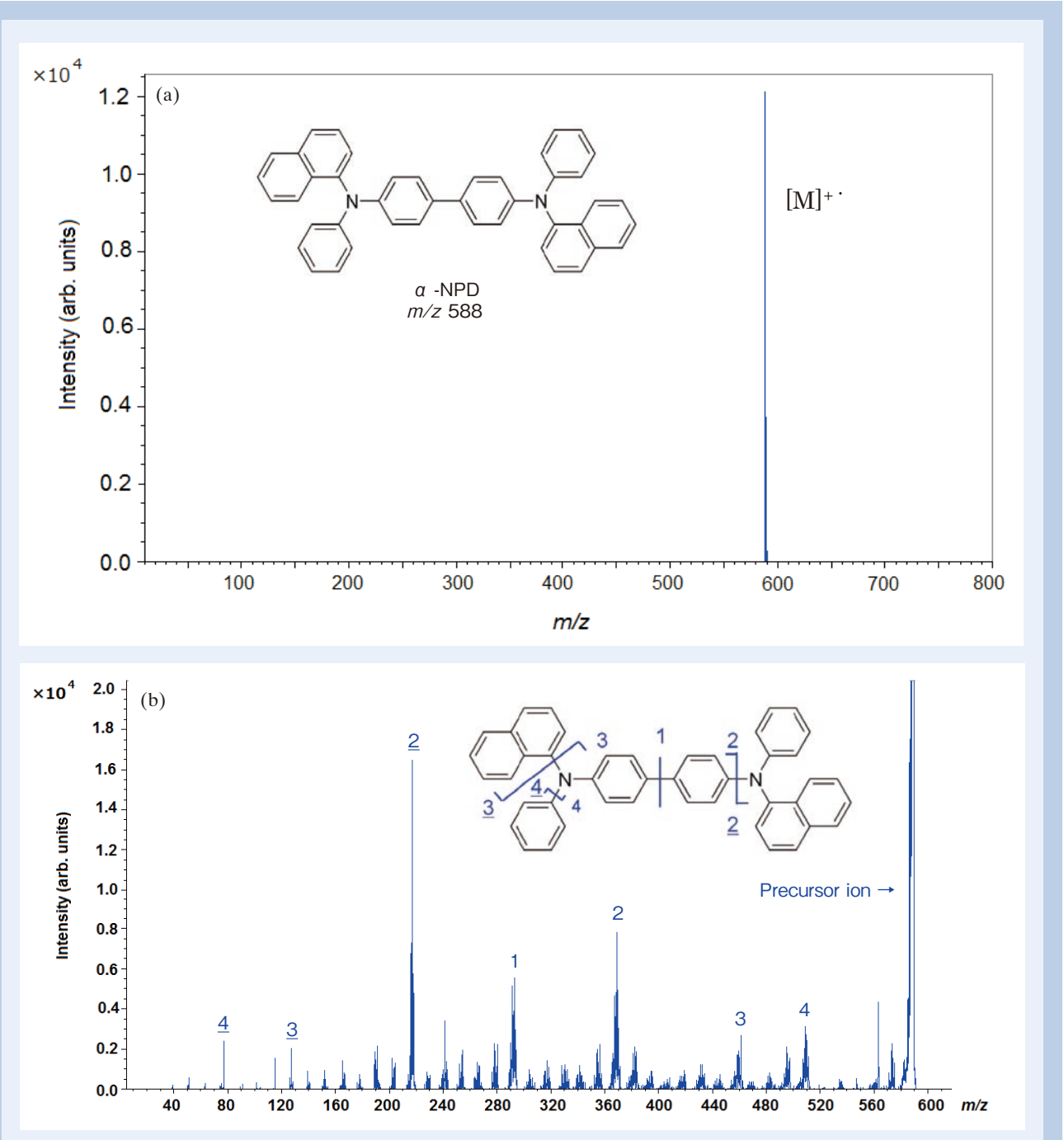

Fig. 2 (a) Mass spectrum of α-NPD acquired by LDI-TOFMS. Peaks indicating the molecular information on α-NPD are clearly observed. (b) MS/MS spectrum of α-NPD. Peaks well reflecting the structures of α-NPD are observed.

organic mixtures which exist on the sample surface. Also in degradation analysis, this technique is expected to allow the analysis of a minor component which is a degradation product created from the major component.

Influence of Laser Irradiation on the Sample Surface

The influence of laser irradiation on the sample surface by using the Scanning Electron Microscope/ Energy-Dispersive X-ray Spectrometer (SEM/EDS) was confirmed. **Figure 5**(a) shows the external view of the instrument used for this experiment, JEOL SEM JSM-7001FTTLLV equipped with the OXFORD Instruments AZtec Energy Standard X-Max50. Fig. 5(b) shows an SEM image of an irradiation scar after the sample surface was irradiated with a laser beam under the conditions of laser intensity 40% and the number of laser shot of 250. From this SEM image, the ablation of organic thin-film layers was observed at a diameter of 35 μm in the scar after the laser irradiation. In addition, Fig. 5(c) and (d) respectively show the analysis result of EDS spectra acquired from the irradiation scar

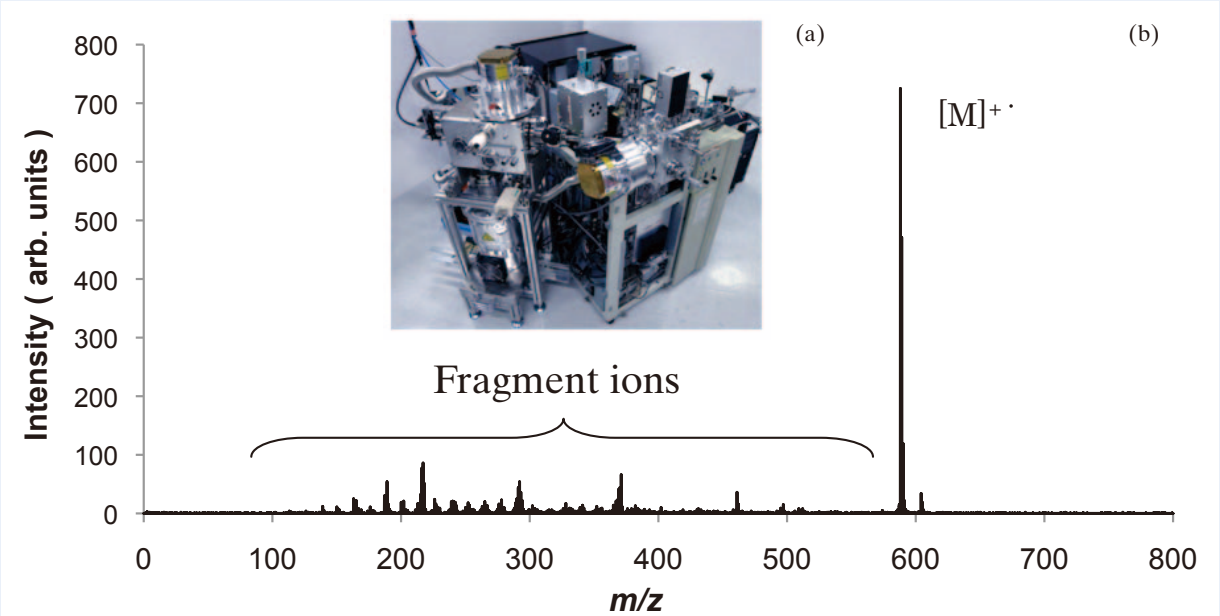

Fig. 3 (a) TOF-SIMS possessed by Matsuo Group, and (b) a mass spectrum of α-NPD mass spectrum acquired with TOF-SIMS. In addition to peaks indicating the molecular information on α-NPD, many peaks are observed, which are considered to originate from the fragment ions of α-NPD and the surface contamination.

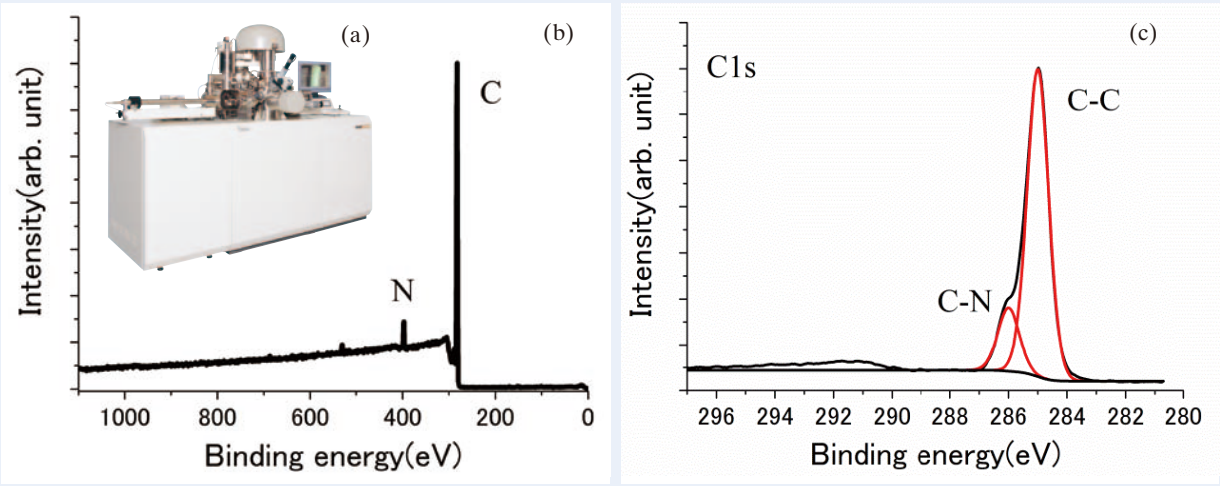

Fig. 4 (a) External view of the JPS-9010, and (b) A wide spectrum of α-NPD/Si. C and N which are constituent elements of α-NPD are clearly observed. (c) A narrow spectrum of α-NPD/Si and a narrow spectrum in the vicinity of C allows observation of peaks indicating the C-C bonding and C-N bonding.

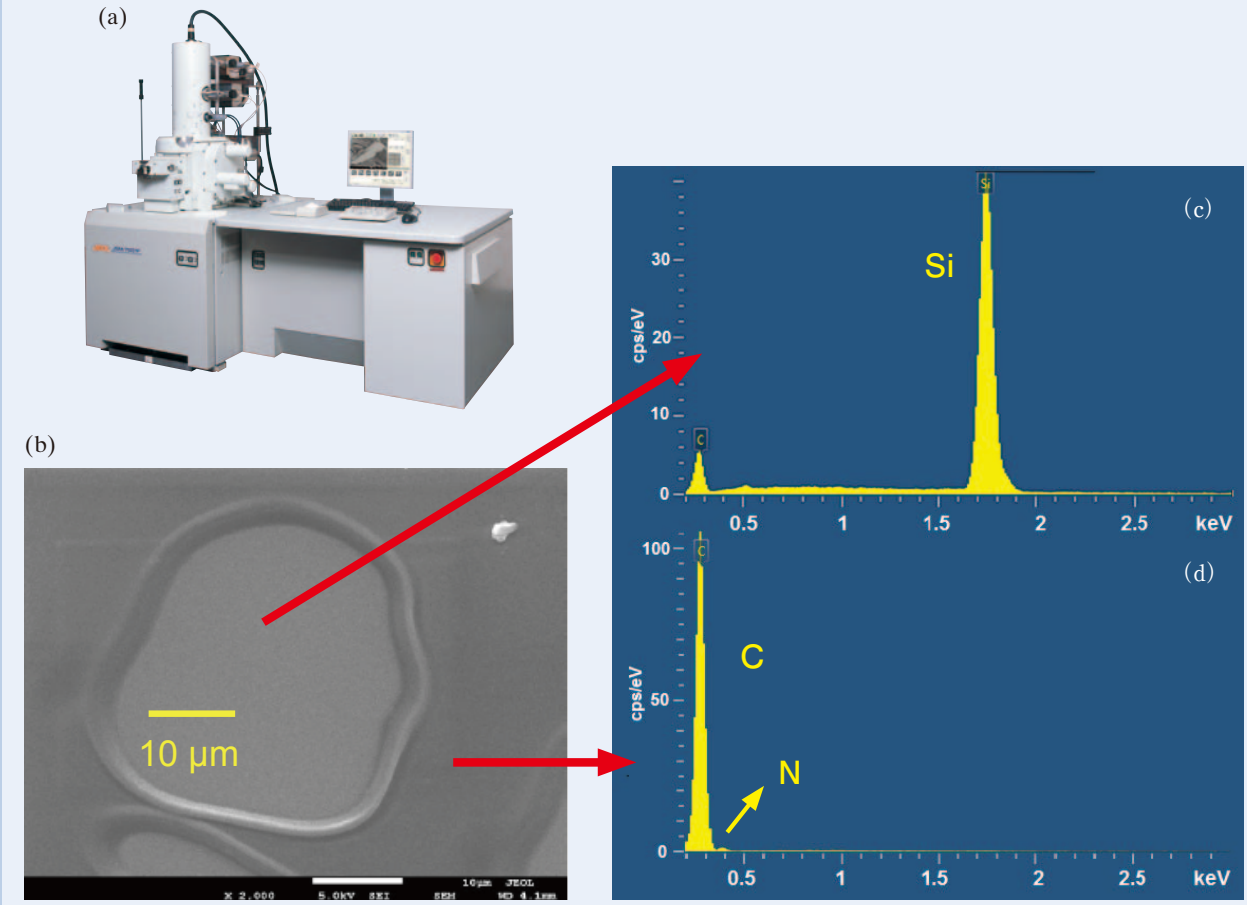

Fig. 5 (a) External view of the JSM-7001FTTLLV. (b) SEM image of an irradiation scar acquired after laser irradiation of the sample surface with laser intensity 40 % and the number of laser spot of 250. (c) EDS analysis result obtained from an area of a laser irradiation scar and an area in the vicinity of a laser irradiation scar. The result indicates that organic thin-film layers penetrate into the scar, confirmed by observation of Si from the laser irradiation scar and of C from the vicinity of the irradiation scar.

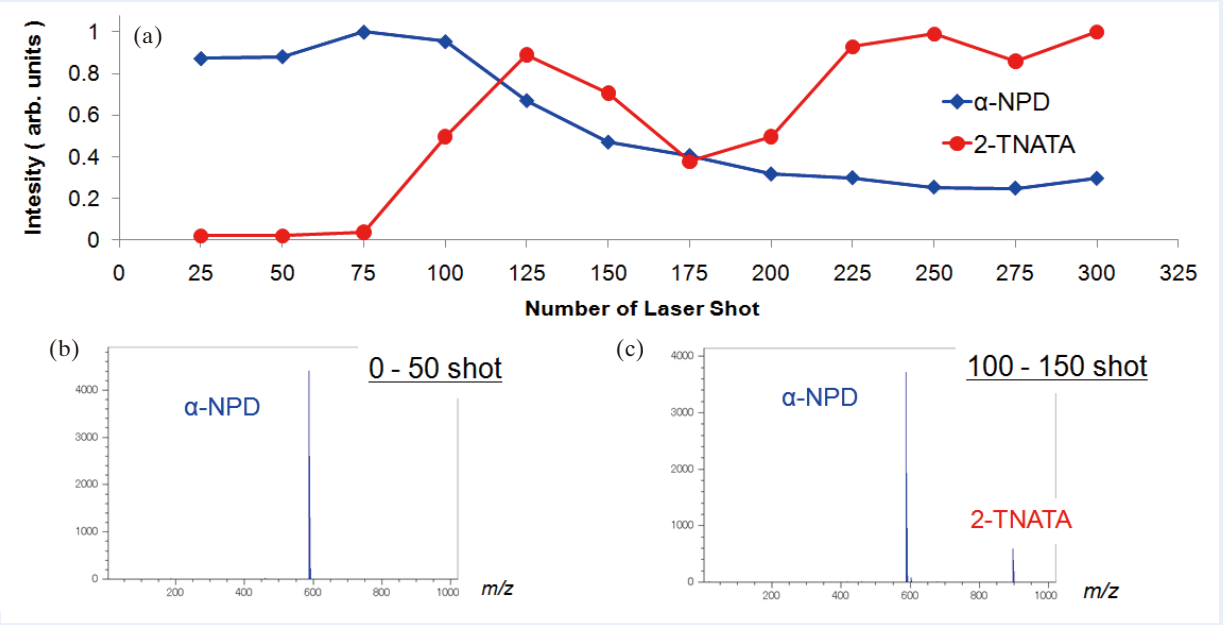

Fig. 6 (a) Ion intensity transitions of α-NPD and 2-TNATA when α-NPD/2-TNATA/Si is fixed and measured. Mass spectra acquired with the number of laser shot of 0 to 50 (b) and 100 to 150 (c) are also shown, respectively.

and from an area on which organic thin-film layers exist near the irradiation scar. The peaks of Si and C were observed from the former and latter spectrum, respectively, indicating that the laser irradiation allows penetration of the organic layers into the scar to be confirmed.

Mass spectra of α-NPD/2-TNATA/Si were acquired under the conditions of laser irradiation position fixed and laser intensity 40%. **Figure 6**(a) shows the plot diagram of ion intensity variations of molecular ions of α-NPD and 2-TNATA with respect to the number of laser shot. The ion intensity of α-NPD on the upper layers decreased as the number of laser shot increases. On the other hand, 2-TNATA on the lower layers started to be observed in the mass spectrum when the number of laser shot reached 100. Fig. 6(b) and (c) respectively show the accumulation mass spectrum acquired with the number of laser shot of 0 to 50 and 100 to 150 are shown in Fig. 6(b) and (c), respectively. The fragment ions are hardly observed in both spectrum and the 2-TNATA is clearly appeared in only Fig. 6(c). However, α-NPD on the upper layers was still observed even after 2-TNATA on the lower layers started to be observed. , It is expected that as the number of laser shot increases, the ionization region spreads in the plane direction as well as in the depth direction. The variation of the number of laser shot for the appearance of 2-TNATA in the mass spectrum according to the laser intensity is shown in **Fig. 7**. It is found that, as the laser intensity increases, 2-TNATA appears even when the number of laser shot is decreased. This result indicates that the influence of depth is affected by the number of laser shot and the laser intensity.

From these results, the author found that the influence of laser irradiation on the sample surface changes greatly depending on the laser irradiation conditions (laser intensity and the number of laser shot). For the depth direction, the present experiments indicate that the comprehensive information on regions between 100 nm and 1 μm is obtained. Compared to the measurement results obtained by top-surface analytical techniques such as XPS and TOF-SIMS, the present depth regions are considerably large. When increasing the number of laser shot and the laser intensity, the ionization region increases for not only in the depth direction but also in the plane direction, thus care is required for mapping.

Summary

This article reported on comparison and examination of organic thin-film analysis for LDI-TOFMS, TOF-SIMS and XPS. The XPS and TOF-SIMS have a difficulty in applying the techniques to multi-component samples. This is because XPS can obtain information only on elements and chemical bonding states, and TOF-SIMS makes a mass spectrum complicated caused by fragment ions. To the contrary, LDI-TOFMS can mainly observe molecular ions, thus it is suitable for the analysis of multi-components. In degradation analysis of organic chemical compounds in electronic parts, it

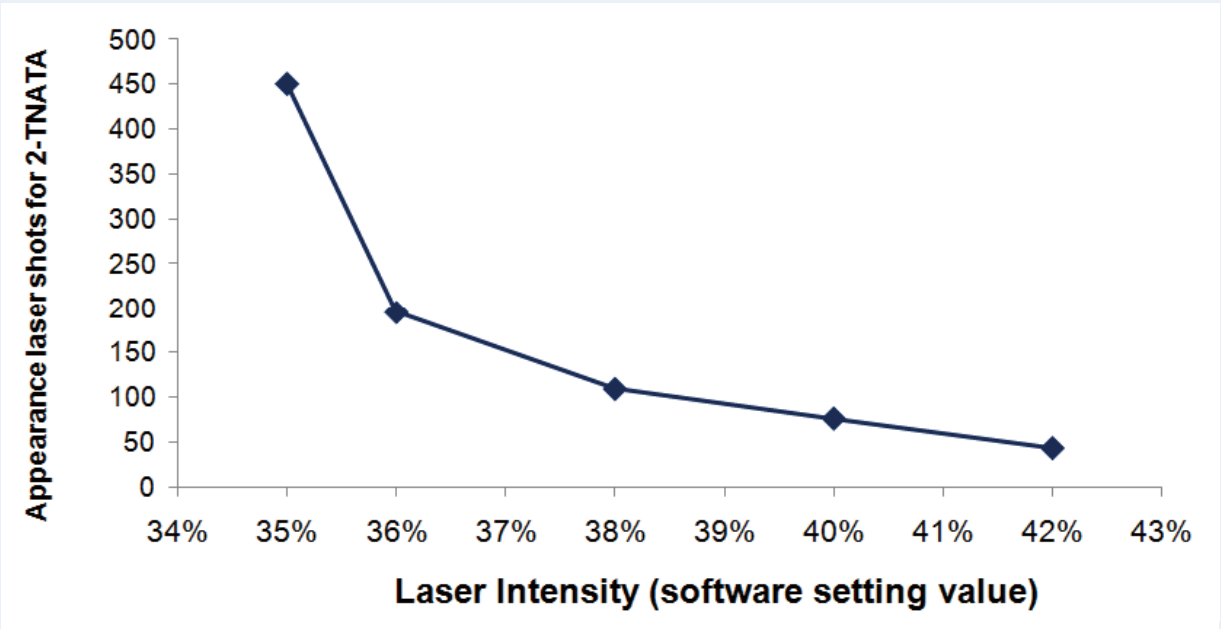

Fig. 7 The number of laser shot at which 2-TNATA starts to be observed when the laser intensity is changed. As the laser intensity increases, the influence of laser irradiation on the sample surface becomes large.

is expected that the total element composition ratio does not change largely, thus LDI-TOFMS can be used as an important tool for identifying degradation components because this technique enables one to confirm molecular ions and to perform structural analysis by MS/MS. In addition, it may be considered that the amount of the degradation product is not so large compared to original compound; therefore, the use of LDI-TOFMS allows one to expect clear analysis because LDI-TOFMS produces almost no fragment ions at the ionization.

Furthermore, the SEM observation result which revealed the sample-surface states after laser irradiation clarified that the comprehensive information of 100 nm or more was obtained in the depth direction of a thin film in an organic EL material. Influence of laser irradiation on the depth direction depends on the laser intensity and the number of laser shot. When LDI-TOFMS is used, the information of depth direction is considerably larger than that obtained by XPS and TOF-SIMS, in which the typical analysis depth is 10 nm or less. In the analysis of thin films having structures in the depth direction using XPS or TOF-SIMS, it is often combined with ion etching because they are top-surface analytical technique. In this case, it is possible to perform depth profiling with high resolution to depth direction. On the other hand, when LDI-TOFMS is used, clear acquisition of the information in the depth direction is rather difficult compared to XPS and TOF-SIMS, but it may be considered that LDI-TOFMS can classify chemical compounds contained in the same thin-film layer.

Now, the use of the (MA) LDI-TOFMS is making it possible to acquire two-dimensional distributions of chemical compounds on the specimen surface in accordance with the progress of Mass Imaging technologies. In the future, by accumulating the knowledge about ionization of samples of thin films and the influence of laser irradiation on the sample surface, LDI-TOFMS will widely be applied as one of powerful surface analytical techniques.

Acknowledgments

We would like to acknowledge Associate Professor J. Matsuo and his group at Quantum Science and Engineering Center, Kyoto University for providing their organic thin-films samples and TOF-SIMS mass spectra.

References

[1] Caprioli, R.M., Farmer, T.B., Gile, J.: Molecular imaging of biological samples: localization of peptides and proteins using MALDI-TOF MS. *Anal. Chem*. **69**, 4751–4760 (1997).

[2] Jungmann, J.H., Heeren, R.M.A.: Emerging technologies in mass spectrometry imaging. *J. Proteomics* **75**, 5077–5092 (2012).

[3] T. Satoh, T. Sato, J. Tamura, "Development of a high-Performance MALDI-TOF mass spectrometer utilizing a spiral ion trajectory": *J. Am. Soc. Mass Spectrom*., **18**, 1318 –1323, (2007).

[4] T. Satoh, T Sato, A. Kubo, J. Tamura, "Tandem Time-of-Flight Mass Spectrometer with High Precursor Ion Selectivity Employing Spiral Ion Trajectory and Improved Offset Parabolic Reflectron": *J. Am. Soc. Mass Spectrom*., **22**, 797-803, (2011).

[5] K. Ichiki, J. Tamura, T. Seki, T. Aoki, J. Matsuo, "Development of gas cluster ion beam irradiation system with an orthogonal acceleration TOF instrument" *Surface and Interface Analysis,* **45**(1), 522-524 (2013).

Table 1 Comparison of LDI-TOFMS with the other surface analytical techniques.

	Probe	Detected signal	Spatial resolution	Depth direction	Chemical information
Energy-Dispersive X-ray Spectroscopy (EDS)	Electron	X-ray	1 μm	< 1 μm	Element
Auger Electron Spectroscopy (AES)	Electron	Auger electron	10 nm	< 10 nm	Element, Chemical bonding states
X-ray Photoelectron Spectroscopy (XPS)	X-ray	Electron	10 μm	< 10 nm	Element, Chemical bonding states, Functional group
Time-of-Flight Secondary Ion Mass Spectrometry (TOF-SIMS)	Ion	Ion	100 nm	< 10 nm	Element,Partial molecular structure
Laser Desorption/ Ionization-Time of Flight Mass Spectrometry(LDI-TOFMS)	UV light	Ion	10 μm	a few 100 nm	Molecular structure

Ultra-Low-Temperature-Probes (UltraCOOL™ probe / SuperCOOL™ probe)

Katsuo Asakura and Naoyuki Fujii

JEOL RESONANCE Inc.

Introduction

Nuclear magnetic resonance (NMR) spectroscopy is an extremely important analytical technique, but its sensitivity is intrinsically very low. (Sensitivity in NMR measurements is defined by the signal-to-noise (S/N) ratio.) This is due to the fact that NMR utilizes radio frequencies, and electromagnetic waves at these frequencies have very low energy. Both Ultra-violet (UV) and visible light spectroscopy have much higher sensitivity than NMR as they utilize much higher energy electromagnetic waves, so allow analysis of micro samples.

Thus a relatively large amount of sample is required for NMR analysis compared to other spectroscopic techniques. However, NMR spectroscopy is of prime importance in chemical analysis because of the wide range of information it offers, often unobtainable by any other means, including the determination of the molecular structure of unknown samples.

But the low sensitivity of NMR is inevitably a major drawback in its use. In order to make structural analysis of e.g. natural products where sample amounts are limited, a realistic practicality, various methods have been devised to achieve higher sensitivity. Established methods, e.g. pulse & Fourier Transform (FT), offer improved accumulation efficiency. The use of higher magnetic fields by researchers and instrument manufacturers has also increased sensitivity and these approaches are now commonly implemented.

In addition, development of a wide range of probes has been on-going with the aim of more efficient detection of NMR signals. For example, a 10mm (large diameter) probe increases the sample volume to be detected and so increases the signal; this is good if there is sufficient sample available. Another example is a 3 1mm diameter (small-diameter) probe which is good for small amounts of samples by keeping the solution more concentrated. Another development is a capillary-type probe using a high-sensitivity solenoid coil instead of the standard Helmholtz coil which is used in probes in most superconducting FT-NMR systems.

As demonstrated in this article, instead of using a general purpose 5 mm diameter NMR probe, a wide range of methods are available for enhancing sensitivity. However, it must be noted that these methods offer complementary features and should be selected according to the requirements of both the sample and the study.

However, when trying to increase the sensitivity using a 'normal' sample, these methods may not be applicable. For example, for samples of low solubility and limited sample quantity, it is inappropriate to use either the large-diameter or small-diameter probe. To overcome this limitation, we have developed probes that operate at ultra-low temperatures.

Ultra-Low Temperature Probes and Sensitivity

Ultra-low temperature probes cool various components (detection coil, etc.) used in the NMR system, to very low temperatures using liquid Helium (4.2K) or liquid nitrogen (77K) as coolant. The cooled detection circuits, which are critical components in signal detection, not only increase the coil sensitivity but also reduce thermal noise. By increasing the signal intensity and reducing noise, sensitivity is greatly enhanced (**Fig. 1**).

With these probes, the detection coil and the pre-amplifier (signal amplification circuit) are cooled separately. As the temperature is reduced, so the electrical resistance of the materials used for these circuits also reduces, resulting in an increase in the Q value. At the same time, thermal noise is also reduced, so the sensitivity of the probe is increased, the increase being inversely proportional to the absolute temperature.
(**Equation 1**)

As is clear in Equation1, the detection circuits cooled down to very low temperatures improve greatly the sensitivity. In UltraCOOL™ probes, the detection coil is cooled with liquid-helium, whereas in SuperCOOL™ probes the detection coil is cooled with liquid-nitrogen.

3-1-2 Musashino, Akishima, Tokyo, 196-8558, Japan

E-mail: katsuo.asakura@j-resonance.com

For cooling the probe and the detection circuits, two systems are available. The 'Closed System' circulates cooled helium gas; the 'Open System' introduces liquid nitrogen directly into the detection coil. The UltraCOOL™ probe uses the 'Closed System', whereas the SuperCOOL™ probe may use either the 'Closed System' or the 'Open System'. The 'Open System' requires a supply of liquid nitrogen, but does not require a coolant-circulation system, thus reducing both the initial probe cost and the maintenance cost. In both probe systems, the sample temperature is independent of the cooled detection circuits. In the UltraCOOL™ probe, the temperature difference between the detection coil and the sample is approximately 300°C. It is important that the coil is thermally isolated from the sample (**Fig. 2** and **Fig. 3**). Therefore, the inside of the probe needs to be kept at high vacuum to ensure thermal insulation. The UltraCOOL™ probe achieves a sensitivity improvement of 4 to 5 times that of the equivalent room-temperature probe. In the case of the SuperCOOL™ probe, a sensitivity improvement of 2 to 3 times higher than that of a room-temperature probe is achieved.

As S/N improves by the square root of the number of accumulations, with an improvement in sensitivity of 4 to 5 times, the number of accumulations required to measure a spectrum to the same S/N ratio is therefore only 1/16 to 1/25. This offers significant time savings as measurements which conventionally required several days to complete may take only a few hours. This leads to a great improvement in operational efficiency of the NMR system (**Fig. 4** and **Fig. 5**). In the measurement example shown in the figure below, the 13C measurement acquired with a conventional room-temperature probe required a large number of times. Use of the UltraCOOL™ probe enabled confirmation of all of the signals in one scan (**Fig. 6)**.

In the INADEQUATE measurement (a famously insensitive experiment which gives information on ^{13}C-^{13}C bonding), almost all of the ^{13}C-^{13}C bonds are detected in an accepted period of time (43 hours) using the UltraCOOL™ probe (**Fig. 7**). The same experiment using a room-temperature probe would take 1075 hours (25 times longer than the UltraCOOL™ probe). Measurement periods of 45-days are generally not acceptable!

The UltraCOOL™ probe and the SuperCOOL™ probe are also capable of stable high-temperature measurements up to 150°C. Measurements at 150°C means a temperature difference greater than 400°C between the coil (near the sample) and the sample itself. However, detection of NMR signals is stable even when measurements require a long period of time (**Fig. 8**).

Summary

The newly developed UltraCOOL™ and SuperCOOL™ probes offer greatly enhanced sensitivity over conventional NMR probes, thus dramatically shortening the measurement time. These new probes can be used for NMR measurements at high temperatures with operability comparable to that of conventional room-temperature probes. Thus, the two new probes are expected to support high-temperature analysis in various fields, including the analysis of polymer samples.

Acknowledgments

We would like to acknowledge Dr. Y. Goda at the National Institute of Health Sciences for his support for our measurements with the 800 MHz UltraCOOL™ probe, and for provision of samples and data. A part of the development of the ultra-low temperature probes is now under progress as S-Innovation (Strategic Promotion of Innovative Research and Development) supported by Japan Science and Technology Agency (JST).

Metal at ambient temperature
The thermal motions of the atoms and the electrons are terrific.

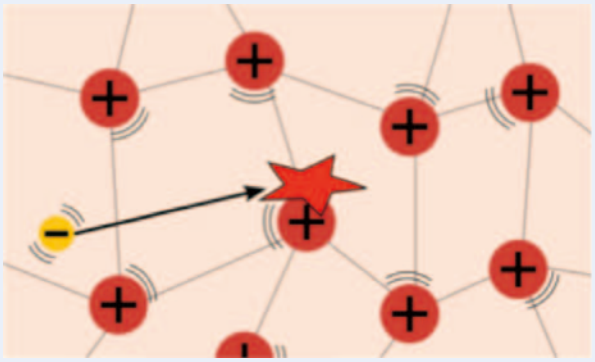

The thermal noise and the electric resistance of circuit are large.

Metal at very low temperature
The thermal motions of the atoms and the electrons are quiet.

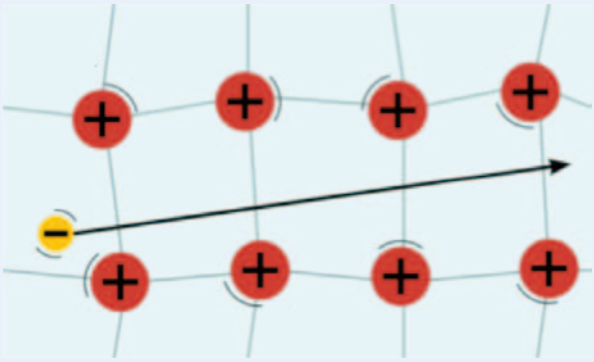

The thermal noise and the electric resistance of circuit are small.

Fig. 1 Electric circuit and temperature.

$$S/N \propto \sqrt{\frac{Q \cdot \eta}{T_c + T_a}}$$

Q : Q value of detection coil
η : Filling Factor
T_c : Coil temperature
T_a : pre-amplifier temperature

Eq.1) Sensitivity (S/N).

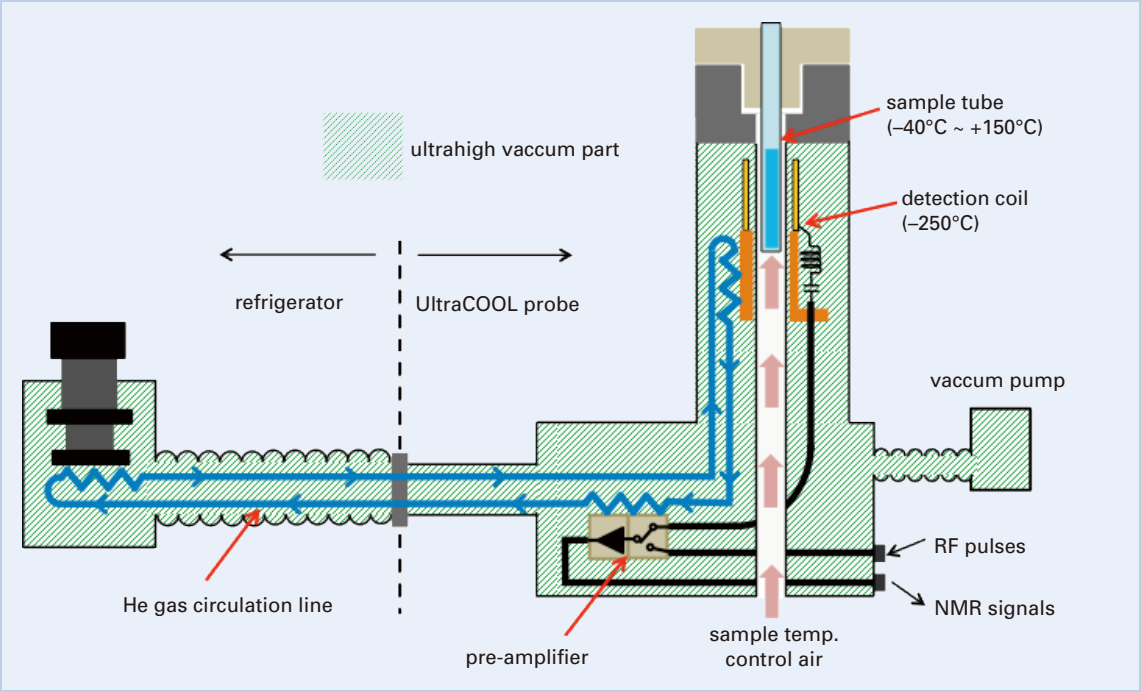

Fig. 2 Schematic illustration of UltraCOOL probe.

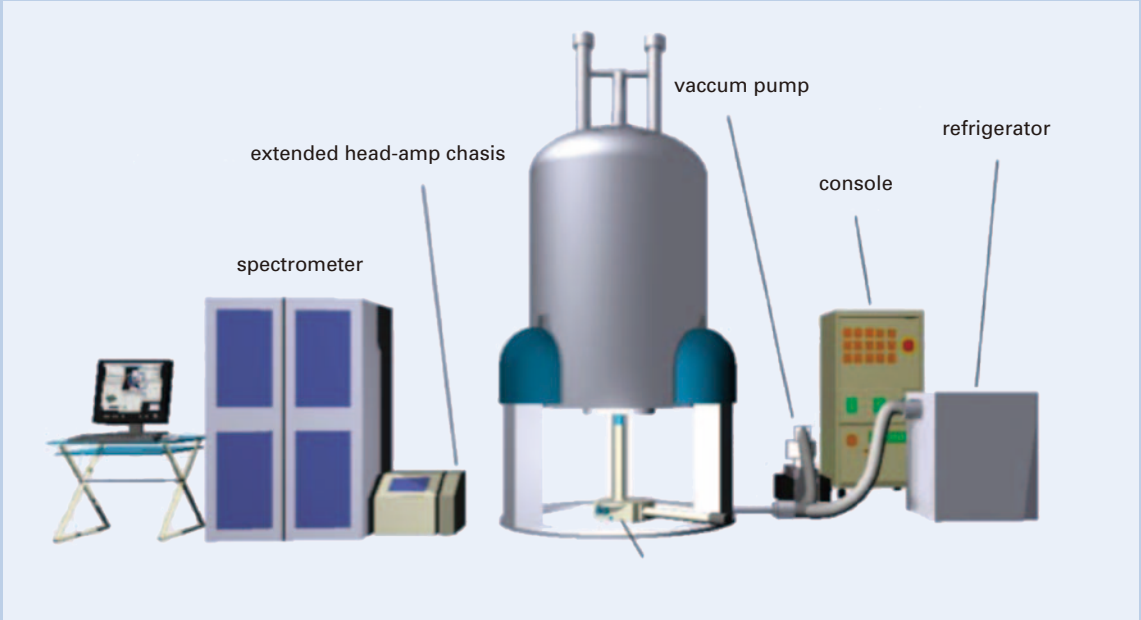

Fig. 3 Peripherals of UltraCOOL probe.

Fig. 4 Appearance of UltraCOOL probe.

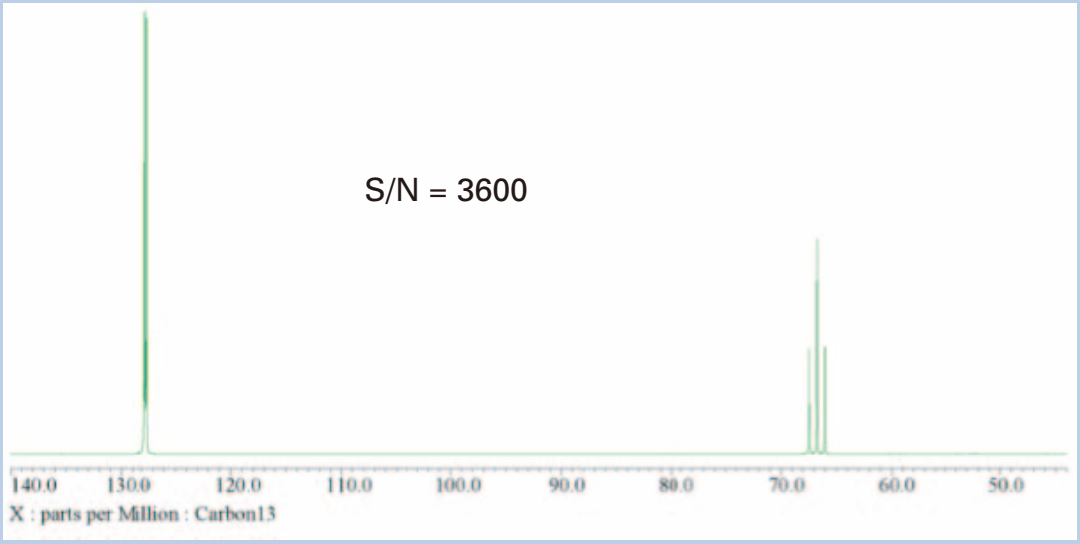

Fig. 5 ^{13}C sensitivity. 800MHz, ASTM, 1 scan.

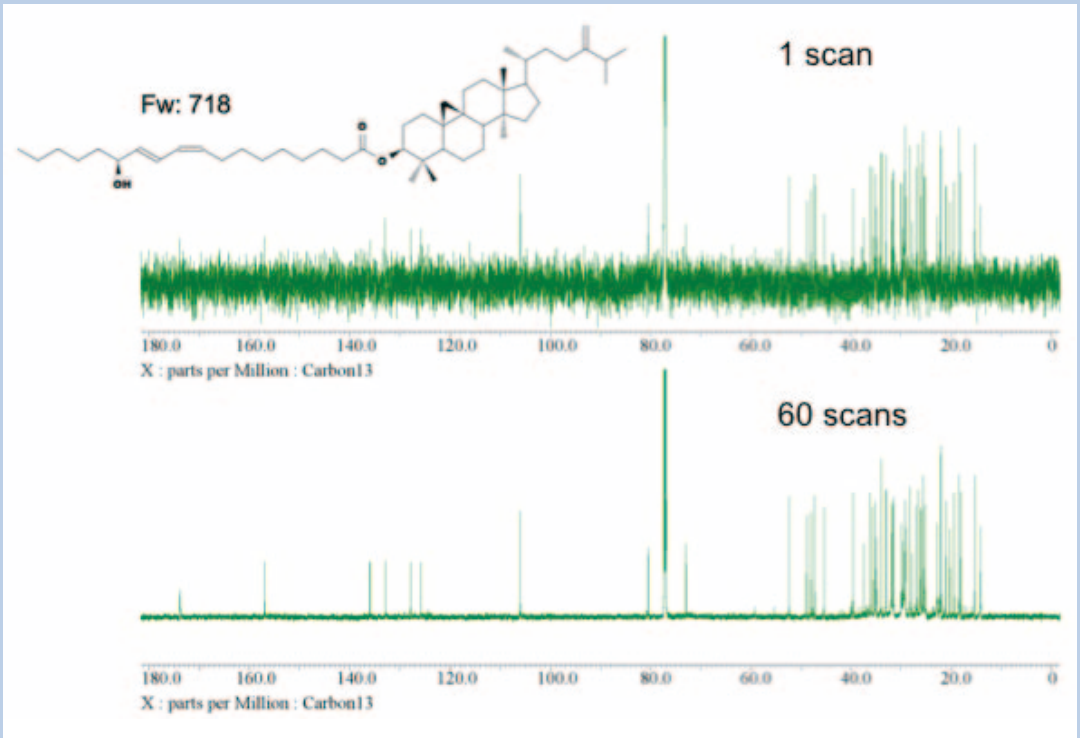

Fig. 6 $^{13}C\{^{1}H\}$ 1D experiment. 800MHz, 29 mg codonopilates in $CDCl_3$.

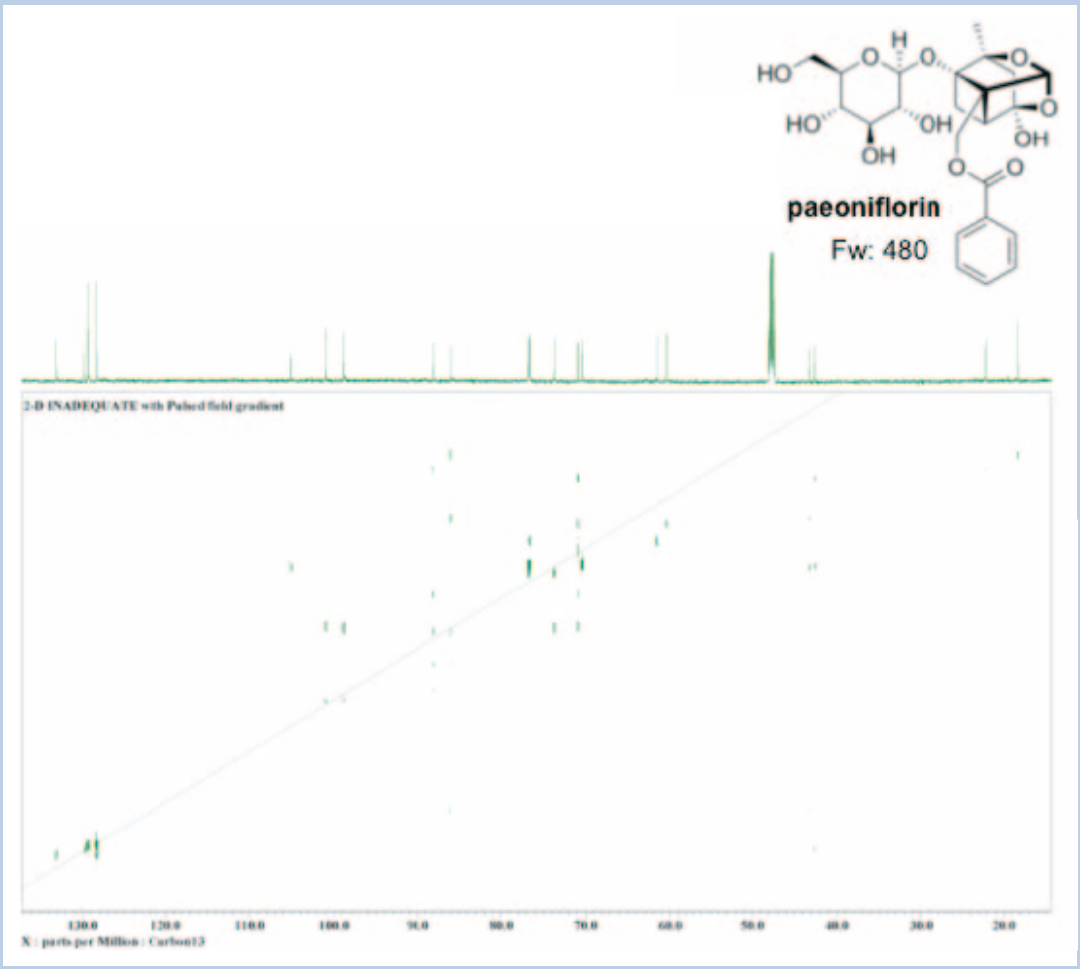

Fig. 7 ^{13}C 2D-INADEQUATE 800MHz, 10 mg paeoniflorin in CD_3OD, 512 scans (ca. 43 h).

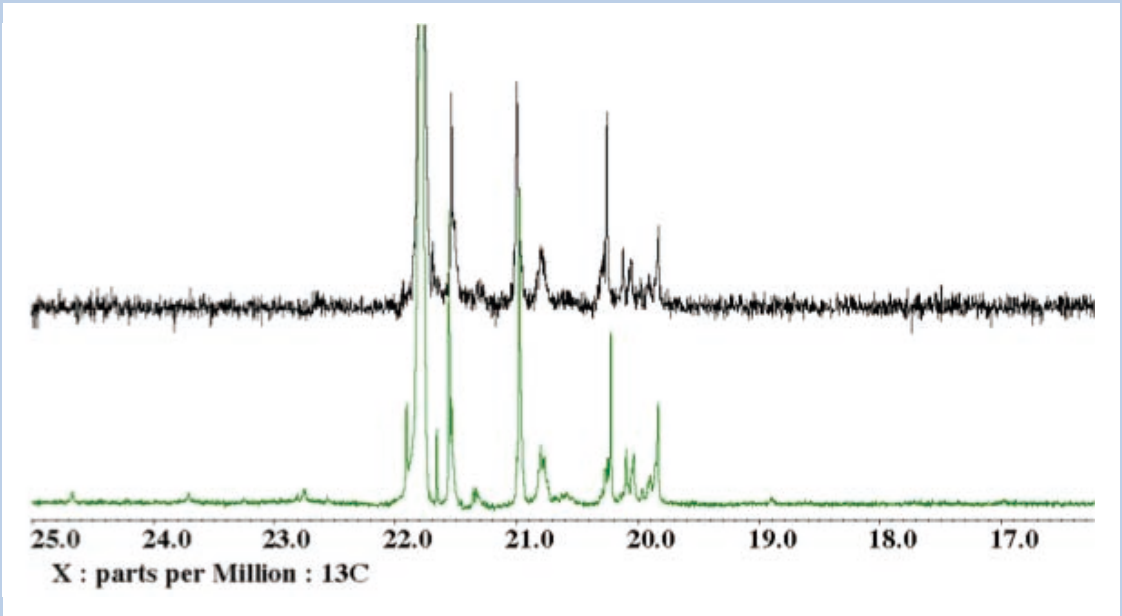

Fig. 8 polypropylene in ODCB-d_4.
above: 750MHz, room temp. probe, 110°C, 20,000 scans.
below: 600MHz, UltraCOOL probe, 150°C, 20,000 scans (19 h).
*750MHz data is kindly provided by Prof. Ute(Tokushima Univ.).

New Series of NMR Spectrometers JNM-ECZ

Kenichi Hachitani

JEOL RESONANCE Inc.

Introduction

New NMR spectroscopic methods continue to be developed for many different purposes, particularly for research. However, to achieve good results, the complex pulse sequences often require high precision RF control depending on the application or properties of the samples to be analyzed. At the same time, the demand for routine NMR measurements, for example in the fields of quality control and simple analysis, is remarkable, thus leading to requests for NMR to be a more 'user-friendly' technique.

Older, conventional NMR systems used analog technologies that would have led to relatively large instruments. However, the use of digital technologies has been advancing and this has enabled development of next-generated NMR systems with increased functionality, higher performance and greater expandability as well as providing improved general versatility.

In order to meet these demands and to anticipate future development of NMR measurements, JEOL RESONANCE Inc has developed a new NMR system, the JNM-ECZ series (* Notice). Building on the experience of the JNM-ECAII/ECXII/ECS series, the JNM-ECZ series uses fully integrated cutting-edge digital technologies. In this report, some of the hardware features of the JNM-ECZ spectrometers (ZETA) are introduced.

ECZ Series Spectrometers (NMR Spectrometer ZETA)

The ECZ series of spectrometers are equipped with Smart Transceiver System (STS), a new technology which achieves high-precision digital RF thus giving performance which greatly surpasses that of currently existing spectrometers. The basic design will enable the spectrometers to operate at ultrahigh frequencies exceeding 1.2 GHz. The high quality performance is complemented by the cutting-edge design in black.

The ECZ spectrometers are controlled by the built-in Spectrometer Control Computer (SCC), and the SCC is controlled by the host computer connected through an Ethernet link. The host computer provides the direct user interface, but the SCC can operate stand-alone. This prevents the danger of measurement omission should a communication problem occur between the SCC and the host computer. The SCC incorporates a large memory and hard disk, thus emphasizing the secure reliability of the pulse-programmed and measured data.

Two "Z" (ECZR/ECZS Series Spectrometers)

There are two spectrometers in the ECZ series. The spectrometers have customized features to meet different application needs.

ECZR series spectrometer (Fig. 1)

The high-end model ECZR spectrometer is configured primarily for a research oriented workplace. With a highly flexible and expandable configuration to meet the demands of various NMR measurements, the ECZR is compact compared to currently available spectrometers, and achieves overwhelming performance.

ECZS series spectrometer (Fig. 2)

The entry model ECZS spectrometer has the same basic functions, performance and capability of the ECZR spectrometer. Furthermore, the ECZS spectrometer is even more compact than the ECZR spectrometer and offers good general versatility. The main console of the ECZS spectrometer is amazingly small, less than 1/2 that of the current ECS series spectrometer.

3-1-2 Musashino, Akishima, Tokyo, 196-8558, Japan

E-mail: khachita@jeol.co.jp

Fig. 1 ECZR series spectrometer (JNM-ECZ500R).

Fig. 2 ECZS series spectrometer (JNM-ECZ400S).

STS (Smart Transceiver System)

The ECZ series spectrometers build on the highly successful system architecture of the ECAII/ECXII/ECS series spectrometers but are equipped with a highly advanced STS (Smart Transceiver System) developed using cutting-edge digital technologies. STS allows the construction of high-precision RF control with high-speed digital circuits mounted on a small logic device. Because of this, the ECZ series dramatically improves the digital functions and performance of the RF transmitter & receiver system. In addition, the ECZ series utilize a compact spectrometer that integrates the basic functions of the conventional NMR system into one board (**Fig. 3**).

Multi-sequencer control

Each DDS (Direct Digital Synthesizer) for the RF transmitter & receiver system is independently controlled at high speed by the respective slave sequencers. This independent control by the slave sequencers is comprehensively managed by the master sequencer. This mechanism allows for highly flexible control, thus allowing the creation of versatile pulse sequences. For example, the ECZR series spectrometer can control over 30 sequencers, that is, more than 3 times those of the ECAII series spectrometer. Thus, the ECZR series will be able to support many kinds of measurement methods that may be required in the future.

High-precision digital control

The time resolution for each of frequency modulation, phase modulation and intensity modulation, which are simultaneously and independently controlled as digital RF signals by the sequencers, is as small as 5 ns. This ultimate high time resolution allows for the control of a duration (modulation time width) of 5 ns (minimum). This corresponds to approximately 10 to 20 times improvement when compared to that offered by currently available spectrometers. Moreover as each characteristic is accurately controlled, the overall performance is also improved (**Fig. 4**). This improved digital-control performance further enhances the effectiveness of phase and intensity modulation pulses such as adiabatic pulse schemes (frequently used nowadays). Also in order to make measurements requiring ultra-high speed control, e.g. in recent solid-state NMR, the STS of the ECZ spectrometers provides high accuracy in controlling the gate signals and the external input & output trigger signals.

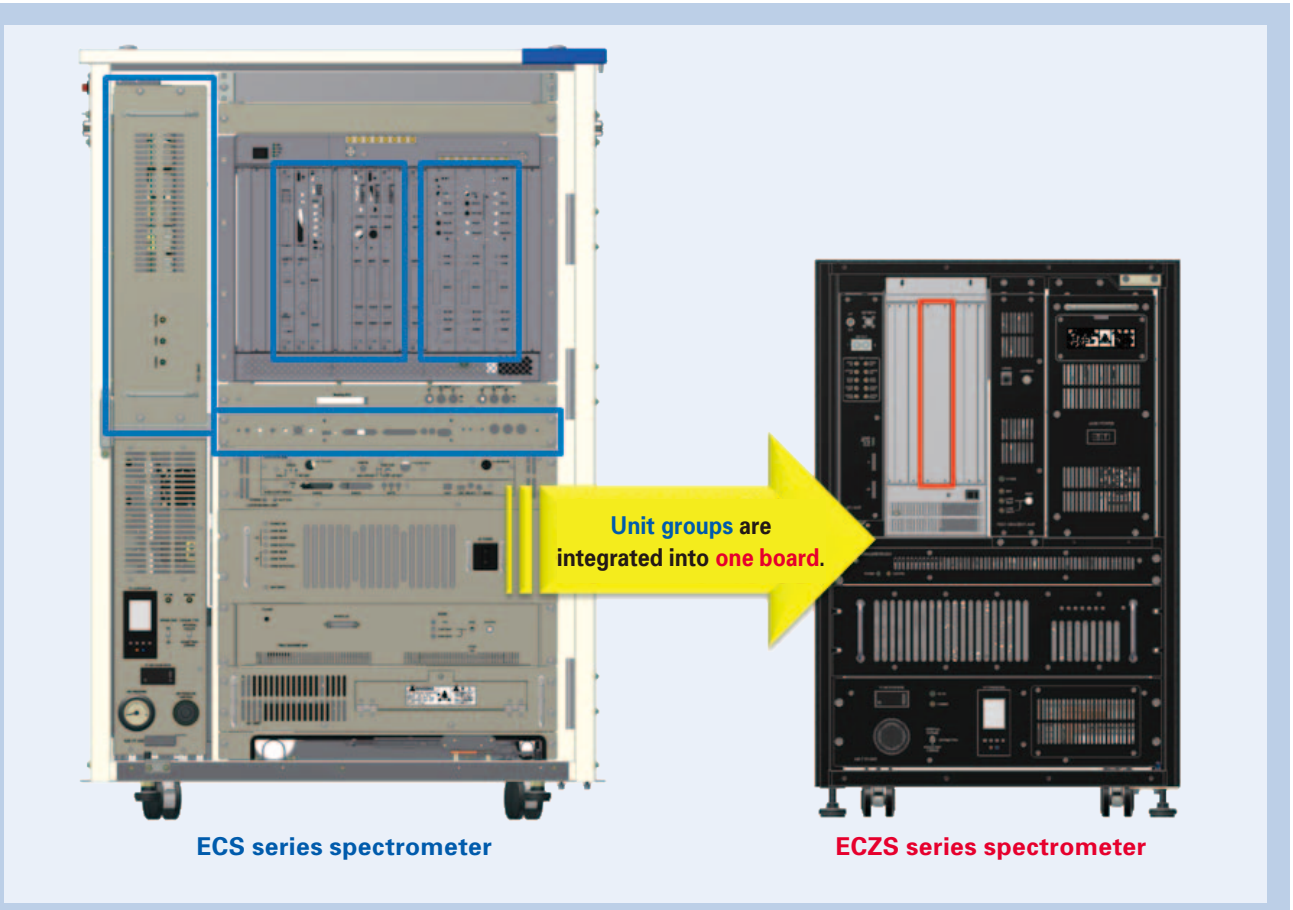

Fig. 3 Compact RF transmitter & receiver system based on STS.

Digital RF control

In this system, conventional RF oscillation and transmission functions are highly integrated. The new RF system can output up to 4 different frequencies for each RF transmitter channel. In addition, an expansion of the variable frequency offset range allows the ECZ spectrometers to support complicated measurements such as simple triple resonance within the standard configuration. The RF detection system is equipped with a sequencer control function comparable to that of the RF oscillation system. This makes it possible for the ECZ series spectrometers to carry out dynamic modulations of frequency and phase with or without synchronism, thus implementing important cutting-edge solid state NMR methods which have recently been published. In addition, DQD (Digital Quadrature Detection) provides a way to reduce artifacts including QD (Quadrature Detection) image and the centre 'spike' at 0 Hz, therefore, the improved digital RF control of the ECZ spectrometers makes the analysis of NMR spectra clearer.

Analog RF control

In the RF transmitter & receiver system, a hybrid system that combines under-sampling with super-heterodyne and over-sampling with direct conversion is achieved using a high-speed D/A (Digital to Analog) converter operating at 800 Msps and high-speed A/D (Analog to Digital) converter operating at 100 Msps. This makes the transmission and receiving efficient depending on the RF signals and linked by an optimized filtering mechanism.

PFG control and Digital-lock control

STS is also used for both PFG (Pulse Field Gradient) and lock control, and provides digital high performance comparable to that of oscillation and detection of RF signals. In particular, the ECZ spectrometers allow for lock-control with higher precision and better flexibility provided by a lock-feedback mechanism based on digital control technologies. This digital-control design enables the ECZ spectrometers to provide magnetic-field correction according to the environment of the

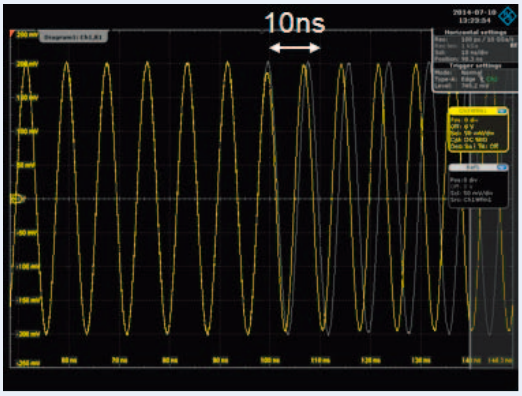

Frequency modulation (0 to 10 MHz)

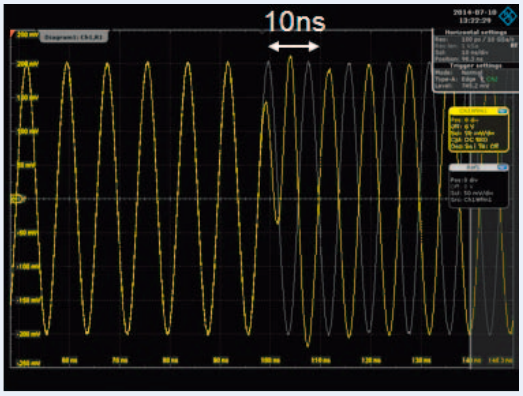

Phase modulation (0 to 180 degrees)

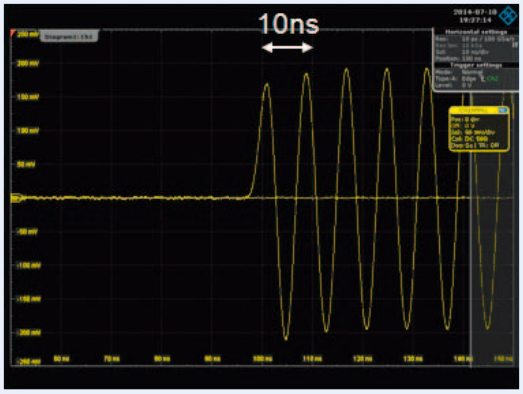

Intensity modulation (0 to 100%)

Fig. 4 RF waveforms generated by modulation control.

instrument and samples. The ECZ spectrometers can also use the lock transmitter & receiver system in application measurements.

Touch panel display (Head amplifier chassis)

The head amplifier chassis displays functions related to the super conducting magnet (SCM) and the probe mounted in the SCM. On top of the head amplifier chassis, a large-screen (5”) touch panel display is mounted, providing an intuitive multi-functional user interface. The spectrometer can display the RF reflection dip or a reflection value (bar display) during probe tuning, and the residual level of magnet cryogens can be displayed in real time (**Fig. 5**). This function improves visual usability as well as operability.

Summary

The new JNM-ECZ series of spectrometers has been developed with basic design concepts that supports excellent functionality, high performance, are highly expandable and offer high general versatility. Furthermore, the JNM-ECZ series has extremely high potential that supports flexible applications for the future development of NMR measurements. We expect that our innovative JNM-ECZ series will meet and exceed a wide range of demands in various scientific fields and to serve in cutting-edge research around the world as well as in general-purpose analyses.

* Notice
Instrument specifications are subject to change without notice.

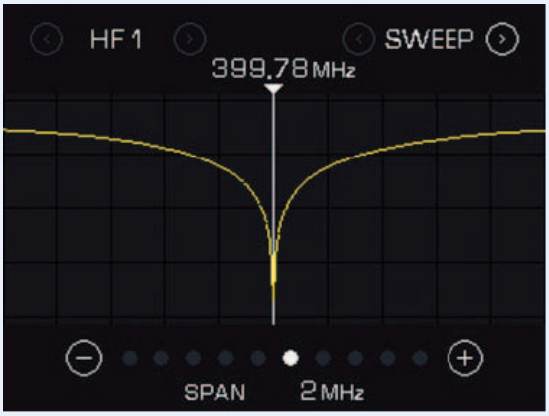

Reflection dip display

Reflection level (bar) display

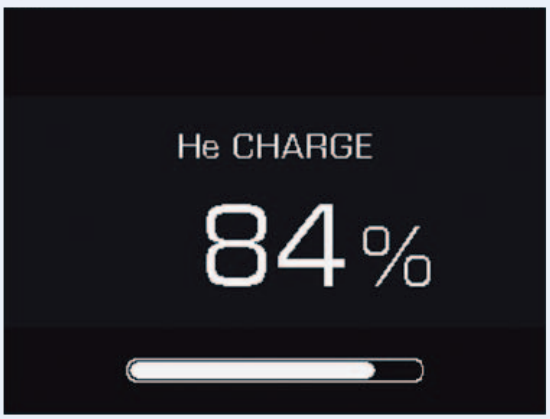

Current He level display

Fig. 5 Touch panel-displays on the head amplifier chassis.

JEOL
ISO 9001 Certificated
ISO 14001 Certificated

High technology for quality assurance and the environment.

Certain products in this brochure are controlled under the "Foreign Exchange and Foreign Trade Law" of Japan in compliance with international security export control. JEOL Ltd. must provide the Japanese Government with "End-user's Statement of Assurance" and "End-use Certificate" in order to obtain the export license needed for export from Japan. If the product to be exported is in this category, the end user will be asked to fill in these certificate forms.

JEOL Ltd. 1-2 Musashino 3-chome Akishima Tokyo 196-8558 Japan Sales Division Telephone:+81-3-6262-3560 Facsimile:+81-3-6262-3577

http://www.jeol.com/

ARGENTINA
COASIN S.A.C.I.yF.
Virrey del Pino 4071,
C1430CAM-Buenos Aires
Argentina
Tel. 54-11-4552-3185
Fax. 54-11-4555-3321

AUSTRALIA & NEW ZEALAND
JEOL(AUSTRALASIA) Pty.Ltd.
Suite 1, L2 18 Aquatic Drive
- Frenchs Forest NSW 2086
Australia
Tel. 61-2-9451-3855
Fax. 61-2-9451-3822

AUSTRIA
JEOL (GERMANY) GmbH
Oskar-Von-Miller-Strasse 1a, 85386
Eching, Germany
Tel. 49-8165-77346
Fax. 49-8165-77512

BANGLADESH
A.Q. CHOWDHURY SCIENCE & SYNERGY PVT. LTD.
87, Suhrwardry Avenue, Floor 2
Baridhara, Dhaka1212
Bangladesh
Tel. 8802-9862272, 8953450, 8953501
Fax. 8802-9854428

BELGIUM
JEOL (EUROPE) B.V.
Planet II, Gebouw B
Leuvensesteenweg 542,
B-1930 Zaventem
Belgium
Tel.32-2-720-0560
Fax.32-2-720-6134

BRASIL
JEOL Brasil Instrumentos Cientificos Ltda.
Av. Jabaquara, 2958 5°andar cj. 52
04046-500 Sao Paulo, SP
Brasil
Tel. 55-11-5070 4000
Fax. 55-11-5070 4010

CANADA
JEOL CANADA, INC.
3275 1ere Rue, Local #8
St-Hubert, QC J3Y-8Y6, Canada
Tel. 1-450-676-8776
Fax. 1-450-676-6694

CHILE
ARQUIMED INNOVATION
Arturo Prat 828,
Santiago, Chile
Tel. 56-2-634-6266
Fax. 56-2-634-4633

CHINA
JEOL(BEIJING) CO., LTD.
Room B1010/1110, Wantong New World Plaza No. 2
Fuchengmenwai Street, Xicheng District,
Beijing 100037, P.R.China
Tel. 86-10-6804-6321
Fax. 86-10-6804-6324

JEOL (BEIJING) CO., LTD., SHANGHAI BRANCH
Room 1505/1506, Nol 300Xi Kang Road,
Jing an Dist., Shanghai, 200040, China
Tel. 86-21-6248-4868/4487/4537/4404
Fax. 86-21-6248-4075

JEOL (BEIJING) CO., LTD., GUANG ZHOU BRANCH
N1601, World Trade Center Building,
#371-375, Huan Shi Road East, Guang Zhou,
Guangdong Prov., 510095, P.R.China
Tel. 86-20-8778-7848
Fax. 86-20-8778-4268

JEOL (BEIJING) CO., LTD., WUHAN BRANCH
Room A2118, Zhongshang Plaza Office Bldg.,
No. 7 Zhongnan Road, Wuhan,
Hubei, 430071, P.R.China
Tel. 86-27-8713-2567
Fax. 86-27-8713-2567

JEOL LTD. (BEIJING) CO., LTD., CHENGDU BRANCH
1807A Zongfu Building,
NO. 35 Zhongfu Road, Chengdu, Sichuan, 610016
P.R. China
Tel. 86-28-86622554
Fax. 86-28-86622564

EGYPT
JEOL SERIVCE BUREAU
3rd Fl. Nile Center Bldg., Nawal Street,
Dokki, (Cairo), Egypt
Tel. 20-2-3335-7220
Fax. 20-2-3338-4186

FRANCE
JEOL (EUROPE) SAS
Espace Claude Monet, 1 Allee de Giverny
78290, Croissy-sur-Seine, France
Tel. 33-13015-3737
Fax. 33-13015-3747

GERMANY
JEOL (GERMANY) GmbH
Oskar-Von-Miller-Strasse 1a, 85386
Eching, Germany
Tel. 49-8165-77346
Fax. 49-8165-77512

GREAT BRITAIN & IRELAND
JEOL (U.K.) LTD.
JEOL House, Silver Court, Watchmead,
Welwyn Garden City, Herts AL7 1LT, U.K.
Tel. 44-1707-377117
Fax. 44-1707-373254

GREECE
N. ASTERIADIS S.A.
56-58,S. Trikoupi Str. P.O. Box 26140
GR-10022, Athens, Greece
Tel. 30-1-823-5383
Fax. 30-1-823-9567

HONG KONG
FARMING LTD.
Unit No. 1009, 10/F., Prosperity
663 King's Road, North Point, Hong Kong
Tel. 852-2815-7299
Fax. 852-2581-4635

INDIA
JEOL INDIA Pvt. Ltd.
Elegance Tower, Level 2, 212B
Old Mathura Road, Jasola Business District Centre,
Near Apollo Hospital Jasola,
New Delhi 110 025, India
Tel. 91-11-6472-2578
Fax. 91-11-4060-1235

JEOL India Pvt. Ltd. Mumbai Branch
Regus Mumbai
Levels Ground & 1, Trade Centre Bandra Kurla Complex 1108,
Bandra (E) Mumbai, 400051,India
Tel : +91-22-40700700

INDONESIA
PT. TEKNOLABindo Penta Perkasa
Komplek Gading Bukit Indah Blok I/11
Jl. Bukit Gading Raya Kelapa Gading Permai,
Jakarta 14240, Indonesia
Tel. 62-21-45847057/58
Fax. 62-21-45842729

ITALY
JEOL (ITALIA) S.p.A.
Palazzo Pacinotti - Milano 3 City,
Via Ludovico il Moro, 6/A
20080 Basiglio(MI) Italy
Tel. 39-02-9041431
Fax. 39-02-90414343

KOREA
JEOL KOREA LTD.
Dongwoo Bldg. 7F, 1443, Yangjae Daero,
Gangdong-Gu, Seoul, 134-010, Korea
Tel. 82-2-511-5501
Fax. 82-2-511-2635

KUWAIT
Ashraf & CO. Ltd.
P.O.Box 3555 Safat 13036, Kuwait
Tel. 965-1805151
Fax. 965-24335373

MALAYSIA
JEOL(MALAYSIA) SDN.BHD.
508, Block A, Level 5,
Kelana Business Center,
97, Jalan SS 7/2, Kelana Jaya,
47301 Petaling Jaya, Selangor, Malaysia
Tel. 60-3-7492-7722
Fax. 60-3-7492-7723

MEXICO
JEOL DE MEXICO S.A. DE C.V.
Arkansas 11 Piso 2
Colonia Napoles
Delegacion Benito Juarez, C.P. 03810
Mexico D.F., Mexico
Tel. 52-5-55-211-4511
Fax. 52-5-55-211-0720

PAKISTAN (Karachi)
ANALYTICAL MEASURING SYSTEM (PVT) LTD.(AMS LTD.)
14-C Main Sehar Commercial Avenue Lane 4,
Khayaban-e-Sehar,
D.H.A-VII, Karachi-75500, Pakinstan
Tel. 92-21-35345581/35340747
Fax. 92-21-35345582

PANAMA
PROMED S.A.
Parque Industrial Costa del Este
Urbanizacion Costa del Este
Apartado 0816-01755, Panama, Panama
Tel. 507-303-3100
Fax. 507-303-3115

PHILIPPINES
PHILAB INDUSTRIES INC.
7487 Bagtikan Street, SAV Makati,
1203 Metro, Manila Phillippines
Tel. 63-2-896-6658
Fax. 63-2-897-7732

PORTUGAL
Izasa Portugal Lda.
R. do Proletariado, 1
2790-138 CARNAXIDE, Portugal
Tel. 351-21-424-73-00
Fax. 351-21-418-60-20

RUSSIA
JEOL (RUS) LLC.
Krasnoproletarskaya Street, 16,
Bld. 2, 127473, Moscow,
Russian Federation
Tel. 7-495-748-7791/7792
Fax. 7-495-748-7793

SAUDI ARABIA
ABDULREHMAN ALGOSAIBI G.T.C. (Riyadh)
Algosaibi Building-Old Airport Road
P.O. Box 215, Riyadh-11411, Saudi Arabia
Tel. 966-1-477-7932

SCANDINAVIA
SWEDEN
JEOL (Skandinaviska)AB:
Hammarbacken 6A, Box 716, 191 27 Sollentuna
Sweden
Tel. 46-8-28-2800
Fax. 46-8-29-1647

SINGAPORE
2 Corporation Road
#01-12 Corporation Place
Singapore 618494
Tel. 65-6565-9989
Fax. 65-6565-7552

SOUTH AFRICA
ADI Scientific (Pty) Ltd.
370 Angus Crescent,
Northlands Business Park, 29 Newmarket Road
Northriding, Ranburg, Republic of South Africa
Tel. 27-11-462-1363
Fax. 27-11-462-1466

SPAIN
IZASA. S.A.
Argoneses, 13, 28100 Alcobendas,
(Poligono Industrial), Madrid, Spain
Tel. 34-91-663-0500
Fax. 34-91-663-0545

SWITZERLAND
JEOL (GERMANY) GmbH
Oskar-Von-Miller Strasse 1,
85386 Eching, Germany
Tel. 49-8165-77346
Fax. 49-8165-77512

TAIWAN
JIE DONG CO., LTD.
7F, 112, Chung Hsiao East Road,
Section 1, Taipei, Taiwan 10023
Republic of China
Tel. 886-2-2395-2978
Fax. 886-2-2322-4655

For NMR & Mass Spectrometer Products
Widetron Technologies Corp.
No.8-2., No.77, Sec.2, Zhonghua E Rd.,
East Dist., Tainan City 701, Taiwan(R.O.C.)
Tel. 886-6-289-1943
Fax. 886-6-289-1743

(For Mass Spectrometer Products)
Tech Max Technical Co., Ltd.
5F., No.11, Wuquan 2nd Rd., Wugu Dist.,
New Taipei City 248, Taiwan (R.O.C.)
Tel. 886-2-8990-1779
Fax. 886-2-8990-2559

For Semiconductor Products:
JEOL TAIWAN SEMICONDUCTORS LTD.
11F-1, No. 346, Pei-Da Road, Hsin-Chu City 300,
Taiwan, Republic of China
Tel. 886-3-523-8490
Fax. 886-3-523-8503

THAILAND
BECTHAI BANGKOK EQUIPMENT & CHEMICAL CO., Ltd.
300 Phaholyothin Rd. Phayathai, Bangkok 10400,
Thailand
Tel. 66-2-615-2929
Fax. 66-2-615-2350/2351

JEOL ASEAN TECHNICAL CENTER (JATC)
MTEC building room 533
114 Moo9, Thailand Science Park
Paholyothin Rd., Klong 1, Klong Luang,
Pathumthani 12120
THAILAND
Tel. 66-2-564-7738
Fax. 66-2-564-7739

THE NETHERLANDS
JEOL (EUROPE) B.V.
Lireweg 4, NL-2153 PH Nieuw-Vennep,
The Netherlands
Tel. 31-252-623500
Fax. 31-252-623501

TURKEY
Tekser A.S.
Kartal Cad. No: 55/3 Inonu Wah.,
Atasehir 34755, Istanbul, Turkey
Tel. 90-216-5736470
Fax. 90-216-5736475

UAE
MRS Group Dubai
P.O.Box: 171612,
Rashid Abdulla Al Noami Building
Suite No: 306, Damascus Street,
Al Qusais-3, Dubai, U.A.E.
Tel. 971-4-2581141
Fax. 971-4-2581151

Gulf Bio Analytical LLC
Office No.902, Saphire Tower,
Al Ittihad Road, Near DNATA Building,
Deira Dubai, UAE
(P.O.Box 28832)
Tel. 971-4250-7300
Fax. 971-4250-7400

JEOL Gulf
c/o Gulf Bio Analytical LLC
Office No.902, Saphire Tower,
Al Ittihad Road, Near Dnata Building,
Deira Dubai, UAE
(P.O.Box 28832)
Tel. 971-4-2579228
Fax. 971-4-2579448

USA
JEOL USA, INC.
11 Dearborn Road, Peabody, MA 01960, U.S.A.
Tel. 1-978-535-5900
Fax. 1-978-536-2205/2206

JEOL USA, INC. WEST OFFICE
5653 Stoneridge Drive Suite #110
Pleasanton, CA 94588, U.S.A.
Tel. 1-925-737-1740
Fax. 1-925-737-1749

VENEZUELA
GOMSA Service and Supply C.A.
Urbanizacion Montalban III
- Residencias Don Andres - Piso 7 - Apartomento 74
Avenida 3, entre calles 7 y 6
Montalban, Caracas, Venezuela
Tel. 58-212-443-4342
Fax. 58-212-443-4342

VIETNAM
TECHNICAL MATERIALS AND RESOURCES
IMPORT-EXPORT JOINT STOCK COMPANY(REXCO)
Hanoi Branch,
No. 13-Lot 12 Trung Yen, Trung Hoa Street,
Cau Giay Dist, Hanoi, Vietnam
Tel. 84-43-562-0516
Fax. 84-43-853-2511

(Ser. No. 132)

No. 9701H449C Printed in Japan, Kp